Přílohy k žádosti o zahájení řízení ke jmenování profesorem

Dalibor Martišek

Ústav matematiky
Fakulty strojního inženýrství
Vysokého učení technického v Brně

listopad 2020

Obsah

1 Životopis

Jméno a příjmení:	**Dalibor Martišek**	
Narozen:	29. května 1956 v Hodoníně	
Vzdělání a akademická kvalifikace:	1971 – 1975:	Gymnázium Brno, Lerchova 53
	1975 – 1979:	Pedagogická fakulta Univerzita J. E. Purkyně (dnešní Masarykova univerzita) Obor: učitelství 5. – 9. ročník aprobace: matematika – fyzika
	1981:	titul PaedDr. Pedagogická fakulta Univerzita J. E. Purkyně (dnešní Masarykova univerzita) obor: pedagogika
	1981 – 1983:	Přírodovědecká fakulta Univerzita J. E. Purkyně (dnešní Masarykova univerzita) obor: učitelství 5.–12. ročník aprobace: matematika – fyzika
	2000:	titul Ph.D. Fakulta strojního inženýrství VUT v Brně, obor Aplikovaná matematika
	2003:	hodnost docent, Fakulta strojního inženýrství VUT v Brně, obor Aplikovaná matematika
Přehled zaměstnání:	1979 – 1985:	středoškolský profesor Matematiky a fyziky, SOU Vojenské stavby Brno
	1986 – 2003:	odborný asistent, katedra matematiky Strojní fakulty VUT v Brně
	2003 – dosud:	docent, Ústav matematiky FSI VUT v Brno

Adresa: Technická 2896/2, 616 69, Brno, Česká republika
Telefon: +420 541 142 713
E-mail: martisek@fme.vutbr.cz

2 Doklady osvědčující vysokoškolské vzdělání

ČESKOSLOVENSKÁ SOCIALISTICKÁ REPUBLIKA

PEDAGOGICKÁ FAKULTA Univerzity J.E.Purkyně v Brně

Číslo: 170/79

Příloha k diplomu č. H 001835

VYSVĚDČENÍ

o státní závěrečné zkoušce

Dalibor MARTIŠEK,

narozený dne 29. května 1956 v Hodoníně

ukončil(a) podle § 13 odst. 1 zákona č. 19/1966 Sb., o vysokých školách, státní závěrečnou zkouškou

na pedagogické fakultě Univerzity J.E.Purkyně v Brně

řádné studium oboru učitelství pro školy I. cyklu

aprobace*) matematika - fyzika

specializace*) ---

větev*) ---

Jmenovaný(á) složil(a) ústní zkoušku

z pedagogiky dne 1. června 1979 s prospěchem výborně

z matematiky dne 31. ledna 1979 s prospěchem výborně

z fyziky dne 21. února 1979 s prospěchem výborně

a diplomovou práci na téma Vývojová interpretace H - R diagramu

---

obhájil(a) dne 11. června 1979 s prospěchem výborně

takže mu (jí) byl přiznán celkový prospěch

výborně.

V Brně dne 11. června 1979

Děkanát pedagog. fakulty Univerzity J. E. Purkyně v Brně

L. S.

Hadaš

děkan

Stupnice prospěchu:	výborně	velmi dobře	dobře	nevyhověl(a)

*) Co se nehodí, škrtněte!

SEVT – 96 149 6 (AKCE 31) Pg 1 – 72737/76

ČESKOSLOVENSKÁ SOCIALISTICKÁ REPUBLIKA

Číslo H * 001835 Čj. 170/79

DIPLOM

Dalibor MARTIŠEK,

narozený(á) dne 29. května 19 56 v Hodoníně

zakončením řádného studia státní závěrečnou zkouškou na pedagogické fakultě

Univerzity J.E.Purkyně v Brně

s celkovým studijním prospěchem S VYZNAMENÁNÍM

a nabývá podle zákona č. 19/1966 Sb., o vysokých školách, vysokoškolské kvalifikace v oboru učitelství pro školy I. cyklu — aprobace:

matematika - fyzika.

L. S.

V Brně dne 11. června 1979

děkan

SEVT - 25 585 1 St 02 - 5123 73

ČESKOSLOVENSKÁ SOCIALISTICKÁ REPUBLIKA

Vysoká škola Univerzita Jana Ev. Purkyně v Brně — Fakulta pedagogická

Číslo diplomu J * 6555 — č. 36/81

DIPLOM

Dalibor Martišek

(jméno a příjmení)

narozen(a) dne 29. května 19 56 v Hodoníně okres Hodonín

vykonal(a) státní rigorózní zkoušku ve studijním oboru teorie vyučování matematice

Podle § 44 odst. 2 nebo § 46 odst. 2 zákona č. 39/1980 Sb., o vysokých školách, se mu (jí) přiznává titul

PaedDr.

V Brně dne 4. prosince 19 81

rektor vysoké školy

LS

děkan fakulty

SEVT - 26 586 1

TZ 4-45 - 0029 81

ČESKOSLOVENSKÁ SOCIALISTICKÁ REPUBLIKA

Univerzita J. E. Purkyně v Brně Fakulta přírodovědecká

VYSVĚDČENÍ

o doplňujícím studiu učitelství všeobecně vzdělávacích předmětů
(příloha k diplomu čís. H 001835 ze dne 11.6.1979)

PaedDr. Dalibor M A R T I Š E K

narozen/a dne 29. května 1956 v Hodoníně

absolvent/ka pedagogické fakulty University J. E. Purkyně v Brně
(škola, fakulta)

s kvalifikací v oboru učitelství pro školy I. cyklu

absolvoval/a ve škol. roce 1981/82, 1982/83 doplňující studium zřízené podle výnosu MŠ ČSR čj. 35 115/78-31 ze dne 31. 1. 1979 v rozsahu 4 semestrů na přírodovědecké fakultě UJEP.

Studium úspěšně zakončil/a vypracováním závěrečné písemné práce na téma

" Vývojová interpretace HRD "

a ústní ~~státní~~ závěrečnou zkouškou před zkušební komisí

z matematiky a did.mat. dne 4. 11. 1982 s prospěchem výborně

z fyziky a did. fyziky dne 5. 10. 1983 s prospěchem výborně

Doplňujícím studiem dosáhl/a vysokoškolské kvalifikace v oboru učitelství všeobecně vzdělávacích předmětů, aprobační předměty matematika - fyzika.

V Brně dne 5. října 1983.

REKTORÁT UNIVERZITY J. E. PURKYNĚ V BRNĚ 1

děkan rektor

Universita J. E. Purkyně v Brně, fakulta přírodovědecká

D o l o ž k a

k diplomu čís. H 001835 vydaného dne 11. června 1979
Pedagogickou fakultou University J. E. Purkyně v Brně.

PaedDr. Dalibor M A R T I Š E K
nar. 29. května 1956 v Hodoníně

podle výnosu MŠ ČSR, jímž se zřizuje doplňující studium učitelství všeobecně vzdělávacích předmětů, ze dne 31.1.1979 čj. 36 115/78-31 dosáhl doplňujícím studiem na fakultě přírodovědecké University J. E. Purkyně v Brně vysokoškolské kvalifikace v oboru učitelství všeobecně vzdělávacích předmětů, aprobační předměty matematika - fyzika.

V Brně dne 5. října 1983.

REKTORÁT UNIVERZITY J. E. PURKYNĚ V BRNĚ 1

. . . . . děkan . . . . rektor

Č E S K Á R E P U B L I K A

VYSOKÉ UČENÍ TECHNICKÉ V BRNĚ
FAKULTA STROJNÍHO INŽENÝRSTVÍ

Příloha k diplomu č. VUT: 00230/2000

VYSVĚDČENÍ
O STÁTNÍ DOKTORSKÉ ZKOUŠCE

PaedDr. Dalibor MARTIŠEK

narozen dne 29. května 1956 v Hodoníně

vykonal podle § 47 odst. 4 zákona č. 111/1998 Sb., o vysokých školách a o změně a doplnění dalších zákonů (zákon o vysokých školách), státní doktorskou zkoušku v doktorském studijním programu

3913 V Aplikace přírodních věd
ve studijním oboru
Matematické inženýrství

na Fakultě strojního inženýrství Vysokého učení technického v Brně dne 13. ledna 2000 s prospěchem

prospěl

a obhájil dne 10. července 2000
disertační práci na téma
3D rekonstrukce výstupů z optických mikroskopů

Školitelem byl Doc. RNDr. Miloslav DRUCKMÜLLER, CSc.

V Brně dne 10. července 2000

VYSOKÉ UČENÍ TECHNICKÉ V BRNĚ Fakulta strojního inženýrství
L.S.

Prof. Ing. Josef VAČKÁŘ, CSc.
děkan

KLASIFIKAČNÍ STUPNICE

prospěl	neprospěl

Č E S K Á R E P U B L I K A

VYSOKÉ UČENÍ TECHNICKÉ V BRNĚ

Registrační číslo VUT: 00230/2000

DIPLOM

PaedDr. Dalibor MARTIŠEK

narozen dne 29. května 1956 v Hodoníně

získal vysokoškolské vzdělání studiem v doktorském studijním programu
3913 V Aplikace přírodních věd
ve studijním oboru
Matematické inženýrství
na Fakultě strojního inženýrství Vysokého učení technického v Brně.
Podle § 47 odst. 5 zákona č. 111/98 Sb., o vysokých školách a o změně a doplnění dalších zákonů (zákon o vysokých školách),
se mu uděluje akademický titul
"doktor"
ve zkratce "Ph.D." uváděné za jménem.

V Brně dne 10. července 2000

Prof. RNDr. Ing. Jan VRBKA, DrSc.
rektor

L.S.

Prof. Ing. Josef VAČKÁŘ, CSc.
děkan

VYSOKÉ UČENÍ TECHNICKÉ V BRNĚ

Vážený pan

PaedDr. DALIBOR MARTIŠEK, Ph.D.

nar. 29. května 1956

Na návrh Vědecké rady Fakulty strojního inženýrství Vysokého učení technického v Brně, podle § 71 zákona č. 111/1998 Sb., o vysokých školách a o změně a doplnění dalších zákonů (zákon o vysokých školách)

Vás jmenuji

s účinností od 9. října 2003

DOCENTEM

pro obor

APLIKOVANÁ MATEMATIKA

V Brně dne 9. října 2003
Č.j. 1077/9121/2003

prof. RNDr. Ing. Jan VRBKA, DrSc., Dr.h.c.
rektor

3 Vědecko-výzkumná činnost

Výzkumné oblasti:	počítačová geometrie	analýza obrazu
	počítačová grafika	vizualizace dat
	3-D rekonstrukce	fraktály

Počet publikací na Web of Science:	21
Počet citací podle ISI Web of Knowledge (bez autocitací):	80
Počet dalších citací (bez autocitací):	99
H-index podle ISI Web of Knowledge	7

4 Pedagogická činnost

Národní akreditační úřad

Člen stále komise pro metodiku hodnocení NAÚ pro VŠ v oblasti vzdělávání Matematika

Vyučovací předměty zavedené uchazečem na FSI VUT:

Počítačová geometrie a grafika (1PG)	– 1. semestr BS (všeobecné studium)
Počítačová grafika (SPG)	– 3. semestr BS (MI)
Vizualizace dat (SVD)	– 4. semestr NMS (MI)
Obrazová analýza v materiálových vědách (WON)	– 1. semestr BS (materiálové inženýrství)
Konstrukční geometrie (1KD)	– 1. semestr BS (všeobecné studium)
Programovací metody I (0S1)	– 1. semestr BS (MI) (nepovinný předmět)
Programovací metody II (0S2)	– 3. semestr BS (MI) (nepovinný předmět)

Další vyučovací předměty garantované uchazečem na FSI VUT:

Konstruktivní a počítačová geometrie (1KG)	– 1. semestr BS (všeobecné studium)
Konstruktivní a počítačová geometrie (1KG-A)	– 1. semestr BS (všeobecné studium – AJ)
Počítačová geometrie a grafika (1PG-K)	– 1. semestr BS (všeobecné studium)
Počítačová geometrie a grafika (1PG-A)	– 1. semestr BS (všeobecné studium – AJ)

5 Univerzitní aktivity

Člen Akademického senátu FSI VUT	2005 – 2017
Předseda Legislativní komise AS FSI VUT	2008 – 2011 a 2014 – 2017
Předseda AS FSI VUT	2011 – 2014
Koordinátor přijímacích zkoušek do 1. ročníku z matematiky na FS VUT	1996 – 2008
Koordinátor přijímacích zkoušek do BS z matematiky na FS VUT	2009 – dosud
Koordinátor přijímacích zkoušek do NMS z matematiky na FS VUT	2012 – dosud
Koordinátor přijímacích zkoušek do DS (inženýrská mechanika) z matematiky	2012 – dosud

6 Další odborné aktivity

Zvané přednášky

Martišek, D.: Matematické principy grafických systémů, Rektorát VUT, Brno, 2002
Martišek, D.: Modelování odrazu a lomu světla geometrickými prostředky, konference Geometry and Computer Graphics, JU České Budějovice 2008
Martišek, D.: Fraktály – matematická monstra, anebo prostá realita? Historicko- didaktická konference MFF UK, Jevíčko 2009
Martišek, D.: Počítač ve středoškolské matematice, MFF UK, Praha 2009
Martišek, D.: Otazníky středoškolské informatiky, Historicko- didaktická konference MFF UK Velké Meziříčí 2010
Martišek, D.: Fraktály – kouzla geometrie a přírody, MZK Brno 2012
Martišek, D.: Od Hausdorffa k Mandelbrotovi (a ještě trochu dál), MFF UK Praha 2013
Martišek, D.: Fraktální dimenze a její měření, MFF UK Praha 2014
Martišek, D.: Trojúhelník v zajetí zákonitostí a náhod, MFF UK Praha 2014
Martišek, D.: Konec geometrie v Čechách a na Moravě, MFF UK Praha 2014
Martišek, D.: Trojúhelník v zajetí zákonitostí a náhod, MZK Brno 2015
Martišek, D.: Trojrozměrné rekonstrukce objektů metodou Shape from Focus, PF MU Brno 2018
Martišek, D.: Fraktály – kouzla geometrie a přírody, MZK Brno 2019

Novinové články

Martišek, D.: Připomínky k rámcovému programu pro gymnaziální vzdělávání, Učitelské noviny 2/2004
Martišek, D.: Konec matematiky, Brněnský deník Rovnost, 15. 10. 2004
Martišek, D.: Jeden hot a druhý čehý, Učitelské noviny 9/2005
Martišek, D.: Katalogy pro novou maturitu byly schváleny, Učitelské noviny, 41/2005
Martišek, D.: Ukončete nástup, primy se zavírají, Brněnský deník Rovnost, 18. 11. 2005
Martišek, D.: Nekamenujte učitele, MF DNES, 2. 11. 2006
Martišek, D.: Méně fyziky a chemie – slepá cesta, MF DNES, 4. 12. 2006
Martišek, D.: Katalogy pro novou maturitu byly schváleny, Učitelské noviny, 18. 7. 2007
Martišek, D.: Průměrný plat – problematická informace, Učitelské noviny 8/2008
Martišek, D.: Příprava odtržená od života, Učitelské noviny 9/2008
Martišek, D.: Ať umělci také platí za naši práci, MF DNES, 27. 11. 2008
Martišek, D.: Současná reforma školství: ryba smrdí od hlavy, Prostějovský deník, 15. 10. 2009
Martišek, D.: Ve zvláštní škole dostávají žáci maximum toho, co zvládnou a co budou potřebovat, Prostějovský deník, 3. 12. 2009
Martišek, D, Bečvář, J, Richterová, H.: Proč propadáme? Učitelské noviny 3/2011
Martišek, D.: Výborné gymnázium, přesto bojuje o přežití, MF DNES, 28. 6. 2011
Martišek, D.: Hvězdárně uškodilo její personální obsazení, 14. 2. 2012
Martišek, D.: Ke státní maturitě 2012, Učitelské noviny 29/2012
Martišek, D.: Nemá domácí úkol, Učitelské noviny 36/2012
Martišek, D.: Proč (ne)maturovat z matematiky, Učitelské noviny 25/2013
Martišek, D.: Jak (ne)maturovat z matematiky, Učitelské noviny 27/2013
Martišek, D.: Stromy u silnic pomáhají, MF DNES, 13. 11. 2013
Martišek, D.: Když matematik střílí do vlastní branky, MF DNES, 19. 10. 2014
Martišek, D.: Ne trojčlenka, logika je třeba, MF DNES, 1. 12. 2016
Martišek, D.: Spor o penál? Pomůže psycholog, MF DNES, 13. 2. 2017
Martišek, D.: Jak se dá snadno zničit maturita, MF DNES, 4. 3. 2017
Martišek, D.: Maturita a středověké trivium, MF DNES, 11. 5. 2020

7 Doporučující dopisy

Carleton UNIVERSITY
Canada's Capital University

School of Mathematics and Statistics
4302 Herzberg Laboratories
1125 Colonel By Drive
Ottawa, ON K1S 5B6 Canada
Tel: (613) 520-2155
Fax: (613) 520-3536
Email: mathstat@carleton.ca
Web site: www.mathstat.carleton.ca

Ottawa, dne 8. října 2018.

Vážený pan
doc. Ing. Jaroslav Katolický, Ph.D.
děkan
Fakulta strojního inženýrství
Vysoké učení technické v Brně
Technická 2896/2
616 69 Brno, Česká republika

Doporučení k zahájení řízení ke jmenování profesorem
pana doc. PaedDr. Dalibora Martiška, Ph.D.

Vážený pane děkane,

dovolte mi vyjádřit svou podporu k zahájení jmenovacího řízení ke jmenování pana doc. Dalibora Martiška profesorem v oboru Aplikovaná matematika. S vědeckou a pedagogickou činností pana doc. Dalibora Martiška jsem se seznámil během svého působení na Karlově univerzitě v Praze, a to především díky jeho vynikajícím, pečlivě připraveným přednáškám na MFF UK a jeho průkopnickým publikacím týkajícím se rekonstrukce prostorových objektů ze serie částečně zaostřených fotografií. To se týká především prací „The 2D and 3D processing of images provided by convencional microscopes", „3D reconstruction of the surface using a standard camera" a „Fast Shape-to-Focus method for 3D object reconstruction". Doc. Martišek v těchto prácích mistrně využívá symbiózu matematiky a technických disciplin. Jeho expertiza a jeho příspěvky jsou vědeckou komunitou vysoce ceněny.
Kromě těchto mezinárodních vědeckých úspěchů je nutné též vyzvednout jeho práci a úspěchy na poli pedagogiky. Ať se už jedná o výuku matematiky a informatiky na předuniverzitní či univerzitní úrovni, jeho vědecké či novinářské prezentace přinášejí odborně zpracované podklady pro budoucí vývoj a mají široký ohlas.
Na základě těchto vědeckých a pedagogických úspěchů doc. Martiška a na základě jeho současných vědeckých a pedagogických aktivit vřele doporučuji jmenování doc. Dalibora Martiška univerzitním profesorem.

V úctě

Dr. Vlastimil Dlab, F.R.S.C.
Professor Emeritus and Distinguished Research Professor, Carleton University
Professor Hospitus, Karlova Universita

MUNI SCI Ústav matematiky a statistiky

Vážený pan
doc. Ing. Jaroslav Katolický, Ph.D.
děkan FSI VUT v Brně
Technická 2896/2
616 69 Brno

Doporučení k zahájení řízení ke jmenování profesorem pana doc. PaeDr. Dalibora Martiška, Ph.D.

Vážený pane děkane,

rád bych vyjádřil podporu zahájení řízení ke jmenování profesorem pana docenta Dalibora Martiška v oboru Aplikovaná matematika. Pana doc. Martiška znám dlouhá léta jako aktivního člena matematické komunity v Brně. Jeho vědecká práce je zaměřena na aplikovanou matematiku, především geometrii. Hlavní oblastí je vizualizace a zpracování obrazu. Oblast jeho zájmu má velice široký záběr. Na WoS má více než 20 publikací a časopisy, ve kterých publikuje, jsou často indexovány v matematice, fyzice a mnoha technických oblastech. Řada těchto časopisů je v 1. kvartilu dané oblasti.
Také pedagogicky se zaměřuje na výuku aplikací geometrie v technických oborech, jeho výuka zahrnuje kurzy od klasické deskriptivní geometrie až po počítačovou grafiku či programování.
Vysoce oceňuji také jeho zájem o výuku matematiky na středních školách, což není u akademických pracovníků technických vysokých škol úplně typické. Svědčí o tom řada jeho novinových článků a přednášek. Záslužná je i jeho popularizační činnost – především formou přednášek pro širokou veřejnost. Sám jsem se několika jeho přednášek zúčastnil a oceňuji jeho schopnost přednést složité odborné téma ve formě srozumitelné i pro laickou veřejnost.

Na základě odborných kvalit a pedagogické činnosti doporučuji jmenování doc. Martiška profesorem v oboru Aplikovaná matematika.

V Brně, 14.10.2019

prof. RNDr. Josef Janyška, DSc.
Ústav matematiky a statistiky PřF MU v Brně
Kotlářská 2, 611 37 Brno
profesor v oblasti Geometrie a topologie

MASARYK UNIVERSITY
FACULTY OF SCIENCE
DEPARTMENT OF MATHEMATICS AND STATISTICS

Vážený pán
doc. Ing. Jaroslav Katolický, Ph.D.
Děkan
Fakulta strojního inženýrství
Vysoké učení technické v Brně
Technická 2896/2
616 69 Brno

V Brně dne 3. října 2018

Věc: Doporučení k zahájení řízení k jmenování profesorem

Vážený pane děkane,

dovoluji si Vám zaslat vyjádření k návrhu na řízení ke jmenování pana doc. PaedDr. Dalibora Martíška,Ph.D. profesorem v oboru Aplikovaná matematika.
Vědecko – výzkumná činnost doc. Martíška je orientována na počítačovou geometrii, počítačovou grafiku, 3-D rekonstrukce a analýzu obrazu. Nejvýznamnější výsledky se týkají trojrozměrné rekonstrukce přírodních objektů. Ve svých článcích uvádí matematické a softwarové nástroje, kterými je možné trojrozměrně rekonstruovat i snímky pořízené běžnými fotoaparáty. Zabýval se take určováním drsnosti ploch v souvislosti s fraktálními dimenzemi a navrhl originální metodu posuzování drsnosti skalních povrchů. Vědeckou komunitou je považován za vynikajícího odborníka v uvedených oblastech. Jeho odborné publikace jsou uváděny v databázích ISI Web a Scopus, počet citací podle ISI Web of Knowledge je 56. Doc. Martíšek je také autorem vynikající monografie *Matematické principy grafických systémů*. Z výše uvedených faktů vyplývá, že doc. Martíšek systematicky a dlouhodobě pracuje v poměrně novém oboru matematického inženýrství, který se snaží budovat mosty mezi matematickými a jinými odbornými disciplínami. Jeho publikace svědčí o širokém přehledu nejen o matematice a počítačové grafice, ale také o mnoha dalších oborech.
Zúčastnila jsem se jeho několika přednášek na konferencích a seminářích. Všechny prezentace měly po stránce odborné a formální vynikající úroveň.
Významné jsou také jeho univerzitní aktivity – byl členem a předsedou AS FSI VUT. Podílel se na organizaci národních a mezinárodních konferenci pořádaných FSI VUT.
V rámci svého pedagogického působení vyučuje a garantuje předměty bakalářského a magisterského studia v oblasti konstruktivní a počítačové geometrie na ÚM FSI VUT.
Vedl řadu úspěšně obhájených bakalářských a diplomových prací. Připravil řadu kvalitně zpracovaných podkladů k výuce. Byl rovněž školitelem 5 studentů doktorského studia Aplikovaná matematika, kteří své disertační práce úspěšně obhájili.
Podle mého názoru je pan doc. PaedDr. Dalibor Martíšek, Ph.D. uznávanou vědeckou osobností v oblasti aplikované matematiky a kvalitním vysokolškolským pedagogem. Na základě těchto skutečností podporuji zahájení jmenovacího řízení k jeho jmenování profesorem v oboru *Aplikovaná matematika.*

Horová

Prof. RNDr. Ivana Horová, CSc.
Ústav matematiky a statistiky
Přírodovědecká fakulta MU
Kotlářská 2, 61137 Brno

MASARYK UNIVERSITY, **FACULTY OF SCIENCE**, Kotlářská 2, 611 37 Brno, Czech Republic
Phone: +420 549 49 1411 • Fax: +420 541 211 214 • www.sci.muni.cz
VAT CZ00216224 • IBAN CZ43 0100 0000 0000 8563 6621

UNIVERZITA PAVLA JOZEFA ŠAFÁRIKA V KOŠICIACH
Prírodovedecká fakulta

ÚSTAV FYZIKÁLNYCH VIED
ÚFV PF UPJŠ, Park Angelinum 9, 041 54 Košice
tel.: +421 (055) 234 6101, fax: +421 (055) 622 21 24, IČO: 00397768
e-mail: ufv@upjs.sk, http://www.science.upjs.sk

Vážený pán
doc. Ing. Jaroslav Katolický, Ph.D.
dekan
Fakulta strojního inženýrství
Vysoké učení technické v Brně
Technická 2896/2
616 69 Brno

V Košiciach 26. 10. 2018

Vec: Odporúčanie pre zahájenie menovacieho konania pre menovanie pána doc. PaedDr. Dalibora Martiška, Ph.D. profesorom v odbore Aplikovaná matematika.

Vážený pán dekan,

dovoľte mi osloviť Vás v súvislosti so začatím menovacieho konania pána doc. PaedDr. Dalibora Martiška, Ph.D. profesorom v odbore Aplikovaná matematika.

Vedecké aktivity pána docenta sú sústredené na analýzu obrazu, rekonštrukcie trojrozmerných objektov, počítačovú geometriu a grafiku. Vysoká úroveň jeho výskumnej činnosti je presvedčivo preukázaná hodnotnými publikáciami uverejnenými v renomovaných vedeckých časopisoch. Uvedené publikácie majú adekvátny citačný ohlas, na ich vzniku má pán docent významný podiel. V oblasti vedecko – výskumnej činnosti pána docenta považujem za vhodné vyzdvihnúť interdisciplinárny aspekt jeho práce, kde dosiahnuté výsledky presahujú rámec samotnej matematiky. Konkrétnejšie, pán docent ako prvý publikoval princíp skupiny metód, ktoré sa v súčasnosti označujú ako Shape-From Focus. Uvedený prístup je založený na analýze série čiastočne zaostrených snímkou pre trojrozmernú rekonštrukciu povrchu. Táto metóda, ktorú pán docent následne významne zovšeobecnil, nachádza svoje použitie pri štúdiu povrchov tuhých látok. Obdobne, metóda určenia fraktálovej dimenzie navrhnutá pánom docentom je prínosná pri charakterizácii štruktúrne neusporiadaných materiálov.

Kvalita a množstvo jeho pedagogickej práce sú dokumentované nielen rozsahom vedených prednášok a cvičení, ale aj počtami vedených študentov na všetkých stupňoch, zameraním prednášok a predovšetkým výberom tém záverečných prác. Doložený rozsah prednášok a praktických cvičení vedených uchádzačom oprávňujú k predpokladu, že pán docent predstavuje skúseného a erudovaného učiteľa, ktorý úspešne vedie záverečné práce na rôznych úrovniach štúdia. Kvalitu hlavných vyučovacích predmetov na magisterskom stupni podporuje priama nadväznosť ich obsahu s jeho výskumnými aktivitami.

Členstvo pána docenta v organizačných výboroch významných konferencií a sympózií dokladuje jeho schopnosť kvalifikovane spolupracovať pri organizácií vedeckých podujatí.

Domnievam sa, že pán doc. PaedDr. Dalibora Martiška, Ph.D. je výraznou vedeckou a pedagogickou osobnosťou, ktorá má všetky predpoklady k tomu, aby v budúcnosti podstatnou mierou ovplyvňoval ďalšie napredovanie svojho pracoviska. Na základe uvedeného podporujem zahájenie menovacieho konania k jeho menovaniu profesorom v odbore Aplikovaná matematika.

s úctou,

prof. Ing. Martin Orendáč, CSc.

8 Publikace v prvním a druhém kvartilu

1. **Martišek, D**.: Mathematical incorrectnes of so called Higuchi‘s fractal dimension, Chaos Solitons & Fractals, under review (2019)

MATHEMATICS, INTERDISCIPLINARY APPLICATIONS.	12 of 105	**Q1**
PHYSICS, MATHEMATICAL	3 of 55	**Q1**
PHYSICS, MULTIDISCIPLINARY	19 of 81	**Q1**

2. **Martišek, D**.: Mathematical Methods for 3D Reconstruction of Cell Structures, Applied Mathematical Modelling, under review (2019)

ENGINEERING, MULTIDISCIPLINARY	18 of 86	**Q1**
MATHEMATICS, INTERDISCIPLINARY APPLICATIONS	15 of 103	**Q1**
MECHANICS	25 of 134	**Q1**

3. Ficker, T, **Martišek, D**.: Alternative Method for Assessing the Roughness Coefficients of Rock Joints, JOURNAL OF COMPUTING IN CIVIL ENGINEERING Volume: 30 Issue: 4 Article Number: 04015059 2016

ENGINEERING, CIVIL	49 of 128	**Q2**

4. Ficker, T, **Martišek, D.:** Digital fracture surfaces and their roughness analysis: Applications to cement-based materials, CEMENT AND CONCRETE RESEARCH Volume: 42 Issue: 6 Pages: 827-833 Published: JUN 2012

CONSTRUCTION & BUILDING TECHNOLOGY	2 of 62	**Q1**
MATERIALS SCIENCE, MULTIDISCIPLINARY	46 of 285	**Q1**

5. Ficker, T. **Martišek, D**., Jennings, H: Roughness of fracture surfaces and compressive strength of hydrated cement pastes, CEMENT AND CONCRETE RESEARCH Volume: 40 Issue: 6 Pages: 947-955, 2010

CONSTRUCTION & BUILDING TECHNOLOGY	2 of 62	**Q1**
MATERIALS SCIENCE, MULTIDISCIPLINARY	46 of 285	**Q1**

6. Ficker, T.; **Martišek, D**, et al. Fracture surfaces of porous materials, EPL Volume: 80 Issue: 1, Article Number: 16002, 2007

PHYSICS, MULTIDISCIPLINARY	36 of 78	**Q2**

9 Publikace na Web of Science

1 **Martišek, D:** Fast Shape-From-Focus method for 3D object reconstruction, Optik - International Journal for Light and Electron Optics 169 (2018) 16–26

2 **Martišek, D.,** Procházková, J.: The Enhancement of 3D Scans Depth Resolution Obtained by Confocal Scanning of Porous Materials, Measurement Science Review, 17, (2017), No. 6, 273–281

3 **Martišek, D**.: 3D Reconstruction of the Surface Using a Standard Camera, Mathematical problems in Engineering, 2017, DOI 10.1155/2017/4642397

4 **Martišek, D,** Druckmüllerová, H.: Registration of Partially Focused Images for 2D and 3D Reconstruction of Oversized Samples, Scanning, 2017, DOI 10.1155/2017/8538215

5 Ficker, T., **Martišek, D**: Alternative Method for Assessing the Roughness Coefficients of Rock Joints, Journal of Computing in Civil Engineering, Vol. 30, Issue 4, 2016, pp. 224 – 238

6 **Martišek, D.:** Elimination of Gibbs and Nyquist–Shannon Phenomena in 3D Image Reconstruction, 3D Research, (2016), vol 7(16)

7 Ficker, T., **Martišek, D.**: Three-dimensional rock Joints and their topology assessments, Proceedings of the 16th International Multidisciplinary Scientific Geoconference SGEM 2016, pp 349 – 345

8 Ficker, T., **Martišek, D:** Database 3D Surfaces for Evaluation of Joint Rock Coefficients, Procedia Engineering, 161:1361-1366, 2016

9 Ficker, T., **Martišek, D**: Three-dimensional reconstructions of solid surfaces using conventional microscopes, Scanning, Vol 38, (2016) pp. 21 – 35

10 Ficker, T., **Martišek, D:** 3D Image Reconstructions and the Nyquist–Shannon Theorem, 3D Research, (2015) 6:23

11 Ficker, T., **Martišek, D.**:Shear strength of rocks by visual assessment, Source of the Document International Multidisciplinary Scientific GeoConference Surveying Geology and Mining Ecology Management, SGEM, 2 (1), 2015, pp. 641-648

12 Ficker, T., **Martišek, D**: Computer Evaluation of Asperity Topology of Rock Joints, Procedia Earth and Planetary Science 15 (2015) pp. 125 - 132,

13 **Martišek, D,** Martišek, K**.:** Direct volume rendering methods for cell structures, Scanning, 2012 Vol 34 (No. 6), pp 367 – 377, ISSN: 0161-0457, IF 1.067 **Top 10 in BioMedLib 2012**

14 Ficker, T., **Martišek, D.**: Digital fracture surfaces and their roughness analysis: Applications to cement-based materials, Cement and Concrete Research (ELSEVIER), 2012 (42), No 6, pp. 827 – 833

15 Ficker, T., **Martišek, D.**: Roughness and fractality of fracture surfaces and Indicators of mechanical quantities of porous solids, Central European Journal of Physics, 2011, Vol. 9, (No 6), pp 1440-1445. ISSN: 1895- 1082

16 Ficker, T., Len, A., **Martišek, D.**: A remark on nano-particle stability of cement C-S-H Gel, Central European Journal of Physics, 2011, Vol 9, (No 2) 2011, pp 553-557, ISSN: 1895 – 1082

17 **Martišek, D.,** Procházková, J.: Relation between algebraic and geometric view on NURBS tensor surfaces, Applications of Mathematics, No. 5/2010, pp. 419-430

18 Ficker, T., **Martišek, D.,** Jennings, M. H.: Roughness of fracture surfaces and compressive strength of hydrated cement pastes, Cement and Concrete Research, 2010, Vol. 40, (No 6), pp. 947-955, ISSN: 0008- 8846

19 Ficker, T., **Martišek, D.,** Chmelík, R., Lovicar, L., Němec, P.: Fracture surfaces of porous materials, EUROPHYSICS LETTERS, 2007, Vol. 80, No. 6, pp 1600-1604, ISSN: 0295-5075

20 **Martišek, D**.: The 2-D and 3-D processing of images provided by conventional microscopes, Scanning, Vol. 24 (No 6) USA 2002, pp. 284-296, ISSN 0161-0457

21 Ficker, T., **Martišek, D.;** Druckmüller, M.: Unconventional Multifractal Formalism and Image Analysis of Natural Fractals, Czechoslovak Journal of Physics, Vol. 49 (1999), No. 10

Souhrn citací a publikací dle Web of Science

AUTHOR: (Martisek, D)

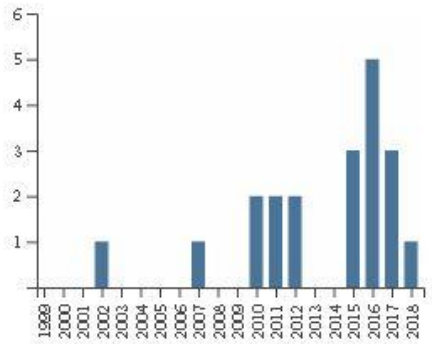

Total Publications by Year

Results found	21
Sum of the Times Cited	121
Withouth self-citation	81
Average Citations per Item	5,76

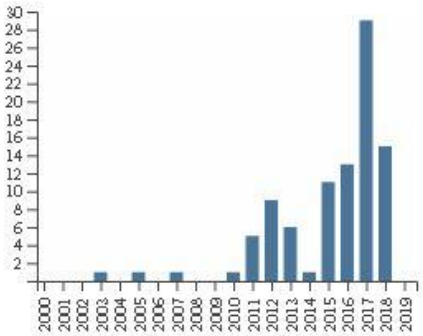

Sum of Times Cited by Year

Citing articles	75
Withouth self-citation	60
h-index	7

10 Souhrnný přehled autoevaluačních kriterií

A (věda a výzkum)	a*)	b*)	c*)	d*)	e*)
1 Monografie	3 za arch	40 archů	120		
2 Původní vědecká práce - časopis IF>0,5	20/10	19	230		
3 Původní vědecká práce - časopis 0,5>IF>0,1	15/7,5	2	15	**793**	**120**
4 Původní vědecká práce - časopis IF<0,1 nebo bez IF	10/5	4	25		
5 Významné inženýrské dílo	8	20	160		
6 Citace jiným autorem podle SCI	3	81	243		
7 Zahraniční patent	15	0	0		
8 Domácí patent/autorské osvědčení	5	0	0		
9 Příspěvek ve sborníku svět. nebo evrop. Kongresu	10/5	21	140		
10 Abstrakt ve sborníku svět. nebo evrop. Kongresu	2/1	1	1	**333,5**	**80**
11 Příspěvek ve sborníku nár. nebo mezinár. Kongresu	4/2	24	92		
12 Publikace v odborném časopise	3/1,5	0	0		
13 Abstrakt ve sborníku nár. nebo mezinár. Kongresu	1/0,5	1,5	1,5		
14 Citace jiným autorem bez SCI	1	99	99		
15 Členství v souč. výboru svět. nebo evrop. společnosti	10	0	0		
16 Členství v současném výboru č-s vědecké společnosti	5	0	0		
17 Členství v red. radě vědeckého časopisu v zahraničí	15	15	15		
18 Členství v red. radě česko-slovenského věd. časopisu	10	0	0		
19 Členství v redakční radě odborného časopisu	5	0	0		
20 Členství ve vědecké radě	3	0	0		
21 Členství v organiz. výboru svět. nebo evrop. kongresu	10	0	0		
22 Členství v organiz. výboru nár. nebo mezinár. kongresu	5	7	35	**283**	**120**
23 Získání zahraničního grantu	10	0	0		
24 Řešitel, spoluřešitel externího grantu	6	15	90		
25 Odborná příručka v oboru	2/1 za arch	42	62		
26 Členství v grantových komisích	2	0	0		
27 Posudek zahraniční publikace nebo projektu	3	9	27		
28 Členství v komisích pro hab. nebo prof. řízení	3	0	0		
29 Posudek domácí publikace nebo projektu	2	14	28		
30 Posudek k obhajobě habilitační nebo disertační práce	2	13	26		
	věda a výzkum			**1 409,5**	**320**

a*) počet bodů za položku (autor/spoluautor)
b*) počet položek
c*) počet bodů dosažených za položku
d*) dosažený mezisoučet
e*) minimální požadovaný mezisoučet

B (pedagogika)	a*)	b*)	c*)	d*)	e*)
1 Za každý rok pedagogického působení na VŠ škole	2	35	70		
2 Zavedení oboru	30	0	0		
3 Zavedení předmětu	15	7	105		
4 Vedoucí obhájené diplomové/bakalářské práce	2/1	31	55		
5 Školitel studenta, který získal Ph.D.	15	5	75		
6 Učebnice	3 za arch	0	0		
7 Překlad cizojazyčné učebnice	15 za arch	0	0	856	80
8 Skripta	2 za arch	114	200		
9 Vytvoření významné výukové pomůcky	10/5	30	295		
10 Recenze učebnice nebo skript	2	1	2		
11 Členství v oborové radě doktorského stud. programu	2	3	6		
12 Komise pro st. dokt. zkoušku nebo obhaj. disert. práce	1	33	33		
13 Členství v komisi pro státní závěrečné zkoušky	1	26	26		
	pedagogika			**895**	**80**

A+B celkem	**2 276,5**	**400**

a*) počet bodů za položku (autor/spoluautor)
b*) počet položek
c*) počet bodů dosažených za položku
d*) dosažený mezisoučet
e*) minimální požadovaný mezisoučet

Minimální požadavky pro vědecké, odborné a pedagogické činnosti dle směrnice rektora č. 54/2017, přílohy podle čl. 3 Směrnice rektora č. 1/2006, jsou splněny ve všech kategoriích i s uvážením autorského podílu na jednotlivých výstupech. Detailní rozpis jednotlivých položek je uveden v následující kapitole.

11 Podrobný rozpis položek autoevaluačních kriterií

A. Vědecká a odborná činnost

A1: Monografie – 3 body za jeden autorský arch (arch = 36 000 znaků)

1. Martišek, D.:Matematické principy grafických systémů, Littera, Brno 2002, pp. 1-299, ISBN 80-85763-19-2 80x60x300 = 40 archů **120 bodů**

A2: Původní vědecká práce ve vědeckém časopisu s IF větším než 0,500 – 20 bodů (u kolektivního díla se započítává počet bodů děleno dvěma)

1. **Martišek, D**.: The 2-D and 3-D processing of images provided by conventional microscopes, Scanning, Vol. 24 (No 6) USA 2002, pp. 284-296, ISSN 0161-0457 IF 1.090 **20 bodů**

2. Ficker, T., **Martišek, D.,** Chmelík, R., Lovicar, L., Němec, P.: Fracture surfaces of porous materials, EUROPHYSICS LETTERS, 2007, Vol. 80, No. 6, pp 1600-1604, ISSN: 0295-5075 IF 2.120 **10 bodů**

3. **Martišek, D**. Martišek, K., Procházková, J.: New methods for space reconstruction of inside cell structures, Journal of Applied Biomedicine, Vol 5 (2007), pp. 151-156 IF 1.689 **10 bodů**

4. Ficker, T., **Martišek, D.,** Jennings, M. H.: Roughness of fracture surfaces and compressive strength of hydrated cement pastes, Cement and Concrete Research, 2010, Vol. 40, (No 6), pp. 947-955, ISSN: 0008- 8846, IF 1.549 **10 bodů**

5. Ficker, T., Len, A., **Martišek, D.**: A remark on nano-particle stability of cement C-S-H Gel, Central European Journal of Physics, 2011, Vol 9, (No 2) 2011, pp 553-557, ISSN: 1895 - 1082, IF 0.728 **10 bodů**

6. Ficker, T., **Martišek, D.**: Roughness and fractality of fracture surfaces and Indicators of mechanical quantities of porous solids, Central European Journal of Physics, 2011, Vol. 9, (No 6), pp 1440-1445. ISSN: 1895- 1082 IF 1.549 **10 bodů**
7. **Martišek, D,** Martišek, K**.:** Direct volume rendering methods for cell structures, Scanning, 2012 Vol 34 (No. 6), pp 367 – 377, ISSN: 0161-0457, IF 1.067 **Top 10 in BioMedLib 2012** **10 bodů**

8. Ficker, T., **Martišek, D.**: Digital fracture surfaces and their roughness analysis: Applications to cement-based materials, Cement and Concrete Research (ELSEVIER), 2012 (42), No 6, pp. 827 – 833, IF 2.781 **10 bodů**

9. **Martišek, D.,** Procházková, J., Ficker, T.: High-quality three-dimensional reconstruction and noise reduction of multifocal images from oversized samples, Journal of Electronic Imaging, 24 (5), 2015; IF 0.672 **10 bodů**

10. Ficker, T., **Martišek, D**: Computer Evaluation of Asperity Topology of Rock Joints, Procedia Earth and Planetary Science 15 (2015) pp. 125 - 132, IF 1.088 **10 bodů**

11. Ficker, T., **Martišek, D:** 3D Image Reconstructions and the Nyquist–Shannon Theorem, 3D Research, (2015) 6:23, **10 bodu**

12. Ficker, T., **Martišek, D**: Three-dimensional reconstructions of solid surfaces using conventional microscopes, Scanning, Vol 38, (2016) pp. 21 - 35 IF 1.067 **10 bodů**

13. Ficker, T., **Martišek, D**: Alternative Method for Assessing the Roughness Coefficients of Rock Joints, Journal of Computing in Civil Engineering, Vol. 30, Issue 4, 2016, pp. 224 – 238, IF 1.855 **10 bodů**

14. Ficker, T., **Martišek, D:** Database 3D Surfaces for Evaluation of Joint Rock Coefficients, Procedia Engineering, 161:1361-1366, 2016, IF 0.73 **10 bodů**

15. **Martišek, D.:** Elimination of Gibbs and Nyquist–Shannon Phenomena in 3D Image Reconstruction, 3D Research, (2016), vol 7(16), IF 0.89 **20 bodů**

16. **Martišek, D,** Druckmüllerová, H.: Registration of Partially Focused Images for 2D and 3D Reconstruction of Oversized Samples, Scanning, (2017) IF 1.345 **10 bodů**

17. Martišek, D., Procházková, J.: The Enhancement of 3D Scans Depth Resolution Obtained by Confocal Scanning of Porous Materials, Measurement Science Review, 17, (2017), No. 6, 273-281 IF 1.344 **10 bodů**

18. Martišek, D.: 3D Reconstruction of the Surface Using a Standard Camera, Mathematical problems in Engineering, 2017, DOI 10.1155/2017/4642397, IF 0.802 **20 bodů**

19. Martišek, D: Fast Shape-From-Focus method for 3D object reconstruction, Optik - International Journal for Light and Electron Optics 169 (2018) 16–26 Manuscript Number: IJLEO-D-17-03215, IF 0.835 **20 bodů**

A3: Původní vědecká práce ve vědeckém časopisu s IF 0,100-0,500 – 15 bodů
(u kolektivního díla se započítává počet bodů děleno dvěma)

1. Ficker, T., **Martišek, D.;** Druckmüller, M.: Unconventional Multifractal Formalism and Image Analysis of Natural Fractals, Czechoslovak Journal of Physics, Vol 49 (1999), No. 10, IF 0.345 **7,5 bodu**

2. **Martišek, D.,** Procházková, J.: Relation between algebraic and geometric view on NURBS tensor surfaces, Applications of Mathematics, No. 5/2010, pp. 419-430, IF 0.410 **7,5 bodu**

A4: Původní vědecká práce ve vědeckém časopisu s IF menším než 0,100 popř. bez IF – 10 bodů (u kolektivního díla se započítává počet bodů děleno dvěma)

1. **Martišek, D**. Koreňová, B.: Zlatý rez v geometrických tvaroch a štruktúrach, Slovenský časopis pre geometriu a grafiku, Vol 13 (2010), pp. 15-36, **5 bodů**
2. Ficker, T., **Martišek, D**, Jennings, H. M.: Surface Roughness and Porosity of Hydrated Cement Pastes, Acta Polytechnica Vol. 51 No. 3/2011 **5 bodů**
3. **Martišek, D**, Druckmüllerová, H.: Multifocal Image Processing, Mathematics for Applications, Vol. 3(1), 2014, pp. 77-90. **5 bodů**
4. **Martišek, D.:** Joint Rock Coefficient Estimation Based on Hausdorff Dimension, Advanced in Pure Matematics, Vol. 7, 2017, pp. 615 – 640. **10 bodů**

A5: Významné inženýrské, umělecké, architektonické, ekonomické dílo podle čl. 2 Směrnice VUT - 20 bodů

1. Martišek, D.: Conventional Microscope (autorizovaný software 2006) **20 bodů**
2. Martišek, D.: Confocal Microscope (autorizovaný software 2006) **20 bodů**
3. Martišek, D.: 16bit Optical Cuts reconstruction (autorizovaný software 2007) **20 bodů**
4. Martišek, D.: Fractal analysis of cavus fibres (autorizovaný software 2007) **20 bodů**
5. Martišek, D.: Scan Calculator (autorizovaný software 2007) **20 bodů**
6. Martišek, D.: Graph2D (autorizovaný software 2008) **20 bodů**
7. Martišek, D.: Graph3D (autorizovaný software 2008) **20 bodů**
8. Martišek, D.: Fast Shape-From-Focus method (autorizovaný software 2016) **20 bodů**

A6: Citace jiným autorem podle *Science Citation Index (SCI)* – 3 body

Položka A2/1: Martišek, D.: The 2-D and 3-D processing of images provided by conventional microscopes, Scanning, Vol. 24 (No 6) USA 2002, pp. 284-296, ISSN 0161-0457

1 Tam, WJ; Yee, AS; Ferreira, J; et al.: Stereoscopic image rendering based on depth maps created from blur and edge information, Conference on Stereoscopic Display and Virtural Reality Systems XII Location: San Jose, CA Date: JAN 17-20, 2005 **3 body**

Položka A2/2: Ficker, T., **Martišek, D.,** Chmelík, R., Lovicar, L., Němec, P.: Fracture surfaces of porous materials, EUROPHYSICS LETTERS, 2007, Vol. 80, No. 6, pp 1600-1604, ISSN: 0295-5075 IF 2.120

2 Ficker, T.: Ficker, T.: Surface Morphology of Porous Cementitious Materials Subjected to Fast Dynamic Fractures, Materials Science, Vol. 51 No. 5/2011 **3 body**

3 Valentini, LA, et al.: Multifractal Analysis of Calcium Silicate Hydrate (C-S-H) Mapped by X-ray Diffraction Microtomography, Journal of the American Ceramic Society, Volume: 95 Issue: 8 Special Issue: SI Pages: 2647 2652, 2012 **3 body**

4 Rogante, M.; Domanskaya, I. K.; Gerasimova, E. S.; et al.: Nanoscale investigation of polymer cement concretes by small angle neutron scattering, SCIENCE AND ENGINEERING OF COMPOSITE MATERIALS, Vol: 24 Issue: 1, Pages: 67-72, 2017 **3 body**

Položka A2/4: Ficker, T., **Martišek, D.,** Jennings, M. H.: Roughness of fracture surfaces and compressive strength of hydrated cement pastes, Cement and Concrete Research, 2010, Vol. 40, (No 6), pp. 947-955, ISSN: 0008- 8846

5 Lee, Seung-Hun; Seo, Seung-Deok; Jin, Yun-Ho; et al. : A graphite foil electrode covered with electrochemically exfoliated graphene nanosheets, ELECTROCHEMISTRY COMMUNICATIONS Volume: 12 Issue: 10 Pages: 1419-1422 Published: OCT 2010 **3 body**

6 Shen, Y., Garnier, J., Allais, L., Crepin, J., Ancelet, O., Hiver, J.-M.: Experimental and numerical characterization of anisotropic damage evolution of forged Al6061-T6 alloy, Procedia Engineering, 2011, 10, pp. 3429-3434, **3 body**

7 Ficker, T., Quasi-static compressive strength of cement-based materials, Cement and Concrete Research, ISSN 0008-8846, Elsevier, USA, 2011 **3 body**

8 Qiang, T., Yu, D.: Correlation between fractal dimension and impact strength for wood plastic composites, Advanced Materials Research 2012, 411, pp. 548-551, **3 body**

9 Ficker, T.: Fracture surfaces and compressive strength of hydrated cement pastes, Construction and buidlding materials Volume: 27 Issue: 1, Pages: 197-205, 2012 **3 body**

10 Akhavan, A., Shafaatian, S., Rajabipour, F.:Quantifying the effects of crack width, tortuosity, and roughness on water permeability of cracked mortars CEMENT AND CONCRETE RESEARCH Volume: 42 Issue: 2 Pages: 313-320 Published: FEB 2012 **3 body**

11 Erdem, S; Blankson, M. A.: Fractal-fracture analysis and characterization of impact-fractured surfaces in different types of concrete using digital image analysis and 3D nanomap laser profilometry, Construction and building materials, Elsevier, 2012, vol. 40 pp: 70-76 **3 body**

12 Erdem, S; Dawson, A. R; Thom, N. H.: Micromechanical structure-Property Relationships for the Damage Analysis of Impact-Loaded Sustainable Concrete, Journal of materials in civil engineering, 2013, Vol.: 25 Issue: 5 pp: 597-609, **3 body**

13 Ficker, T et al.: Is componential strength analysis of concrete possible? Magazine of concreate research, Volume: 65 Issue: 24 Pages: 1480-1485 (2013) **3 body**

14 Chen, Xudong; Wu, Shengxing; Zhou, Jikai: Experimental study and analytical model for pore structure of hydrated cement paste, APPLIED CLAY SCIENCE, Vol: 101, pp: 159-167, 2014 **3 body**

15 Fernandino, D., O.; Boeri, R.: Fracture of pearlitic ductile cast iron under different loading Conditions; FATIGUE & FRACTURE OF ENGINEERING MATERIALS & STRUCTURES Vol 38, Issue: 1, pp 80-90, 2015 **3 body**

16 Apedo, K. L.; Munzer, C.; He, H.; et al. Cement paste surface roughness analysis using coherence scanning interferometry and confocal microscopy MATERIALS CHARACTERIZATION, Vol: 100, pp 108-119, 2015 **3 body**

17 Yio, M. H. N.; Mac, M. J.; Wong, H. S.; et al.: 3D imaging of cement-based materials at submicron resolution by combining laser scanning confocal microscopy with serial sectioning, JOURNAL OF MICROSCOPY, Vol: 258, Issue 2, pp. 151-169, 2015 **3 body**

18 Limandri, S et al: 3D scanning electron microscopy applied to surface characterization of fluorosed dental enamel, MICRON, Vol. 84 pp. 54-60, 2016 **3 body**

19 Apedo, K. L.; Montgomery, P.; Serres, N.; et al.: Geometrical roughness analysis of cement paste surfaces using coherence scanning interferometry and confocal microscopy, Materials characterization Vol. 118, pp: 212-224, 2016 **3 body**

20 Hilloulin, B et al: Monitoring of autogenous crack healing in cementitious materials by the nonlinear modulation of ultrasonic coda waves, 3D microscopy and X-ray microtomography, Construction and Building Materials 123:143-152, 2016 **3 body**

21 Ficker, T.: Sectional techniques for 3D imaging of microscopic and macroscopic objects Optik, Volume: 144, Pages: 289-299, 2017 **3 body**

22 Ficker, T.: Rupture Strength and Irregularity of Fracture Surfaces World Multidisciplinary Civil Engineering-Architecture-Urban Planning Symposium (WMCAUS) Location: Prague, CZECH REPUBLIC Date: JUN 12-16, 2017 WORLD MULTIDISCIPLINARY CIVIL ENGINEERING-ARCHITECTURE-URBAN PLANNING SYMPOSIUM - WMCAUS Book Series: IOP Conference Series-Materials Science and Engineering Volume: 245 Article Number: UNSP 032009, 2017 **3 body**

23 Ficker, T.: Fractal properties of joint roughness coefficients, International Journal of Rock Mechanics and Mining Sciences, Vol 94, pp 27-31, 2017 **3 body**

24 Santos, Winnie F.; Quattrone, Marco; John, Vanderley M.; et al. Roughness, wettability and water absorption of water repellent treated recycled aggregates, Construction and Building Materials, Vol: 146, pp. 502-513 (2017) **3 body**

25 Al-Saadi, Nihad Tareq Khshain; Mohammed, Alyaa; Al-Mahaidi, Riadh: Assessment of residual strength of concrete girders rehabilitated using NSM CFRP with cementitious adhesive made with graphene oxide after exposure to fatigue loading, Construction and Building Materials Volume: 153 Pages: 402-422,(2017) **3 body**

26 Mohammed, Alyaa; Al-Saadi, Nihad Tareq Khshain; Al-Mahaidi, Riadh: Assessment of bond strength of NSM CFRP strips embedded in concrete using cementitious adhesive made with graphene oxide, Construction and Building Materials, Volume: 154 Pages: 504-513 (2017) **3 body**

27. Zhang, Hongzhi; Savija, Branko; Figueiredo, Stefan Chaves; et al: Experimentally validated multi-scale modelling scheme of deformation and fracture of cement paste, Cement and Concreate research, Volume: 102 Pages: 175-186, 2017 **3 body**

28 Fan Yuzhou, Luou Liangping, Duric, Maria: Extracting Cross-Sectional Clinical Images Based on Their Principal Axes of Inertia, Scanning 2017(10):1-8, 2017 DOI 10.1155/2017/1468596 **3 body**

29 Mohammed, A., Al-Saadi, N.T.K., Al-Mahaidi, R.: Assessment of bond strength of NSM CFRP strips embedded in concrete using cementitious adhesive made with graphene oxide, Construction and Building Materials, 154 (2017), pp. 504-513 **3 body**

30 Mohammed, Alyaa; Al-Saadi, Nihad T. K.; Al-Mahaidi, Riadh: Assessing the Contribution of the CFRP Strip of Bearing the Applied Load Using Near-Surface Mounted Strengthening Technique with Innovative High-Strength Self-Compacting Cementitious Adhesive (IHSSC-CA), Polymers, Volume: 10 Issue: 1 Article Number: 66, 2018 **3 body**

31 Erdem, Savas; Hanbay, Serap; Guler, Zeynel: Micromechanical damage analysis and engineering performance of concrete with colloidal nano-silica and demolished concrete aggregates, CONSTRUCTION AND BUILDING MATERIALS Volume: 171 Pages: 634-642, 2018 **3 body**

32 Gang Xu, et al: Influence of Graphene oxide in a chemically activated fly ash, Fuel, 226 (2018) pp. 664-657 **3 body**

33 Hilloulin, Benoit; Robira, Maxime; Loukili, Ahmed: Coupling statistical indentation and microscopy to evaluate micromechanical properties of materials: Application to viscoelastic behavior of irradiated mortars CEMENT & CONCRETE COMPOSITES Volume: 94 Pages: 153-165 Published: NOV 2018 **3 body**

34 Ficker, T.: Rock joint coefficients and their computerized classification, INTERNATIONAL JOURNAL OF MINING SCIENCE AND TECHNOLOGY Volume: 29 Issue: 5 Pages: 701-709 Published: SEP 2019 **3 body**

35 Wang, Cuicui; Smith, Lee M.; Wang, Ge; et al.: Characterization of interfacial interactions in bamboo pulp fiber/high-density polyethylene composites treated by nano CaCO3 impregnation modification using fractal theory and dynamic mechanical analysis INDUSTRIAL CROPS AND PRODUCTS Volume: 141, Article Number: UNSP 111712 Published: DEC 1 2019 **3 body**

36 Ding, Yining; Zeng, Wei; Wang, Qing; et al.: Topographical analysis of fractured surface roughness of macro fiber reinforced concrete and its correlation with flexural toughness, CONSTRUCTION AND BUILDING MATERIALS Volume: 235 Article Number: UNSP 117466, 2020 **3 body**

37 Shirakawa, M. A.; de Lima, L. N.; Gaylarde, C. C.; et al.: Effects of natural aging on the properties of a cool surface exposed in different Brazilian environments, ENERGY AND BUILDINGS Volume: 221 Article Number: UNSP 110031, 2020 **3 body**

38 Xi, Xian; Shi, Quanlin; Jiang, Shuguang; et al.: Effects of Graphene Oxide on the Mechanical and Microscopic Characteristics of Cement-Based Plugging Material for Preventing Spontaneous Combustion of Coal, ENERGY & FUELS, Vol: 34, Issue:5 , Pages: 6346-6354, 2020 **3 body**

Položka A2/5: Ficker, T., Len, A., **Martišek, D.**: A remark on nano-particle stability of cement C-S-H Gel, Central European Journal of Physics, 2011, Vol 9, (No 2) 2011, pp 553-557, ISSN: 1895- 1082, IF 0.728

39 Ficker, T; Topolar, L; Kusak, I.: Is componential strength analysis of concrete possible? Volume: 65 Issue: 24 Pages: 1480-1485 (2013) **3 body**

40 Prabhu, A, et al: Effect of Nano Seeds in C-S-H Gel Formation: Simulation Study from the Colloidal Point of View, CONCREEP 10: Mechanics and Physics of Creep Shrinkage and Durability of Concreate and Coincreate Structures, 2015, pp: 877-886 Published: 2015 **3 body**

Položka A2/6.Ficker, T., **Martišek, D.**: Roughness and fractality of fracture surfaces and Indicators of mechanical quantities of porous solids, Central European Journal of Physics, 2011, Vol. 9, (No 6), pp 1440-1445. ISSN: 1895- 1082

41 Ficker, T. et al.: Is componential strength analysis of concrete possible? Magazine of concreate research, Volume: 65 Issue: 24 Pages: 1480-1485 (2013) **3 body**

42 Ficker, T.: Rock Joint Surfaces and their Calibration curves, 16th International Multidisciplinary Scientific Geoconference (SGEM 2016) **3 body**

43 Ficker, T.: Sectional techniques for 3D imaging of microscopic and macroscopic objects Optik, Volume: 144, Pages: 289-299, 2017 **3 body**

44 Ficker, T, Komarkova, T: Rock Joint Asperities and Mechanical Strength of Concrete, World Multidisciplinary Civil Engineering-Architecture-Urban Planning Symposium (WMCAUS)Location: Prague, CZECH REPUBLIC Date: JUN 12-16, 2017 WORLD MULTIDISCIPLINARY CIVIL ENGINEERING-ARCHITECTURE-URBAN PLANNING SYMPOSIUM - WMCAUS Book Series: IOP Conference Series-Materials Science and Engineering, Volume: 245 Article Number: UNSP 032011, 2017 **3 body**

45 Ficker, T.: Fractal properties of joint roughness coefficients, International Journal of Rock Mechanics and Mining Sciences, Vol 94, pp 27-31, 2017 **3 body**

46 Ficker, T.: Rock joint coefficients and their computerized classification, INTERNATIONAL JOURNAL OF MINING SCIENCE AND TECHNOLOGY Volume: 29 Issue: 5 Pages: 701-709 Published: SEP 2019 **3 body**

47 Ding, Yining; Zeng, Wei; Wang, Qing; et al.: Topographical analysis of fractured surface roughness of macro fiber reinforced concrete and its correlation with flexural toughness, CONSTRUCTION AND BUILDING MATERIALS Volume: 235 Article Number: UNSP 117466, 2020 **3 body**

Položka A2/8 Ficker, T., **Martišek, D.**: Digital fracture surfaces and their roughness analysis: Applications to cement-based materials, Cement and Concrete Research (ELSEVIER), 2012 (42), No 6, pp. 827 – 833

48 Erdem, S; Blankson, M. A.: Fractal-fracture analysis and characterization of impact-fractured surfaces in different types of concrete using digital image analysis and 3D nanomap laser profilometry, Construction and building materials, Elsevier, 2012, vol. 40 pp: 70-76 **3 body**

49 Apedo, K. L.; Munzer, C.; He, H.; et al. Cement paste surface roughness analysis using coherence scanning interferometry and confocal microscopy Materials characterization, Vol: 100, pp 108-119, 2015 **3 body**

50 Apedo, K. L.; Montgomery, P.; Serres, N.; et al.: Geometrical roughness analysis of cement paste surfaces using coherence scanning interferometry and confocal microscopy, Materials characterization Vol. 118, pp: 212-224, 2016 **3 body**

51 Al-Saadi, Nihad Tareq Khshain; Mohammed, Alyaa; Al-Mahaidi, Riadh: Assessment of residual strength of concrete girders rehabilitated using NSM CFRP with cementitious adhesive made with graphene oxide after exposure to fatigue loading, Construction and Building Materials, Volume: 153 Pages: 402-422, 2017 **3 body**

52 Olkowicz, M; Dambrowski, M; Pluymakers, A.: Focus stacking photogrammetry for micro-scale roughness reconstruction: a methodological study, PHOTOGRAMMETRIC RECORD, Vol. 34, Issue: 165, pp: 11-35, 2019 **3 body**

53 Konkol, J.: Fracture Toughness and Fracture Surface Morphology of Concretes Modified with Selected Additives of Pozzolanic Properties, BUILDINGS, Volume: 9, Issue: 8, 2019 **3 body**

54 Ding, Yining; Zeng, Wei; Wang, Qing; et al.: Topographical analysis of fractured surface roughness of macro fiber reinforced concrete and its correlation with flexural toughness, CONSTRUCTION AND BUILDING MATERIALS Volume: 235 Article Number: UNSP 117466, 2020 **3 body**

Položka A2/10: Ficker, T., **Martišek, D**: Computer Evaluation of Asperity Topology of Rock Joints, Procedia Earth and Planetary Science 15 (2015) pp. 125 - 132,

55 Ficker, T.: Some remarks on the dynamical conformity of rock joints, International Journal of Mining Science and Technology, Vol. 28 Issue: 3, 2018 Pages: 385-390 **3 body**

Položka A2/12: Ficker, T., **Martišek, D**: Three-dimensional reconstructions of solid surfaces using conventional microscopes, Scanning, Vol 38, (2016) pp. 21 - 35

56 Ficker, T.: Sectional techniques for 3D imaging of microscopic and macroscopic objects Optik, Volume: 144, Pages: 289-299, 2017 **3 body**

57 Audy, O., Ficker, T.: Rock Joint Coefficients Derived from the Three-Dimensional Fourier Reliefs, World Multidisciplinary Civil Engineering-Architecture-Urban Planning Symposium (WMCAUS) Location: Prague, CZECH REPUBLIC Date: JUN 12-16, 2017 WORLD MULTIDISCIPLINARY CIVIL ENGINEERING-ARCHITECTURE-URBAN PLANNING SYMPOSIUM – WMCAUS Book Series: IOP Conference Series-Materials Science and Engineering Volume: 245 Article Number: UNSP 032005, 2017 **3 body**

58 Mouralova,K. et al: Using a DoE for a comprehensive analysis of the surface quality and cutting speed in WED-machined hadfield steel, Journal of Mechanical Science and Technology, Volume 33, Issue 5, pp 2371–2386, 2019 **3 body**

59 Ficker, T.: Rock joint coefficients and their computerized classification, INTERNATIONAL JOURNAL OF MINING SCIENCE AND TECHNOLOGY Volume: 29 Issue: 5 Pages: 701-709 Published: SEP 2019 **3 body**

60 Ding, Yining; Zeng, Wei; Wang, Qing; et al.: Topographical analysis of fractured surface roughness of macro fiber reinforced concrete and its correlation with flexural toughness, CONSTRUCTION AND BUILDING MATERIALS Volume: 235 Article Number: UNSP 117466, 2020 **3 body**

Položka A2/13: Ficker, T., **Martišek, D**: Alternative Method for Assessing the Roughness Coefficients of Rock Joints, Journal of Computing in Civil Engineering, Vol. 30, Issue 4, 2016, pp. 224 – 238

61 Ficker, T.: Sectional techniques for 3D imaging of microscopic and macroscopic objects Optik, Volume: 144, Pages: 289-299, 2017 **3 body**

62 Audy, O., Ficker, T.: Rock Joint Coefficients Derived from the Three-Dimensional Fourier Reliefs, World Multidisciplinary Civil Engineering-Architecture-Urban Planning Symposium (WMCAUS) Location: Prague, CZECH REPUBLIC Date: JUN 12-16, 2017 WORLD MULTIDISCIPLINARY CIVIL ENGINEERING-ARCHITECTURE-URBAN PLANNING SYMPOSIUM – WMCAUS Book Series: IOP Conference Series-Materials Science and Engineering Volume: 245, Article Number: UNSP 032005 **3 body**

63 Audy, O., Ficker, T.: Large Rock Reliefs and Their 3D Reconstructions, World Multidisciplinary Civil Engineering-Architecture-Urban Planning Symposium (WMCAUS) Location: Prague, CZECH REPUBLIC Date: JUN 12-16, 2017 WORLD MULTIDISCIPLINARY CIVIL ENGINEERING-ARCHITECTURE-URBAN PLANNING SYMPOSIUM – WMCAUS Book Series: IOP Conference Series-Materials Science and Engineering Volume: 245, Article Number: UNSP 032005 **3 body**

64 Ficker, T.: Fractal properties of joint roughness coefficients, International Journal of Rock Mechanics and Mining Sciences, Vol 94, pp 27-31, 2017 **3 body**

65 Yong, Rui; Ye, Jun; Li, Bo; et al. Determining the maximum sampling interval in rock joint roughness measurements using Fourier series, INTERNATIONAL JOURNAL OF ROCK MECHANICS AND MINING SCIENCES, Vol. 101, Pages: 78-88, 2018 **3 body**

66 Ficker, T.: Some remarks on the dynamical conformity of rock joints, International Journal of Mining Science and Technology, Vol. 28 Issue: 3, 2018 Pages: 385-390 **3 body**

67 Ficker, T.: Rock joint coefficients and their computerized classification, INTERNATIONAL JOURNAL OF MINING SCIENCE AND TECHNOLOGY Volume: 29 Issue: 5 Pages: 701-709 Published: SEP 2019 **3 body**

68 Mouralova, A, et al.: Analysis of subsurface defects occurrence in abrasion resistant Creusabro steel after WEDM including the study of morphology and surface topography October 2019, Machining Science and Technology DOI: 10.1080/10910344.2019.1669166 **3 body**

Položka A2/14: Ficker, T., **Martišek, D:** Database 3-D Surfaces for Evaluation of Joint Rock Coefficients, Procedia Engineering, 161:1361-1366, 2016,

69 Audy, O., Ficker, T.: Fractal Analysis of Rock Joint Profiles, World Multidisciplinary Civil Engineering-Architecture-Urban Planning Symposium (WMCAUS) Location: Prague, CZECH REPUBLIC Date: JUN 12-16, 2017 WORLD MULTIDISCIPLINARY CIVIL ENGINEERING-ARCHITECTURE-URBAN PLANNING SYMPOSIUM - WMCAUS Book Series: IOP Conference Series-Materials Science and Engineering Volume: 245 Article Number: UNSP 032006 **3 body**

70 Ficker, T.: Some remarks on the dynamical conformity of rock joints, International Journal of Mining Science and Technology, Vol. 28 Issue: 3 , 2018 Pages: 385-390 **3 body**

Položka A2/15: **Martišek, D.:** Elimination of Gibbs and Nyquist–Shannon Phenomena in 3D Image Reconstruction, 3D Research, (2016), vol 7(16)

71 Elkattan, Mohamed; Kamel, Aladin: Characterization of electromagnetic parameters through inversion using metaheuristic technique, INVERSE PROBLEMS IN SCIENCE AND ENGINEERING, 2020 **3 body**

Položka A2/16: **Martišek, D,** Druckmüllerová, H.: Registration of Partially Focused Images for 2D and 3D Reconstruction of Oversized Samples, Scanning, (2017)

72 Fan, Y., Luo, L., Djuric, M: Extracting Cross-Sectional Clinical Images Based on Their Principal Axes of Inertia, Scanning 2017,Article Number: 1468596 **3 body**

Položka A2/17. Martišek, D., Procházková, J.: The Enhancement of 3D Scans Depth Resolution Obtainedby Confocal Scanning of Porous Materials, Measurement Science Review, 17, (2017), No. 6, 273-281

73 Li, Haolin; Dong, Shuhao; Liu, Jiantao; et al.: Finite Element Modeling of Porous Microstructures With Random Holes of Different-Shapes and -Sizes to Predict Their Effective Elastic Behavior, APPLIED SCIENCES-BASEL Volume: 9 Issue: 21 Article Number: 4536 Published: NOV 2019 **3 body**

74. Teng, Xu; Li, Feng; Lu, Chao: Visualization of materials using the confocal laser scanning microscopy technique, CHEMICAL SOCIETY REVIEWS Volume: 49 Issue: 8 Pages: 2408-2425 , apr. 2020 **3 body**

Položka A2/17. Martišek, D.: 3D Reconstruction of the Surface Using a Standard Camera, Mathematical problems in Engineering, 2017, DOI 10.1155/2017/4642397

75. Bayazid, Seyed Mahmoud; Brodusch, Nicolas; Gauvin, Raynald: Investigation of the Effect of Magnification, Accelerating Voltage, and Working Distance on the 3D Digital Reconstruction Techniques **3 body**

Položka A2/19: Martišek, D: Fast Shape-From-Focus method for 3D object reconstruction, Optik - International Journal for Light and Electron Optics 169 (2018) 16–26 Manuscript Number: IJLEO-D-17-03215,

75 Lu Rongsheng; Shi Yanqiong; Hu Haibing: Review of Three-Dimensional Imaging Techniques for Robotic Vision, LASER & OPTOELECTRONICS PROGRESS Volume: 57 Issue:4 , Article Number: 040001, 2020 **3 body**

Položka A3/1: Ficker, T., **Martišek, D.;** Druckmüller, M.: Unconventional Multifractal Formalism and Image Analysis of Natural Fractals, Czechoslovak Journal of Physics, Vol 49 (1999), No. 10,

76 Ficker, T.: Normalized multifractal spectra within the box-counting method, Czechoslovac Journal of Physics, Vol. 50, Issue: 3, pp.: 389-403 (2000) **3 body**

77 Ficker, T.: Electron avalanches II - fractal morphology of partial microdischarge spots on dielectric barriers, Conference: 20th International Symposium on Discharges and Electrical Insulation in Vacuum Location IEEE Transactions on dielectrics and electrical insulation, Vol. 10 Issue: 4 pp: 700-707 (2003) **3 body**

78 Ficker, T.: Fractal multiplication of electron avalanches and streamers: new mechanism of electrical breakdown? Journal of Physics, D – Applied Physics, Vol. 40 Issue: 24 pp. 7720-7733 (2007) **3 body**

79 Ficker, T. Fractality of fracture surfaces, Acta Polytechnica, Vol. 50 No. 6/2010 **3 body**

Položka A4/2: Ficker, T., **Martišek, D**, Jennings, H. M.: Surface Roughness and Porosity of Hydrated Cement Pastes, Acta Polytechnica Vol. 51 No. 3/2011

80 Ficker, T et al.: Is componential strength analysis of concrete possible? Magazine of concreate research, Volume: 65 Issue: 24 Pages: 1480-1485 (2013) **3 body**

Součet kriterií A1 až A6: požadováno minimálně 120 bodů, dosaženo 793 bodů

A9: Příspěvek ve sborníku světového nebo evropského kongresu, sympózia, vědecké konference – 10 bodů

1. Martišek, D.:Automatic Detection and Correction of Defective Pixel Clusters by Means of Nonlinear Regression, Digital Image Processing, An International Workshop, České Budějovice, 1996 **10 bodů**

2. Martišek, D, Mikulášek, K.: Inverse mapping and its use for 3-D data visualisation, Proceedings of The 4th Japan-Central Europe Joint Workshop on Energy and Information in Nonlinear Systems, Brno 2001, Czech Society of Applied Elektromagnetics, Brno 2001, pp. 60-63, **5 bodů**
3. Martišek, D.: 3-D filters and their use for computer modelling, Aplimat, Bratislava 2002 **10 bodů**
4. Martišek, D.: The 2-D processing of images provided by confocal microscopes, Mendel, Brno 2002 **10 bodů**
5. Martišek, D.:Methods of detection of equipotential surfaces in cell structures, Proceedings of 4th Conference on Cell Biology, České Budějovice, 2002, pp.47-54, SBN 80-75232-181-1 **10 bodů**
6. Martišek, D, Druckmüller M.: Mathematical principles of Graphics Systems, The International Konference The Decidable and Undecidable in Mathematic Education, Brno. 2003 ½ **5 bodů**
7. Martišek, D.: The numerical methods of 3-D cell structures reconstruction, Mendel, Brno 2004 **10 bodů**
8. Martišek, D.: New methods of transparent volume rendering, Mendel, Brno 2005 **10 bodů**,
9. Martišek, D., Žák, V.: Mathematical pixel theory and fast graphic algorithms using Maple and .NET technology, Proceedings of the International Maple Conference, Canada 2006, pp. 146-161, ISSN 0124-0242 ½ **5 bodů**
10. Martišek, D., Žák, V.: Fast graphic algorithm of implicit surfaces construction, Proceedings of Symposium on Computer Geometry SCG'2006, Kocovce 2006, pp. 180-184, ISBN 80-227-2489-0 ½ **5 bodů**
11. Ficker, T., **Martišek, D**.: Unstable ground beneath large civil engineering structures, Part II: Unstable Material Discontinuities and their Digital Imaging, 12th International Conference on New Trends in Statics and Dynamics of Buildings (id 22332), Bratislava 2014 **5 bodů**
12. Ficker, T., **Martišek, D**.: Unstable ground beneath large civil engineering structures, Part III: Fourier Reconstruction of Material Discontinuities, 12th International Conference on New Trends in Statics and Dynamics of Buildings (id 22332), Bratislava 2014 **5 bodů**
13. Ficker, T., **Martišek, D**.: Unstable ground beneath large civil engineering structures, Part IV: Classification and Evaluation of Material Discontinuities, 12th International Conference on New Trends in Statics and Dynamics of Buildings (id 22332), Bratislava 2014 **5 bodů**
14. **Martišek, D.,** Druckmüllerová, H.: Power-function method of fractal dimension estimation, 20th International Conference on Soft Computing, MENDEL 2014 (id 22122) **5 bodů**
15. Štarha, P., **Martišek, D**., Matoušek, R.: Numerical Method of Object Reconstruction Using Moment Method, 20th International Conference on Soft Computing, MENDEL 2014 (id 22122) **5 bodů**

16. Ficker, T., **Martišek, D.**:Shear strength of rocks by visual assessment, Source of the Document International Multidisciplinary Scientific GeoConference Surveying Geology and Mining Ecology Management, SGEM, 2 (1), 2015, pp. 641-648 **5 bodů**

17. Ficker, T., **Martišek, D.**: Confocal and non-confocal 3D reconstructions, 12th Workshop NDT 2014 (id 22528) **5 bodů**

18. Ficker, T., **Martišek, D.**: Three-dimensional rock Joints and their topology assessments, Proceedings of the 16th International Multidisciplinary Scientific Geoconference SGEM 2016, pp 349 - 345 **5 bodů**

19. Procházková, J.; **Martišek, D.:**Notes on iterative closest point algorithm, 17th. conference on Applied Mathematics Aplimat 2018, pp. 876 - 884 **5 bodů**

20. Štarha, P.; Procházková, J.; **Martišek, D**.: The 3D Reconstruction of Material Surfaces Using Lens Intentional Colour Defects. Mendel 2018: 24th International conference on soft computing. June 2018 **5 bodů**

21. **Martišek, D;** Procházková, J.: Measurement of Rock Surface Asperities based on Shape from Focus Method, Mendel 2018: 24th International conference on soft computing. June 2018 **5 bodů**

A10: Abstrakt ve sborníku světového nebo evropského kongresu, sympózia, vědecké konference – 2 body

1. Martišek, D, Mikulášek, K.: Inverse mapping and its use for 3-D data visualisation, Proceedings: The 4th Japan-Central Europe Joint Workshop on Energy and Information in Nonlinear Systems, 2000 **1 bod**

A11: Příspěvek ve sborníku národního nebo mezinárodního kongresu, sympózia, vědecké konference – 4 body

1. Martišek, D.:Využití počítače k motivaci teorie Euklidovského prostoru, in: Pedagogický software - sborník přednášek a programů České Budějovice, 1995 **4 body**
2. Martišek, D.:Výuka počítačové grafiky ve speciálních oborech na FS VUT v Brně in: Sborník XIII. vědeckého kolokvia o řízení osvojovacího procesu zaměřeného na problémy modelování a simulace, Vyškov, 1995 **4 body**
3. Martišek, D.:Geometrické modelování ve výuce speciálních oborů na FS VUT v Brně in: Sborník XIV vědeckého kolokvia o řízení osvojovacího procesu zaměřeného na problémy modelování a simulace, Vyškov, 1996 **4 body**
4. Martišek, D.:Využití semestrálních prací z počítačové grafiky a analýzy obrazu k motivaci studia, in: Pedagogický software - sborník přednášek a programů, České Budějovice, 1997 **4 body**
5. Martišek, D.:Postavení počítačové grafiky na FS VUT Brno, in: Sborník XV vědeckého kolokvia o řízení osvojovacího procesu zaměřeného na problémy modelování a simulace, Vyškov, 1997 **4 body**
6. Martišek, D.: Elektronické učební texty, in: Sborník XVI vědeckého kolokvia o řízení osvojovacího procesu zaměřeného na problémy modelování a simulace, Vyškov, 1998 **4 body**

7. Martišek, D.: Fraktální geometrie a modelování přírodních útvarů, in Sborník XVII mezinárodního vědeckého kolokvia o řízení osvojovacího procesu zaměřeného na problémy modelování a simulace, Vyškov, 1999 **4 body**

8. Martišek, D.: Měření fraktálů, in Sborník XVIII mezinárodního vědeckého kolokvia o řízení osvojovacího procesu zaměřeného na problémy modelování a simulace, Vyškov, 2000 **4 body**

9. Martišek, D.: 3D rekonstrukce výstupů z optických mikroskopů, Pedagogicko-vědecká konference, II sborník příspěvků doktorandů, FSI Brno, 2000 **4 body**

10. Martišek, D.: Dimenze množin z hlediska teorie míry, in Sborník XIV mezinárodního vědeckého kolokvia o řízení osvojovacího procesu zaměřeného na problémy modelování a simulace, Vyškov, 2001 **4 body**

11. Martišek, D.: Iterační systémy, atraktory a soběpodobné množiny, in Sborník XV mezinárodního vědeckého kolokvia o řízení osvojovacího procesu zaměřeného na problémy modelování a simulace, Vyškov, 2002 **4 body**

12. Martišek, D.: Trojrozměrná rekonstrukce optických řezů v klasické a konfokální mikroskopii Digitální zobrazování v biologii a medicíně, České Budějovice, 2002 **4 body**

13. Martišek, D.: Animace ve výuce počítačové grafiky specializovaných oborů, in: Sborník konference FS VUT, Brno 1996 **4 body**

14. Martišek, D., Martišek, I.: Softwarové zaostřování snímků z optických mikroskopů, in: Pedagogický software - sborník přednášek a programů, České Budějovice, 1998 **2 body**

15. Martišek, D.: Historie a současnost výuky počítačové grafiky na FSI VUT Brno, seminář o matematice a fyzice na VŠT, KMF VAAZ, Brno 1999 **4 body**

16. Martišek, D., Martišek, I.: Vrstevnice a soustavy nelineárních rovnic, Pedagogický software, České Budějovice, sborník přednášek a programů, 2000 **2 body**

17. Martišek, D.: K některým chybám a omylům počítačových grafiků, seminář o matematice a fyzice na VŠT, KMF VAAZ, Brno 2001 **4 body**

18. Martišek, D.: Matematické metody modelování mikroskopických objektů, SolidWorks, FSI VUT Brno 2002 **4 body**

19. Martišek, D.: Matematické principy grafických systémů, sborník 3. konference o matematice a fyzice na VŠT s mezinárodní účastí, VA Brno 2003 **4 body**

20. Martišek, D.: Softwarové modelování lomu světla, in Sborník XV. Mezinárodního vědeckého kolokvia o řízení osvojovacího procesu zaměřeného na problémy modelování a simulace, Vyškov, 2004 **4 body**

21. Martišek, D.: Softwarové modelování odrazu světla, Pedagogický software, České Budějovice - sborník přednášek a programů, 2004 **4 body**

22. Martišek, D.: Počítačová grafika jako motivace studia matematiky, in Sborník 25. konference o geometrii a počítačové grafice, JČMF, ČVUT Praha 2005 **4 body**

23. Martišek, D.: Výuka numerické matematiky v éře počítačů Pedagogický software, České Budějovice - sborník přednášek a programů, 2006 **4 body**

24. Martišek, D.: Výukový software pro předmět Konstruktivní a počítačová geometrie, in Sborník příspěvků 27. konference o geometrii a počítačové grafice, Nedvědice 2007 **4 body**

A13: Abstrakt ve sborníku národního nebo mezinárodního kongresu, sympózia, vědecké konference – 1 bod

1. Martišek, D., Cápal, J.: Složení víceohniskového obrazu užitím statistických metod in: Sborník 37. sjezdu České anatomické společnosti s mezinárodní účastí, Brno 1996 **0,5 bodu**

2. Martišek, D.: 3D rekonstrukce snímků z optického mikroskopu, 38. zjazd Slovenskej anatomickej spoločnosti s medzinárodnou účasťou, zborník abstaktov, Bratislava 1999 **1 bod**

A14: Citace jiným autorem v publikaci bez SCI – 1 bod

1 Ficker, T.: Electrostatic discharges and multifractal analysis of their Lichtenberg figures, J. Phys. D: Appl. Phys. 32 (1999) pp 219–226, citována položka A3/1 **1 bod**

2 Ficker, T.: Electrostatic surface microdischarges and viscous fingering in liquid dielectrics, Proceedings of the 1999 IEEE 13th International Conference on Dielectric Liquids, 1999, citována položka A3/1. **1 bod**

3 Chvalinová, L.: Výuka předmětu Počítačová geometrie a grafika na FSI VUT v Brně, in: Sborník XIV mezinárodního vědeckého kolokvia o řízení osvojovacího procesu zaměřeného na problémy modelování, Vyškov, 2001, citována položka B8/2 **1 bod**

4 Malina, P.: Matematické principy grafických systémů, Science World 15.01.2003, http://www.scienceworld.cz/neziva-priroda/matematicke-principy-grafickych-systemu-recenze-knihy-3288/ citována položka A1/1 **1 bod**

5 Druckmüller, M.:3D visualization techniques for confocal microscope images, CELLS IV, Kopp Publishing, České Budějovice 2002, citovány položky A3/1, A9/2, A9/3, A9/4 **4 body**

6 Niederost, M et al.: Automatic 3D reconstruction and visualization of microscopic objects from a monoscopic multifocus image sequence, International Archives of the Photogrammetry, Remote Sensing and Spatial Infoirmation Sciences, Vol. XXXIV-5/W10, 2003, citována položka A2/1 **1 bod**

7 Druckmüller, M.: Opacity simulation technique for confocal microscope images, Journal of Applied Biomedicine, No. 2., 2003, citovány položky A1/1, A3/2, A9/2, A9/3, A9/4, A9/5 **6 bodů**

8 Běhounek, T.: Imaging Reflectometry – measuring optical charakteristic, pojednání ke státní doktorské zkoušce, VUT Brno, 2004, citována položka A1/1 **1 bod**

9 Tomáš, J.: The measurement of the Hausdorff dimension of the real objects, pojednání ke státní doktorské zkoušce, VUT Brno, 2004, citována položka A1/1 **1 bod**

10 Nový, J.: Digital Filtering and Compression in Image Processing and Volume Rendering pojednání ke státní doktorské zkoušce, VUT Brno, 2004, citovány položky A2/1, A9/3, A9/6 **3 body**

11 Janíček, P.: Systémové pojetí vybraných oborů pro techniky, VUTIUM, Brno, 2007, citována položka A1/1 **1 bod**

12 Ficker, T.: Electrical breakdown in gases via a new mechanism of avalanche and streamer Multiplications - Plasma Fusion Res. Series, 2008, , citována položka A3/1. **1 bod**

13 Jihoon Kwak, Chun-Taek Oh, Sung-Jun Han, Myungjoo Kang, Auguste Genovesio: Hair Separation and Detection in Mutant Drosophila Hair Images, The National Research Foundation of Korea (NRF) grant funded by the Korea government(MEST)(No. 2009-0090095), 2009, citována položka A2/1 **1 bod**

14 Sedlák, J., Charvát, O., Madaj, M.: Technology of processing CT data of the Knee Joint, Manufacturing technology - Abstracts, vol. X., pp. 18 – 19, 2010, citována položka A1/1 **1 bod**

15 Lee, S.-H., Seo, S.-D., Jin, Y.-H., Shim, H.-W., Kim, D.-W.: A graphite foil electrode covered with electrochemically exfoliated graphene nanosheets, Electrochemistry Communications 2010, 12 (10), citována položka A2/4 **1 bod**

16 Ficker, T.: Surface morphology of porous cementitious materials subjected to fast dynamic fractures, Acta Polytechnica, 51(5), pp 118 - 119, 2011, citovány položky A2/4, A4/2 **2 body**

17 Ficker, T.: Fracture surfaces of porous material, Acta Polytechnica 2011, 5(3), pp21 – 24 citovaná položka A2/4 **1 bod**

18 Amin, M. S., Haslem, F, S.: Hydration characteristics of hydrothermal treated cement kiln dust–sludge–silica fume pastes, Construction and Building Materials, 25(4):1870-1876 · April 2011, citována položka A2/4 **1 bod**

19 Stastny, J., Procházka, D., Koubek, T., Landa, J.: Augmented reality usage for prototyping speed up, Acta Universitatis Agriculturae et Silviculturae Mendelianae Brunensis 2011,59 (2), pp. 353-360, citována položka A3/2 **1 bod**

20 Wang, S., Wang, K., Sun, X., Liu, X: Study on solid molding and reverse metod for the inner helicoids of helical stator, Consumer Electronics, Communications and Networks (CECNet), 2011 International Conference on, XianNing, 2011, pp. 4457-4460, doi: 10.1109/CECNET.2011.5768623, citována položka A3/2 **1 bod**

21 Shen, Y., Garnier, J., et al.: Experimental and numerical characterization of anisotropic damage evolution of forged Al6061-T6 alloy, Procedia Engineering 10, pp. 3429-3434, 2011 citována položka A2/4 **1 bod**

22 Trojovská, E., Trojovský, P.: On Animation Creating in System Maple, DIVAI 2012 - 9th International Scientific Conference on Distance Learning in Applied Informatics, 2012, citována položka A1/1 **1 bod**

23 Goldson, M.: CFRP Strengthening of Reinforced Concrete Beams for Blast and Impact Loads, University of Wollongong 2012, p. 1 – 251 citována položka A2/4 **1 bod**

24 Qiang, T., Yu, D., Gao, H: Fractal characteristic and impact strength of PLA-based wood plastic composites, Advanced Materials Research 532-533, pp. 49-52, 2012, citována položka A2/4 **1 bod**

25 Restin, C. B.: Applications of confocal microscopy to the study of vascular biology, Current Microscopy Contributions to Advances in Science and Technology, Vol 5 (2012), citována položka A2/7 **1 bod**

26 Ficker, T.: An optimal procedure for determining the height parameters of fracture surfaces, Acta Polytechnica, 52 (2), pp. 31 – 33, 2012, citovány položky A2/4, A4/2 **2 body**

27. Goldston, M (2012) CFRP Strengthening of Reinforced Concrete Beams for Blast and Impact Loads, master thesis, citovaná položka A4/2 **1 bod**

28 Pokorný, P., Petráš, R.: A Raster Image Processing Application, Recent Advances in Automatic Control, Information and Communications, pp 346-349, 2013, citována položka A1/1 **1 bod**

29 Landa, J., Prochazka, D., Štastny, J.: Point cloud processing for smart systems,Acta Universitatis Agriculturae et Silviculturae Mendelianae Brunensis 61 (7), pp. 2415-2421, 2013, citována položka A2/3 **1 bod**

30 Qiang, T., Yu, D., Gao, H.: Impact strength and fractal characteristic of PLA-based wood plastic Composites Applied Mechanics and Materials 174-177, pp. 683-686, 2012, citovaná položka A2/4 **1 bod**

31 Chen, X., et al: Experimental study and analytical model for pore structure of hydrated cement paste, Applied Clay Science 101, 2014, citovaná položka A2/4 **1 bod**

32 Ma, A., Wu, F., Sha, P., Wang, D.: Fractal characteristic of fragment surface from rock burst test based on confocal laser scanning microscope, Yanshilixue Yu Gongcheng Xuebao/Chinese Journal of Rock Mechanics and Engineering 33, pp. 3595-3600, 2014, citovaná položka A2/4 **1 bod**

33 Pavlík, J.: Thresholding of a Digital Image by Free Terms, Journal of Mathematical Imaging and Vision 51(2) · 2014, citována položka A1/1 **1 bod**

34 Druckmüllerová, H.: Decomposition of a Bunch of Objects in Digital Images, International Workshop on Combinatorial Image Analysis, At Brno, Czech Republic, Volume: 2014, citována položka A1/1 **1 bod**

35 Apedo, K.: Cement paste surface roughness analysis using Coherence Scanning Interferometry and Confocal Microscopy, Materials Characterization, 100 (2014), citována položka A4/2 **1 bod**

36 Satoh, A., Yamada, K., Ishiyama, S.: Fractal characteristic of fragment surface from rock burst test based on confocal laser scanning microscope, Yanshilixue Yu Gongcheng Xuebao/Chinese Journal of Rock Mechanics and Engineering 33, pp. 3595-3600, 2014, citována položka A2/4 **1 bod**

37 Satoh, A.: Experimental study on major parameters of fractography for concrete, Journal of Structural and Construction Engineering (Transactions of AIJ) 79(698): 437-444, 2014, citovaná položka A2/4 **1 bod**

38 Růžička, M., Mašek, P.: Visual SLAM based on phase correlation and particle filters, Advances in Intelligent Systems and Computing, 378, 2015, pp. 353 – 362 citovaná položka A9/15 **1 bod**

39 Prabhu, A., Gimel, J.-C., Ayuela, A., Dolado. J. S.: Effect of Nano Seeds in C-S-H Gel Formation: Simulation Study from the Colloidal Point of View, CONCREEP 2015, Proceedings of the 10th International Conference on Mechanics and Physics of Creep, Shrinkage, and Durability of Concrete and Concrete Structures pp. 877-886, citována položka A2/5 **1 bod**

40 Duperay, P.A., Kamp, A.M.: On the analytical estimation of fracture porosity from fracture permeability - Influence of fracture roughness, tortuosity and connectivity, EUROPEC 2015, pp. 880 – 908, citována položka A2/8 **1 bod**

41 Jarušek, R., Volna, E., Kotyrba, M.: Neural network approach to image steganography techniques, Advances in Intelligent Systems and Computing, 378, 2015 pp. 317 – 327, citovaná položka A9/15 **1 bod**

42 Sadowski, L.: Evaluation of the height 3D roughness parameters of concrete substrate and the adhesion to epoxy resin, International Journal of Adhesion and Adhesives, Vol 67 (2015), citovány položky A2/11, A2/12, A4/2 **3 body**

43 Topič, J.: Effect of PVA modification on the properties of cement composites, Acta Polytechnica 55(1):pp. 64-75 (2015) citována položka A4/2 **1 bod**

44 Petrasova, A. et. all.: Tangible Modeling with open source GIS, book, Springer 2015 DO 10.007/978-3-319-89303-7_3, Citována položka A3/2 **1 bod**

45 Ahmed, K,B.: Etude de l'encrassement biologique de matériaux cimentaires en eau de rivière: analyse de l'influence des paramètres de surface des pâtes cimentaires, https://tel.archives-ouvertes.fr/tel-01544842/, 2016, Citována položka A4/2 **1 bod**

46 Hillouin, B. et al.: Monitoring of autogenous crack healing in cementitious materials by the nonlinear modulation of ultrasonic coda waves, 3D microscopy and X-rays microphotography Construction and Building Materials, Vol 123(1) 2016, pp. 143-152 citovaná položka A2/4 **1 bod**

47 Marada, T.: PID controler parameters settings based on genetic algorithm for inverted pendulum purpose stabilization, Mendel 2016, pp. 31 – 38, citovaná položka A9/15 **1 bod**

48 Apedo, K.: Geometrical roughness analysis of cement paste surfaces using Coherence Scanning Interferometry and Confocal Microscopy, Materials Characterization, Vol. 118 (2016) pp. 212–224, citovány položky A2/4, A2/8, A4/2,
3 body

49 Limandri, S. P.: 3D scanning electron microscopy applied to surface characterization of fluorosed dental enamel, Micron 84 (2016), citována položka A2/11
1 bod

50 Procházková, J., Kratochvíl, J.: Direct Point Cloud Visualization Using T-spline with Edge Detection, : Recent Advances in Soft Computing, 2017 pp.240-251 citovány položky A3/2, A9/15 **2 body**

51 Ficker, T.: Sectional techniques for 3D imaging of microscopic and macroscopic objects, Optik 144 (2017), pp. 289-299, citovány položky A2/4, A2/6, A2/12, A2/13,
4 body

52 Al-Saadi, N.T.K., Mohammed, A., Al-Mahaidi, R. Assessment of residual strength of concrete girders rehabilitated using NSM CFRP with cementitious adhesive made with graphene oxide after exposure to fatigue loading, Construction and Buildings materials, 153 (2017), pp. 402 – 422, Citované položky A2/4, A2/8
2 body

53. Gilmas, M.: Endommagement des aciers frittés utilisés dans la conception automobile, Optimisation de l'élaboration et de la tenue mécanique, Normandie Universite, 2016, Citovaná položka A4/2. **1 bod**

54 Georges, V.: Comportement de matériaux cimentaires en eau douce naturelle: analyse de l'influence des micro-organismes. Matériaux. Université de Lorraine, 2017. Français. Citována položka A4/2 **1 bod**

55. Ficker, T.: Fractal properties of joint roughness coefficients, International Journal of Rock Mechanics and Mining Sciences 94:27-31 DOI: 10.1016/j.ijrmms.2017.02.014 Citována položka A4/2 **1 bod**

56 Ficker, T., Komárková, T.: Rock Joint Asperities and Mechanical Strength of Concrete, IOP Conf. Ser.: Mater. Sci. Eng. 245, 2017, Citována položka A4/2
1 bod

57 Ficker, T.: A numerical technique for assessing joint rock coefficients, International Multidisciplinary Scientific GeoConference Surveying Geology and Mining Ecology Management, SGEM 17(12), pp. 25-32, 2017, citována položka A2/13
1 bod

58 Mouralova, K. et al.: Analysis of surface and subsurface layers after WEDM for Ti-6Al-4V with heat treatment, Measurement, 2017.11.053, DOI 10.1016, Citována položka A2/12
1 bod

59 Restrepo, C., C.: Monoscopic Multifocus In Polarization Images For Biological Samples Segmentation Latin America Optics and Photonics Conference, DOI: 10.1364/LAOP.2018.W2B.4, January 2018, citována položka A4/2
1 bod

60 Safiullah, O. et al.: Effet de l'hydratation et du rapport E/C sur les paramètres de la rugosité de surface de pâtes cimentaires, 36èmes Rencontres de l'AUGC, ENISE/LTDS, Saint Etienne, 19 au 22 juin 2018, citována položka A4/2 **1 bod**

61 Petrasova, A. et al.: Building Physical 3D Models, In book: Tangible Modeling with Open Source GIS Projects: Tangible LandscapeOpen source geospatial
DOI: 10.1007/978-3-319-89303-7_3 May 2018
citována položka A3/2 **1 bod**

62 Beyhan ÖztürkHıdır Serkendiz: Location Selection for Wind Turbines in Balikesir, NW Turkey, Using GIS, International Journal of Environment and Geoinformatics (IJEGEO), Vol: 5 Issue:3, December 2018, citována položka A2/9 **1 bod**

63. Xiao, M., Sun, Z., Shen, X., Shi, L., Zhang, J.: Research on 3D reconstruction technology of tool wear area, Manufacturing Technology 19(2), pp. 345-349, 2019,
Citována položka A2/19 **1 bod**

64 Yao, Y.: Study on three-dimensional reconstruction of green plants landscape on both sides of highway,Academic Journal of Manufacturing Engineering 17(1), pp. 158-164, 2019,
Citována položka A2/12 **1 bod**

65. Konkol, J.: Fracture Toughness and Fracture Surface Morphology of Concretes Modified with Selected Additives of Pozzolanic Properties, Buildings, 2019, 9, 174, 2019
Citována položka A2/8 **1 bod**

66 Okan YÜCESES & Cüneyt ERENOĞLU: Deformation Analysis by Geomatic and Geotechnical Methods in Highway Tunnels, International Journal of Environment and Geoinformatics (IJEGEO), Vol: 6 Issue:2 July 2019
Citovány položky A2/9, A9/21 **2 body**

67 Haolin Li, et al: Finite Element Modeling of Porous Microstructures With Random Holes of Different-Shapes and -Sizes to Predict Their Effective Elastic Behavior, Applied Sciences, 2019, 9, 4536; doi:10.3390/app9214536, Citována položka A2/17
1 bod

68 Ficker: Rock joint coefficients and their computerized classification, International Journal of Mining Science and Technology 29 (2019) 701–709, Citována položka A4/2
1 bod

69. Lotfi, M., Tokhmechi, B.: Paradigm Shift in Studying Joint Micro-Roughness Coefficients using Graph Theory, Int. J. Min. & Geo-Eng. (IJMGE), 53-2 (2019) 165-174
1 bod

70. Lotfi, M., Tokhmechi, B.: Fractal-wavelet-fusion-based re-ranking of joint roughness coefficients, Journal of Mining and Environment (JME)
DOI: 10.22044/jme.2019.7489.1614
1 bod

71 Xu Teng, Feng Li: Visualization of materials using the confocal laser scanning microscopy Technique Chemical Society Reviews, 2020, DOI: 10.1039/C8CS00061A
1 bod

72. Olesia A. BotsiuraIgor P. Zakharov: Improving the reliability of the expanded uncertainty evaluation at calibration of measuring instruments, Metrologiya, 2020, Citována položka A2/17 **1 bod**

73. Shirakawa L.N,. de Lima,C et al: EFFECTS OF NATURAL AGEING ON THE PROPERTIES OF A COOL SURFACE EXPOSED IN DIFFERENT BRAZILIAN ENVIRONMENTS, Energy and Buildings, Citována položka A2/4
1 bod

74 Margaux Gilmas,Eric Hug: Endommagement des aciers frittés utilisés dans la conception automobile. Optimisation de l'élaboration et de la tenue mécanique., Normandie Université, Jul 2016, Citována položka A4/2 **1 bod**

75 Mohamed Elkattana and Aladin Kamelb: Characterization of electromagnetic parameters through inversion using metaheuristic technique, INVERSE PROBLEMS IN SCIENCE AND ENGINEERING, DOI: 10.1080/17415977.2020.1797718 **1 bod**

Součet kriterií A7 až A14: požadováno minimálně 80 bodů, dosaženo 333,5 bodu

---

A17: Členství v redakční radě vědeckého časopisu v zahraničí – 15 bodů

1. Členství v redakční radě časopisu Mathematical Problems in Engineering **15 bodů**

A22: Členství v organizačním výboru národního nebo mezinárodního kongresu, sympóziia, vědecké konference - 5 bodů

1. Členství v organizačním výboru národní konference SolidWorks, Brno 2002 **5 bodů**
2. Členství v organizačním výboru 3. konference o matematice a fyzice na VŠT s mezinárodní účastí, VA Brno 2003 **5 bodů**
3. Členství v organizačním výboru národní konference SolidWorks, Brno 2004 **5 bodů**
4. Členství v organizačním výboru národní konference Pedagogický software, České Budějovice 2006 **5 bodů**
5. Členství v organizačním výboru mezinárodni konference Geometry and Computer Graphics 07, Nedvědice 2007 **5 bodů**
6. Členství v programovém výboru mezinárodni konference Geometry and Computer Graphics 08, Lednice 2008 **5 bodů**
7. Členství v organizačním výboru mezinárodni konference IWCIA, Brno 2014 **5 bodů**

A24: Získání externího grantu (řešitel, spoluřešitel) – 6 bodů

1. Výzkumný záměr – CEZ:J22/98:261100009 Netradiční metody výzkumu komplexních a neurčitých systémů (spoluřešitel) **6 bodů**
2. Národní grant – Grantová agentura České republiky, č. 202/97/1407 Fraktální geometrie v°transportních procesech (spoluřešitel) **6 bodů**
3. Studie – Karpíšek, Z. a kol.: Studie proveditelnosti meteoradarové sítě ŘLP ČR, (spoluřešitel) Úvodní studie projektu 2000 (dílo podléhá zákonu 148/1998 sb. ze dne 11. června 1998 o ochraně utajovaných skutečností) **6 bodů**
4. Studie – Karpíšek, Z. a kol.: Studie proveditelnosti meteoradarové sítě ŘLP ČR, Studie modifikace meteoradarového systému CZRAD pro potřeby

ŘLP ČR s. p. a°prováděcí plán, Brno 2000 – spoluřešitel (dílo podléhá zákonu 148/1998 Sb. Ze dne 11. června 1998 o ochraně utajovaných skutečností) **6 bodů**

5. Studie – Karpíšek, Z. a kol.: Studie meteoradarové infrastruktury ŘLP ČR s. p. Realizační studie využití meteoradarových dat CZRAD.v systémech ŘLP ČR s.p., Brno 2001 - spoluřešitel (dílo podléhá zákonu 148/1998 Sb. ze dne 11. června 1998 o ochraně utajovaných skutečností) **6 bodů**
6. Studie – Karpíšek, Z. a kol.: Studie proveditelnosti meteoradarové sítě ŘLP ČR Projektová studie rozšíření CZRAD o meteoradarové čidlo umístěné v centrální poloze, Brno 2001 - spoluřešitel (dílo podléhá zákonu 148/1998 Sb. ze dne 11. června 1998 o ochraně utajovaných skutečností) **6 bodů**
7. Národní grant – Grantová agentura České republiky, č. 202/03/0011 Bariérové mikrovýboje a jejich degradační účinky (spoluřešitel) **6 bodů.**
8. Národní grant – Grantová agentura České republiky, č. 202/07/2007 Statistické dilema elektronových lavin (spoluřešitel) **6 bodů.**
9. Projekt FRVŠ – Elektronická podpora předmětu Matematické výpočty pomocí Maple 2006 (spoluřešitel) **6 bodů**
10. Projekt FRVŠ – Tvorba multimediálních studijních materiálů pro předmět Počítačová grafika, 2007 (spoluřešitel) **6 bodů**
11. Projekt FRVŠ – Modernizace počítačové učebny pro podporu projektové výuky matematických předmětů 2009 (hlavní řešitel) **6 bodů**
12. Národní grant – Grantová agentura Vývoj nové nedestruktivní metody pro posuzování pevnosti v tlaku hydratovaných cementovaných materiálů (2009 - 2012) (spoluřešitel) **6 bodů**
13. Projekt FRVŠ – Multimediální učebny 2013 (hlavní řešitel) **6 bodů**
14. Národní grant – Grantová agentura České republiky, č. 13-03403S Morfologická analýza lomových povrchu a její důsledky pro stabilitu velkých civilně-inženýrských staveb (2013 - 2017) (spoluřešitel) **6 bodů**
15. Project LO1202 NPU (MŠMT) (spoluřešitel) **6 bodů**

A25: Odborná příručka v oboru – za jeden autorský arch 2 body

1. Martišek, D., Faltusová, M: Matematika, příručka pro přípravu k přijímacím zkouškám, CERM, Brno, 2004, 50 x 80 x 198 = 22 archů 0.5 **22 bodů**
2. Martišek, D.: Algoritmizace a programování v Delphi, Littera Brno, 2007, ´ 80 x 40 x 220 = 20 archů **40 bodů**

A27: Posudek zahraniční publikace nebo projektu – 3 body

1. Vyžádaná recenze článku: Dobes, M.: Comparison of Discrete Cosine Transform and Wavelet Transform compression algorithms, Aplimat, Bratislava 2007 **3 body**
2. Vyžádaná recenze článku: Dobes, M.: Comparisson of statistical methods in steganography, Aplimat, Bratislava 2007 **3 body**

3. Vyžádaná recenze článku: Écsi Ladislav: Cyclic bending of a solid bar with and without plastic heating – further way to improve our energy conservation equation, Aplimat, Bratislava 2007 **3 body**

4. Vyžádaná recenze článku: Dobes, M.: Iterative Image Restoration and the Stopping Criteria, Proceedings of the 11th World Multi-Conference on Systemics, Cybernetics and Informatics: WMSCI 2007 Orlando, Florida, USA **3 body**

5. Vyžádaná recenze článku: Saiedian, H.: Performance Evaluation of Hierarchical Data Labeling Schemes in Relational Database Systems, Computer, COMSI-2007-10-0113 for Special Issue April 2008 Data-Intensive Computing, February, 2008 **3 body**

6. Vyžádaná recenze článku: Chih-Wei Yi: A Unified Analytic Framework Based on Minimum Scan Statistics for Wireless Ad Hoc and Sensor Network, Transactions on Parallel and Distributed System, for Issue September 2008, April, 2008 **3 body**

7. Vyžádaná recenze článku: Zhu, Jia-yuan; Liu, Peng; Tang, Bing; Hu, Zhi-cheng: Three dimensional digital reconstruction of skin epidermis and dermis, Journal of Microscopy, March 2017. **3 body**

8. Vyžádaná recenze článku Peng He, Shangqu Sun, Gang Wang, WeiTeng Li: Gaussian process model of surrounding rock classification based on digital representation of rock mass structural information, Journal of Mathematical Problems in Engineering, August, 2019 **3 body**

9 Vyžádaná recenze článku Zhongjun Qiu, Junjie Tang: 3D information measurement and reconstruction for micro-hole array by laser beam drilling based on shape from focus, Optics and Lasers in Engineering, October, 2019 **3 body**

A29: Posudek domácí publikace nebo projektu – 2 body

1. Posudek přihlášky grantu GAČR reg. č. 102/03/0030 **2 body**
2. Posudek projektu „Matematický model proudění v bezlopatkových tekutinových strojích“ pro firmu MIRIS Praha, 2004 **2 body**
3. Posudek přihlášky grantu GAČR reg. č. 101/07/P450 **2 body**
4. Posudek přihlášky grantu GAČR reg.č. 102/08/P518 **2 body**
5. Recenze knihy: Janíček, P.: Systémové pojetí vybraných oborů pro techniky, VUTIUM, Brno, 2007 **2 body**
6. Posudek přihlášky grantu grantové agentury PEF - Mendelova univerzita v Brně: Procházka, D.: Vizualizace komplexních grafických dat pro podporu rozhodovacího procesu, Brno, 2010 **2 body**
7. Posudek přihlášky grantu grantové agentury PEF - Mendelova univerzita v Brně: Procházka, D.: Využití nástroj; rozšřené reality pro zefektivnění výrobního procesu, Brno, 2011 **2 body**
8. Posudek přihlášky grantu grantové agentury PEF - Mendelova univerzita v Brně: Procházka, D.: Zvýšení efektivity správy majetku prostřednictvím mraku bodů, Brno, 2012 **2 body**

9. Recenze článku Jak neztratit hlavu z fraktálních dimenzí, Elektrorevue 2014 **2 body**

10 Vyžádaná recenze knihy: Bečvářová, M., Netuka, I.: Dopady první světové války na mezinárodní spolupráci matematiků, ČVUT Praha, 2019 **2 body**

11. Posouzení žádosti FPřHPed TU v Liberci o akreditaci Bc. SP Matematika (NAU-527/2018). **2 body**

12. Posouzení žádosti FStav ČVUT v Praze o akreditaci Dr. SP Matematika ve stavebním inženýrství (také v AJ) (NAU-566/2018). **2 body**

13. Posouzení žádosti FJFI ČVUT v Praze o udělení akreditace MSP Aplikovaná algebra a analýza (také v AJ) (NAU 118/2019). **2 body**

14. Posouzení žádosti FJFI ČVUT v Praze o udělení akreditace MSP Aplikovaná algebra a analýza (také v AJ) (NAU-543/2020). **2 body**

A30: Posudek k obhajobě habilitační nebo dizertační práce – 2 body

1. Posudek disertační práce: Šrubař, P.: Matematický model výroby ploch, Pojednání ke státní doktorské zkoušce, Brno 2000 **2 body**

2. Posudek disertační práce: Nový, J.: Filtering and Compression in Image Processing and Volume Rendering, Brno 2005 **2 body**

3. Posudek disertační práce: Nagy, I.: Segmentace tomografických snímků pomocí metody aktivních kontur, Brno 2005 **2 body**

4. Posudek přepracované disertační práce: Nagy, I.: Segmentace tomografických snímků pomocí metody aktivních kontur, Brno 2006 **2 body**

5 Posudek rigorózní práce: Moser, M.: Počítačem podporovaná výuka zobrazovacích metod, Katedra matematiky Přírodovědecké fakulty MU, Brno 2007 **2 body**

6 Posudek disertační práce Tomáš, J.: Měření Hausdorffovy dimenze reálných objektů, Brno 2009 **2 body**

7 Posudek disertační práce Berjak, J.: Automatická analýza a rozpoznávání objektů v obraze pomocí fázové korelace, Brno 2009 **2 body**

8 Posudek disertační práce Tonner, J.: Overcomplete mathematical models with application, Brno 2010 **2 body**

9 Posudek disertační práce Španěl, M.: Delaunay-based Vector Segmentation of Volumetric Medical Images, Brno 2010 **2 body**

10 Posudek disertační práce Knápek, A.: Zobecněná tolerance tvaru, polohy a rozměru, Ostrava 2010 **2 body**

11 Posudek disertační práce Týč, M.: Trojrozměrná rekonstrukce obrazu v digitální holografické mikroskopii, Brno 2015 **2 body**

12. Posudek disertační práce Honková, M.: Numerické metody analýzy obrazu v astronomii Brno 2018 **2 body**

13. Posudek disertační práce Kratochvíl, J.: Detekce a vizualizace specifických rysů v mračnu bodů, Brno 2018 **2 body**

Součet kriterií A ostatní: požadováno minimálně 120 bodů, dosaženo 283 bodů

Součet kriterií A celkem: požadováno minimálně 320 bodů, dosaženo 1 409,5 bodu

---

B. Pedagogická činnost

B1: Za každý rok pedagogického působení na VŠ na plný úvazek – 2 body

Na ÚM FSI VUT plný úvazek 35 let **70 bodů**

B3: Zavedení předmětu, který byl vyučován v posledních pěti letech – 15 bodů

1 Počítačová grafika pro matematické inženýry, III. semestr, od akad. r. 1995/96 dosud **15 bodů**

2 Vizualizace dat (Matematické inženýrství – magisterské studium, 2. ročník) od akad. r. 2004/05 dosud **15 bodů**

3 Programovací metody I (Matematické inženýrství – III. semestr) od akad. r. 2004/05 dosud **15 bodů**

4 Programovací metody II (Matematické inženýrství – V. semestr) od šk. r. 2005/06 dosud **15 bodů**

5 Počítačová geometrie a grafika pro bakalářské studium, I. semestr, od akad. roku 2011/2012 **15 bodů**

6 Obrazová analýza v materiálových vědách (WON) od akad. roku 2014/15 **15 bodů**

7 Konstruktivní geometrie (1KD) bakalářské studium 1. semestr od akad. roku 2020/21 **15 bodů**

B4 Vedoucí obhájené diplomové/bakalářské práce – 2 body/1 bod

1. Červeňan Roman: Fotometrická kalibrace snímků vesmírných těles, diplomová práce 1998 **2 body**

2. Pícka Vladimír: 3D projekce povrchu vesmírných těles, diplomová práce 1998 **2 body**

3. Prokop Pavel: Automatická detekce a korekce vadných clusterů pomocí ortogonálních bází, diplomová práce 1999 **2 body**

4. Doubravský Karel: Metrické metody jako podklad pro analýzu silničních nehod, diplomová práce 1999 **2 body**

5. Kohout Robert: Prostorové rekonstrukce stereoskopických fotografií, diplomová práce 2000 **2 body**

6. Hodál, Jaroslav: Vizualizace vícerozměrných statistických a optimalizačních veličin, diplomová práce 2000 (1/2) **1 bod**

7. Unucka Marek: Modelování optických jevů metodou sledování paprsku, diplomová práce 2001 **2 body**

8. Tkáč Daniel: Rychlé grafické algoritmy při konstrukci 3D objektů, diplomová práce 2002 **2 body**

9. Pešek, Jiří: Matematické metody modelování terénu a výšky hladin vodních toků, diplomová práce 2002 **2 body**

10. Běhounek Tomáš: Vícerozměrné filtry a jejich použití, diplomová práce 2004 **2 body**

11. Škoda Jiří: Matematické metody vizualizace skalárních polí v konfokální mikroskopii, diplomová práce 2004 **2 body**

12. Juriga, Antonín: Matematické metody modelování lomu světla, diplomová práce 2005 **2 body**

13. Diviš, Petr: Softwarové měření Hausdorffovy dimenze, diplomová práce 2005 **2 body**

14. Farkaš, Tibor: Matematické metody zpracování dat Visible Human Project, diplomová práce 2005 **2 body**

15. Vaněk, Pavel: Modelování přírodních útvarů pomocí statistické soběpodobnosti, diplomová práce 2006 **2 body**

16. Michal, Jiří: Modelování odrazu a lomu světla metodou fotonových map, diplomová práce 2006 **2 body**

17. Slabáková, Jana: Zobrazovací metody počítačové grafiky, bakalářská práce 2007 **1 bod**

18. Kala, Miroslav: Zobrazovací metody počítačové grafiky, bakalářská práce 2007 **1 bod**

19. Martišek, Karel: Numerical methods for multispectral confocal microscopy, diplomová práce 2007, 2. místo v česko-slovenském kole SVOČ, Olomouc 2007, Cena Josefa Hlávky 2007 **2 body**

20. Turek, Vojtěch: Vícehodnotová logika pro technické aplikace, diplomová práce 2008 (2. místo v česko-slovenském kole SVOČ 2008) **2 body**

21. Novotný, Jan: Multispektrální analýza obrazových dat, diplomová práce 2009 **2 body**

22. Slabáková, Jana: Modelování NURBS křivek a ploch v projektivním prostoru, diplomová práce 2009 **2 body**

23. Janoutová, Růžena: Matematické modelování pomocí L-systémů, bakalářská práce 2010 **1 bod**

24. Komínek, Jan: Vizualizace statických úloh metodami počítačové grafiky, bakalářská práce 2010 **1 bod**

25. Druckmullerová, H.: Phase-correlation based image registration
(cena ministra školství), diplomová práce 2010 **2 body**

26. Grísa, Tomáš: Fraktální komprese obrazu, bakalářská práce 2011
(3. místo v česko-slovenském kole SVOČ) **1 bod**

27. Janoutová, Růžena: Matematické metody modelování morfologie jehličnanů,
diplomová práce 2012 **2 body**

28. Vostal, Jiří: Numerické metody měření Hausdorffovy dimenze,
bakalářská práce 2015 **1 bod**

29. Maruniaková, Zuzana: 3D rekonstrukce objektů pomocí metod analýzy obrazu,
diplomová práce 2018 **2 body**

30. Gurecká, Hana: Visualization of scalar Fields by Back-toFront Methods,
diplomová práce 2020 **2 body**

31. Le Huy: Numerical methods of Measurement of fractal dimensions and fractal measures,
diplomová práce 2020 **2 body**

B 5: Školitel/školitel specialista studenta, který získal Ph.D.; Dr. 15 bodů

1. Procházková, Jana.: Modelování matematických ploch v CAD systémech, Ph.D. 2007
15 bodů

2. Druckmüllerová, Hana: Aplikace adaptivních filtrů při zpracování snímků sluneční
koróny, Ph.D. 2014 **15 bodů**

3. Novotný, Jan: Matematické metody Segmentace obrazu pro dálkový průzkum Země
Ph.D. 2015 **15 bodů**

4. Janoutová, Růžena: Modelování 3D struktury lesa pro zlepšení odhadů biofyzikálních
vlastností lesa Ph.D. 2017 **15 bodů**

5. Pivovarník, Marek: Nové přístupy zpracování leteckých obrazových termálních dat ke
zhodnocení krajiny, Ph.D. 2017 **15 bodů**

B 8: Skripta: za jeden autorský arch – 2 body

1. Martišek, D.: Počítačová grafika pro matematické inženýry, PC DIR Brno 1999
60 x 100 x 70 = 12 archů **24 bodů**

2. Martišek, D.: Počítačová geometrie a grafika, VUTIUM Brno 2000
50 x 90 x 96 =12 archů **24 bodů**

3. Martišek, D: Základy počítačové geometrie a grafiky, 2012 MathOnLine, ÚM FSI VUT
Brno 2012, 80 x 60 x 200 = 27 archů **54 bodů**

4. Martišek, D: Analýza obrazu v materiálových vědách, 2016
80 x 60 x 88 znaků = 12 archů
https://math.fme.vutbr.cz/cz/zamestnanci
Martišek, Soubory ke stažení, WON_Studijni_Text_2017.pdf
24 bodů

5. Martišek, D: Počítačová grafika v matematickém inženýrství, 2017
80 x 60 x 170 znaků = 23 archů
https://math.fme.vutbr.cz/cz/zamestnanci
Martišek, Soubory ke stažení, SPG_Text_2017.pdf **46 bodů**

6. Martišek, D: Konstruktivní geometrie pro obory B3S-P Strojírenství a B-PRP Profesionální pilot, 2020
80 x 60 x 100 znaků = 14 archů
https://math.fme.vutbr.cz/cz/zamestnanci
Martišek, Soubory ke stažení, 1 KD_Text_2020.pdf **28 bodů**

B 9: Vytvoření významné výukové pomůcky (film, video, software…) – 10 bodů

1. Martišek, D.: Propagační software ke Dni otevřených dveří 2001 **10 bodů**

2. Martišek, D.: Grafický návrh a realizace propagačního letáku oboru Matematické inženýrství, 2001 (používán v letech 2001-2005) **10 bodů**

3. Martišek, D.: Propagační software ke Dni otevřených dveří 2002 **10 bodů**

4. Martišek, D.: Propagační software ke Dni otevřených dveří 2003 **10 bodů**
5. Martišek, D.: Grafický návrh a realizace propagačního plakátu (90x60 cm) oboru Matematické inženýrství, 2003 (používán v letech 2003 – 2014) **10 bodů**

6. Martišek, D.: Grafický návrh a realizace propagačních plakátů (130x60 cm – 4 ks) oboru Matematické inženýrství - vitrina UM FSI VUT, 18. poschodí, (používán v letech 2003 - 2014 **10 bodů**

7. Martišek, D.: Počítačová geometrie a grafika – elektronická učebnice používáno ve výuce od r. 2003 do 2011 **10 bodů**

8. Martišek, D.: Grafický návrh a realizace propagačního plakátu (90x130 cm) Ústavu matematiky nástěnka ve 2. NP A4, 2004 (používán v letech 2004 - 2014) **10 bodů**

9. Martišek, D.: Grafický návrh a realizace propagačního letáku oboru Matematické inženýrství, 2005 (používán v letech 2005 – 2009) **10 bodů**

10. Martišek, D.: Propagační software ke Dni otevřených dveří 2004 **10 bodů**

11. Martišek, D.: Soubor výukových programů pro výuku předmětu Konstruktivní geometrie používáno ve výuce (přednášky) od r. 2003 do r. 2010 **10 bodů**

12. Martišek, D.: Soubor výukových programů pro výuku předmětu Programovací metody I používáno ve výuce od r. 2004 dosud **10 bodů**

13. Martišek, D.: Soubor výukových programů pro výuku předmětu Programovací metody II používáno ve výuce od r. 2004 dosud **10 bodů**

14. Martišek, D.: Propagační software ke Dni otevřených dveří 2005 **10 bodů**

15. Martišek, D.: Soubor výukových programů pro výuku předmětu Vizualizace dat používáno ve výuce od r. 2004 dosud **10 bodů**

16. Martišek, D.: Soubor výukových programů pro výuku předmětu Numerické metody I používáno ve výuce od r. 2006 dosud **10 bodů**

17. Martišek, D.: Konstruktivní a počítačová geometrie – interaktivní elektronická učební pomůcka, Matematika on Line, http://mathonline.fme.vutbr.cz/1kg používáno jako elektronická podpora výuky od r. 2006 do r. 2010 **10 bodů**

18. Martišek, D.: Počítačová grafika – interaktivní elektronická učební pomůcka, Matematika on Line, http://mathonline.fme.vutbr.cz/pg, používáno jako elektronická podpora výuky od r. 2006 do r. 2010 **10 bodů**

19. Martišek, D., Hoderová, J.: Matematika je užitečná i zábavná, tak proč ji nejít studovat? Brožura + CD používáno k propagaci oboru Matematické inženýrství na středních školách od r. 2006 dosud **5 bodů**

20. Martišek, D.: Grafický návrh a realizace propagačního letáku oboru Matematické inženýrství, 2009 (používán v letech 2009- dosud) **10 bodů**

21. Martišek, D.: Počítačová geometrie a grafika - interaktivní elektronická učební pomůcka, používáno jako elektronická podpora výuky od r. 2011 **10 bodů**

22. Martišek, D.: Numerická matematika - interaktivní elektronická učební pomůcka, používáno jako elektronická podpora výuky od r. 2012 **10 bodů**

23. Martišek, D.: Noc vědců 2014, propagační software **10 bodů**

24. Martišek, D.: Noc vědců 2015, propagační software **10 bodů**

25. Martišek, D.: Soubor výukových programů pro výuku předmětu Obrazová analýza v matematických vědách používáno ve výuce od r. 2016 dosud **10 bodů**

26. Martišek, D.: VUT – Slovník vybraných technických termínů český jazyk – český znakový jazyk; http://slovnikczj.vutbr.cz/. Animovaný výklad pojmů z geometrie **10 bodů**

27. Martišek, D.: Noc vědců 2016, propagační software **10 bodů**

28. Martišek, D.: Noc vědců 2017, propagační software **10 bodů**

29 Martišek, D.: Elektronická podpora cvičení předmětu 1KD, 2020 **10 bodů**

30 Martišek, D.: Propagační software ke Dni otevřených dveří 2020 **10 bodů**

B10 Posudek domácí učebnice nebo skript – 2 body

1. Recenze učebnice Stereometrie pro SŠ, Didaktis 2014 **2 body**

B11 Členství v oborové radě doktorského studijního programu – 2 body

1. Členství v oborové radě doktorského studijního programu Obecné otázky matematiky (přírodovědecká fakulta MU) **2 body**

2. Členství v oborové radě doktorského studijního programu Obecné otázky matematiky a informatiky (MFF UK) **2 body**

3. Místopředseda oborové rady doktorského studijního programu Aplikovaná matematika (FSI VUT) **2 body**

B12 Členství v komisi pro státní doktorskou zkoušku nebo obhajobu dizertační práce – 1 bod

1. Člen komise pro státní doktorskou zkoušku ing. P. Šrubaře 16. 2. 2001 **1 bod**

2. Člen komise pro státní doktorskou zkoušku ing. Pavla Jelínka 21. 5. 2004 **1 bod**

3. Člen komise pro státní doktorskou zkoušku ing. Petra Juráka 21. 5. 2004 **1 bod**

4. Člen komise pro státní doktorskou zkoušku ing. Jindřicha Nového 18. 6. 2004 **1 bod**

5. Člen komise pro obhajobu doktorské práce ing. Karla Doubravského (obor Matematické inženýrství) 4.5.2005 **1 bod**

6. Člen komise pro obhajobu doktorské práce ing. Jindřicha Nového (obor Matematické inženýrství) 15.6.2005 **1 bod**

7. Člen komise pro státní doktorskou zkoušku Mgr. Jany Procházkové (obor Matematické inženýrství) 13. 6. 2006 **1 bod**

8. Člen komise pro státní doktorskou zkoušku Ing. Vladimíra Žáka (obor Matematické inženýrství) 13. 6. 2006 **1 bod**

9. Člen komise pro státní doktorskou zkoušku Ing. Dalibora Pospíšila (obor Matematické inženýrství) 13. 6. 2006 **1 bod**

10. Člen komise pro státní doktorskou zkoušku Ing. Jana Tomáše (obor Matematické inženýrství) 21. 6. 2006 **1 bod**

11. Člen komise pro státní doktorskou zkoušku Ing. Lukáše Dvořáka (obor Matematické inženýrství) 13. 6. 2006 **1 bod**

12. Člen komise pro obhajobu doktorské práce ing. Ivana Nagyho (Ústav mechaniky těles) 2006 **1 bod**

13. Člen komise pro státní doktorskou zkoušku Ing. Tomáše Běhounka (obor Matematické inženýrství) 13. 12. 2006 **1 bod**

14. Člen komise pro obhajobu doktorské práce ing. Jana Tomáše (obor Aplikovaná matematika) 4.5.2009 **1 bod**

15. Člen komise pro státní doktorskou zkoušku Ing. Adama Kracíka (obor Matematické inženýrství) 15. 12. 2009 **1 bod**

16. Člen komise pro obhajobu doktorské práce Ing. Tomáše Běhounka (obor Matematické inženýrství) 15. 12. 2009 **1 bod**

17. Člen komise pro obhajobu doktorské práce Mgr. Jaromíra Tonnera (obor Matematické inženýrství) 20. 5. 2010 **1 bod**

18. Člen komise pro státní doktorskou zkoušku Ing. Čeňka Šandery (obor Matematické inženýrství) 6. 5. 2011 **1 bod**

19. Člen komise pro obhajobu doktorské práce Ing. Adama Kracíka (obor aplikovaná matematika) 2. 12. 2011 **1 bod**

20. Člen komise pro státní doktorskou zkoušku Ing. Petra Vosynka (Ústav mechaniky těles, mechatroniky a biomechaniky) 8. 3. 2012 **1 bod**

21. Člen komise pro státní doktorskou zkoušku Ing. Lubomíra Klimeše (Ústav konstrukčního a procesního inženýrství) 20. 9. 2012 **1 bod**

22. Člen komise pro státní doktorskou zkoušku Ing. Horešovského (Ústav matematiky) 2014 **1 bod**

23. Člen komise pro státní doktorskou zkoušku Mgr. Honkové (Ústav matematiky) 2014 **1 bod**

24. Člen komise pro státní doktorskou zkoušku RNDr. Petra Šatného, obor Obecné otázky matematiky, Masarykova univerzita, 2015 **1 bod**

25. Člen komise pro státní doktorskou zkoušku RNDr. Evy Zelendové obor, Obecné otázky matematiky, Masarykova univerzita, 2015 **1 bod**

26. Člen komise pro státní doktorskou zkoušku Ing. Marka Pivovarníka, obor Aplikovaná matematika, 2015 **1 bod**

27. Člen komise pro obhajobu dizertační práce Ing. Týče (Ústav fyziky) 2015 **1 bod**

28. Člen komise pro státní doktorskou zkoušku Mgr. Kratochvíla, Ing Jakuba Kůdely a Ing. Barbory Navrátilové (Ústav matematiky) 27. 6. 2017 **1 bod**

29. Člen komise pro obhajobu dizertační práce Mgr. Honkové (Ústav matematiky) 2018 **1 bod**

30. Člen komise pro obhajobu dizertační práce Mgr. Kratochvíla (Ústav matematiky) 2018 **1 bod**

31. Člen komise pro státní doktorskou zkoušku ing. Z Kratochvíla 2. 3. 2020 **1 bod**

32. Člen komise pro obhajobu doktorské práce Mgr. Jiřího Vančury (MU) 2020 **1 bod**

32. Člen komise pro obhajobu doktorské práce Mgr. Jakuba Nováka (MU) 2020 **1 bod**

B13 Členství v komisi pro státní závěrečnou zkoušku – 1 bod

1. Člen komise pro státní zkoušku oboru Technická aplikovaná ekologie 11. 6. 2003 (komise K4) **1 bod**
2. Člen komise pro státní zkoušku oboru Matematické inženýrství 2004 **1 bod**
3. Člen komise pro státní zkoušku oboru Matematické inženýrství 2005 **1 bod**
4. Člen komise pro státní zkoušku oboru Matematické inženýrství 2006 **1 bod**
5. Člen komise pro státní bakalářskou zkoušku oboru Matematické inženýrství 2007 **1 bod**
6. Člen komise pro státní zkoušku oboru Matematické inženýrství 2008 **1 bod**
7. Člen komise pro státní bakalářskou zkoušku oboru Matematické inženýrství 2009 **1 bod**
8. Člen komise pro státní zkoušku oboru Matematické inženýrství 2009 **1 bod**
9. Člen komise pro státní zkoušku oboru Matematické inženýrství 2010 **1 bod**
10. Člen komise pro státní bakalářskou zkoušku oboru Matematické inženýrství 2010 **1 bod**
11. Člen komise pro státní bakalářskou zkoušku oboru Matematické inženýrství, jaro 2011 **1 bod**
12. Předseda komise pro státní bakalářskou zkoušku oboru Matematické inženýrství, podzim 2011 **1 bod**
13. Člen komise pro státní zkoušku oboru Matematické inženýrství, podzim 2012 **1 bod**
14. Předseda komise pro státní bakalářskou zkoušku oboru Matematické inženýrství, jaro 2012 **1 bod**
15. Předseda komise pro státní zkoušku oboru Informační management jaro 2013 **1 bod**
16. Předseda komise pro státní bakalářskou zkoušku oboru Matematické inženýrství, jaro 2013 **1 bod**
17. Člen komise pro státní zkoušku oboru Matematické inženýrství, jaro 2014 **1 bod**
18. Předseda komise pro státní bakalářskou zkoušku oboru Matematické inženýrství, jaro 2015 **1 bod**
19. Předseda komise pro státní bakalářskou zkoušku oboru Matematické inženýrství, jaro 2016 **1 bod**
20. Předseda komise pro státní bakalářskou zkoušku oboru Matematické inženýrství, 13. 6. 2017 **1 bod**

21. Předseda komise pro státní bakalářskou zkoušku oboru Matematické inženýrství, 14. 6. 2017 **1 bod**

22. Člen komise pro státní zkoušku oboru Matematické inženýrství, 20. 6. 2018 **1 bod**

23. Člen komise pro státní zkoušku oboru Matematické inženýrství, 10. 6. 2019 **1 bod**

24. Člen komise pro státní zkoušku oboru Matematické inženýrství, 11. 6. 2019 **1 bod**

25. Člen komise pro státní zkoušku oboru Matematické inženýrství, 15. 7. 2020 **1 bod**

26. Člen komise pro státní zkoušku oboru Matematické inženýrství, 16. 7. 2020 **1 bod**

Součet kriterií B	**požadováno minimálně 80 bodů, dosaženo**	**895 bodů**
Součet A + B celkem požadováno minimálně	**400 bodů, dosaženo**	**2 276,5 bodů**

12 Vybrané publikační výstupy a realizované grafické návrhy

Optik - International Journal for Light and Electron Optics 169 (2018) 16–26

Contents lists available at ScienceDirect

Optik

journal homepage: www.elsevier.com/locate/ijleo

Fast Shape-From-Focus method for 3D object reconstruction

Dalibor Martišek

Institute of Mathematics, Faculty of Mechanical Engineering, Brno University of Technology, Czech Republic

ARTICLE INFO

Keywords:
Shape-From-Focus method
Fourier transform
Phase correlation
3D reconstruction

ABSTRACT

Shape-From-Focus method (SFF method) is a method for recovering depth from an image series which are taken with different focus settings. For method presented in this paper, the series must be taken with an optical device (optical microscope, CCD or classic camera) with very small depth of focus, different images must be focussed to different planes and may be taken with inconsiderable angle of view. Proposed method is capable to registered images with different scaling, it makes possible to construct full sharpened 2D image and also the 3D model of scanned object. Accuracy of the method is tested by comparing with 3D models obtained by confocal microscope in hardware supported confocal mode.

1. Introduction

Three-dimensional reconstructions of object surfaces play an important role in many branches. As an example, morphological analysis of fracture surfaces reveals information on mechanical properties of construction materials (see [1–4]). In our paper we will deal with the 3D reconstruction using the Shape-From-Focus method (SFF method). This is a method for recovering depth from an image series which are taken with different focus settings – so caled multifocal image. For an image to be sharp, the object must be placed exactly in the plane to which the microscope or camera is focused (so caled a sharpness plane). However, in many cases, we cannot take the observed object to be a plane, and therefore this condition cannot be fulfilled. The points which are placed in the sharpness plane and its nearby surrounding will be displayed as sharp. These points create so caled optical cut (or optical section), the others are displayed as blur. To create a sharp $2D$ image, it is necessary to obtain a series of images of the same object, each of them with different focussing, optical cuts must cover whole image. $2D$ reconstruction involves the composition of the optical cuts to a new image. There is also a simple method for constructing a rough $3D$ model, where all points belonging to the same optical cut have the same height – we obtain a staircase approximation. This is a principle of a confocal microscope. Optical cuts are recognized by hardware (using laser beam), following staircase approximation may be very precisely because the microscope is able to recognize up several hundreds levels.

Standard optical devices (optical microscopes, CCD or classic cameras) are able to acquire several tens of optical cuts. The main problem is, how recognize the optical cut between blured parts on the analysed image. Tenebaum [5] developed the gradient magnitude maximization method that uses the sharpness of edges to optimize focus quality. Jarvis [6] proposed the sum-modulus-difference that is computed by summing the first intensity differences between neighboring pixels along a scan-line and is used as a measure of focus quality. Schlag et al. [7] implemented and tested various automatically focusing algorithms. More recently, Krotkov [8,9] evaluated and compared the performance of different focus criterion functions. Krotkov also proposed a method to estimate the depth of an image area. Pentland [10] suggested the evaluation of image blur to determine the depth of image points. Grossmann [11] has proposed the estimation of depth of edge points by analyzing the blur of the edges due to defocusing. Darrell and Wohn [12] have developed a depth from focus method that obtains an image sequence by varying the focus level and uses Laplacian and Gaussian pyramids to calculate depth. Subbarao [13] suggests the change of intrinsic camera parameters to recover the depth map of a scene. Ohta et al. [14] and Kaneda et al. [15] have used images corresponding to different focus levels to obtain a single level of high focus quality.

https://doi.org/10.1016/j.ijleo.2018.05.014
Received 19 October 2017; Accepted 2 May 2018
0030-4026/

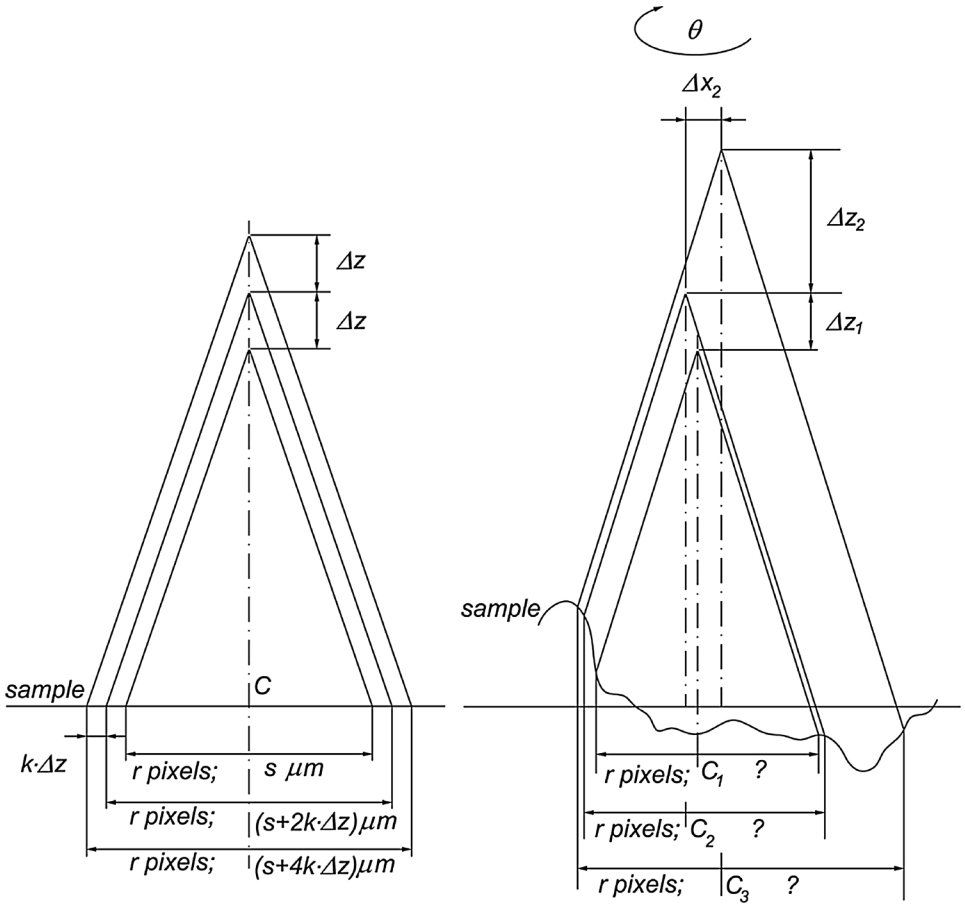

Fig. 1. The central projection of large sample – ideal case on the left is solvable using elementary mathematics, real case on the right requires sophisticated mathematical tools.

Some publications recomend to use sharpness detectors based on Fourier transform – Martišek [16], Ficker [17], Martišek et al. [18]. One of the last publications in this branch (Ficker [19]) uses software based on Fast Fourier Transform (FFT). We can read: *„The software realizing the 3D reconstructions within the SFF method was completely written in our laboratory.“* This statement is at least very inaccurate. This software – Shape-From-Focus Modeller (SFFM) – has been continuously developed since 2000 by the author of this article, independently of any laboratory. First results author published in [16]. Various authors used it for achievement and publication their results – see [17–22] for example. Unfortunately, in some publications, outdated versions of this software was used, moreover, no reconstruction was made in an optimal way [19,22,23,25,26].

2. Non-confocal reconstruction

2.1. Preprocessing

SFFM assumed that the field of view is small and the used projection is parallel until version 2011. The paper [16] and many other works ([17,18,20,21–23,25,26] for example) presume this projection. In parallel projection, all images are provided in field of view with the same size. However, this assumption is not valid in case of a standard camera and larger samples – projection lines angle is not negligible and view fields of individual images are different.

Various image scale was solved using elementary mathematics only until 2015. We presumed the image size is proportional to the camera shifting (see Fig. 1 on the left). However, the practical situation is more complicated. The images differ not only in used scale but also in displayed content (different parts are focussed in different images). Due to mechanical inaccuracies, the step in the z axis may be not fully constant, the images can also be mutually shifted in x - or y -axis and even rotated. Image registration is also complicated by non-planarity of samples (see Fig. 1 on the right). Therefore, sophisticated preprocessing of the image series is necessary. A suitable tool for this preprocessing is the Fourier transform and phase correlation.

The standard definition of the Fourier transform of a function of two variables is as follows [27].

Let $f(x; y)$: $\mathbb{R}^2 \to \mathbb{C}$ be a function such that $\iint_{\mathbb{R}^2} |f(x; y)|\, dxdy$ exists and is finite. The *Fourier transform* of f is

$$F(m;\,n) = \iint_{\mathbb{R}^2} f(x;\,y)\exp(-i(xm + yn))\mathrm{d}x\mathrm{d}y \tag{1}$$

Function $F(m;\,n)$ is also called the Fourier spectrum of function f. Function $A(m;\,n) = |F(m;\,n)|$ is called amplitude spectrum of $f(x;\,y)$.

Let $F(m;\,n)$: $\mathbb{R}^2 \to \mathbb{C}$ be a function such that $\iint_{\mathbb{R}^2} |F(m;\,n)|\,\mathrm{d}m\mathrm{d}n$ exists and is finite. The *inverse Fourier transform* of function F is function $\mathscr{F}^{-1}\{F(x;\,y)\}\,(x;\,y) = f(x;\,y)$: $\mathbb{R}^2 \to \mathbb{C}$

defined as

$$f(x;\,y) = \frac{1}{4\pi^2}\iint_{\mathbb{R}^2} F(m;\,n)\exp[i(xm + yn)]\mathrm{d}m\mathrm{d}n \tag{2}$$

The phase correlation proved to be a powerful tool (not only) for registration of partially focussed images. For functions f_1; f_2 it is defined as

$$P_{f_1;f_2}(x;\,y) = \mathscr{F}^{-1}\left\{\frac{F_1(m;\,n)\bullet\overline{F}_2(m;\,n)}{|F_1(m;\,n)\bullet F_2(m;\,n)|}\right\} \tag{3}$$

and its modification as

$$P_{f_1;f_2;;p;q}(x;\,y) = \mathscr{F}^{-1}\left\{H(m;\,n)\bullet\frac{F_1(m;\,n)\bullet\overline{F}_2(m;\,n)}{(|F_1(m;\,n)| + p)\bullet(|F_2(m;\,n)| + q)}\right\} \tag{4}$$

where bar means complex conjugation, $H(m;\,n)$ is a bounded real function such that $H(m;\,n) = H(-m;\,-n)$ and $p;\,q > 0$ are arbitrary constants. It can be proved that for real functions f_1; f_2 the phase-correlation function is real [28]. This is of great value, since it enables us to search for extremes of the phase-correlation function which can be also used for estimation of image shift. The method was first published by Kuglin and Hines [29]

If two functions are shifted in arguments, i. e. $f_2(x;\,y) = f_1(x{-}x_0;\,y{-}y_0)$ their Fourier transforms are shifted in phase, i.e.

$$F_2(m;\,n) = F_1(m;\,n)\bullet\exp(-i(mx_0 + ny_0)) \tag{5}$$

and their phase-correlation function is the δ-distribution shifted in arguments by the opposite shift vector

$$P_{f_1;f_2}(x;\,y) = \mathscr{F}^{-1}\{\exp(i(mx_0 + ny_0))\} = \delta(x + x_0;\,y + y_0) \tag{6}$$

This is the main idea of phase correlation. The task to find a shift between two images is converted by the phase correlation to the task of finding the only non-zero point in a matrix (computation using the discrete Fourier transform). If the images are not identical (up to a shift) i. e. if the images are not ideal, the phase-correlation function is more complicated, but it still has a global maximum at the coordinates corresponding to the shift vector.

The phase-correlation function can be also used for estimation of image rotation and rescale. The method was first published by Reddy and Chatterji [30]. Let f_2 be function f_1 rotated and shifted in arguments, i.e.

$$f_2(x;\,y) = f_1(x\cos\theta{-}y\sin\theta{-}x_0;\,x\sin\theta + y\cos\theta{-}y_0) \tag{7}$$

Their Fourier spectra and amplitude spectra are related as follows:

$$F_2(\xi;\,\eta) = \exp(-i(\xi x_0 + \eta y_0))\bullet F_1(\xi\cos\theta{-}\eta\sin\theta;\,\xi\sin\theta + \eta\cos\theta) \tag{8}$$

$$A_2(\xi;\,\eta) = A_1(\xi\cos\theta{-}\eta\sin\theta;\,\xi\sin\theta + \eta\cos\theta) \tag{9}$$

The shift results in a phase shift and the spectra are rotated in the same way as the original functions. A crucial step here is transformation of the amplitude spectra into the polar coordinate system to obtain functions A_1^p; A_2^p: $\mathbb{R}_0^+ \times \langle 0;\,2\pi) \to \mathbb{R}_0^+$ such that $A_2^p(\rho;\,\varphi) = A_1^p(\rho;\,\varphi + \Theta)$. The rotation around an unknown center of rotation was transformed to a shift. This shift is estimated with the standard phase correlation after rotating back by the measured angle.

Scaling may be determined in following way. If f_2 is the function f_1 rotated, shifted and scalled in arguments, i.e.

$$f_2(x;\,y) = f_1(\alpha(x\cos\theta{-}y\sin\theta){-}x_0;\,\alpha(x\sin\theta + y\cos\theta){-}y_0) \tag{10}$$

then their Fourier spectra and amplitude spectra are related as follows:

$$F_2(m;\,n) = \frac{1}{\alpha^2}\exp(-i(mx_0 + ny_0))F_1\left(\frac{1}{\alpha}(m\cos\theta{-}n\sin\theta);\,\frac{1}{\alpha}(m\sin\theta + n\cos\theta)\right) \tag{11}$$

$$A_2(m;\,n) = \frac{1}{\alpha^2}A_1\left(\frac{1}{\alpha}(m\cos\theta{-}n\sin\theta);\,\frac{1}{\alpha}(m\sin\theta + n\cos\theta)\right) \tag{12}$$

The shift results in a phase shift, the spectra are rotated in the same way as the original functions and scaled with a reciprocal factor. A crucial step here is transformation of the amplitude spectra into the logarithmic-polar coordinate system

$$\exp\rho = \sqrt{x^2 + y^2};\;\; x = \exp\rho\cos\varphi;\;\; y = \exp\rho\sin\varphi \tag{13}$$

to obtain functions A_1^{lp}; A_2^{lp}: $\mathbb{R}_0^+ \times \langle 0;\,2\pi) \to \mathbb{R}_0^+$; $A_2^{lp}(\rho;\,\varphi) = A_1^{lp}(\rho{-}\ln\alpha;\,\varphi + \theta)$

Both rotation and scale change were transformed to a shift. The unknown angle θ and

unknown factor α can be estimated by means of the phase correlation applied on the amplitude spectra in the logarithmic-polar coordinate system $A_1^{lp}; A_2^{lp}$. After rotating function f_2 back by the estimated angle θ and scaling by factor α the shift vector $(x_0; y_0)$ is estimated by means of the standard phase correlation

2.2. Focusing criteria

In technical practice, the confocal microscope is used as a standard tool for imaging microscopic three-dimensional surfaces. The depth of focus (DOF) of the microscope is very small and its advanced hardware is capable of removing non-sharp points from the images. However, the confocal microscope is often not suitable for technical purposes due to the small size of the visual field (maximal visual field is approximately 2 cm [20–23]). Nevertheless, the same principle may be used even in the case of a CCD camera, classical microscope or camera.

The difference between confocal microscope and conventional optical microscope or standard camera concerns in non-sharp regions that are displayed by classic device, whereas they are missing in case of a confocal microscope. However, the sharp and blurred areas can be detected by software.

For optimal work of the reconstruction procedure, it is necessary to know precise DOF. Some methods of its measure are very subjective and, as a result, incorrect. For example, DOF is estimated by the number of focused lines on a scale, whereas focalization is evaluated visually ([19]). However, the DOF is dependent on required contrast which is given either by point spread function – PSF (used obviously in case of the microscope) or by modular transfer function – MTF (for standard cameras).

The next dissimilarity lies in a central projection which caused different scaling of partial images in the image series (see Fig. 1). Different image scaling (include possibly shift and rotation) may be also quantified and corrected.

Focused area detection was already solved in the first version of Shape-From-Focus Modeller (SFFM2002) – see [16]. Among others, the criterion

$$
\begin{aligned}
{}^{(k)}T({}^{(k)}F(m;n)) &= \sum_{m=0}^{H}\sum_{n=0}^{H}(m+n)\cdot|{}^{(k)}F(m;n)| = \\
&= \sum_{m=0}^{H}\sum_{n=0}^{H}(m+n)\cdot\sqrt{{}^{(k)}U_{mn}^2 + {}^{(k)}V_{mn}^2}
\end{aligned}
\tag{14}
$$

could be used in SFFM2002 ($|{}^{(k)}F(m;n)| = |{}^{(k)}U_{mn} + i\bullet{}^{(k)}V_{mn}|$ determines amplitude of the spatial frequency that exists in the pixel $[m; n]$ in the neighbourhood K_{ij} of the pixel $[i; j]$ in the particular image ${}^{(k)}O$; $k = 1; 2; ...n$). This formula was pioneering in 2002, when it worked with several cuts whose heigth was several milimeters. Its use in 2017 for several hundreds cuts whose heigth is several micrometers (see [19]) is a great error. This formula assigns the highest weights to the highest frequencies which means a noise only. Moreover, standard Fourier transform suffers by jumps at the edges of the square and it causes practicaly random access in case of large number of narrow cuts. Therefore, cosine Fourier transform is preferable from version SFFM2010. This transform is obtained from the standard Fourier transform which is applied to even extension of the neighborhood to be processed and does not suffers by edge jump. Formula

$$
{}^{(k)}K({}^{(k)}C(m;n)) = \sum_{m=-H}^{H-1}\sum_{n=H}^{H-1}\left[|{}^{(k)}C(i+m;j+n)|\sin^2\left(\pi\frac{\sqrt{m^2+n^2}}{H}\right)\right]
\tag{15}
$$

provides the best results so far ($|{}^{(k)}C(i;j)|$ is the value of the amplitude spectrum of the cosine Fourier transform in pixel $[i; j]$ of the k -th image) – see [20].

As was said in introduction, using the maxima of the focussing criterion in separate pixels, opical cuts may be reconstructed. All points belonging to the same optical cut may be assigned to the same height – we obtain a staircase approximation.

2.3. Refinement of the staircase approximation

The staircase approximation is usually not sufficient for following use. For its refinement, different methods were used. Low-pass filter method is the simplest. Its principle is to reduce signals with high spatial frequencies (stair edges mean high-frequency information for Fourier transform). But low-pass filters are not able to differentiate if high-frequency information is a useful signal or the noise. As the consequence some details are missing or unfocused parts appear in the final image. Therefore, this method was doomed already in 2002 (see [16]).

Another methods were developed within the SFF methods. The corrections are based on interpolations of the surroundings of the total maxima of the profiles. Preferred interpolations were parabolic or Gaussian fits – see [30–33]. Parabolic and Gaussian fitting was implemented to SFFM since 2013. However, these methods are very problematic from mathematic point of view.

The main imperfection of these methods is the hypothesis that the profile height in given pixel is exactly determined by values of choosen sharpness detector. This hypothesis implies that these values can be interpolated. However, this conclusion is quite false. We have available the series $\{{}^{(k)}F({}^{(k)}X_{ij})\}$; $k = 1; 2; ..;n$ for assessment of the height of pixel $[i; j]$. This series is not deterministic but it is a random variable. It cannot be interpolated, it must be processed by statistical method. One of the possibilities is a regression analysis but it would be very complicated. Direct calculation of the expeced value is much easier.

For each pixel $[i; j]$, we can construct theoretically infinitely many probablity distribution functions $p_{ij}^{(r)}$ using different exponents r applied to series members ${}^{(k)}K({}^{(k)}C(m;n))$ which we briefly mark K_{ijk}:

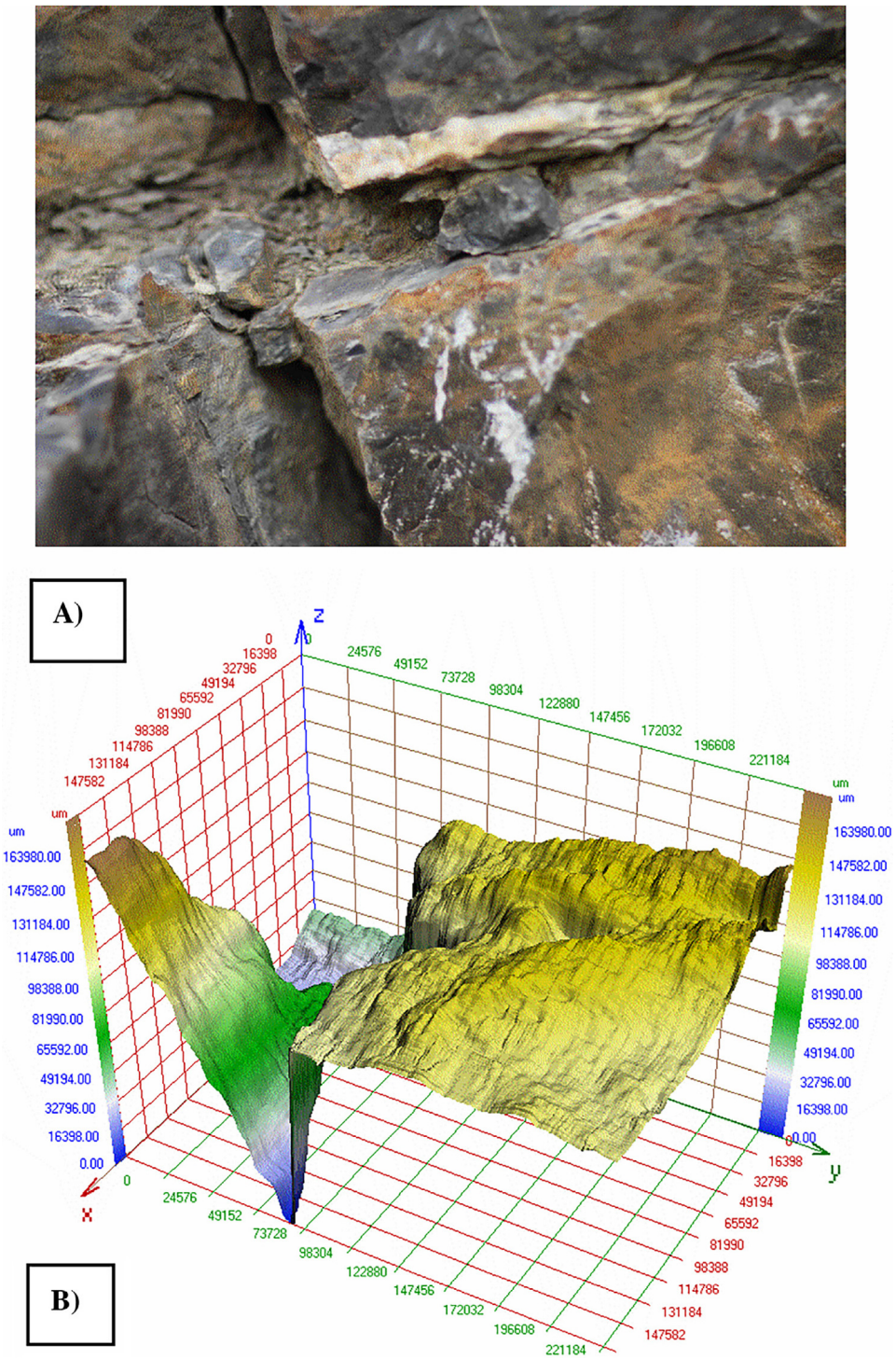

Fig. 2. Limestone sample and its 3*D* reconstruction taken from [19]. The reconstruction has been made by SFFM2013. Elementary mathematics acording to Fig. 1 on the left has been used for the registration. Image A is poorly focused and also poorly registered. Therefore, very strong noise appeared in 3*D* reconstruction. Brutaly low-pass filter has been applied for its decreasing and lot of usefull high frequency information has been lost.

$$p_{ij}^{(r)}(k) = \frac{K_{ijk}^{r}}{\sum_{s=1}^{n} K_{ijs}^{r}} \tag{16}$$

Expeced values $P_{ij}^{(r)}$ of random variables $p_{ij}^{(r)}(k)$ given by these probablity functions estimate the height $h_{ij}^{(r)}$ of surface in its pixel $[i; j]$:

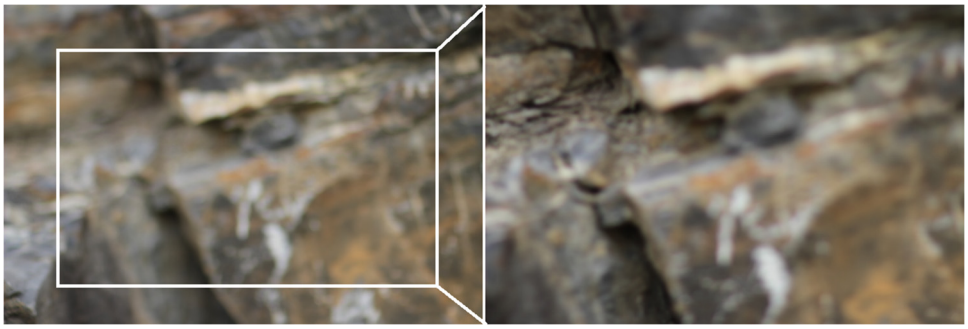

Fig. 3. The first and the fourteenth image of the series of optical sections of the limestone from Fig. 2. Optical sections differs evidently by scaling, image registration had to be made.

Table 1
Scalings, rotations and shift registered in the series of limestone images from Figs. 2 and 3 (relatively to the first).

Image no.	Scaling	Rotation (min)	Shift (pixels)	
			x axis	y axis
2	0.9871	2.6202	2.0180	−2.9935
3	0.9779	2.6520	1.9969	−4.0083
4	0.9652	2.6340	3.9820	−6.0160
5	0.9545	2.6250	5.9870	−6.0186
6	0.9439	5.2458	8.9997	−11.0162
7	0.9352	5.2758	10.9985	−11.0176
8	0.9265	5.2752	10.9894	−12.0075
9	0.9179	5.2548	9.9928	−12.9939
10	0.9077	2.6340	9.9904	−15.9907
11	0.8993	2.6124	9.9960	−17.9887
12	0.8894	0.0252	12.0007	−20.9833
13	0.8794	0.0102	11.0174	−20.0147
14	0.8697	−0.0126	10.9841	−20.0173

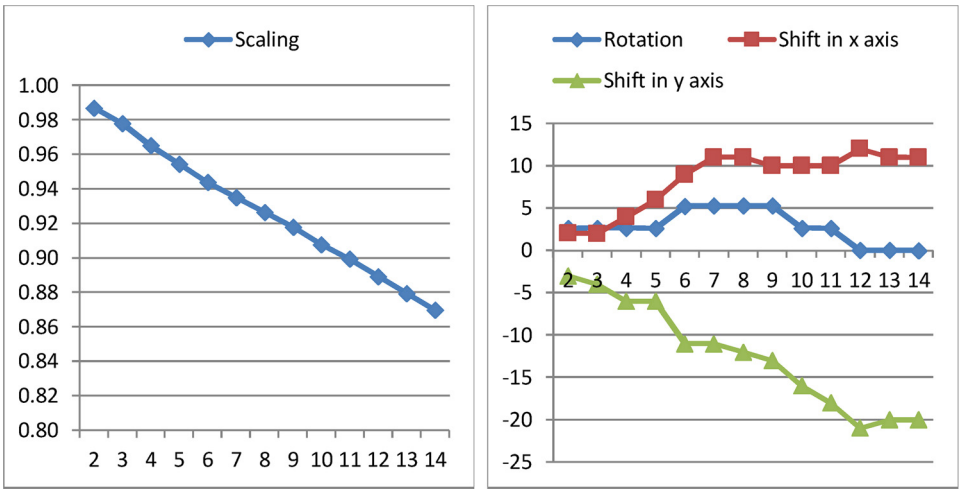

Fig. 4. Scalings, rotations and shift registered in the series of limestone images from Figs. 2 and 3 (relatively to the first).

$$h_{ij}^{(r)} = E(P_{ij}^{(r)}) = \sum_{k=1}^{n} k \cdot p_{ij}^{(r)}(k) = \sum_{k=1}^{n} k \cdot \frac{K_{ijk}^{r}}{\sum_{s=1}^{n} K_{ijs}^{r}} \tag{17}$$

3. Material and methods

In this paper, data taken by Tomáš Ficker from Faculty of Civil Engineering Brno University of Technology and Pavel Štarha from

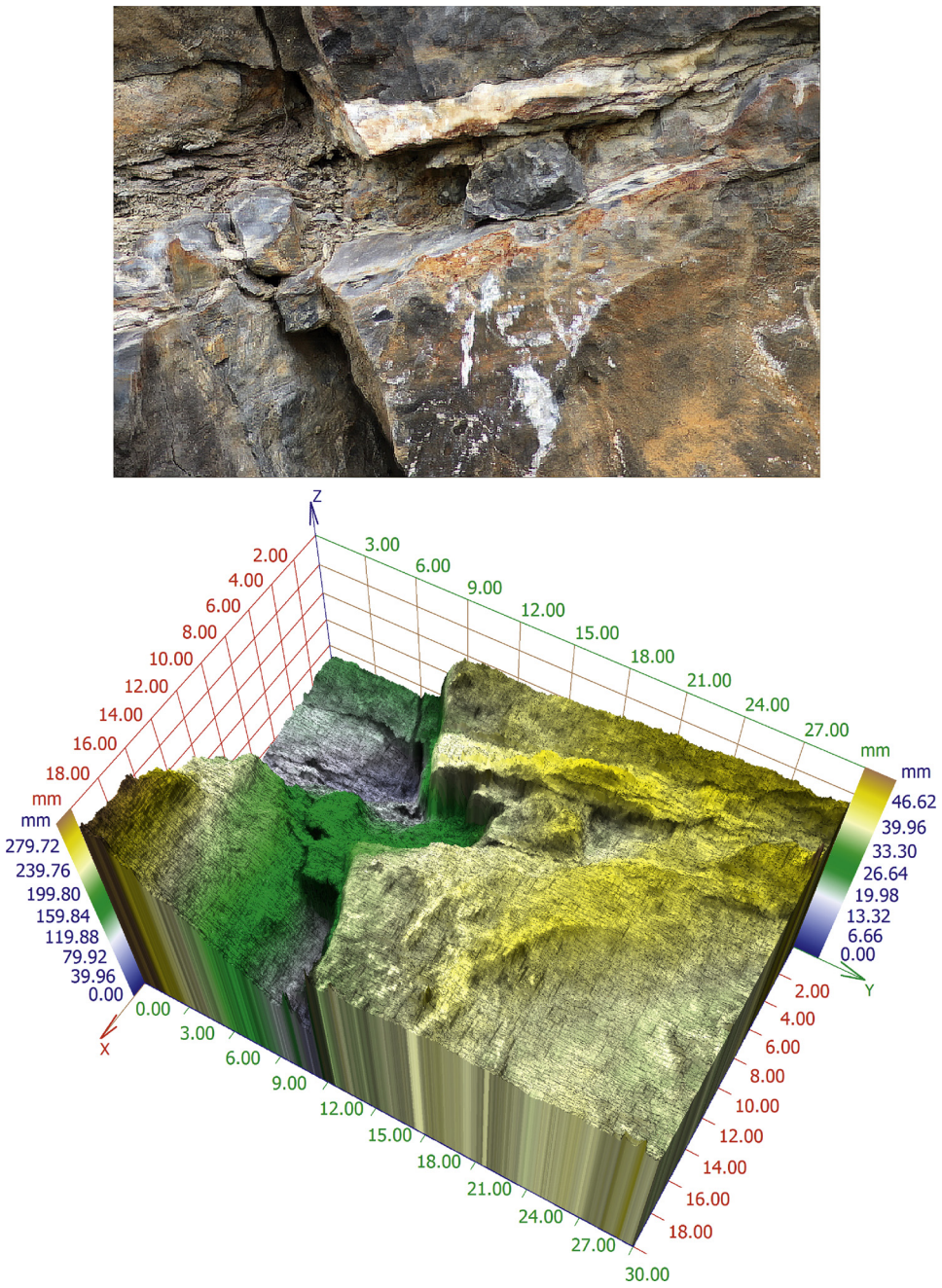

Fig. 5. 2*D* and 3*D* sample reconstruction with software SFFM2017. 14 optical cuts, data resolution 720 × 480. Registration according Section 2.1, its parameters – see Table 1 and Fig. 4. Focussing criterion (15), refinement (16) (17). Limestone, locality Brno – Hády, Czech Republic. Data Tomáš Ficker.

Faculty of Mechanical Engineering BUT have been used. The confocal images were created by using the confocal microscope Olympus OLS 3100 and its commercial software. The non-confocal data in parallel projection (without visible scale change) have been obtained by the same microscope OLS 3100 which was set in the non-confocal mode. The non-confocal data in central projection (with visible scale change) have been taken by the camera Canon EOS 600D with objective EF 85 mm f-1.2 L II USM and Canon EOS 30D with objective Pentacon f 50/1.8.

The 3*D* non-confocal reconstructions were carried out by means of computer program SFFM the algorithms of which has been described in the second section. Presented results are achieved by the newest version SFFM2017. Some outputs obtained by older version of the SFFM (probably SFFM2013) have been taken from [19] for comparison with the newest results.

In [19], there is stated: "*The confocal mode of the microscope Olympus OLS 3100 is capable of capturing and processing 791 optical*

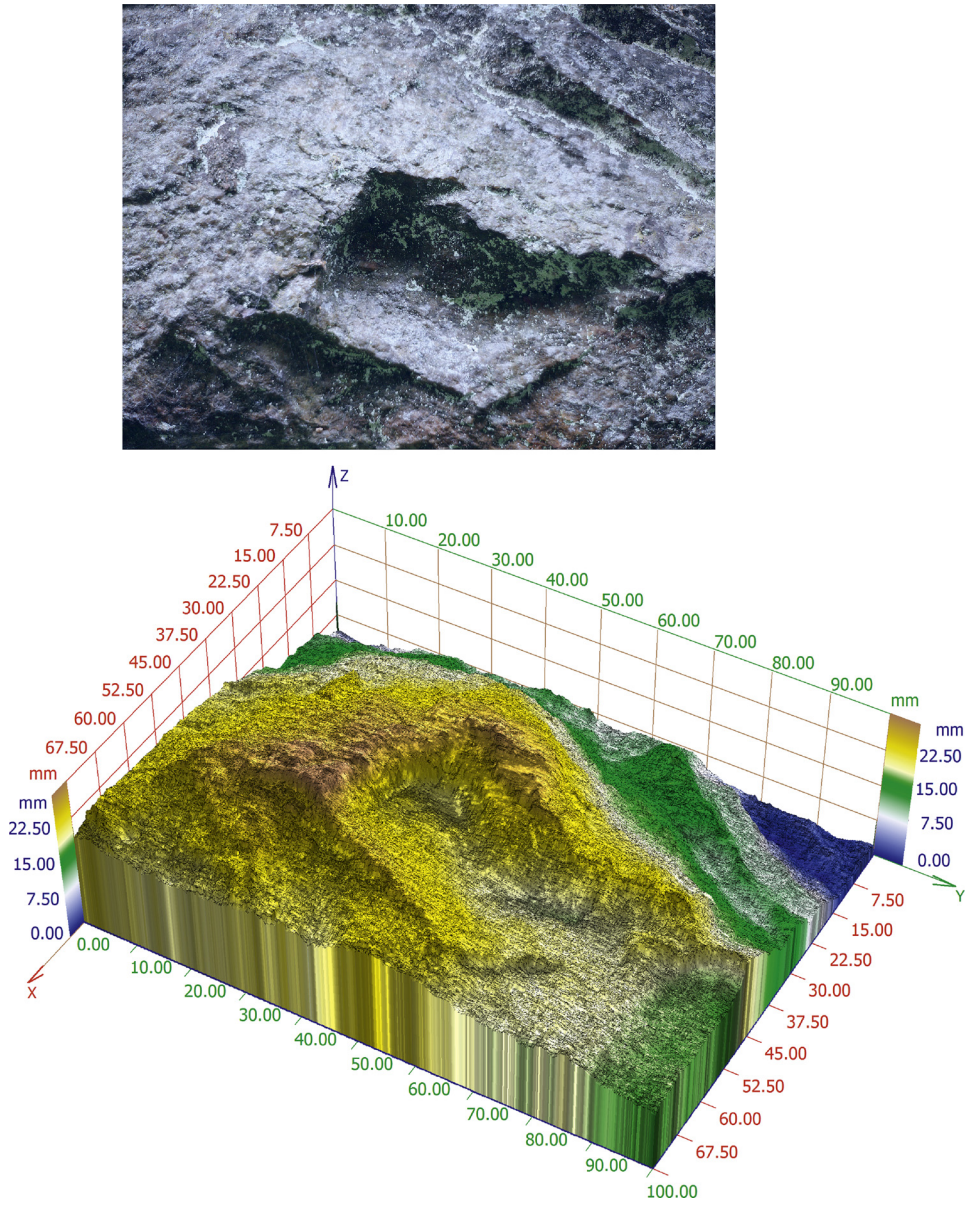

Fig. 6. 2*D* and 3 *D* sample reconstruction with software SFFM2017. 16 optical cuts, data resolution 1600 × 1200. Registration according Section 2.1. Focussing criterion (15), refinement (16) (17). Blue marble, locality Nedvědice, Czech Republic. Data Pavel Štarha.

sections in a relatively short time period amounting about 6 min but the SFF software would process those 490 conventional sections for several days." This statement is outdated for several years.

Up to version SFFM2014, the SFFM software was designed as one-core and 32 bits system. Therefore, the program worked sequentially and it could allocate at most 2 GB arrays. It means (for example) 190 images with resolution 1280 × 1024 pixels, 8 bytes per pixel for matrix of the focussing criteria. In case of larger data, neded operations were realised on hard disk files. These procedures was very time consuming.

Newer versions of SFFM are designed as parallel and 64 bits, i.e. several images can be processed at the same time (number of these parallel calculations is given by the number of computer cores or theads respectively), 64 bit addressing means the possibility to work with practically infinite fields in Random Access Memory (RAM) which is significantly faster. The actual size of the data which can be processed depends only on the size of computer RAM.

At the conclusion of this section, let us note that a hunting for great number of optical cuts and their great resolution is mostly counterproductive. Decreasing z -step combined by increasing resolution namely increases the role of a noise and neither the newly proposed criteria (15)–(17) may always reliably detect high frequency usefull information from this noise.

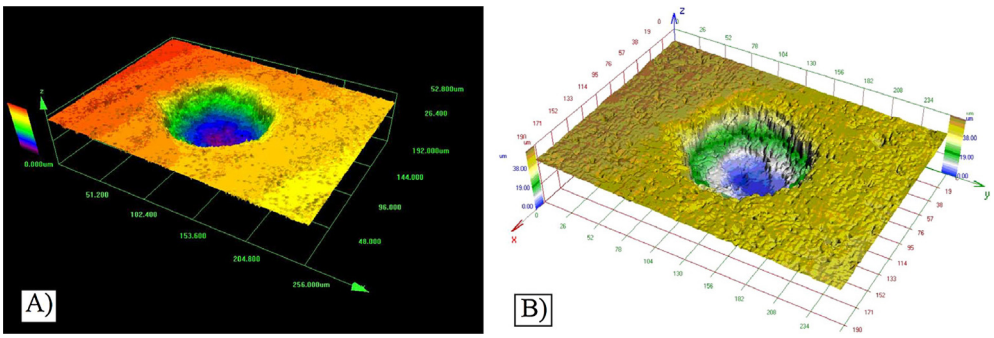

Fig. 7. 3*D* reconstruction of a single pore of hydrated Portland cement paste. Both the optical data were acquired by the microscope Olympus OLS 3100, data resolution 1024 × 768, 47 cuts, z -step 1.2 µm. On the left – confocal mode processed by Olympus software, on the right – non-confocal mode processed by SFFM2013. Data and processing Tomáš Ficker (taken from [19]).

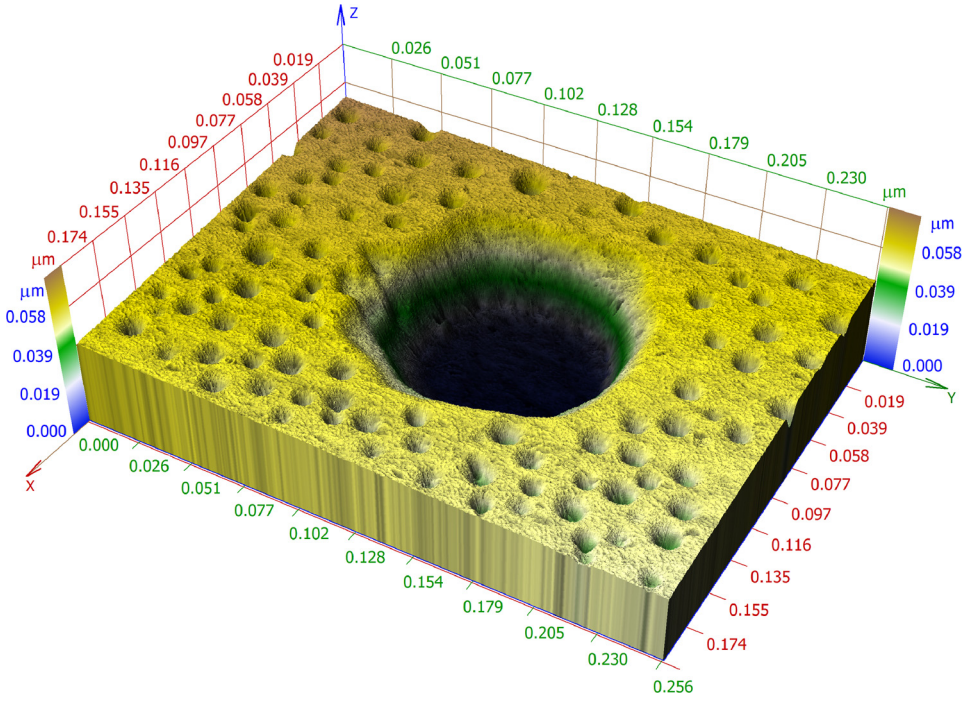

Fig. 8. 3*D* reconstruction of the data from Fig. 7. Each third image has been taken to the reconstruction, i. e. 15 cuts, z -step 3.6 µm. Software SFFM2017, registration according Section 2.1, focussing criterion (15), refinement (16) (17).

4. Results and discussion

The limestone reconstruction in Fig. 2 has been taken from [19]. According to this source, size of the limestone rock viewport is 30 × 20 cm and reconstruction has been made from 14 optical sections with vertical step 20 mm – it means sample height 28 cm. None of these numbers fits with the scales in Fig. 2B. The data have been taken by the camera Canon EOS 600D with objective EF 85 mm f-1.2 L II USM. It implies a central projection – see Fig. 3, i. e. images had to be registered and this registration is not described in [19]. Reconstruction was realized using SFFM2013 – i. e. elementary mathematics acording to Fig. 1 on the left is used for scaling calculation. Registration is inaccurate, parameter k from Fig. 1 on the left has been probably poorly estimated. Moreover, archaic focussing criterion (14) was used. Therefore, 2*D* reconstruction (focussing) is not very precisse (see the lower left corner in Fig. 2A) and subsequent 3*D* reconstruction propably contained a lot of noise. Therefore brutaly low-pass filter has been applied for its decreasing and massive loss of useful high frequency information is evident.

The same data have been processed by software SFFM2017, OS W7 64 on hardware from 2011 ⁻ processor Intel Core i7 2600 with four cores and eight threads, memory DDR3, 24 GB. Preprocessing according to Section 2.1, values of scalings, rotations and shifts are sumarized in Table 1. It is clear to see that scaling dependence on the image number is not precisely linear – see Fig. 4 on the left. Indispensable image shifts and even rotation have been registered. According Table 1, the data have been transformed. As the next step, focussing criterion (15) has been used for 2*D* reconstruction (focussing) and expressions (16), (17) for 3*D* reconstruction.

These reconstructions are shown in Fig. 5.

In the same way, image series of blue marble sample has been processed. The data have been taken by the camera Canon EOS 30D with objective Pentacon f 50/1.8. Result of 2D and 3D reconstruction is possible to seen in Fig. 6.

Fig. 7 is also taken from [19]. It shows results of 3*D* reconstruction of hydrated Portland cement paste achieved in [19]. The reliefs were acquired by the microscope Olympus OLS 3100 using 47 optical cuts with the vertical stepping of 1.2 μm, resolution 1024 × 768 pixels. The left half of this figure shows the confocal 3*D* relief of the central large pore whereas the right half of the figure presents the non-confocal 3D relief of the same pore.

Author of [19] writes: "*While the confocal relief does not show a clear structure of tiny pores that are scattered over the whole investigated surface, the conventional relief reproduces all those porous depressions and even their various sizes and shapes are distinquised.*" In my opinion, what the author considers the pores, are in fact artifacts caused by additive and impulse noise decreased by low-pass filter similarly as in Fig. 2B. The inadequacy of the criterion (14) is forced by a very small step here. The sample has a large part which is practically horizontal. The source of the noise is almost random selecting of the height between several cuts. Therefore, number of cuts must be changed except focussing criterion (14) and parabolic interpolation.

Fig. 8 shows 3*D* reconstruction of hydrated Portland cement paste which is calculated by SFFM2017. Original resolution 1024 × 768 was preserved, z -step was increased to threefold (each third image has been taken to the reconstruction). Reconstruction was performed as desribed above. The result is significantly better.

5. Conclusion

Reconstructions of three-dimensional objects are an important task in many branches of research. Even through the standard method of 3*D* imaging is the use of confocal microscopes or 3*D* scaners, there are methods that use optical microscopes or standard cameras, sophisticated mathematical apparatus and advanced programming techniques. Qualified user of these systems can obtain results similar or even better than this from confocal microscope or 3*D* scaner with equipment by order less expensive. This paper described one of them – method introducing more precise methods both for 2*D* and 3*D* reconstruction based on the Fourier transform. In this way we can obtain results better than reconstructions taken from confocal microscopes or 3*D* scaners with affortable and much less expensive instruments.

Acknowledgements

This work was supported by the project LO1202 with financial subvence of the Ministry of Education of the Czech Republic under the NPU I programme. Thanks are due to Tomáš Ficker and Pavel Štarha for providing data.

References

[1] T. Ficker, D. Martišek, R. Chmelík, L. Lovicar, P. Němec, Fracture surfaces of porous materials, Europhys Lett. 80 (2007) 1600–1604.
[2] T. Ficker, D. Martišek, M.H. Jennings, Roughness of fracture surfaces and compressive strength of hydrated cement pastes, Cem. Concr. Res. 40 (6) (2010) 947–955.
[3] T. Ficker, A. Len, D. Martišek, A remark on nano-particle stability of cement C-S-H gel, Cent. Eur. J. Phys. 9 (2) (2011) 553–557.
[4] T. Ficker, D. Martišek, Digital fracture surfaces and their roughness analysis: applications to cement-based materials, Cem. Concr. Res. (ELSEVIER) 42 (6) (2012) 827–833.
[5] J.M. Tenebaum, Accomodation in Computer Vision, Ph.D. Thesis Stanford University, 1970.
[6] R.A. Jarvis, Focus optimisation criteria for computer image processing, Microscope 24 (2) (1976) 163–180.
[7] J.F. Schlag, A.C. Sanderson, C.P. Neumann, F.C. Wimberly, Implementation of Automatic Focusing Algorithms for a Computer Vision System with Camera Control, Carnegie Mellon University, 1983 CMU-RI-TR-83-14, August.
[8] E. Krotkov, Focusing, Int. J. Comput. Vis. 1 (1987) 223–237.
[9] E. Krotkov, Exploratory Visual Sensing with an Agile Camera, Ph.D. Dissertation, TR- 87-29 University of Pennsylvania, 1987.
[10] A. Pentland, A new sense for depth of field, Proc. IJCAI, Los Angeles (August) (1985) 988–994.
[11] P. Grossmann, Depth from focus, Pattern Recognit. Lett. 5 (1987) 63–69.
[12] T. Darrell, K. Wohn, Pyramid based depth from focus, Proc. CVPR (1988) 504–509.
[13] M. Subbarao, Direct Recovery of Depth Map 2: A New Robust Approach Technical Report, 87-03, State University of New York, Stony Brook, 1987.
[14] T. Ohta, K. Sugihara, N. Sugie, A Method for Image Composition using Image Variance Transactions of IECE, vol. J66-D, No. 10 pp. 1245-1246.
[15] K. Kaneda, Y. Wakasu, E. Nakamae, E. Tazawa, A method of pan-focused and stereoscopic display using a series of optical microscopic images, Proc. Fourth Symp. Image Sens. Technol. Ind. (June) (1988) 189–194.
[16] D. Martišek, The 2-D and 3-D processing of images provided by conventional microscopes, Scanning 24 (6) (2002) 284–296.
[17] T. Ficker, D. Martišek, Digital fracture surfaces and their roughness analysis: applications to cement-based materials, Cem. Concr. Res. (ELSEVIER) 42 (6) (2012) 827–833.
[18] D. Martišek, H. Druckmüllerová, Multifocal image processing, Math. Appl. 3 (1) (2014) 77–90.
[19] T. Ficker, Sectional techniques for 3D imaging of microscopic and macroscopic objects, Optik 144 (2017) 289–299.
[20] D. Martišek, J. Procházková, T. Ficker, High-quality three-dimensional reconstruction and noise reduction of multifocal images from oversized samples, J. Electron. Imaging 24 (5) (2015).
[21] T. Ficker, D. Martišek, D: alternative method for assessing the roughness coefficients of rock joints, J. Comput. Civil Eng. 30 (4) (2016) 224–238.
[22] T. Ficker, D. Martišek, Three-dimensional reconstructions of solid surfaces using conventional microscopes, Scanning 38 (2016) 21–35.
[23] T. Ficker, D. Martišek, Database 3D surfaces for evaluation of joint rock coefficients, Procedia Engineering 161 (2016) 1361–1366.
[25] T. Ficker, D. Martišek, 3D image reconstructions and the nyquist–shannon theorem, 3D Res. 6 (2015) 23.
[26] T. Ficker, D. Martišek, Three-dimensional reconstructions of solid surfaces using conventional microscopes, Scanning 38 (2016) 21–35.
[27] H. Druckmüllerová, Application of Adaptive Filters in Processing of Solar Corona Images, doctoral thesis Brno University of Technology, 2014.
[28] E.M. Stern, M. Elias, G.L. Weiss, Introduction to Fourier Analysis on Euclidean Spaces, Princeton University Press, Princeton, N.J, 1975, p. 297.
[29] C.D. Kuglin, D.C. Hines, The phase correlation image alignment method, Proceeding of IEEE International Conference on Cybernetics and Society, (1975), pp. 163–165.

[30] B.S. Reddy, B.N. Chatterji, An FFT-based technique for translation, rotation, and scale-invariant image registration, IEEE Trans. Image Process. 5 (8) (1996) 1266–1271.
[31] S.K. Nayar, Y. Nakagawa, Shape from focus, IEEE Trans. Patt. Anal. Mach. Intell. 16 (1984) 824–831.
[32] M. Niederost, J. Niederost, J. Scucka, Automatic 3D reconstruction and visualization of microscopic objects from a monoscopic multifocus image sequence, International Archives of the Photogrammetry, Remote Sensing and Spatial Information Sciences XXXIV-5/W10: Proceedings of the International Workshop on Visualization and Animation of Reality-based 3D Models, Tarasp-Vulpera, Switzerland, 24–28 February, 2003.
[33] C. Kammerud, B. Abidi, S. Huq, M. Abidi, 3D nanovision for the inspection of micro-elctro mechanical systems, ICECS 2005. Proceedings of the International Conference on Electronics, Circuits and Systems, Gammarth, Tunisia, 11–14, 2005, pp. 1–4.

Hindawi
Mathematical Problems in Engineering
Volume 2017, Article ID 4642397, 11 pages
https://doi.org/10.1155/2017/4642397

Research Article

3D Reconstruction of the Surface Using a Standard Camera

Dalibor Martišek

Faculty of Mechanical Engineering, Institute of Materials Science and Engineering, NETME Center, Brno University of Technology, Technická 2, 616 69 Brno, Czech Republic

Correspondence should be addressed to Dalibor Martišek; martisek@fme.vutbr.cz

Received 5 August 2017; Accepted 10 October 2017; Published 29 November 2017

Academic Editor: Yakov Strelniker

This paper deals with 3D reconstructions of series of partially focussed images. Some of these methods are known in case of images which were acquired in small field of view (by confocal microscope or CCD camera, e.g.). In this case, recorded images do not differ in any geometrical transformation from each other. In case of larger samples (oversized for microscope or CCD camera), it is necessary to use wider viewing field (standard cameras, e.g.), and taken images primarily differ in scaling but may also differ in shifting and rotation too. These images cannot be used for reconstruction directly; they must be registered; that is, we must determine all transformations which the images differ and eliminate their effects. There are several ways to do this. This paper deals with the registration based on phase correlation. After this registration, it is necessary to identify the sharp parts and to compose a 2D and 3D model. Present methods are very sensitive to noise and their results are not satisfactory in many cases. We introduce a new method for 3D reconstruction which is significantly better.

1. Introduction

The three-dimensional reconstruction of general surfaces plays an important role in many branches; for example, the morphological analysis of fracture surfaces reveals information on mechanical properties of natural or construction materials.

There are more techniques capable of producing digital three-dimensional (3D) replicas of solid surfaces. Mechanical engineers can use contacting electronic profilometers to determine digital two-dimensional (2D) profiles that can be combined into 3D surface profiles; see [1, 2], for example. The contacting mode of atomic force microscopes actually belongs to this mechanical category [3]. Besides the mechanical tools, there exist different optical devices [2], light section microscopy [4, 5], coherence scanning interferometry [6], speckle metrology [7], stereo projection [8], photogrammetry [9], and various kinds of light profilometry [10], to mention some of them.

3D laser scanning techniques are the next possibilities of how to obtain the 3D data. These techniques have also been tested in some rock engineering projects, such as 3D digital fracture mapping [11–13].

However, these devices are not of universal use. Each of them has technical limits [14, 15]. For example, very rough surfaces can hardly be measured by atomic force microscopes, which work in the nanoregions. On the other hand, plane surfaces with microscopically small irregularities may be measured, for example, by the microscopic sectional technique within the so-called confocal microscopes [16–19]. However, confocal microscope is often not suitable for technical purposes due to the small size of the visual field (maximal visual field is approximately 2 cm [5, 20–22]).

In this paper, how to perform the 3D reconstruction of larger surfaces using a standard camera will be shown.

2. Materials and Methods

2.1. Equipment. In technical practice the confocal microscope is used as a standard tool for imaging microscopic three-dimensional surfaces. The depth of the optical field of the microscope is very small and its advanced hardware is capable of removing nonsharp points from the images. The points of the object close to the focal plane are visible as sharp points. The parts lying above or beneath the focal plane are

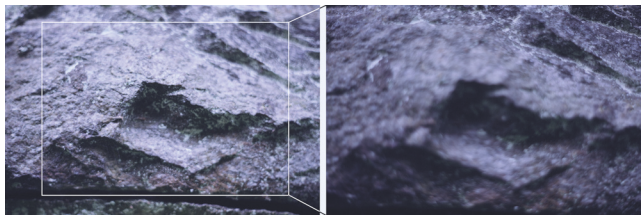

Figure 1: Different scaling and different sharp and nonsharp regions in images acquired by classic camera placed in different distances from the 3D relief, the first and the fifteenth images from the series of fifteen images of blue marble. Frame size 10 × 7.5 cm. Locality Nedvědice, Czech Republic, photo Pavel Štarha.

invisible and represented as black regions. To create a 2D and 3D reconstruction, it is necessary to obtain a series of images of the same object, each of them with different focusing, and each point of the object focussed in one of the images (in the ideal case). The sharp parts are identified and composed of a 2D and 3D model.

However, the confocal microscope is often not suitable for technical purposes due to the small size of the visual field (maximal visual field is approximately 2 cm [5, 20–22]). Nevertheless, the same principle may be used even in the case of a CCD camera, classical microscope, or camera. For nondestructive scanning, the camera must be mounted on a stand which enables a movement in the direction approximately orthogonal to the surface with a controlled step.

The difference between confocal microscope and standard camera concerns nonsharp regions that are displayed by classic camera, whereas they are missing in the case of a confocal microscope. However, the sharp and blurred areas can be detected by software. The next dissimilarity lies in a central projection which caused different scaling of partial images in the image series (see Figure 1). Different image scaling (including possibly shift and rotation) may be also quantified and corrected. This problem has not been solved in available sources.

2.2. Present Methods. Probably the first attempts to carry out nonconfocal reconstructions come from the seventies and eighties of the last century [23–28]. Blurred areas detectors (or so-called focusing criteria) are based on various principles. Present methods work in three steps.

The First Step. Three-dimensional matrix $\{C_{ijk}\}$ is stated. Its element C_{ijk} determines statistical range, variance, or standard Fourier transform of certain neighborhood of the pixel $[i; j]$ in kth image in the series of n images [29].

The Second Step. Maxima $\max_k\{C_{ijk}\}$ in the columns $\{C_{ij1}; C_{ij2}; \ldots; C_{ijn}\}$ are found. Height h_{ij} is assigned to the pixel $[i; j]$ if and only if the maximum is detected on the hth image. In this way, a stair-approximation is obtained.

The Third Step. The stair-approximation from the second step is obviously refined by various interpolation of detector values adjacent with these maxima, that is, values $C_{i;j;h-1}$; $C_{i;j;h+1}$: inverse proportionality [29, 30], parabolic fits [31–33], or Gaussian fits [34].

In [35], it is stated: "We have verified that there are only small differences between the three-point Gaussian and the three-point parabolic approximations." However, this statement does not indicate an accuracy of the reconstruction. As shown below, this fact can only mean that both reconstructions are roughly equally bad.

A noise is the fundamental problem of the second and the third step. This problem was solved by several ways: varying size of computational pixel windows [33, 36], averaging multiple snapshots taken at each vertical position [26], or input data averaging [37]. However, these methods are able to decrease a noise but the noise cannot be zeroed. Therefore, the maxima computed in the second step need not indicate the height correctly; moreover, any interpolation (the third step) is not useable for noise data from point of view of numerical mathematics.

Except for these inaccuracies, methods cited above must assume the same scale of all images in the series because they are not able to detect image transformations. In the following sections, we will introduce the 3D reconstruction method which is able to process a series of noisy images acquired using central projection with variable center, that is, in various scaling (various shift and rotation eventually).

2.3. The Fourier Transform and Phase Correlation

2.3.1. Standard Fourier Transform and Inverse Transform. Standard (continuous) Fourier transform of function $f(x) : \mathbb{R} \to \mathbb{C}$ is function

$$\mathcal{F}(f)(x) = F(\xi) = \int_{-\infty}^{\infty} f(x)\, e^{-ix\xi} \mathrm{d}x \tag{1}$$

(if this integral exists and is finite).

Standard (continuous) Fourier transform of function $f(x; y) : \mathbb{R}^2 \to \mathbb{C}$ is function

$$\mathcal{F}(f)(x; y) = F(\xi; \eta) = \iint_{\mathbb{R}^2} f(x; y)\, e^{-i(x\xi+y\eta)} \mathrm{d}x\, \mathrm{d}y \tag{2}$$

(if this integral exists and is finite).

Inverse (continuous) Fourier transform of function $G(\xi) : \mathbb{C} \to \mathbb{C}$ is function

$$\mathcal{F}^{-1}(G)(\xi) = g(x) = \frac{1}{2\pi} \int_{-\infty}^{\infty} G(\xi)\, e^{ix\xi} \mathrm{d}\xi \tag{3}$$

(if this integral exists and is finite).

Inverse (continuous) Fourier transform of function $G(\xi; \eta) : \mathbb{C}^2 \to \mathbb{C}$ is function

$$\begin{aligned} \mathcal{F}^{-1}(G)(\xi; \eta) &= g(x; y) \\ &= \frac{1}{4\pi^2} \iint_{\mathbb{R}^2} G(\xi; \eta)\, e^{i(x\xi+y\eta)} \mathrm{d}\xi\, \mathrm{d}\eta \end{aligned} \tag{4}$$

(if this integral exists and is finite).

Standard discrete Fourier transform of function $f(x;y)$: $\{0;1;\ldots;N-1\}^2 \to \mathbb{C}$ is function

$$\mathscr{F}(f)(\xi;\eta) = F(\xi;\eta) = \sum_{x=0}^{N-1}\sum_{y=0}^{N-1} f(x;y)\, e^{-(2\pi i/N)(x\xi+y\eta)}. \tag{5}$$

Function F is also called the Fourier spectrum of function f. It is possible to obtain the function f from its Fourier spectrum $F(\xi;\eta)$ using inverse discrete Fourier transform

$$\mathscr{F}^{-1}(F)(x;y) = f(x;y) = \frac{1}{N^2}\sum_{\xi=0}^{N-1}\sum_{\eta=0}^{N-1} F(\xi;\eta)\, e^{(2\pi i/N)(x\xi+y\eta)} \tag{6}$$

(see [38] for proof). Function $A(\xi;\eta) = |F(\xi;\eta)|$ is called amplitude spectrum of $f(x;y)$.

2.3.2. δ-Distribution. One-dimensional δ-distribution $\delta(x)$ is a limit of a sequence of functions $\delta_n(x)$; $n \in \mathbb{N}$ such that

$$\text{(a)}\quad \lim_{n\to\infty}\int_{-\infty}^{\infty}\delta_n(x)\,dx = 1;$$
$$\text{(b)}\quad \lim_{n\to\infty}\frac{\delta_n(x_0)}{\lim_{x\to 0}\delta_n(x)} = 0; \quad x_0 \in \mathbb{R}-\{0\}. \tag{7}$$

Two-dimensional δ-distribution $\delta(x;y)$ is a limit of a sequence of functions $\delta_n(x;y)$; $n \in \mathbb{N}$ such that

$$\lim_{n\to\infty}\int_{-\infty}^{\infty}\int_{-\infty}^{\infty}\delta_n(x;y)\,dx\,dy = 1;$$
$$\lim_{n\to\infty}\frac{\delta_n(x_0;y_0)}{\lim_{(x;y)\to(0;0)}\delta_n(x;y)} = 0; \tag{8}$$
$$(x_0;y_0) \in \mathbb{R}^2-\{(0;0)\}.$$

Example 1. One of the well-known examples (which we demonstrate in 1D for simplicity) is the series of expanding rectangular signals $\delta_n^*(\xi)$ with constant unitary intensity on $(-n;n)$; $n \in \mathbb{N}$ and zeroed elsewhere. Inverse Fourier transform gives

$$\mathscr{F}^{-1}(\delta_n^*)(\xi) = \delta_n(x) = \frac{1}{2\pi}\int_{-\infty}^{\infty} e^{ix\xi}d\xi = \frac{1}{2\pi}\int_{-n}^{n} e^{ix\xi}d\xi = \frac{1}{2\pi}\left[\frac{e^{ix\xi}}{ix}\right]_{\xi=-n}^{n} = \frac{e^{ixn}-e^{-ixn}}{2\pi ix} = \frac{\sin nx}{\pi x}. \tag{9}$$

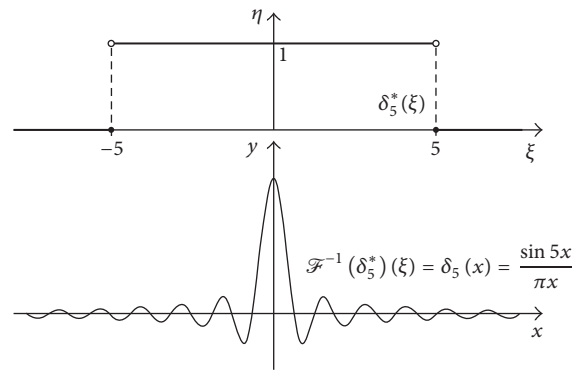

Figure 2: Fourier transforms of the fifth member of the series of expanding rectangular signals. The series converges to δ-distribution.

Because $\int_{-\infty}^{\infty}((\sin nx)/\pi x)dx = 1$ for each $n \in \mathbb{N}$ (see [36] for proof), condition (a) is fulfilled. Because $\lim_{x\to 0}((\sin nx)/\pi x) = (n/\pi)\lim_{x\to 0}((\sin nx)/nx) = n/\pi$ for each $n \in \mathbb{N}$, there is

$$\lim_{n\to\infty}\frac{\delta_n(x_0)}{\lim_{x\to 0}\delta_n(x)} = \lim_{n\to\infty}\frac{\sin nx_0}{nx_0} = 0 \quad \text{for each } x_0 \neq 0. \tag{10}$$

It means that also condition (b) holds and limit $\delta(x) = \lim_{n\to\infty}\delta_n(x)$ is the (one-dimensional) δ-distribution. Expanded unitary signal and its Fourier transform are illustrated in Figure 2.

2.3.3. Phase Correlation. For image processing, it is necessary to transform the images so that the studied structures are at the same position in all the images. This is the task of image registration, to find the transformation. In some applications we assume that images were shifted only; in others we allow shift, rotation, and scale change (i.e., similarity), general linear transformation, or even general transformations. The methods used for registration depend on the expected transformation and on the structures in the image. Some methods use corresponding structures or points in the images and then find a global transformation using the measurements of positions of the structures or points [39–41]. These methods require these structures to be clearly visible. Other methods are based on correlation and work with the image as a whole. The phase correlation proved to be a powerful tool (not only) for registration of particular focussed images. For functions f_1; f_2, it is defined as

$$P_{f_1;f_2}(x;y) = \mathscr{F}^{-1}\left\{\frac{F_1(\xi;\eta)\cdot\overline{F}_2(\xi;\eta)}{|F_1(\xi;\eta)|\cdot|F_2(\xi;\eta)|}\right\} \tag{11}$$

and its modification as

$$P_{f_1;f_2;p;q}(x;y) = \mathscr{F}^{-1}\left\{H(\xi;\eta)\cdot\frac{F_1(\xi;\eta)\cdot\overline{F}_2(\xi;\eta)}{(|F_1(\xi;\eta)|+p)\cdot(|F_2(\xi;\eta)|+q)}\right\}, \tag{12}$$

where strip means complex conjugation and $H(\xi;\eta)$ is a bounded real function such that $H(\xi;\eta) = H(-\xi;-\eta)$ and $p;q > 0$ are arbitrary constants. It can be proved that for real functions f_1; f_2 the phase-correlation function is real [42]. This is of great value, since it enables us to search for extremes of the phase-correlation function.

2.4. Image Transformation

Identical Images. Let F be the infinity periodic expansion of an image. Denote $a + bi$ as its value $F(\xi;\eta)$ in the point $(\xi;\eta)$, $a + bi \neq 0$. It is evident that the value of the phase correlation of the F with itself is

$$\begin{aligned}\frac{F(\xi;\eta)\cdot\overline{F}(\xi;\eta)}{\left|F(\xi;\eta)\cdot F(\xi;\eta)\right|} &= \frac{(a+bi)(a-bi)}{|(a+bi)|\cdot|a+bi|} = \frac{a^2+b^2}{a^2+b^2} \\ &= 1.\end{aligned} \tag{13}$$

According to Example 1 in Section 2.3.2, one has

$$\begin{aligned}P_{f;f}(x;y) &= \mathscr{F}^{-1}\left\{\frac{F(\xi;\eta)\cdot\overline{F}(\xi;\eta)}{|F(\xi;\eta)|\cdot|F(\xi;\eta)|}\right\} = \mathscr{F}^{-1}\{1\} \\ &= \delta(x;y).\end{aligned} \tag{14}$$

It means that the inverse Fourier transform of the convolution of two identical images is the two-dimensional δ-distribution $\delta(x;y)$.

Shifted Images. If two functions are shifted in arguments, that is, $f_2(x;y) = f_1(x - x_0; y - y_0)$, their Fourier transforms are shifted in phase; that is,

$$F_2(\xi;\eta) = F_1(\xi;\eta)\cdot\exp\left(-i\left(\xi x_0 + \eta y_0\right)\right), \tag{15}$$

and their phase-correlation function is the δ-distribution shifted in arguments by the opposite shift vector

$$\begin{aligned}P_{f_1;f_2}(x;y) &= \mathscr{F}^{-1}\left\{\exp\left(i\left(\xi x_0 + \eta y_0\right)\right)\right\} \\ &= \delta(x + x_0; y + y_0).\end{aligned} \tag{16}$$

This is the main idea of phase correlation. The task to find a shift between two images is converted by the phase correlation to the task of finding the only nonzero point in a matrix. If the images are not identical (up to a shift), that is, if the images are not ideal, the phase-correlation function is more complicated, but it still has a global maximum at the coordinates corresponding to the shift vector.

Rotated Images. The phase-correlation function can be also used for estimation of image rotation and rescale. Let f_2 be function f_1 rotated and shifted in arguments; that is,

$$\begin{aligned}&f_2(x;y) \\ &\quad = f_1(x\cos\theta - y\sin\theta - x_0; x\sin\theta + y\cos\theta - y_0).\end{aligned} \tag{17}$$

Their Fourier spectra $F_1; F_2$ and amplitude spectra $A_1; A_2$ are related as follows:

$$\begin{aligned}F_2(\xi;\eta) &= \exp\left(-i\left(\xi x_0 + \eta y_0\right)\right) \\ &\quad\cdot F_1\left(\xi\cos\theta - \eta\sin\theta; \xi\sin\theta + \eta\cos\theta\right), \\ A_2(\xi;\eta) &= A_1\left(\xi\cos\theta - \eta\sin\theta; \xi\sin\theta + \eta\cos\theta\right).\end{aligned} \tag{18}$$

The shift results in a phase shift and the spectra are rotated in the same way as the original functions. A crucial step here is transformation of the amplitude spectra into the polar coordinate system to obtain functions $A_1^p; A_2^p : \mathbb{R}_0^+ \times \langle 0; 2\pi) \to \mathbb{R}_0^+$ such that $A_1^p(\rho;\varphi) = A_2^p(\rho;\varphi+\theta)$. The rotation around an unknown center of rotation was transformed to a shift. This shift is estimated with the standard phase correlation (see the previous paragraph) after rotating back by the measured angle; the shift $(x_0; y_0)$ is measured with another computation of the phase correlation.

Scaled Images. Let f_2 be function f_1 rotated, shifted, and scaled in arguments; that is,

$$\begin{aligned}f_2(x;y) &= f_1\left(\alpha\left(x\cos\theta - y\sin\theta\right)\right. \\ &\quad \left. - x_0; \alpha\left(x\sin\theta + y\cos\theta\right) - y_0\right).\end{aligned} \tag{19}$$

Their Fourier spectra and amplitude spectra are related as follows:

$$\begin{aligned}F_2(\xi;\eta) &= \frac{1}{\alpha^2}\exp\left(-i\left(\xi x_0 + \eta y_0\right)\right) \\ &\quad\cdot F_1\left(\frac{1}{\alpha}\left(\xi\cos\theta - \eta\sin\theta\right); \frac{1}{\alpha}\left(\xi\sin\theta + \eta\cos\theta\right)\right), \\ A_2(\xi;\eta) &= \frac{1}{\alpha^2} \\ &\quad\cdot A_1\left(\frac{1}{\alpha}\left(\xi\cos\theta - \eta\sin\theta\right); \frac{1}{\alpha}\left(\xi\sin\theta + \eta\cos\theta\right)\right).\end{aligned} \tag{20}$$

The shift results in a phase shift, and the spectra are rotated in the same way as the originalfunctions and scaled with a reciprocal factor. A crucial step here is transformation of theamplitude spectra into the logarithmic-polar coordinate system

$$\exp\rho = \sqrt{x^2 + y^2}; \quad x = \exp\rho\cos\varphi; \quad y = \exp\rho\sin\varphi \tag{21}$$

to obtain $A_1^p; A_2^p : \mathbb{R}_0^+ \times \langle 0; 2\pi) \to \mathbb{R}_0^+$ such that $A_2^{1p}(\rho;\varphi) = A_2^{1p}(\rho - \ln\alpha; \varphi + \theta)$.

Both rotation and scale change were transformed to a shift. The unknown angle θ and unknown factor α can be estimated by means of the phase correlation applied on the amplitude spectra in the logarithmic-polar coordinate system $A_1^{1p}; A_2^{1p}$. After rotating function f_2 back by the estimated angle θ and scaling by factor α, the shift vector $(x_0; y_0)$.

2.5. Proposed Method of Surface Approximation

2.5.1. Preprocessing: Image Registration. Before 3D profile calculation, it is necessary to identify all geometric

transformation in the image series and to eliminate them. The images are analyzed as geometrically similar. Generally, similarity is a combination of rotation, scale change, shift, and axial symmetry. Axial symmetry is not possible in our case.

The discrete Fourier transform described above is used for the image registration. It either works with periodic functions or makes them periodic. In general case, an image has not the same values on the edges and by periodizing an image, we obtain a function with jumps at the edges of the original image. These jumps are often the most contrast structures in the function and may lead to incorrect registration. Therefore, it is necessary to remove such edges from the image used for the shift estimation, to smooth them out. This is done by multiplying the image by a suitable function, a so-called window function. Such function must be zero or almost zero at the image edges and one on a large part of the image. We can primarily use the Gaussian window function and the Hanning window function. Let $\sigma \in \mathbb{R}^+$ be a given number and set

$$\begin{aligned} \mathscr{R} &= \langle -a; a\rangle \times \langle -b; b\rangle\,; \quad a; b \in \mathbb{R}_0^+, \\ \mathscr{C} &= \left\{(x; y) \in \mathbb{R}^2 \mid x^2 + y^2 \le r\right\}; \quad r \in \mathbb{R}_0^+. \end{aligned} \tag{22}$$

Let $\rho(X; \mathcal{S})$ be the distance of point $X = (x; y)$ from set $\mathcal{S}$; that is,

$$\rho(X; \mathcal{S}) = \inf\{d \in \mathbb{R} \mid d = \|XY\|\,;\ Y \in \mathcal{S}\}. \tag{23}$$

Functions

$$\begin{aligned} g_{\mathrm{GR}}(x; y) &= e^{-\rho^2(X;\mathscr{R})/\sigma^2} \\ \text{or } g_{\mathrm{GC}}(x; y) &= e^{-\rho^2(X;\mathscr{C})/\sigma^2} \end{aligned} \tag{24}$$

are called rectangular or circular Gaussian window function. Functions

$$\begin{aligned} &g_{\mathrm{HR}}(x; y) \\ &\quad = \begin{cases} \dfrac{1}{2} + \dfrac{1}{2}\cos\dfrac{\pi\rho(X;\mathscr{R})}{\sigma} & \text{if } (X;\mathscr{R}) \le \sigma \\ 0 & \text{if } (X;\mathscr{R}) > \sigma \end{cases} \\ &\text{or } g_{\mathrm{HC}}(x; y) \\ &\quad = \begin{cases} \dfrac{1}{2} + \dfrac{1}{2}\cos\dfrac{\pi\rho(X;\mathscr{C})}{\sigma} & \text{if } (X;\mathscr{C}) \le \sigma \\ 0 & \text{if } (X;\mathscr{C}) > \sigma \end{cases} \end{aligned} \tag{25}$$

are called rectangular or circular Hanning window function.

Let $\{I_1; I_2; \ldots; I_n\}$ be the image series to be registered; image I_1 was acquired by means of the biggest angle of view. This image will be not transformed or (formally) it will be transformed by identity mapping to the image I_1^*. Now we must find transform $I_2 \to I_1^*$ to obtain image I_2^* which differs from I_1^* in focussed and blurred parts only. In the same way, transforms $I_3 \to I_2^*; \ldots; I_k \to I_{k-1}^*; \ldots; I_n \to I_{n-1}^*$ must be found.

After the multiplying both images I_k; I_{k-1}^* by the chosen window function, we determine the rotation angle θ_k and scale factor α_k by means of the method described in Section 2.4. Then, image I_k is rotated by angle $-\theta_k$ and scaled by factor α_k^{-1} to compensate the rotation and scale change found by the phase correlation, creating image $\overline{I_k}$. Only shift and different focussed and blurred parts remain between image $\overline{I_k}$ and image I_{k-1}^*. Now we can apply phase correlation to find the shift $(x_0; y_0)$ and image $\overline{I_k}$ is shifted by vector $(-x_0; -y_0)$ to compensate the shift, creating image I_k^* which differs from I_{k-1}^* in focussed and blurred parts only.

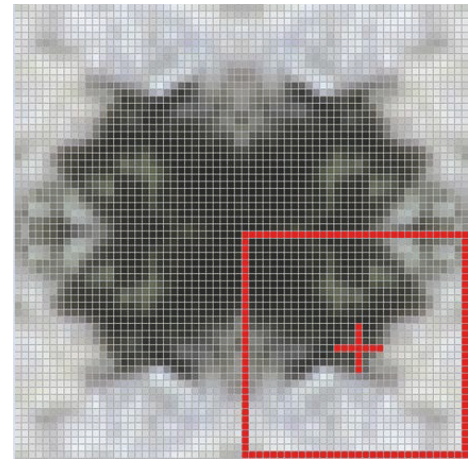

Figure 3: Even extension of the 32×32 neighborhood (framed) of the processing pixel (cross).

2.5.2. The First Step: Matrix of Sharpness Detectors. As was said in Section 2.2, statistical range, variance, or standard Fourier transform of certain neighborhood of the pixel $[i; j]$ may be used as the sharpness detectors (focusing criteria). The neighborhood of the pixel $[i; j]$ is a square of $s \times s$ pixels where s is obviously ten to twenty. In case of the standard Fourier transform, algorithm FFT is used. It requires the square with the side $s = 2^n$; that is, $s = 8$ or $s = 16$ is used in this case. However, standard Fourier transform suffers from jumps at the edges of the square and it is necessary to use a suitable window function like in Section 2.5.1. Therefore, cosine Fourier transform is preferable. This transform is obtained from the standard Fourier transform which is applied to even extension of the neighborhood to be processed. This extension is illustrated in Figure 3. Due to this extension, there are no jumps at the edges. Sine frequencies in (5) are zeroed and application of any window function is not necessary.

However, low frequencies in amplitude spectrum detect blurred parts of image and very height frequencies are given by noise. Therefore, suitable weight must be assigned to each frequency in sharpness detector calculation. In our software, the following detectors may be used:

$$\begin{aligned} {}_aC_{ijk} &= \sum_{m=-s}^{s}\sum_{n=-s}^{s} {}_ac_{i+m;j+n;k} \\ &= \sum_{m=-s}^{s}\sum_{n=-s}^{s} (|m| + |n|) \cdot \left|F_{i+m;j+n;k}\right|, \end{aligned} \tag{26}$$

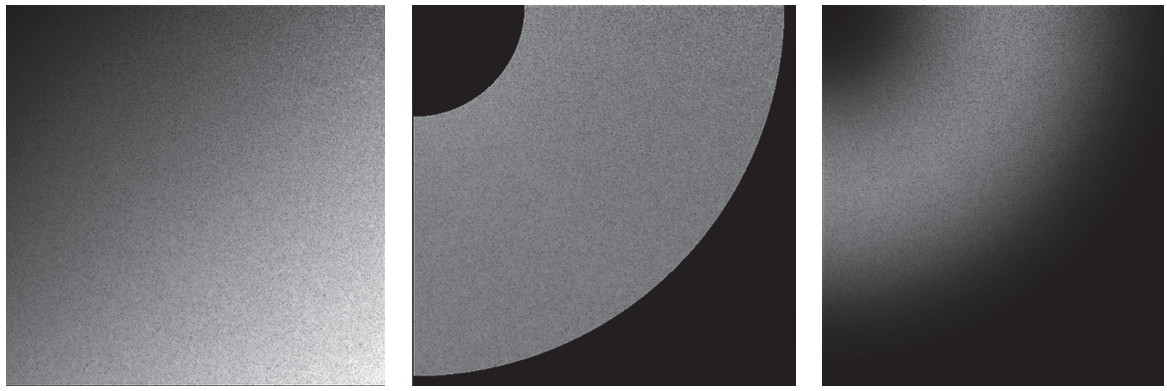

(a) (b) (c)

Figure 4: Graphical representation of sharpness detectors ${}_aC$ (a); ${}_bC$ (b); and ${}_cC$ (c).

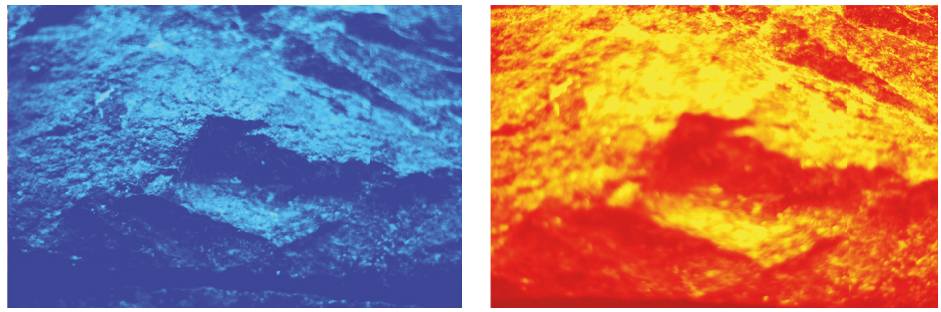

(a) (b)

Figure 5: The first and the fifteenth images from the series of fifteen images of blue marble (see Figure 1) displayed in supplementary pseudocolors. Real surface size 10×7.5 cm (b).

$$ {}_bC_{ijk} = \sum_{m=-s}^{s} \sum_{n=-s}^{s} {}_bc_{i+m;j+n;k} = \frac{1}{S\left(\mathscr{A}_{ij}\right)} \sum_{(m;n)\in\mathscr{A}_{ij}} \left|F_{mnk}\right|, \quad (27) $$

$$ \begin{aligned} {}_cC_{ijk} &= \sum_{m=-s}^{s} \sum_{n=-s}^{s} {}_cc_{i+m;j+n;k} \\ &= \sum_{m=-s}^{s} \sum_{n=-s}^{s} \left|F_{i+m;j+n;k}\right| \cdot \sin^2\left(\frac{\pi}{s}\sqrt{m^2+n^2}\right), \end{aligned} \quad (28) $$

where F is the cosine spectrum of the pixel neighborhood and $S(\mathscr{A}_{ij})$ is volume of the annulus $\mathscr{A}_{ij}$ with the center $(i; j)$. Elements ${}_ac$; ${}_bc$; ${}_cc$ which are summed in (26); (27); (28) are illustrated as pixel values in Figure 4. Size of detectors really used in software is 16×16 or 32×32 pixels. In Figure 4, higher resolution is used for better illustration.

2.5.3. The Second Step: Profile Heights Calculation. The main imperfection of current methods is the hypothesis that the profile height in given pixel is exactly determined by values of chosen sharpness detector. This hypothesis implies that these values can be interpolated. However, this conclusion is quite false. We have available the series $\{C_{ijk}\}$; $k = 1; 2; \ldots; n$ for assessment of the height of pixel $(i; j)$. This series is not deterministic but it is a random variable. It cannot be interpolated, and it must be processed by statistical method. One of the possibilities is a regression analysis but it would be very complicated. Direct calculation of the expected value is much easier.

For each pixel $(i; j)$, we can construct theoretically infinitely many probability distribution functions $p_{ij}^{(r)}$ using different exponents r applied to series members C_{ijk}:

$$ p_{ij}^{(r)}(k) = \frac{C_{ijk}^r}{\sum_{s=1}^{n} C_{ijs}^r}. \quad (29) $$

Expected values of random variables $P_{ij}^{(r)}$ given by these probability functions estimate the height $h_{ij}^{(r)}$ of surface in its pixel $(i; j)$:

$$ h_{ij}^{(r)} = E\left(P_{ij}^{(r)}\right) = \sum_{k=1}^{n} k \cdot p_{ij}^{(r)}(k) = \sum_{k=1}^{n} k \cdot \frac{C_{ijk}^r}{\sum_{s=1}^{n} C_{ijs}^r}. \quad (30) $$

3. Results and Discussion

3.1. The Preprocessing: Image Registration. In Figure 5, we can see the photos from Figure 1 but they are displayed in so-called supplementary pseudocolors. If these images were completely identical, then arithmetic mean of the blue-green image on Figure 5(a) and orange image on Figure 5(b) would be "perfectly grey." Arithmetic mean of these images

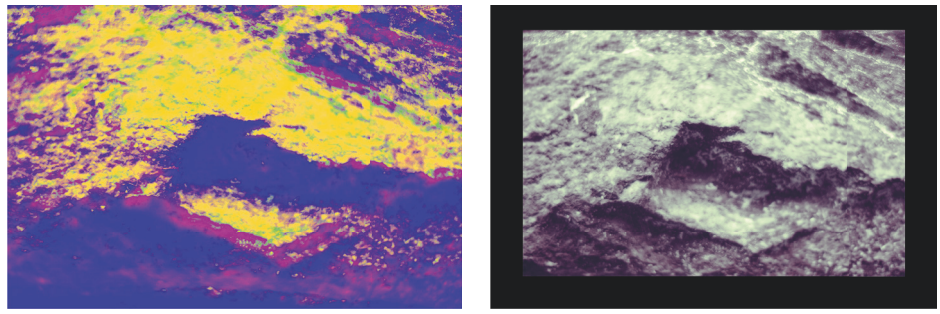

(a) (b)

Figure 6: The arithmetic mean of the images from Figure 5: before registration (a) and after registration (b). Real surface size 10 × 7.5 cm (b).

is constructed in Figure 6(a). It is clear that components of this mean are very different, values of the orange image are bigger in yellow parts of the mean, and values of the blue-green image are bigger in blue-violet parts of the mean.

In Figure 6(b), the same construction after the registration is realized. Very low color saturation of arithmetic mean confirms very good conformity. Of course, arithmetic mean cannot be "perfectly grey" in our case because components of the mean differs in blurred and sharp parts.

In Table 1, indicated and applied transforms in separated images of the blue marble are summarized. All transformations have been detected with subpixel precision; they are listed with a precision of one thousandths pixels. It is obvious that the scaling plays most important role; however, nor shifts are negligible. Rotation angle between the first and the last image is over five arcminutes; it means approximately one pixel on the image periphery (used data resolution is 1600 × 1200 pixels). This transformation is marginal in our case.

3.2. The First Step: Sharpness Detectors. As is clear from (26), (27), and (28) and Figure 4, detector ${}_aC$ increased high frequencies (right bottom corner of squares in Figure 4) too much; it means that it is very noise sensitive. The disadvantages of the detector ${}_bC$ are too sharp cuts which remove low and height frequencies.

Differences between the sharpness detectors stated in Section 2.5.2 are best demonstrated by their maxima. The graphical representation of detector ${}_cC$ (i.e., corresponding stair-approximation of the surface) is shown in Figure 7.

Differences between representations ${}_aC$; ${}_bC$; and ${}_cC$ are visually quite miniscule (therefore, ${}_aC$ and ${}_bC$ are not illustrated); however, differences exist. For their quantification, Root Mean Square Error is as follows:

$$\mathrm{RMSE}\left(h^{(1)};h^{(2)}\right)=\sqrt{\frac{1}{WH}\cdot\sum_{i=0}^{W-1}\sum_{j=0}^{H-1}\left(h_{ij}^{(1)}-h_{ij}^{(2)}\right)^2}. \quad (31)$$

Average Deviation is as follows:

$$\mathrm{AD}\left(h^{(1)};h^{(2)}\right)=\frac{1}{WH}\cdot\sum_{i=0}^{W-1}\sum_{j=0}^{H-1}\left|h_{ij}^{(1)}-h_{ij}^{(2)}\right|. \quad (32)$$

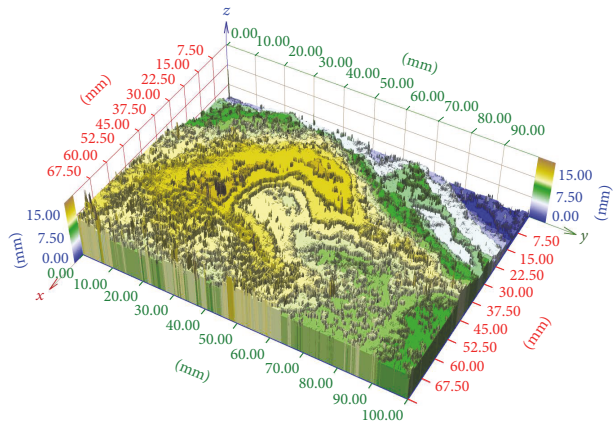

Figure 7: The stairs-approximation of the data from Figure 1 constructed by means of the sharpness detector ${}_cC$; see expression (28) and Figure 4(c).

Pearson Correlation Coefficient is as follows:

$$\mathrm{PCC}\left(h^{(1)};h^{(2)}\right)=\frac{\sum_{i=0}^{W-1}\sum_{j=1}^{H-1}\left(h_{ij}^{(1)}-\overline{h^{(1)}}\right)\left(h_{ij}^{(2)}-\overline{h^{(2)}}\right)}{\sqrt{\sum_{i=0}^{W-1}\sum_{j=0}^{H-1}\left(h_{ij}^{(1)}-\overline{h^{(1)}}\right)^2\sum_{i=0}^{W-1}\sum_{j=0}^{H-1}\left(h_{ij}^{(2)}-\overline{h^{(2)}}\right)^2}} \quad (33)$$

and Difference of surface Information Entropy is as follows:

$$\mathrm{DIE}\left(h^{(1)};h^{(2)}\right)=\left|\mathrm{IE}\left(h^{(1)}\right)-\mathrm{IE}\left(h^{(2)}\right)\right|, \quad (34)$$

where W; H are width and height of surface domain in pixels; $h_{ij}^{(1)}$; $h_{ij}^{(2)}$ are height of first (second) surface in the pixel $(i; j)$; $\overline{h^{(1)}}$; $\overline{h^{(2)}}$ are the average height of the first (second) surface; and

$$\mathrm{IE}\left(h\right)=-\sum_{i=1}^{W-1}\sum_{j=1}^{H-1}\left(\frac{h_{ij}}{\sum_{m=1}^{W-1}\sum_{n=1}^{H-1}h_{mn}}\log_2\frac{h_{ij}}{\sum_{m=1}^{W-1}\sum_{n=1}^{H-1}h_{mn}}\right) \quad (35)$$

is the Information Entropy of the surface h.

Table 1: Parameters of the transforms indicated and applicated to separate images in the series (stated relative to the first image).

Image number	Indicated transforms				Applicated transforms			
	Scale	Rotation (arcmin.)	Shift vector		Scale	Rotation (arcmin.)	Shift vector	
			x (pixels)	y (pixels)			x (pixels)	y (pixels)
(2)	1.01343	−0.554	−1.011	1.064	0.98675	0.554	1.011	−1.064
(3)	1.02351	−0.221	−0.990	1.861	0.97703	0.221	0.990	−1.861
(4)	1.03796	−0.061	−1.869	3.027	0.96343	0.061	1.869	−3.027
(5)	1.04888	0.053	−2.903	3.032	0.95340	−0.053	2.903	−3.032
(6)	1.06228	−0.409	−4.085	5.142	0.94137	0.409	4.085	−5.142
(7)	1.07055	−0.140	−4.947	4.987	0.93410	0.140	4.947	−4.987
(8)	1.08105	−0.027	−4.964	5.856	0.92503	0.027	4.964	−5.856
(9)	1.09173	0.134	−4.847	6.141	0.91598	−0.134	4.847	−6.141
(10)	1.10340	4.652	−4.988	7.003	0.90629	−4.652	4.988	−7.003
(11)	1.11426	5.215	−5.003	7.934	0.89746	−5.215	5.003	−7.934
(12)	1.12590	5.728	−5.895	8.972	0.88818	−5.728	5.895	−8.972
(13)	1.13784	5.278	−5.907	8.872	0.87886	−5.278	5.907	−8.872
(14)	1.14940	5.378	−5.928	8.980	0.87002	−5.378	5.928	−8.980
(15)	1.16066	5.275	−6.935	9.137	0.86158	−5.275	6.935	−9.137
(16)	1.17297	5.324	−8.036	9.095	0.85254	−5.324	8.036	−9.095

Table 2: Root Mean Square Error (RMSE) and Average Deviation (AD) in millimeters, Pearson Correlation Coefficient (PCC), and Difference of surface Information Entropy (DIE) (dimensionless quantities) for separate pairs of stairs-approximations ${}_aC$, ${}_bC$, and ${}_cC$.

PCC (DL)	RMSE (mm)			DIE (DL)	AD (mm)		
	${}_aC$	${}_bC$	${}_cC$		${}_aC$	${}_bC$	${}_cC$
${}_aC$	\	0.51228	0.69630	${}_aC$	\	0.15258	0.30171
${}_bC$	0.99320	\	0.56214	${}_bC$	0.00505	\	0.13145
${}_cC$	0.98740	0.99158	\	${}_cC$	0.00812	0.00307	\

Table 3: Root Mean Square Error (RMSE), Average Deviation (AD), Pearson Correlation Coefficient (PCC), and Difference of surface Information Entropy (DIE) for separate pairs of parabolic interpolation approximations ${}_aC$, ${}_bC$, and ${}_cC$.

PCC (DL)	RMSE (mm)			DIE (DL)	AD (mm)		
	${}_aC$	${}_bC$	${}_cC$		${}_aC$	${}_bC$	${}_cC$
${}_aC$	\	0.27750	0.38644	${}_aC$	\	0.15066	0.27180
${}_bC$	0.99850	\	0.24776	${}_bC$	0.00464	\	0.18216
${}_cC$	0.99627	0.99810	\	${}_cC$	0.00714	0.00250	\

Values of these characteristics are summarized in Table 2. Note that it is RMSE = AD = DIE = 0; PCC = 1 for a pair of identical surfaces.

Similar summary is made in Table 3 for the present reconstruction methods: parabolic interpolation of the stair-approximations ${}_aC$, ${}_bC$, and ${}_cC$. In Table 4, there are summarized RMSE, AD, PCC, and DIE for parabolic and Gaussian interpolation of the same stair-approximation ${}_cC$ and proposed method of the expected values of columns $\{{}_cC_{ijk}\}$; $k = 1; 2; \ldots; n$.

As was already stated in [35], only small differences are between parabolic and Gaussian interpolation. Really, values of RMSE, AD, and DIE for parabolic and Gaussian interpolation are approximately thousand times smaller than for interpolation and proposed method. Correlation between interpolations is stated even as one in Table 4. Therefore, it might seem that interpolations are much better than expected value estimation but the opposite is true. Small differences between these methods mean only that these reconstructions are roughly equally bad as shown in Figures 8 and 9.

Table 4: Root Mean Square Error (RMSE), Average Deviation (AD), Pearson Correlation Coefficient (PCC), and Difference of surface Information Entropy (DIE) for separate pairs of parabolic interpolation, Gaussian interpolation, and the proposed method applied to the same matrix ${}_cC$. The expected values of columns $\{{}_cC_{ijk}\}$; $k = 1; 2; \ldots; n$ was calculated according to expression (31) where $r = 5$ was used.

PCC (DL)	RMSE (mm)			DIE (DL)	AD (mm)		
	Parabolic	Gaussian	Mean		Parabolic	Gaussian	Mean
Parabolic	\	0.00592	0.49098	Parabolic	\	0.00477	0.34745
Gaussian	1.00000	\	0.48993	Gaussian	0.00002	\	0.34679
Mean	0.99377	0.99379	\	Mean	0.00309	0.00468	\

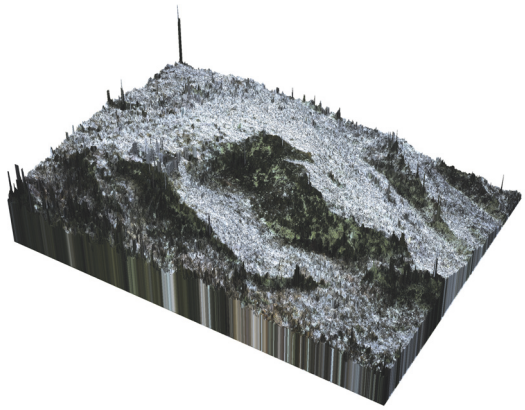

Figure 8: 3D reconstruction of the data from Figure 1: preprocessing according to Section 2.5.1 (new method), the first step according to Section 2.5.2 (new method), and the second and the third steps according to Section 2.2 (present method). Expression (28) with $s = 16$ was used in calculation of the matrix of sharpness detectors, its columns $\{{}_cC_{ijk}\}$; $k = 1; 2; \ldots; n$ was interpolated by the parabolic interpolation (present method).

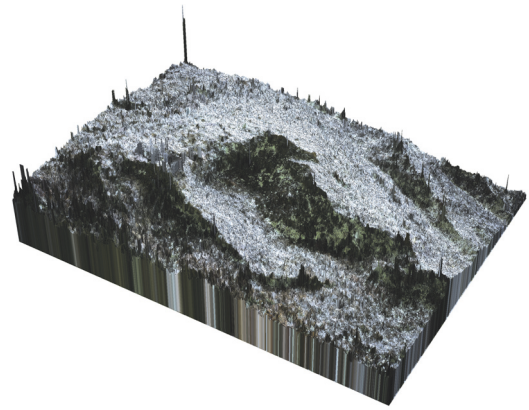

Figure 9: 3D reconstruction of the data from Figure 1: preprocessing according to Section 2.5.1 (new method), the first step according to Section 2.5.2 (new method), and the second and the third steps according to Section 2.2 (present method). Expression (28) with $s = 16$ was used in calculation of the matrix of sharpness detectors, its columns $\{{}_cC_{ijk}\}$; $k = 1; 2; \ldots; n$ was interpolated by the Gaussian interpolation (present method).

Results illustrated in Figures 8 and 9 have been obtained by combination of present and proposed method (they are not realized by present methods only due to different scaling of the input data). Visualization of the parabolic interpolation of ${}_cC$ is shown in Figure 8; Gaussian interpolation is illustrated in Figure 9. Practically the same and large noise is evident in these reconstructions.

Low-pass filters are commonly used to reduce the noise, but these filters are not ableto differentiate whether high-frequency information is caused by noise or by small details of useful information. Therefore, the loss of useful information is inevitable as shown in Figure 10.

In Figure 11, there is illustrated significantly better result of proposed method applied to the same matrix ${}_cC$. There is no visible noise at the output, and high-frequency useful information (small surface details) is retained.

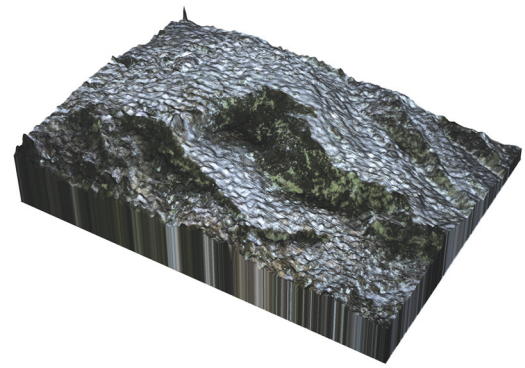

Figure 10: Gaussian low-pass filter with dispersion $\sigma^2 = 5$ applied to noisily output data from Figure 9. The noise is indeed reduced (but still visible); however useful high-frequency information is already lost.

4. Conclusion

Reconstructions of three-dimensional object surfaces are an important task in many branches of research. Even though the standard method of imaging object surfaces is the use of confocal microscopes or laser scanners, there exist sophisticated mathematical methods that are able to process images acquired by classic cameras and to construct 3D reconstruction similar to these from confocal microscopes or laser scanners. This enables us to obtain similar results with substantially less expensive equipment.

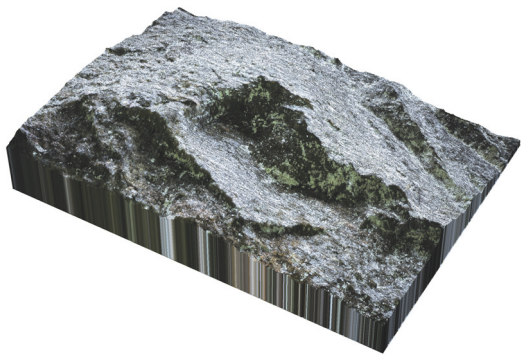

Figure 11: Completely new 3D reconstruction of the data from Figure 1: preprocessing according to Section 2.5.1, the first step according to Section 2.5.2—expression (28) with $s = 16$ was used—and the second step according to Section 2.5.3, the expected values of its columns $\{{}_cC_{ijk}\}$; $k = 1; 2; \ldots; n$ was calculated according to expression (29) where $r = 5$ was used.

Conflicts of Interest

The author declares that they have no conflicts of interest.

Acknowledgments

This work was supported by the Ministry of Education of the Czech Republic, Project LO1202 with financial subsidy, under the NPU I Programme. Thanks are due to Pavel Štarha for providing data.

References

[1] J. Halling, *Introduction to tribology*, Wykeham Books, London, UK, 1976.

[2] J. Bennett and L. Matton, *Introduction to surface roughnessand scattering*, Optical Society of America, Washington, DC, USA, 1999.

[3] W. Bowen and N. Hilal, *Atomic force microscopy in proces engineering*, Butterworth-Heinemann, Oxford, UK, 2009.

[4] S. Tolansky, "A light-profile microscope for surface studies," *Zeitschrif tfur Elektrochemie*, vol. 56, pp. 263–267, 1952.

[5] V. Thiery and D. I. Green, "The multifocus imaging technique in petrology," *Computers & Geosciences*, vol. 45, pp. 131–138, 2012.

[6] P. de Groot, "Principles of interference microscopy for the measurement of surface topography," *Advances in Optics and Photonics*, vol. 7, no. 1, pp. 1–65, 2015.

[7] G. H. Kaufmann, *Advances in speckle metrology and related techniques*, Weinheim: Wiley, 2011.

[8] M. Mettanen and U. Hirn, "A comparison of five optical surface topography measurement methods," *TAPPI Journal*, vol. 14, no. 1, pp. 27–38, 2015.

[9] S. Bertin, H. Friedrich, P. Delmas, E. Chan, and G. Gimel'farb, "Digital stereo photogrammetry for grain-scale monitoring of fluvial surfaces: error evaluation and workflow optimisation," *ISPRS Journal of Photogrammetry and Remote Sensing*, vol. 101, pp. 193–208, 2015.

[10] S. Tang, X. Zhang, and D. Tu, "Micro-phase measuring profilometry: its sensitivity analysis and phase unwrapping," *Optics and Lasers in Engineering*, vol. 72, pp. 47–57, 2015.

[11] Q. Feng, "Novel methodsfor 3-D semi-automatic mapping of fracture geometry at exposed rock surfaces," *KTH Dokotorsavhandling*, 2001.

[12] S. Slob, B. Van Knapen, R. Hack, K. Turner, and J. Kemeny, "Method for automated discontinuity analysis of rock slopes with three-dimensional laser scanning," *Transportation Research Record*, no. 1913, pp. 187–194, 2005.

[13] S. Slob and R. Hack, "3D terrestrial laser scanning as a new field measurement and monitoring technique," in *Engineering Geology for Infrastructure Planning in Europe*, R. Hack, R. Azzam, and R. Charlier, Eds., pp. 179–189, Springer Verlag, Berlin, Heidelberg, Germany, 2004.

[14] P. Pawlus, M. Wieczorowski, and T. Mathia, *The errors of stylus methods in Surface topography measurements*, ZAPOL, Szczecin, Poland, 2014.

[15] J. Hoła, Ł. Sadowski, J. Reiner, and S. Stach, "Usefulness of 3D surface roughness parameters for nondestructive evaluation of pull-off adhesion of concrete layers," *Construction and Building Materials*, vol. 84, pp. 111–120, 2015.

[16] D. A. Agard, Z. Hiraoka, P. Shaw, and J. Sedat, "Flourescence microscopy in three dimensions," in *Methods in Cell Biology, Part B: Quantitative flourescence microcopy-imaging and spectroscopy*, vol. 30, pp. 359–362, San Diego: AcademicPress, California, CA, USA, 1989.

[17] J. B. Pawley, *Handbook of Biological Confocal Microscopy*, Springer US, Boston, MA, 1995.

[18] J. Pawley, *Handbook of Confocal Microscopy*, Plenum Press, New York, NY, USA, 1990.

[19] N. Logali, *Confocal laser microscopy - principles, applicationsin medicine, biology, and the food sciences*, Rijeka, Croatia, 2013.

[20] D. A. Lange, H. M. Jennings, and S. P. Shah, "Analysis of surface roughness using confocal microscopy," *Journal of Materials Science*, vol. 28, no. 14, pp. 3879–3884, 1993.

[21] Y. Ichikawa and J. Toriwaki, "Confocal microscope 3D visualizing method for fine surface characterization of microstructures," in *Proceedings of SPIE 2862, Flatness, Roughness, and Discrete Defect Characterization for Computer Disks, Wafers, and Flat Panel Displays*, pp. 96–101, Denver, Colo, USA.

[22] K. Nadolny, "Confocal laser scanning microscopy for characterisation of surface microdiscontinuities of vitrified bonded abrasive tools," *International Journal of Mechanical Engineering and Robotics Research*, vol. 1, pp. 14–29, 1.

[23] J. F. Brenner, B. S. Dew, J. B. Horton, T. King, P. W. Neurath, and W. D. Selles, "An automated microscope for cytologic research a preliminary evaluation," *Journal of Histochemistry & Cytochemistry*, vol. 24, no. 1, pp. 100–111, 2017.

[24] R. J. Pieper and A. Korpel, "Image processing for extended depth of field," *Applied Optics*, vol. 22, no. 10, pp. 1449–1453, 1983.

[25] S. A. Sugimoto and Y. Ichioka, "Digital composition of images with increased depth of focus considering depth information," *Applied Optics*, vol. 24, no. 14, pp. 2076–2080, 1985.

[26] E. Krotkov, "Focusing," *International Journal of Computer Vision*, vol. 1, no. 3, pp. 223–237, 1988.

[27] J. Gillespie and R. A. King, "The use of self-entropy as a focus measure in digital holography," *Pattern Recognition Letters*, vol. 9, no. 1, pp. 19–25, 1989.

[28] D. Agard, A. Hiraoka, Z. Shaw, and P. Sedat, "Flourescence microscopy in three dimensions," in *Methods in Cell Biology, Part B: Quantitative flourescence microcopy-imaging and spectroscopy*, D. L. Taylor and Y. Wang, Eds., vol. 30, pp. 359–362, Academic Press, San Diego, USA, 1989.

[29] D. Martišek, "The two-dimensional and three-dimensional processing of images provided by conventional microscopes," *Scanning*, vol. 24, no. 6, pp. 284–295, 2002.

[30] D. Martišek and H. Druckmüllerová, "Multifocal image processing," *Mathematics for Applications*, vol. 3, no. 1, pp. 77–90, 2014.

[31] M. Niederost, J. Niederost, and J. Ščučka, "International Archives of the Photogrammetry, Remote Sensing and Spatial Information Sciences XXXIV-5/W10," in *Proceedings of the International Workshop on Visualization and Animation of Reality-based 3D Models*, Tarasp-Vulpera, Switzerland, 2003.

[32] C. Kammerud, B. Abidi, S. Huq, and M. Abidi, "3D nanovision for the inspection of micro-electro-mechanical systems," in *Proceedings of the 12th IEEE International Conference on Electronics, Circuits and Systems (ICECS 2005)*, Tunisia, December 2005.

[33] A. Thelen, S. Frey, S. Hirsch, and P. Hering, "Improvements in shape-from-focus for holographic reconstructions with regard to focus operators, neighborhood-size, and height value interpolation," *IEEE Transactions on Image Processing*, vol. 18, no. 1, pp. 151–157, 2009.

[34] S. K. Nayar and Y. Nakagawa, "Shape from Focus," *IEEE Transactions on Pattern Analysis and Machine Intelligence*, vol. 16, no. 8, pp. 824–831, 1994.

[35] T. Ficker and D. Martišek, "Three-dimensional reconstructions of solid surfaces using conventional microscopes," *Scanning*, vol. 38, no. 1, pp. 21–35, 2016.

[36] A. Thelen, *Optimized surface extraction from Holographic data*, Fakultat der Heinrch-Heine-Universitat Dusseldorf, Germany, 2006.

[37] D. Martišek, J. Procházková, and T. Ficker, "High-quality three-dimensional reconstruction and noise reduction of multifocal images from oversized samples," *Journal of Electronic Imaging*, vol. 24, no. 5, Article ID 053029, 2015.

[38] H. Druckmüllerová, *Phase-correlation based image registration*, Brno University of technology, Czech Republic, 2010.

[39] W. K. Pratt, *Digital Image Processing: PIKS Inside*, John Wiley & Sons, Inc., New York, USA, 3rd edition, 2001.

[40] B. Zitova and J. Flusser, "Image registration methods: a survey," *Image and Vision Computing*, vol. 21, no. 11, pp. 977–1000, 2003.

[41] M. V. Wyawahare et al., "Image registration techniques: an overview," *International Journal of Signal Processing, Image Processing and Pattern Recognition*, vol. 2, no. 3, 2009.

[42] E. M. Stern et al., *Introduction to Fourier analysis on Euclidean spaces*, Princeton, N. J. Princeton University Press, 1975.

Scientific Research Publishing

Advances in Pure Mathematics, 2017, 7, 615-640
http://www.scirp.org/journal/apm
ISSN Online: 2160-0384
ISSN Print: 2160-0368

Joint Rock Coefficient Estimation Based on Hausdorff Dimension

Dalibor Martišek

Institute of Mathematics, Faculty of Mechanical Engineering, Brno University of Technology, Brno, Czech Republic
Email: martisek@fme.vutbr.cz

How to cite this paper: Martišek, D. (2017) Joint Rock Coefficient Estimation Based on Hausdorff Dimension. *Advances in Pure Mathematics*, **7**, 615-640.
https://doi.org/10.4236/apm.2017.711037

Received: September 11, 2017
Accepted: November 12, 2017
Published: November 15, 2017

Abstract

The strength of rock structures strongly depends inter alia on surface irregularities of rock joints. These irregularities are characterized by a coefficient of joint roughness. For its estimation, visual comparison is often used. This is rather a subjective method, therefore, fully computerized image recognition procedures were proposed. However, many of them contain imperfections, some of them even mathematical nonsenses and their application can be very dangerous in technical practice. In this paper, we recommend mathematically correct method of fully automatic estimation of the joint roughness coefficient. This method requires only the Barton profiles as a standard.

Keywords

Hausdorff Dimension, Self-Similarity, Self-Affinity, Box Counting Method, Power Function Method, Barton Profile, JRC Index

1. Introduction

A shape of geological discontinuities plays an important role in influencing the stability of rock masses. Many approaches have been used for its determination. The method of Barton and Choubey (1977) is well known in geotechnical practice. These authors introduced the method which is able to calculate the shear strength τ of rock joints as

$$\tau = \sigma_n \cdot \tan\left(\varphi_r + JRC \cdot \log\frac{JCS}{\sigma_n}\right) \tag{1}$$

where JRC is the joint roughness coefficient, JCS is the joint compressive strength, φ_r is the residual friction angle, and σ_n is the normal stress.

The method of Barton and Choubey [1] is well known in geotechnical prac-

tice-a visual comparison a fracture rock surface to be analysed with the standard Barton profiles is preferred way for determining *JRC* values.

A quick and easy estimate is probably one of the main reasons for this preference. However, this method is very subjective. Therefore, objective methods for *JRC* estimation are searched—see [2] [3] [4] [5] [6] for example. Unfortunately, some published papers contain many inaccuracies and even mathematical nonsenses. Application of some published "indicators of similarity" may be very dangerous in civil engineering. We refer to some of them and we recommend a mathematically correct method of fully automatic estimation of the *JRC* index in the following text.

2. Some Errors of Present Methods Based on Fractal Dimension

As was said in Introduction, subjective visual comparison a fracture rock surface to be analyzed with the standard Barton profiles (see **Figure 1**) is preferred way for determining *JRC* values. Objective methods for *JRC* are searched, unfortunately, many of them are incorrect.

Many researchers believe that the surface roughness of rock joints needs to be characterized using scale invariant parameters such as fractal parameters. Several researchers have suggested using the fractal dimension to quantify rock joint roughness (see [7]-[13] for example).

In [14], there is "derived" a "direct relationship" between the *JRC* index and fractal dimension D

$$JRC \approx 50 \cdot (D-1) \tag{2}$$

However, it is a nonsense as the following example illustrates.

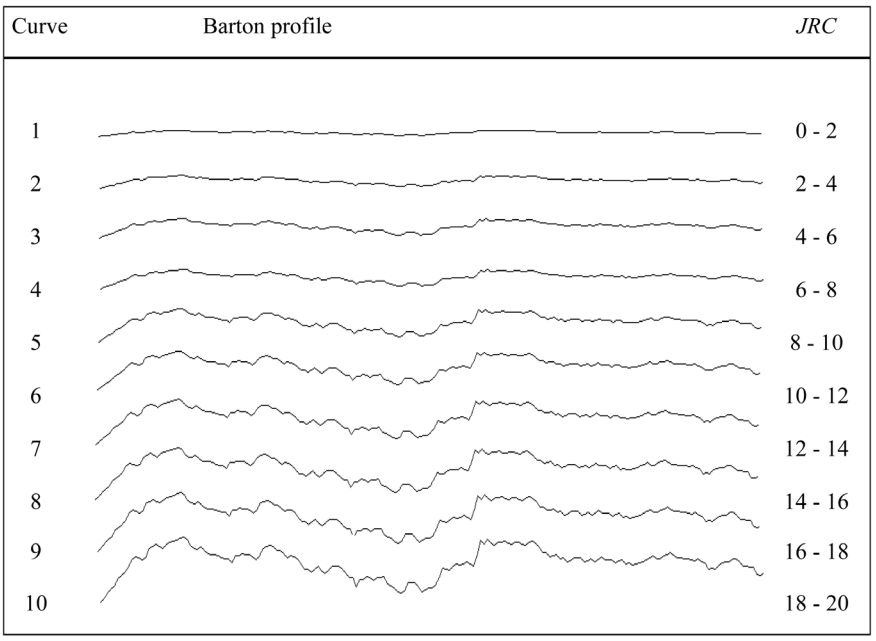

Figure 1. Standard Barton roughness profiles and their joint rock coefficients.

Example: A fractal dimension is namely affine invariant, *i.e.* each bijective affine transformation of the profile has the same dimension as an original. The profile $p(x)$ in **Figure 2** was generated as a fractional Brownian motion and for every x is $P(x)=4\cdot p(x)$. To easily determine the dimension of the resulting fractal, a random number must be generated by the Gaussian distribution $N(0;1)$ and the i-th iteration step variations σ_i have to be adjusted in accordance with

$$\sigma_i^2=\frac{\sigma_0^2}{2^{2Hi}} \tag{3}$$

where $H\in\langle 0;1\rangle$ is so called Hurst exponent.

Due to affine invariance, both profiles have the same dimension ($D=1.5$) and should have the same roughness therefore. This is evidently not true. Moreover, *JRC* of both profiles is $JRC\approx 25$ according to (1). This is also not true.

In [14] [15], another „direct relationship" between dimension and *JRC* was published:

$$JRC=-0.87804+37.7844\cdot\left(\frac{D-1}{0.015}\right)-16.9304\cdot\left(\frac{D-1}{0.015}\right)^2 \tag{4}$$

This relationship is often cited (see [16] [17] [18] [19] for example) but it is quite false. Equation (4) gives a totally nonsensical results for Barton profiles as will be shown in 2.5 (see the last column of **Table 3**).

Table 1. Hausdorff dimension and grid measure of the original Koch curve *A* and its affine representation *B* estimated by box-counting method and power-function method. Used affinity is $[x;y]\to[x;2y]$.

Koch curve *A*				Koch curve *B*			
ε	N (ε)	ln(ε)	ln(p)	ε	N (ε)	ln(ε)	ln(p)
5	4322	1.6094	8.3715	5	32474	1.6094	10.3882
10	20449	2.3026	9.9257	10	13364	2.3026	9.5003
15	12296	2.7081	9.4170	15	7978	2.7081	8.9844
20	8701	2.9957	9.0712	20	5470	2.9957	8.6070
25	6512	3.2189	8.7814	25	4222	3.2189	8.3481
30	5201	3.4012	8.5566	30	3351	3.4012	8.1170
35	4250	3.5553	8.3547	35	2718	3.5553	7.9077
40	3585	3.6889	8.1845	40	2316	3.6889	7.7476
45	3049	3.8067	8.0226	45	2014	3.8067	7.6079
50	2674	3.9120	7.8913	50	1743	3.9120	7.4634
	Power. f.	Box-counting			Power. f.	Box-counting	
Dim.	**1.2621**		**1.2662**		**1.2627**		**1.2599**
Meas.	33365	exp (10.4184)	=33470		52739	exp (10.8730)	=52733

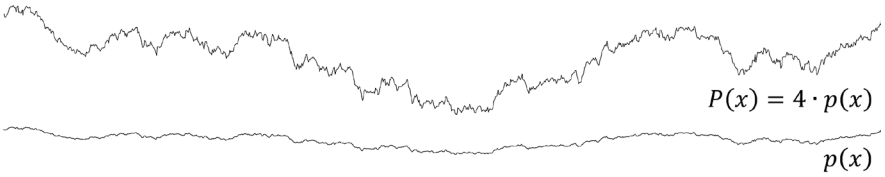

Figure 2. The profile $p(x)$ was generated as a fractional Brownian motion. Due to affine invariance, the profiles $p(x)$; $P(x)$ have the same dimension but evidently different roughness.

We can often read that for computing of fractal dimension, it is necessary to decide whether the object is self-similar or self-affine (see [20] [21] [22] [23]). It is said that "the computation of fractal dimensions of self-affine fractals requires modified computational methods" [14] [20] and their dimensions D have to be computed by others methods than the dimension of self-similar curves. Alleged reason is "different scaling" in the x-and y-directions which changes its dimensionality (see [14] for example). However, it is a deep mistake. One example for all: The curve B in **Figure 3** contains two its copies with the same scaling (red and pink). These copies required "non-modified" method. However, the same curve contains two copies with different scaling (green and blue). These copies required "modified" method. Can we use the modified or the non-modified method for its dimensionality estimation?

3. Hausdorff Measure and Hausdorff Dimension

Hausdorff defined the first dimension that allows non-integer values. Hausdorff s-dimensional outer measure of a set A is defined as

$$ {}^{*}H^{(s)}(A) = \lim_{n\to\infty} \inf_{A\subseteq\bigcup A_{n;i}} \left\{ \sum_{i\in I} \left(diam A_{n;i} \right)^{s} \middle| diam A_{n;i} \le \frac{1}{n} \right\} \tag{5} $$

where I is an at most countable index set. Restriction of $H^{(s)}$ to the sets measurable with ${}^{*}H^{(s)}$ (H-measurable sets) is called Hausdorff s-dimensional measure of the set A. The number

$$ D_H(A) = \sup\left\{ d \in \mathbb{R}_0^+ \cup \{\infty\} \middle| H^{(d)}(A) = \infty \right\} = \inf\left\{ d \in \mathbb{R}_0^+ \cup \{\infty\} \middle| H^{(d)}(A) = 0 \right\} \tag{6} $$

is called Hausdorff dimension of the set A.

Mandelbrot [24] defined fractal as a set which Hausdorff dimension is sharply greater than the topologic dimension. Ever after several dimension which allows non-integer values was defined (see [25] for example). Each of them is called the fractal dimension.

For estimation of the Hausdorff dimension of sets which are constructed on digital devices, so called grid measure and grid dimension are used. The grid s-dimensional outer measure is defined as

$$ {}^{*}G^{(s)}(A) = \lim_{n\to\infty} \inf_{A\subseteq\bigcup A_{n;i}} \left\{ \sum_{i\in I} \left(diam A_{n;i} \right)^{s} \middle| diam A_{n;i} = \frac{1}{n} \right\} \tag{7} $$

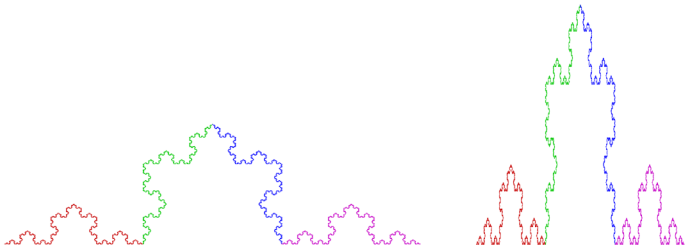

(a) (b)

Figure 3. "Different scaling" in *x*- and *y*-directions can change the self-similar set (a) to self-affine set (b). However, "different scaling" in *x*- and *y*-directions can change the self-affine (b) to self-similar set (a).

Its restriction $G^{(s)}$ to the sets measurable with ${}^{*}G^{(s)}$ (*G*-measurable set) is called the grid measure. The grid dimension (*G*-dimension) of the set A is defined as

$$D_G(A)=\sup\left\{d\in\mathbb{R}_0^+\cup\{\infty\}\middle|G^{(d)}(A)=\infty\right\}=\inf\left\{d\in\mathbb{R}_0^+\cup\{\infty\}\middle|G^{(d)}(A)=0\right\} \quad (8)$$

The *G*-dimension is suitable for digital data and since the limit condition $n\to\infty$ in Formula (7) cannot be realized, the limit is omitted and the Formula (7) is replaced with the approximate equality

$${}^{*}G^{(s)}(A)\approx\inf_{A\subseteq\cup A_{n;i}}\left\{\sum_{i\in I}\left(diamA_{n;i}\right)^s\middle|diamA_{n;i}=\frac{1}{n}\right\} \quad (9)$$

4. Box Counting and Power-Function Method

For the infimum to be computed in (9), only those sets $A_{n;i}$ are taken to the union $\cup A_{n;i}$ for which $A_{n;i}\cap A\neq\varnothing$. Due to the fact that only bounded sets (or more precisely their approximations containing finite elements) can be represented in the computer, the system $\{A_{n;i}\}$ is always finite. Let us denote its cardinality by $N(n)$. The measured approximations are always *G*-measurable. In software implementations of the measurement, used metric is a square metric, where the diameter of a square is equal to its side. According to Formula (9) we obtain for measure in Hausdorff dimension

$$G^{(D)}(A)\approx\sum_{i=1}^{N(n)}\left(diamA_{n;i}\right)^D=\sum_{i=1}^{N(n)}\frac{1}{n^D}=N(n)\cdot n^{-D} \quad (10)$$

Therefore,

$$N(n)\approx G^{(D)}\cdot n^D \quad (11)$$

Applying the logarithm on both sides of the approximate equality (11) we obtain

$$\ln N(n)\approx D\cdot\ln n+\ln G^{(D)} \quad (12)$$

Measuring with a specified n, a $N(n)$ is obtained for a covering of the measured set. The values D and $G^{(D)}$ are calculated by fitting the straight line in the form (12) using the least square method. It is evident that for a high enough n we can calculate D as

$$D \approx \frac{\ln N(n)}{\ln n} \tag{13}$$

and even define the dimension as the limit of that fraction, *i.e.*

$$D_B = \lim_{n\to\infty} \frac{\ln N(n)}{\ln n} \tag{14}$$

This dimension and the method for its measurement are known as the box counting.

Note that n is the reciprocal value of the diameter of covering sets, which is often marked as ε. Therefore, if we denote the cardinality $N(n)$ of the covering of the set to be measured as $N(\varepsilon)$, we obtain

$$N(\varepsilon) \approx G^{(D)}(A) \cdot \varepsilon^{-D} \tag{15}$$

from (11)

$$\ln N(\varepsilon) \approx -D \cdot \ln \varepsilon + \ln G^{(D)}(A) \tag{16}$$

from (12) or

$$D_B = \lim_{\varepsilon\to 0+} \frac{\ln N(\varepsilon)}{\ln \varepsilon^{-1}} \tag{17}$$

from (14) respectively.

To calculate this dimension for the fractal F, it is necessary to insert this fractal into an evenly spaced grid and count how many squares (2D case) or boxes (3D case) are required to cover the set. The box-counting dimension is calculated by seeing how this number changes as we make the grid finer by applying a box-counting algorithm.

It is possible to shown that the theoretically defined box counting dimension (14) is equal to the Hausdorff dimension—see Formula (8). A problem is that the dimension (14) has to be estimated with the least-square method form the linear function (12). If we denote the power function (11) as $f(x) = G \cdot x^D$, sum of its residues is $R_n = \Sigma\left[N(n) - f(n)\right]^2$, while sum of residues for the linear function (12) is $R_n^* = \Sigma\left[\ln N(n) - \ln f(n)\right]^2$. Of course $R_n^* \ll R_n$. Thus the box-counting method systematically overestimates residues of low values and underestimates residues of its high values. Moreover, negative values of the difference $\ln N(n) - \ln f(n)$ have lower weights than positive values. This somehow lowers the tangent of the straight line as thus the value of the estimated dimension.

This problem can be overcome by searching for the power function (11) instead of the linear function (12). The least square method requires in this case minimization of the function

$$f(N, D) = \sum_n \left(N - G \cdot n^D\right)^2 \tag{18}$$

This leads to the equation

$$\sum_n \left(Nn^D \ln n\right) \sum_n n^{2D} - \sum_n Nn^D \sum_n \left(n^{2D} \ln n\right) = 0 \tag{19}$$

This equation is then solved numerically—see [26] for more information.

5. Self-Similarity and Self-Affinity

Many technical papers describe the fractals. We can read that the fractals can be either self-similar or self-affine and the original box counting method is a self-similar method and it provides accurate results only for self-similar profiles. Natural rock joint profiles are self-affine, therefore, the box-counting method is not useable for their fractal dimension—see [27] for example. However, these affirmations are very inaccurately. It is said that self-affine curves, in contrast to self-similar ones, are not identically scaled in *x*- and *y*-directions (see [14] [20] [21] [22] for example). This "definition" is unprofessional and very narrow (restricted). Many others fractals are self-affine.

A self-affine fractal is any fractal F, for which there exist affine mappings $\varphi_i; i=1;2;\cdots;n$ so it holds

$$F=\bigcup_{i=1}^{n}\varphi_i(F)=\bigcup_{i=1}^{n}F_i \tag{20}$$

If all affinities φ_i are the similarities then the self-affine fractal is concurrently self-similar. It means that the self-similarity is a special case of the self-affinity, *i.e.* each self-similar set is self-affine concurrently.

In Euclidean space, each affinity is given by

$$X'=\boldsymbol{F}_i\cdot X+\boldsymbol{v}_i \tag{21}$$

where $\boldsymbol{F}_i$ is any square matrix and $\boldsymbol{v}$ is any vector. If

$$\boldsymbol{F}_i\cdot\boldsymbol{F}_i^{\mathrm{T}}=\lambda^2\cdot\boldsymbol{I} \tag{22}$$

(where $\boldsymbol{I}$ is the identity matrix) then the affinity is called the similarity, number λ is its coefficient. Except self-similar and self-affine fractals, there exist sets which are neither self-similar nor self-affine (Mandelbrot set for example).

According of the definition of the Hausdorff dimension is

$$0<H^{(D)}(A)=\inf_{A\subseteq\bigcup_k A_{nk}}\left\{\sum_{k\in I}\left(diam A_{n;i}\right)^s\middle|\,diam A_{n;i}\le\frac{1}{n}\right\}<\infty \tag{23}$$

If a set A is self-similar and $\lambda_1;\lambda_2;\cdots;\lambda_p$ are coefficients of the similarities φ_i from (20), and for each $i\neq j$ is $H^{(D)}\left(\varphi_i(A)\cap\varphi_j(A)\right)=0$ then

$$\begin{aligned}H^{(D)}(A)&=\inf_{A\subseteq\bigcup_k A_{nk}}\left\{\sum_{k\in I}\left(diam A_{n;i}\right)^D\middle|\,diam A_{n;i}\le\frac{1}{n}\right\}\\&=\underbrace{\inf_{A\subseteq\bigcup_k A_{nk}}\left(\mathrm{diam}A\right)^D}_{H^{(D)}(A)}\sum_{i=1}^{p}\lambda_i^D\end{aligned} \tag{24}$$

It means that

$$H^{(D)}(A)=H^{(D)}(A)\cdot\sum_{i=1}^{p}\lambda_i^D \tag{25}$$

$$\lambda_1^D+\lambda_2^D+\cdots+\lambda_p^D=1 \tag{26}$$

In case of $\lambda_1=\lambda_2=\cdots=\lambda_p=\lambda$ is

$$\lambda_1^D + \lambda_2^D + \cdots + \lambda_p^D = p \cdot \lambda^D = 1 \Rightarrow D = \frac{\ln p}{\ln \frac{1}{\lambda}} \tag{27}$$

Example: the Koch curve is self-similar with four copies of itself, each scaled by the factor one third, its dimension is $D = \frac{\ln 4}{\ln 3}$. The Sierpinski triangle or Sierpinski square are also self-similar with three copies scaled by one half or eight copies scaled by one third respectively, their dimensions are $D = \frac{\ln 3}{\ln 2}$ or $D = \frac{\ln 8}{\ln 3}$ respectively.

For *H*-measure of any fractal, the *H*-measure of its covering $\mathrm{C} = \bigcup_k A_{nk}$ is determinative. This covering consists of cubes in case of square metric. The measure of self-affine fractals (19) is equal to the sum of measures its affine copies φ_i. Each affinity φ_i transforms a cubical covering C to the set of parallelepipeds $\varphi_i(\mathrm{C})$. We have to find how the volume of cube will change by its transform to the parallelepiped.

Each cube is given by orthonormal vectors $\boldsymbol{a} = (a_1; a_2; a_3)$; $\boldsymbol{b} = (b_1; b_2; b_3)$; $\boldsymbol{c} = (c_1; c_2; c_3)$ which are transform to linearly independent vectors $\boldsymbol{a}' = (a_1'; a_2'; a_3')$; $\boldsymbol{b}' = (b_1'; b_2'; b_3')$; $\boldsymbol{c}' = (c_1'; c_2'; c_3')$ by bijective affinity φ_i, *i.e.*

$$\boldsymbol{a}'^{\mathrm{T}} = \boldsymbol{F}_i \cdot \boldsymbol{a}^{\mathrm{T}};\ \boldsymbol{b}'^{\mathrm{T}} = \boldsymbol{F}_i \cdot \boldsymbol{b}^{\mathrm{T}};\ \boldsymbol{c}'^{\mathrm{T}} = \boldsymbol{F}_i \cdot \boldsymbol{c}^{\mathrm{T}} \tag{28}$$

or

$$\boldsymbol{a}' = \boldsymbol{a} \cdot \boldsymbol{F}_i^{\mathrm{T}};\ \boldsymbol{b}' = \boldsymbol{b} \cdot \boldsymbol{F}_i^{\mathrm{T}};\ \boldsymbol{c}' = \boldsymbol{F}_i^{\mathrm{T}} \cdot \boldsymbol{c}^{\mathrm{T}} \tag{29}$$

where $\boldsymbol{F}_i$ is the matrix of the affinty φ_i. This implies

$$(a_1'; a_2'; a_3') = (a_1; a_2; a_3) \cdot \begin{pmatrix} z_{11} & z_{21} & z_{31} \\ z_{12} & z_{22} & z_{32} \\ z_{13} & z_{23} & z_{33} \end{pmatrix} = \big((\boldsymbol{a}; \boldsymbol{f}_1); (\boldsymbol{a}; \boldsymbol{f}_2); (\boldsymbol{a}; \boldsymbol{f}_3)\big) \tag{30}$$

By analogy

$$(b_1'; b_2'; b_3') = \big((\boldsymbol{b}; \boldsymbol{f}_1); (\boldsymbol{b}; \boldsymbol{f}_2); (\boldsymbol{b}; \boldsymbol{f}_3)\big) \tag{31}$$

$$(c_1'; c_2'; c_3') = \big((\boldsymbol{c}; \boldsymbol{f}_1); (\boldsymbol{c}; \boldsymbol{f}_2); (\boldsymbol{c}; \boldsymbol{f}_3)\big) \tag{32}$$

Volume of the parallelepiped which is given by vectors $\boldsymbol{a}'; \boldsymbol{b}'; \boldsymbol{c}'$ is equal to the scalar triple product. Therefore, we obtain

$$\begin{aligned} \begin{vmatrix} a_1' & a_2' & a_3' \\ b_1' & b_2' & b_3' \\ c_1' & c_2' & c_3' \end{vmatrix} &= \begin{vmatrix} (\boldsymbol{a}; \boldsymbol{f}_1) & (\boldsymbol{a}; \boldsymbol{f}_2) & (\boldsymbol{a}; \boldsymbol{f}_3) \\ (\boldsymbol{b}; \boldsymbol{f}_1) & (\boldsymbol{b}; \boldsymbol{f}_2) & (\boldsymbol{b}; \boldsymbol{f}_3) \\ (\boldsymbol{c}; \boldsymbol{f}_1) & (\boldsymbol{c}; \boldsymbol{f}_2) & (\boldsymbol{c}; \boldsymbol{f}_3) \end{vmatrix} \\ &= \begin{vmatrix} a_1 & a_2 & a_3 \\ b_1 & b_2 & b_3 \\ c_1 & c_2 & c_3 \end{vmatrix} \cdot \begin{vmatrix} f_{11} & f_{21} & f_{31} \\ f_{12} & f_{22} & f_{32} \\ f_{13} & f_{23} & f_{33} \end{vmatrix} \end{aligned} \tag{33}$$

from (30), (31), (32). Therefore

$$V(\boldsymbol{a}'; \boldsymbol{b}'; \boldsymbol{c}') = \left|\det \boldsymbol{F}_i^{\mathrm{T}}\right| \cdot V(\boldsymbol{a}; \boldsymbol{b}; \boldsymbol{c}) = \left|\det \boldsymbol{F}_i\right| \cdot V(\boldsymbol{a}; \boldsymbol{b}; \boldsymbol{c}) \tag{34}$$

It is possible to obtain

$$S(\boldsymbol{a}';\boldsymbol{b}') = \det \boldsymbol{F}_i \cdot S(\boldsymbol{a};\boldsymbol{b})$$

for the area of the parallelogram in two-dimensional space. The diameter of cube (or square) which have the same volume (or area) in square metric is

$$\operatorname{diam} A'_{nk} = \sqrt[3]{\left|\det \boldsymbol{F}_i\right| \cdot V(\boldsymbol{a};\boldsymbol{b};\boldsymbol{c})} = \sqrt[3]{\left|\det \boldsymbol{F}_i\right|} \cdot \operatorname{diam} A_{nk} \tag{35}$$

or

$$\operatorname{diam} A'_{nk} = \sqrt{\left|\det \boldsymbol{F}_i\right| \cdot S(\boldsymbol{a};\boldsymbol{b})} = \sqrt{\left|\det \boldsymbol{F}_i\right|} \cdot \operatorname{diam} A_{nk} \tag{36}$$

respectively.

For the H-measure of a self-affine fractal A which contains p affine copies of itself, we obtain

$$\begin{aligned}
H^{(D)}(A) &= \inf_{A\subseteq\bigcup_k A_{nk}} \left\{ \sum_{k\in I} \left(\operatorname{diam} A_{n;i}\right)^D \middle| \operatorname{diam} A_{nk} \le \frac{1}{n} \right\} \\
&= \inf_{A\subseteq\bigcup_k A_{nk}} \left\{ \sum_{k\in I} \left(\sqrt{\left|\det \boldsymbol{F}_i\right|} \cdot \operatorname{diam} A_{nk} \right)^D \middle| \operatorname{diam} A_{nk} \le \frac{1}{n} \right\} \\
&= \inf_{A\subseteq\bigcup_k A_{nk}} \left\{ \sum_{i=1}^{p} \left[\left(\sqrt{\left|\det \boldsymbol{F}_i\right|} \right)^D \sum_{k\in I} \left(\operatorname{diam} A_{nk}\right)^D \right] \middle| \operatorname{diam} A_{nk} \le \frac{1}{n} \right\} \\
&= \underbrace{\inf_{A\subseteq\bigcup_k A_{nk}} \sum_{k\in I} \left(\operatorname{diam} A_{nk}\right)^D}_{H^{(D)}(A)} \sum_{i=1}^{p} \left(\sqrt{\left|\det \boldsymbol{F}_i\right|} \right)^D \\
&= H^{(D)}(A) \sum_{i=1}^{p} \left(\sqrt{\left|\det \boldsymbol{F}_i\right|} \right)^D
\end{aligned}$$

i.e.

$$H^{(D)}(A) = H^{(D)}(A) \sum_{i=1}^{p} \left(\sqrt{\left|\det \boldsymbol{F}_i\right|} \right)^D \tag{37}$$

Therefore

$$\sum_{i=1}^{p} \left(\sqrt{\left|\det \boldsymbol{F}_i\right|} \right)^D = 1 \tag{38}$$

and

$$\sum_{i=1}^{p} \left(\sqrt[3]{\left|\det \boldsymbol{F}_i\right|} \right)^D = 1 \tag{39}$$

in three-dimensional space by analogy.

6. Experiments with Approximations of Theoretical Sets

According to [27], the original box counting methods are the self-similar methods and they provide accurate results only for self-similar profiles. Problems are supposedly encountered when self-similar methods are used in the calculation of fractal dimensions for the self-affine objects. However, this is incorrect. The box counting method gives accurate or inaccurate results in case of self-similarity or self-affinity in the same way. However, the power function method does not suffer by any systematic error and is more precise as was said in the previous section.

Bijective affine transform (scaling in one direction for example) changes the measure of the transformed set but it does not change its dimensionality. For these measurement, the same methods may be used (without any modification). We estimated the dimensionality and measure of the Koch curve (see **Figure 3**), *i.e.* namely the self-similar original A and further its self-affine scaling $B:[x;y]\to[x;2y]$. The box counting method and power function method with the same parameters are used in both cases. Both curves have been generated as image with resolution 4096×4096 pixels. Results of these measurement are summarised in **Table 1** and graphically represented in **Figure 4** (box counting) and **Figure 5** (power function). For both curves (self-similar and self-affine), approximately the same dimension has been measured ($D\approx 1.26$) using two methods (box counting and power function) with the same parameters ($\varepsilon = 5,10,\cdots,50$) and withouth any modification. Theoretical dimension is $D=\dfrac{\ln 4}{\ln 3}=2.261859\cdots$ in both cases.

Straightlines (in case of the box counting) or power curves (in case of the power function) differs in shifting (extension) in vertical direction only. By this shifting (extension), set measure in corresponding fractal dimension is determined. Remind that the measure is the length in case of $D=1$ which is measured in linear micrometers (μm[1]) for example. In case of $D=2$, the measure is caled the area which is measured in square micrometers (μm[2]) for example. In case of Koch curve which dimension is $D=\dfrac{\ln 4}{\ln 3}$, we must measure in micrometers powered by $D=\dfrac{\ln 4}{\ln 3}$. If we presume that the pixel is a square with a side 1 μm then the measure of the curve A is

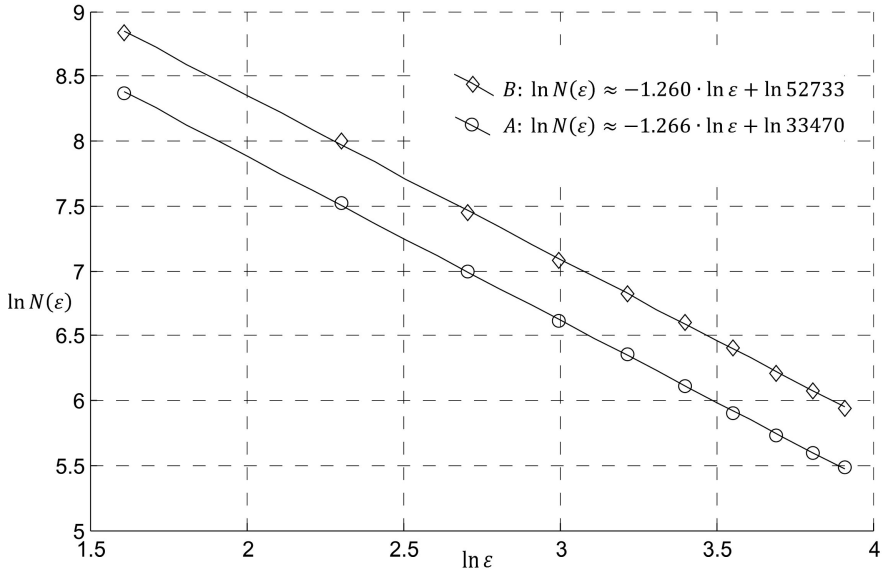

Figure 4. Box-counting dimension and box-counting measure of the Koch curve A and its affine representation B. Used affinity is $[x;y]\to[x;2y]$.

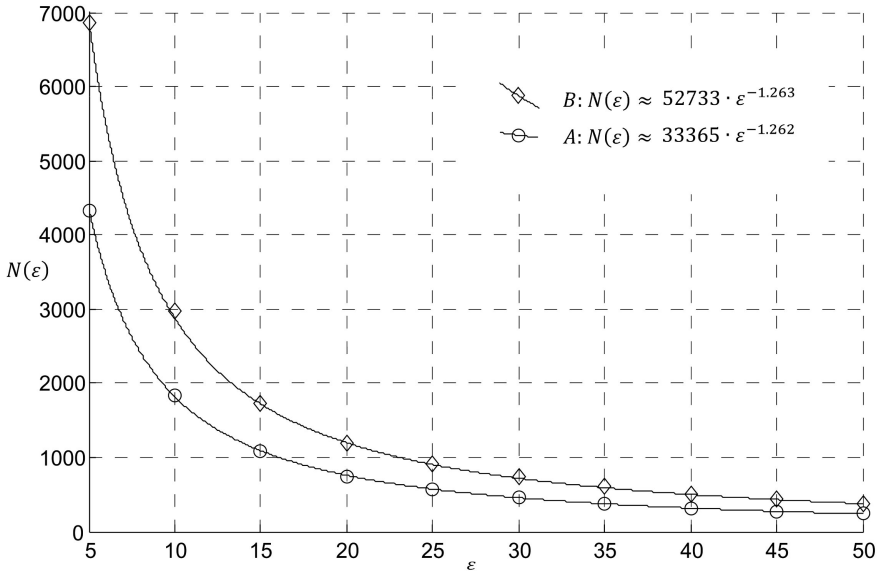

Figure 5. Hausdorff dimension and grid measure of the Koch curve A and its affine representation B. Power-function method, used affinity is $[x;y]\to[x;2y]$.

$$G^{(D)}(A)\approx\exp(10.4184)\approx 33470\ \mu\mathrm{m}^D \tag{40}$$

according to box counting method and

$$G^{(D)}(A)\approx 33365\ \mu\mathrm{m}^D \tag{41}$$

according to power function method. For the affine representation B of the curve A, these values are

$$G^{(D)}(B)\approx\exp(10.8730)\approx 52733\ \mu\mathrm{m}^D \tag{42}$$

according to box counting method and

$$G^{(D)}(B)\approx 52739\ \mu\mathrm{m}^D \tag{43}$$

according to power function method.

For testing of the power function method, following fractals has been chosen: Koch curve, Sierpinski triangle and Sierpinski square (see previous example). The subsequent set (triangle) is constructed as the union of three affine copies of itself, matrices of the affinities—see Equation (21)—are

$$\boldsymbol{F}_1=\begin{pmatrix}0.36 & 0.48\\ 0.48 & -0.36\end{pmatrix};\ \boldsymbol{F}_2=\begin{pmatrix}0.36 & -0.48\\ -0.48 & -0.36\end{pmatrix};\ \boldsymbol{F}_3=\begin{pmatrix}-0.28 & 0\\ 0 & 0.28\end{pmatrix} \tag{44}$$

(vectors $\boldsymbol{v}_i$ are irrelevant for its dimension) then it implies from (38)

$$\left(\sqrt{|\det\boldsymbol{F}_1|}\right)^D+\left(\sqrt{|\det\boldsymbol{F}_2|}\right)^D+\left(\sqrt{|\det\boldsymbol{F}_3|}\right)^D=1 \tag{45}$$

in our case

$$\left(\sqrt{0.36}\right)^D+\left(\sqrt{0.36}\right)^D+\left(\sqrt{0.0784}\right)^D=1 \tag{46}$$

and $D=1.622339\cdots$

This triangle is self-affine, however it also holds

$$\boldsymbol{F}_1\boldsymbol{F}_1^{\mathrm{T}} = \boldsymbol{F}_2\boldsymbol{F}_2^{\mathrm{T}} = 0.6^2 \cdot \boldsymbol{I};\ \ \boldsymbol{F}_3\boldsymbol{F}_3^{\mathrm{T}} = 0.28^2 \cdot \boldsymbol{I} \tag{47}$$

It means that this fractal is not only self-affine but also self-similar. It consists of two contractions with $\lambda_1 = \lambda_2 = 0.36$ and one contraction with $\lambda_3 = 0.28$. Therefore, we can also use Equation (26)

$$0.6^D + 0.6^D + 0.28^D = 1 \tag{48}$$

It is the same equation as (46) and gives the same result. This fractal is illustrated in Figure 6 on the left and it is called "subsequent triangle" in Table 2.

As the next fractal, a self-affine set is constructed (see Figure 6 on the right, it is named as "self-affine square" in Table 2). It contains five affine copies of itself, matrices of the affinities are

$$\boldsymbol{F}_1 = \boldsymbol{F}_2 = \boldsymbol{F}_3 = \boldsymbol{F}_4 = \boldsymbol{F}_5 = \begin{pmatrix} \frac{1}{3} & 0 \\ 0 & \frac{1}{2} \end{pmatrix} \tag{49}$$

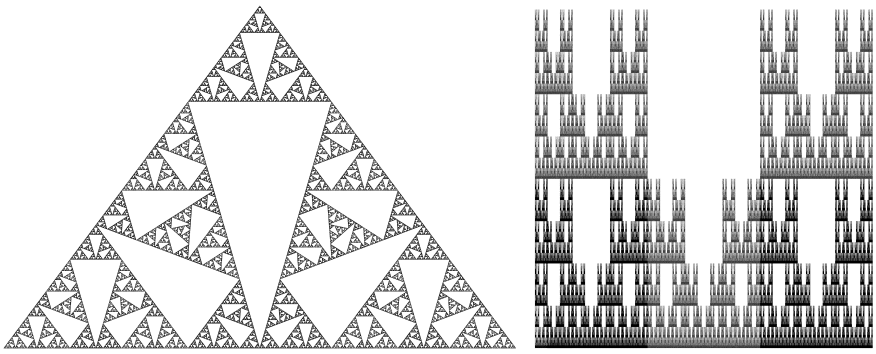

Figure 6. The self-affine triangle and self-affine square.

Table 2. The theoretical dimension of some self-similar and self-affine fractals and the dimension estimated by the power function method.

	self-	theoretical	Dimension estimated	error (%)
Koch curve	-similary	$\frac{\ln 4}{\ln 3} \approx 1.26185$	1.26377	0.152
Sierpinski triangle	-similary	$\frac{\ln 3}{\ln 2} \approx 1.58496$	1.58466	0.019
Sierpinski square	-similary	$\frac{\ln 8}{\ln 3} \approx 1.89279$	1.88729	0.291
Subsequent triangle	-similary	1.62234	1.62342	0.067
Self-affine square	-affine	1.79649	1.79134	0.287
Barnsley fern	-affine	1.76462	1.76249	0.121
Tree	-affine	1.81616	1.80511	0.612
Sea horse	-affine	1.79616	1.78110	0.846

its dimension is

$$\sum_{i=1}^{5}\left(\sqrt{|\det \boldsymbol{M}_i|}\right)^D = 1 \Rightarrow 5\cdot\left(\sqrt{\frac{1}{6}}\right)^D = 1 \Rightarrow D = 2\cdot\frac{\ln 5}{\ln 6} \approx 1.796488\cdots \tag{50}$$

Sixth set in Table 2 is the Barnsley fern (see Figure 7 on the left), it has the affinity matrices

$$\boldsymbol{F}_1 = \begin{pmatrix} 0.01 & 0 \\ 0 & 0.2 \end{pmatrix}; \boldsymbol{F}_2 = \begin{pmatrix} 0.2 & 0.2 \\ -0.3 & 0.2 \end{pmatrix}; \boldsymbol{F}_3 = \begin{pmatrix} -0.1 & 0.3 \\ 0.3 & 0.2 \end{pmatrix}; \boldsymbol{F}_4 = \begin{pmatrix} 0.83 & -0.05 \\ 0.05 & 0.83 \end{pmatrix} \tag{51}$$

According to (37) its dimension is $D = 1.764625\cdots$

Seveth tested fractal is a tree (see Figure 7 in the middle) with matrices

$$\begin{aligned} \boldsymbol{F}_1 &= \begin{pmatrix} 0.195 & -0.488 \\ 0.344 & 0.443 \end{pmatrix}; \ \boldsymbol{F}_2 = \begin{pmatrix} 0.462 & 0.414 \\ -0.252 & 0.361 \end{pmatrix}; \\ \boldsymbol{F}_3 &= \begin{pmatrix} -0.058 & -0.070 \\ 0.453 & -0.111 \end{pmatrix}; \ \boldsymbol{F}_4 = \begin{pmatrix} -0.637 & 0 \\ 0 & 0.501 \end{pmatrix} \end{aligned} \tag{52}$$

and dimension $D = 1.816162\cdots$

The last fractal-"sea horse" has matrices

$$\boldsymbol{F}_1 = \begin{pmatrix} 0.8 & 0.3 \\ -0.3 & 0.8 \end{pmatrix}; \ \boldsymbol{F}_2 = \begin{pmatrix} -0.3 & 0.3 \\ -0.4 & -0.3 \end{pmatrix} \tag{53}$$

and dimension $D = 1.796166\cdots$ (see Figure 7 on the right).

In Table 2, we can compare these theoretical dimensions of previous eight sets with the dimension which was estimated by the power function method. Data was generated by the IFS method (original resolution 4096×4096 pixels). It is clear that the results of this method are sufficiently precise for both types of fractals.

7. Estimation of Hausdorff Dimension of Barton Profiles

Some authors alerts, that any fractal dimension itself cannot be used for roughness modelling (see [7] [28] [29] [30] for example). It is also clear from the example in Section 2 and from Figure 2. We illustrate this fact also in the case of the Barton Profile.

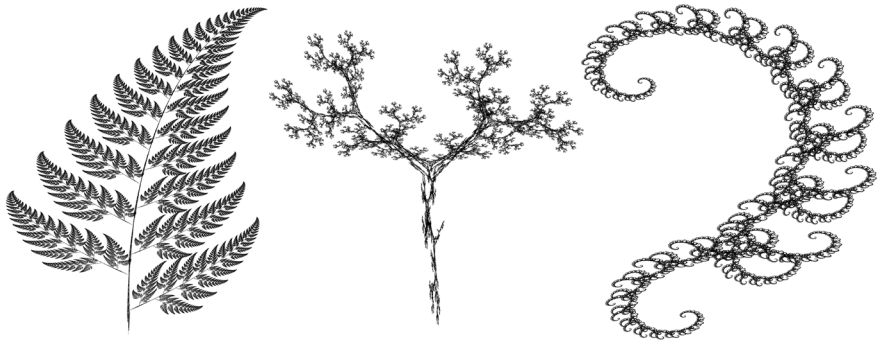

Figure 7. The self-affine fractals—fern, tree and sea horse.

In Figure 8, we can see the original of fourth Barton profile (K) and its scalings $L:[x;y]\to[x;5y]$; $M:[x;y]\to[x;10y]$. These three profiles have been measured by the power function method with the same parameters.

These measurement are graphically represented in Figure 9. For all three profiles, approximately the same dimension has been measured.

8. *JRC* Estimators

As is clear from previous text, *JRC* depends not only on the fractal dimension, but also on its statistical variability. Remember that the important variability characteristics are:

The square root of average of the squared differences from the mean, *i.e.*

$$\sigma(n)=\sqrt{\frac{1}{n}\sum_{i=1}^{n}(x_i-\bar{x})^2} \tag{54}$$

where n is the number of elements of the set, x_i are its elements and $\bar{x}$ is arithmetic mean (standard deviation) and the arithmetic mean of absolute values of differences between elements of statistical sets and their arithmetic mean, *i.e.*

$$\rho(n)=\frac{1}{n}\sum_{i=1}^{n}|x_i-\bar{x}| \tag{55}$$

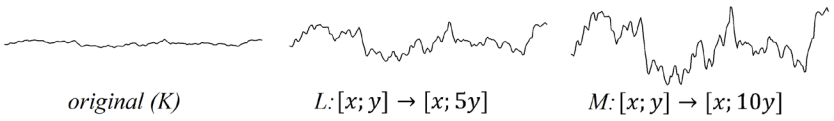

Figure 8. The fourth Barton profile and its affine copies.

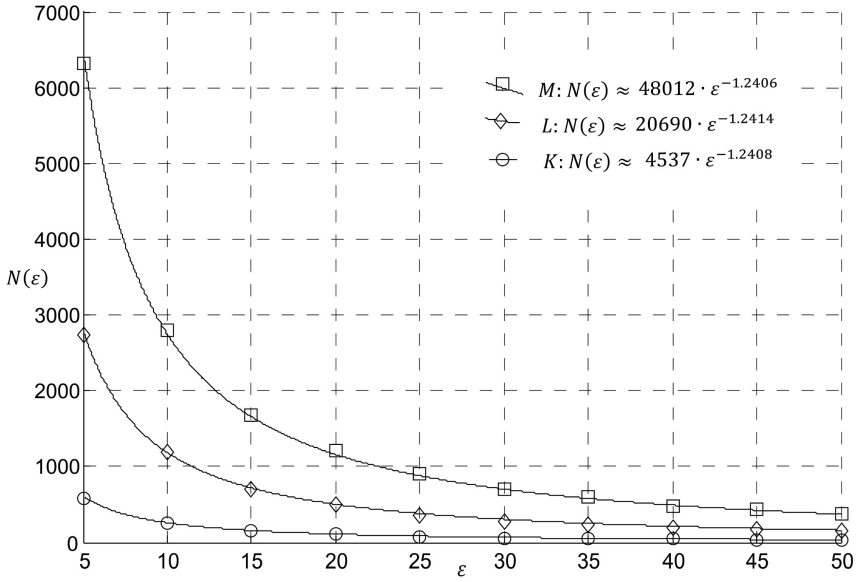

Figure 9. Hausdorff dimension and grid measures of the fourth Barton profile (K) and its affine representations K, M. Power-function method, used affinities are $[x;y]\to[x;5y]$ or $[x;y]\to[x;10y]$ respectively.

(average deviation).

The Hurst exponent is directly related to the fractal dimension, which measures the smoothness of a surface, or, in our case, the smoothness of a rock profiles. The relationship between the fractal dimension D and the Hurst exponent H, is given by

$$H = n + 1 - D \tag{56}$$

where n is the topological dimension of the measured set (see (59) for example). The Equation (56)—see [31] or [32] for proof—enables to compare the roughness in different topological dimensions and also to compare the standard Barton $2D$ profile with the real $3D$ profiles to be measured. Therefore, a roughness estimator can be designed to be able to determine the *JRC* in different topological dimensions, *i.e.* the *JRC* of fractal curves and the *JRC* of fractal surfaces as well. Therefore, it works with the Hurst exponent for which values is $H \in \langle 0;1 \rangle$ in both cases instead the fractal dimension for which is $D \in \langle 1;2 \rangle$ in case of the fractal curves and $D \in \langle 2;3 \rangle$ in case of the fractal surfaces.

The *JRC* is given not only by the Hurst exponent but also by heights of curve or surface irregularities. These irregularities can be quantified using the standard deviation (54) or average deviation (55).

Increasing irregularities heights denotes increasing of the *JRC* and conversely. Therefore, the standard deviation (53) or average deviation (55) must be placed to numerator of expression to be found. Thus, corresponding formulas are:

$$E_\sigma = \frac{\sigma}{H} \tag{57}$$

(standard deviation estimator)

$$E_\rho = \frac{\rho}{H} \tag{58}$$

(average deviation estimator), σ and ρ are given by (54), (55).

For *JRC* estimation of any profile or surface, so called characteristic functions $JRC_\sigma(E_\sigma)$; and $JRC_\rho(E_\rho)$ have been constructed. Each of them has been designed to pass through the origin of the coordinate system (if surface variability is equal to zero then surface is completely smooth horizontal plane, Hurst exponent is equal to one and $JRC = 0$). Each of them must be non-negative and increasing (as the *JRC*). Each of them must describe a dependence of the *JRC* on E_σ or E_ρ respectively and has been found using of the least squares method.

9. Estimation of the Characteristic Functions

In this section, Hausdorff dimension of all standard Barton profiles has been estimated using power function method and values of E_σ; E_ρ for the standard Barton profiles have been measured. Results of these measurements are summarized in **Table 3**.

For *JRC* estimation of any profile or surface, so called characteristic functions $JRC_\sigma(E_\sigma)$; and $JRC_\rho(E_\rho)$ have been constructed. Each of them has been de-

Table 3. Hausdorff dimensions, Hurst exponents, standard deviations, average deviations, standard deviation estimators and average deviation estimators of the standard Barton profiles. In the last column, "*JRC*" assigned to corresponding dimension by present used and often cited expression (4).

No	Dim	Hurst	σ	ρ	E_σ	E_ρ	*JRC*	*JRC* (2)
1	1.023	0.977	0.081	0.030	0.083	0.031	1	17.253
2	1.147	0.853	0.159	0.124	0.187	0.146	3	−1256.586
3	1.192	0.808	0.334	0.272	0.414	0.337	5	−2291.114
4	1.241	0.759	0.498	0.397	0.656	0.524	7	−3764.184
5	1.286	0.714	0.646	0.552	0.904	0.773	9	−5435.295
6	1.314	0.686	0.894	0.760	1.303	1.108	11	−6628.901
7	1.335	0.665	1.134	0.933	1.705	1.403	13	−7601.534
8	1.357	0.643	1.416	1.186	2.202	1.844	15	−8691.665
9	1.365	0.635	1.641	1.460	2.585	2.299	17	−9106.136
10	1.398	0.602	1.910	1.693	3.172	2.813	19	−10917.635

signed to pass through the origin of the coordinate system (if surface variability is equal to zero then surface is completely smooth horizontal plane, Hurst exponent is equal to one and $JRC = 0$). Each of them must be non-negative and increasing (as the *JRC*). Each of them must describe a dependence of the *JRC* on E_σ or E_ρ respectively and has been found using of the least squares method.

Equations of these functions are

$$JRC_\sigma\left(E_\sigma\right) = 9.186 \cdot E_\sigma^{0.651} \tag{59}$$

(see **Figure 10**)

$$JRC_\rho\left(E_\rho\right) = 10.095 \cdot E_\rho^{0.612} \tag{60}$$

(see **Figure 11**).

10. Estimation of the *JRC* Index of Real Samples

All geological data used in this paper has been acquired by prof. Tomáš Ficker from the Faculty of Civil Engineering of our university. All the samples are specimens of limestone (locality Brno-Hády, Czech Republic). All processing and visualization of these data have been made by original author's software. For more information of these reconstructions and visualizations see [33] [34] [35] [36].

In this section, limestone surfaces in **Figure 12** have been used for testing.

If we presume that the surface is isotropic, *i.e.* its joint roughness coefficient is not dependent on the direction, one *JRC* may be assigned to $3D$ surface. In this case, the surface is covered by diminishing cubes (thickening spatial grid) for estimation of the Hausdorff dimension using power function method according to (21). There is $D \in (2;3)$, $n = 3$ and $H \in (0;1)$ in expression (56) which serves for *JRC* estimation. This *JRC* we call the global *JRC*.

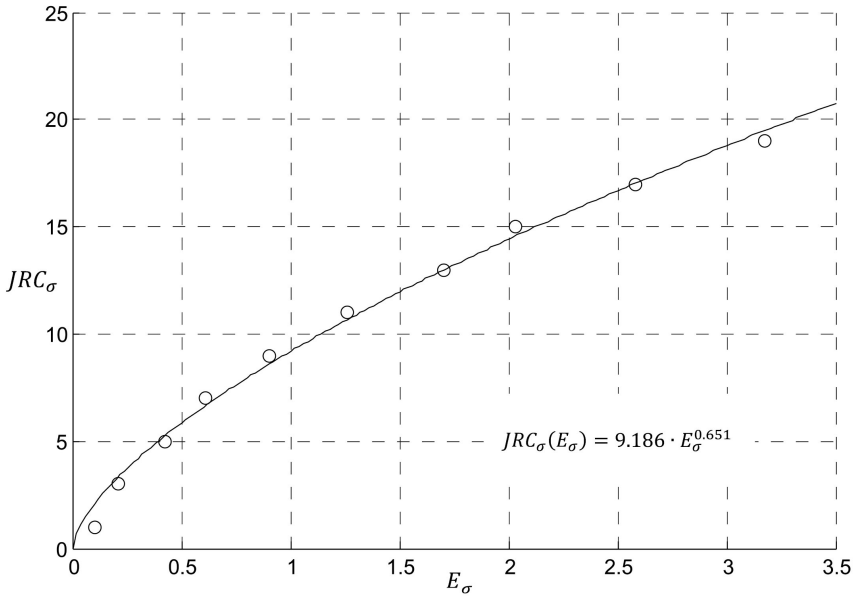

Figure 10. The *JRC* as function of standard deviation estimator E_σ —see (59).

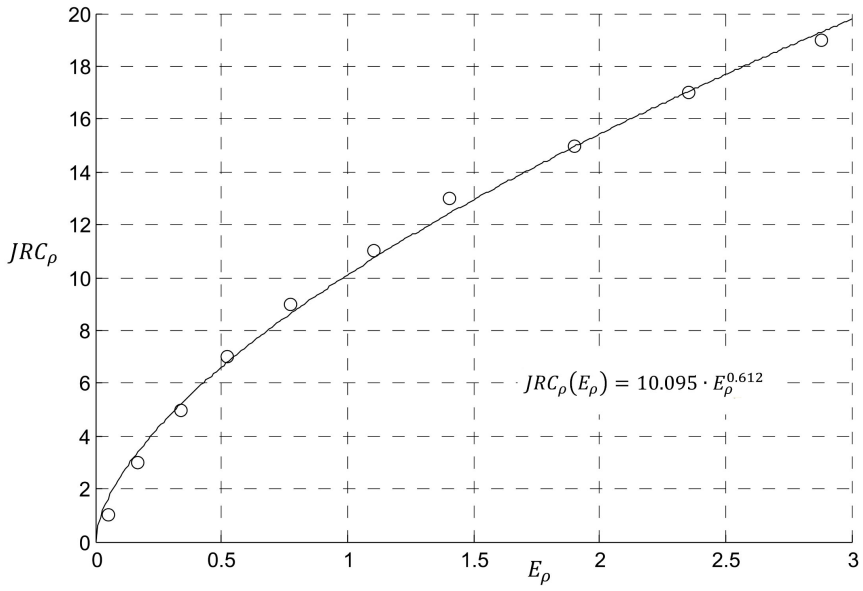

Figure 11. The *JRC* as function of average deviation estimator E_ρ —see (60).

However, the *JRC* may have different values along different orientations on a rock surface. In this case, we can choose the direction of the *JRC* estimation. The profile curve is generated for selected direction and its Hausdorff dimension is measured by power function method according to (11). There is $D \in (1;2)$, $n = 2$ in expression (56) and also $H \in (0;1)$ in expressions (57), (58) which serves for *JRC* estimation. This *JRC* we call the directional *JRC*.

The global *JRC* has been estimated for the samples $A; B; C; D$ from **Figure 12**. For each of them, thirty six directions have been chosen for estimation of the directional *JRC*. These directions are illustrated in **Figure 13** for the sample *D*.

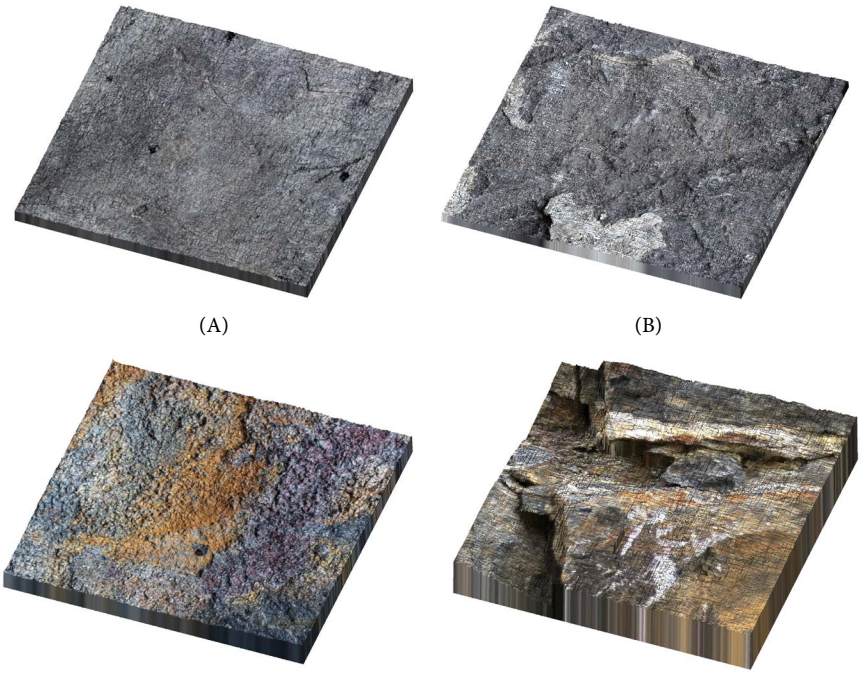

(A) (B)

(C) (D)

Figure 12. The limestone samples under tests. 3*D* reconstruction from the series of partially focused images (see [33] [34] [35] [36] for more information).

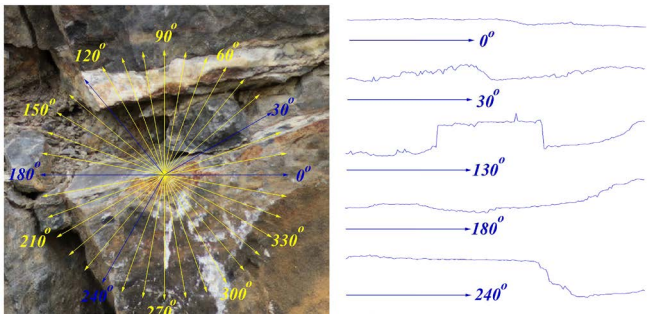

Figure 13. Directions that were used for estimation of the directional *JRCs* of the samples $A; B; C; D$. The profiles marked as blue on the left are illustrated on the right.

Results of these measurements are summarized in **Table 4** and **Table 5** and graphically represented in **Figures 14-19**. In **Figure 14** we can see dimension estimation of the profile with direction 0˚ on the sample *A*, the profile with direction 90˚ on the sample *B*, the profile with direction 100˚ on the sample *C* and the profile with direction 200˚ on the sample *D* using box counting method. In **Figure 15**, there are illustrated estimation of the same profiles using power function method.

In the second last row of **Table 2** and **Table 3**, averages of Hausdorff dimensions, Hurst exponents, standard deviations, average deviations and *JRCs* in individual directions are stated. In the last row of **Table 4** and **Table 5**, the Hausdorff dimension, Hurst exponent, standard deviation, average deviation and *JRCs* measured over the whole surface are stated. In **Figures 16-19**.

Table 4. Hausdorff dimensions estimated by power function method, Hurst exponents, standard deviations, average deviations and directional *JRCs* of the samples A, B. Averaged values on these quantities are in the second last row, corresponding values of the global *JRCs* are in the last row.

Angle	Sample *A*						Sample *B*					
	Dim	Hurst	σ	ρ	JRC_σ	JRC_ρ	Dim	Hurst	σ	ρ	JRC_σ	JRC_ρ
0˚	1.330	0.670	1.028	1.076	5.523	5.481	1.280	0.720	1.405	1.519	6.450	6.464
10˚	1.381	0.619	0.960	1.037	5.560	5.620	1.269	0.731	1.484	1.543	6.622	6.469
20˚	1.448	0.552	0.934	0.989	5.886	5.856	1.195	0.805	1.706	1.854	6.806	6.818
30˚	1.395	0.605	0.914	0.971	5.468	5.479	1.250	0.750	1.894	2.040	7.630	7.545
40˚	1.373	0.627	0.808	0.869	4.931	5.011	1.250	0.750	1.893	2.133	7.624	7.751
50˚	1.403	0.597	0.698	0.668	4.632	4.403	1.237	0.763	1.480	1.941	6.425	7.242
60˚	1.337	0.663	0.656	0.650	4.156	4.060	1.262	0.738	1.348	1.586	6.183	6.539
70˚	1.316	0.684	0.551	0.538	3.638	3,553	1.250	0.750	1.141	1.328	5.492	5.814
80˚	1.218	0.782	0.584	0.562	3.463	3.363	1.214	0.786	1.385	1.416	6.040	5.875
90˚	1.277	0.723	0.603	0.556	3.722	3.504	1.268	0.732	1.141	1.204	5.577	5.558
100˚	1.448	0.552	0.505	0.502	3.951	3.879	1.299	0.701	0.807	1.255	4.586	5.854
110˚	1.367	0.633	0.581	0.604	3.959	3.996	1.264	0.736	0.775	1.303	4.328	5.813
120˚	1.376	0.624	0.613	0.694	4.139	4.385	1.381	0.619	0.803	1.063	4.954	5.708
130˚	1.260	0.740	0.918	0.914	4.811	4.674	1.262	0.738	0.838	1.262	4.546	5.692
140˚	1.289	0.711	1.074	1.081	5.466	5.299	1.466	0.534	0.936	1.066	6.018	6.252
150˚	1.262	0.738	1.211	1.231	5.768	5.607	1.313	0.687	1.248	1.322	6.163	6.114
160˚	1.296	0.704	1.213	1.212	5.952	5.713	1.350	0.650	1.522	1.500	7.265	6.828
170˚	1.244	0.756	1.202	1.214	5.651	5.479	1.316	0.684	1.620	1.705	7.314	7.152
180˚	1.306	0.694	1.036	0.983	5.424	5.075	1.268	0.732	2.141	2.344	8.385	8.327
190˚	1.286	0.714	0.933	0.915	4.974	4.775	1.334	0.666	2.241	2.427	9.189	9.012
200˚	1.279	0.721	0.930	0.868	4.934	4.601	1.249	0.751	2.541	2.683	9.220	8.903
210˚	1.246	0.754	0.889	0.828	4.653	4.349	1.233	0.767	2.777	2.902	9.629	9.213
220˚	1.283	0.717	0.717	0.708	4.185	4.079	1.143	0.857	3.139	3.692	9.701	9.970
230˚	1.334	0.666	0.669	0.600	4.196	3.858	1.141	0.859	3.653	4.028	10.689	10.498
240˚	1.305	0.695	0.576	0.554	3.705	3.580	1.066	0.934	4.256	4.565	11.179	10.766
250˚	1.326	0.674	0.541	0.510	3.629	3.470	1.184	0.816	4.395	4.850	12.460	12.124
260˚	1.291	0.709	0.474	0.443	3.222	3.090	1.084	0.916	4.730	5.288	12.126	11.913
270˚	1.273	0.727	0.488	0.434	3.234	3.006	1.179	0.821	4.651	5.155	12.878	12.538
280˚	1.368	0.632	0.480	0.426	3.500	3.234	1.107	0.893	4.713	5.053	12.296	11.768
290˚	1.350	0.650	0.511	0.474	3.581	3.393	1.094	0.906	4.410	4.679	11.664	11.130
300˚	1.350	0.650	0.541	0.525	3.715	3.610	1.180	0.820	4.010	4.349	11.708	11.318
310˚	1.348	0.652	0.631	0.636	4.098	4.048	1.116	0.884	3.858	4.270	10.871	10.690
320˚	1.359	0.641	0.684	0.673	4.364	4.232	1.124	0.876	3.633	4.060	10.521	10.428
330˚	1.320	0.680	0.819	0.781	4.723	4.471	1.165	0.835	3.412	3.833	10.421	10.367
340˚	1.351	0.649	0.879	0.868	5.092	4.903	1.218	0.782	2.421	2.281	8.700	7.867
350˚	1.340	0.660	0.998	0.996	5.471	5.276	1.280	0.720	1.418	1.804	6.491	7.177
Aver.	1.326	0.674	0.774	0.766	4.538	4.400	1.228	0.772	2.441	2.720	8.370	8.424
3D	2.312	0.688	0.783	0.761	4.549	4.369	2.205	0.795	2.349	2.468	8.443	8.174

Table 5. Hausdorff dimensions estimated by power function method, Hurst exponents, standard deviations, average deviations and directional *JRCs* of samples C, D. Averaged values on these quantities are in the second last row, corresponding values of $3D$ surface are in the last row.

Angle	Sample C						Sample D					
	Dim	Hurst	σ	ρ	JRC_σ	JRC_ρ	Dim	Hurst	σ	ρ	JRC_σ	JRC_ρ
0˚	1.318	0.682	3.994	4.156	13.149	12.306	1.087	0.913	2.765	3.232	8.579	8.852
10˚	1.459	0.541	3.319	3.689	13.564	13.185	1.109	0.891	3.404	3.933	9.970	10.119
20˚	1.494	0.506	2.909	3.495	12.992	13.275	1.161	0.839	3.511	4.508	10.578	11.403
30˚	1.455	0.545	3.500	3.411	13.968	12.514	1.157	0.843	3.517	4.607	10.555	11.518
40˚	1.401	0.599	3.888	4.073	14.063	13.158	1.156	0.844	4.151	4.693	11.743	11.640
50˚	1.372	0.628	4.749	4.507	15.526	13.598	1.150	0.850	4.427	4.776	12.192	11.718
60˚	1.399	0.601	4.283	4.656	14.945	14.246	1.117	0.883	4.449	4.821	11.932	11.514
70˚	1.346	0.654	4.284	4.504	14.137	13.253	1.116	0.884	4.057	4.713	11.232	11.349
80˚	1.293	0.707	4.260	4.166	13.402	12.064	1.105	0.895	3.730	4.286	10.549	10.631
90˚	1.415	0.585	3.120	3.356	12.385	11.872	1.132	0.868	2.953	3.397	9.248	9.406
100˚	1.481	0.519	2.142	2.488	10.491	10.645	1.094	0.906	4.227	4.147	11.351	10.346
110˚	1.385	0.615	1.939	2.104	8.809	8.670	1.086	0.914	5.082	4.872	12.721	11.350
120˚	1.396	0.604	1.865	1.846	8.689	8.099	1.103	0.897	5.948	6.555	14.253	13.741
130˚	1.419	0.581	1.783	1.809	8.656	8.190	1.047	0.953	7.430	10.987	15.831	18.124
140˚	1.474	0.526	1.609	1.819	8.636	8.729	1.142	0.858	8.048	11.253	17.850	19.603
150˚	1.398	0.602	1.705	1.797	8.220	7.986	1.059	0.941	9.160	12.247	18.281	19.509
160˚	1.338	0.662	2.288	2.540	9.345	9.295	1.062	0.938	8.338	10.554	17.234	17.857
170˚	1.357	0.643	2.630	2.903	10.420	10.256	1.061	0.939	6.999	8.614	15.376	15.776
180˚	1.270	0.730	3.976	4.447	12.550	12.307	1.050	0.950	5.728	7.242	13.408	14.104
190˚	1.279	0.721	4.487	4.769	13.679	12.933	1.082	0.918	6.110	6.520	14.293	13.510
200˚	1.256	0.744	3.871	3.862	12.179	11.164	1.076	0.924	6.594	7.103	14.948	14.170
210˚	1.341	0.659	2.901	2.715	10.938	9.709	1.104	0.896	7.429	9.604	16.480	17.344
220˚	1.389	0.611	2.006	1.724	9.038	7.712	1.044	0.956	9.084	12.200	17.998	19.277
230˚	1.464	0.536	1.476	1.475	8.069	7.599	1.059	0.941	9.968	12.504	19.312	19.758
240˚	1.293	0.707	2.257	2.359	8.878	8.539	1.047	0.953	9.273	12.537	18.282	19.641
250˚	1.359	0.641	2.206	2.253	9.322	8.813	1.061	0.939	6.954	7.819	15.318	14.881
260˚	1.299	0.701	2.556	3.251	9.680	10.432	1.126	0.874	4.916	4.973	12.810	11.803
270˚	1.258	0.742	2.704	3.393	9.675	10.343	1.156	0.844	3.479	2.549	10.476	8.038
280˚	1.269	0.731	3.062	3.612	10.589	10.841	1.168	0.832	2.007	1.992	7.402	6.981
290˚	1.283	0.717	3.271	4.590	11.189	12.685	1.203	0.797	1.653	1.454	6.711	5.918
300˚	1.229	0.771	4.576	6.858	13.262	15.480	1.223	0.777	2.021	2.052	7.771	7.407
310˚	1.273	0.727	5.372	7.117	15.294	16.415	1.219	0.781	2.294	2.474	8.410	8.274
320˚	1.255	0.745	5.775	7.138	15.770	16.198	1.131	0.869	2.798	3.073	8.924	8.845
330˚	1.224	0.776	5.668	6.636	15.178	15.120	1.154	0.846	2.435	2.700	8.303	8.315
340˚	1.298	0.702	4.931	5.576	14.793	14.452	1.111	0.889	2.514	2.735	8.205	8.128
350˚	1.376	0.624	4.124	4.400	14.221	13.445	1.089	0.911	2.406	2.584	7.849	7.736
Aver.	1.350	0.650	3.319	3.708	11.825	11.542	1.112	0.888	4.996	5.953	12.399	12.461
3D	2.398	0.602	3.356	3.612	12.739	12.193	2.081	0.919	5.144	5.487	12.775	12.159

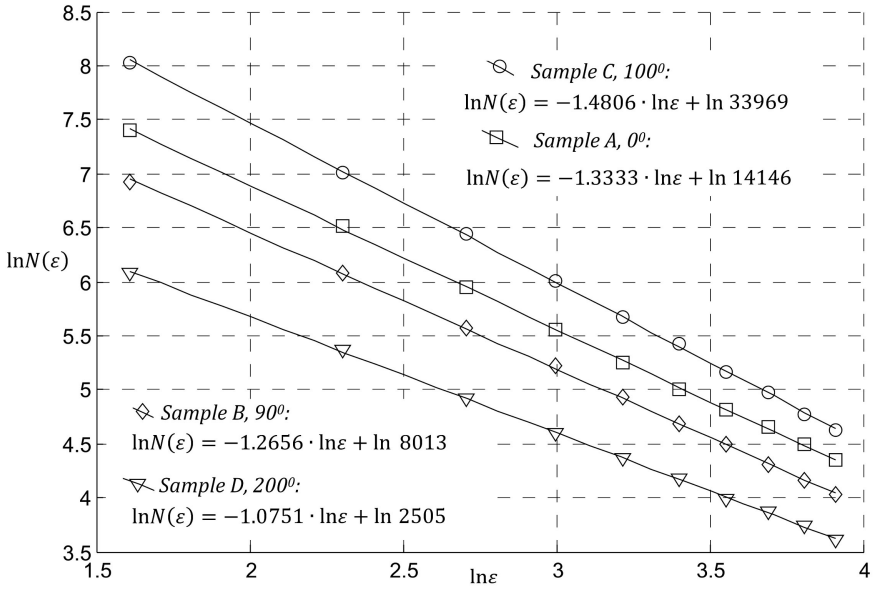

Figure 14. Graphical representation of profile dimension estimation: sample *A*, direction 0˚, sample *B*, direction 90˚, sample *C* direction 100˚, sample *D*, direction 200˚ (box counting method).

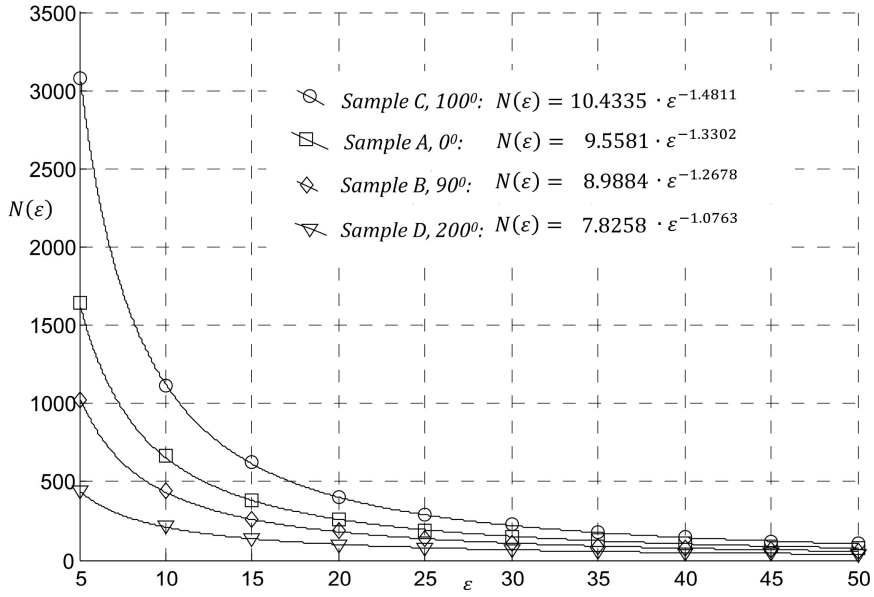

Figure 15. Graphical representation of profile dimension estimation: sample *A*, direction 0˚, sample *B*, direction 90˚, sample *C* direction 100˚, sample *D*, direction 200˚ (power function method).

1) Directional JRC_σ is marked as red solid
2) Directional JRC_ρ is marked as green solid
3) Average of directional JRC_σ is marked as red dashed
4) Average of directional JRC_ρ is marked as green dashed
5) Global JRC_σ is marked as blue
6) Global JRC_ρ is marked as dark pink

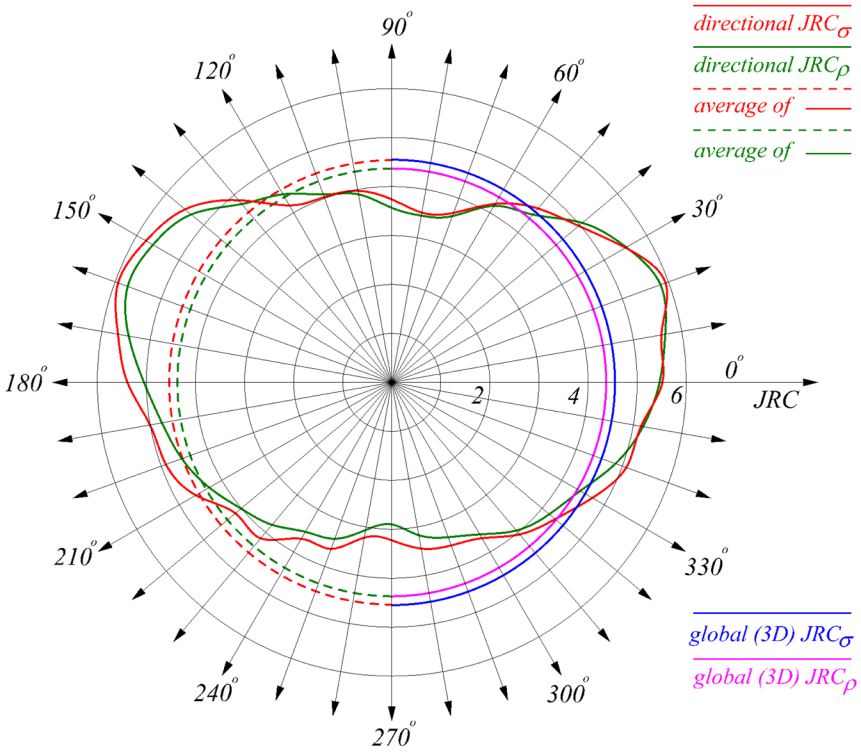

Figure 16. Directional JRC_σ and JRC_ρ, average of directional JRC_σ and JRC_ρ, global (3) JRC_σ and JRC_ρ of the sample *A*.

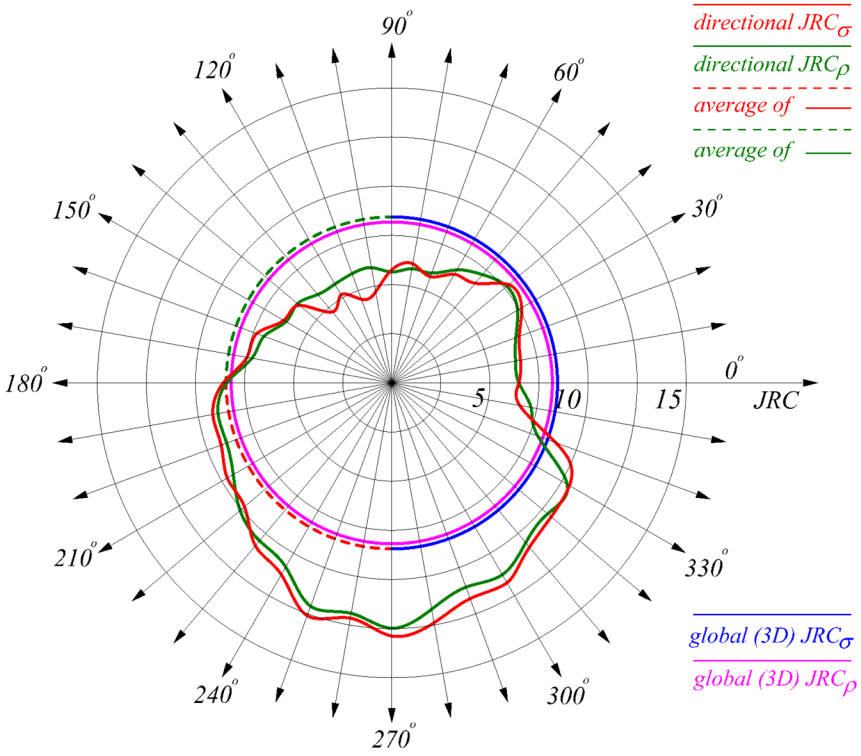

Figure 17. Directional JRC_σ and JRC_ρ, average of directional JRC_σ and JRC_ρ, global (3*D*) JRC_σ and JRC_ρ of the sample *B*.

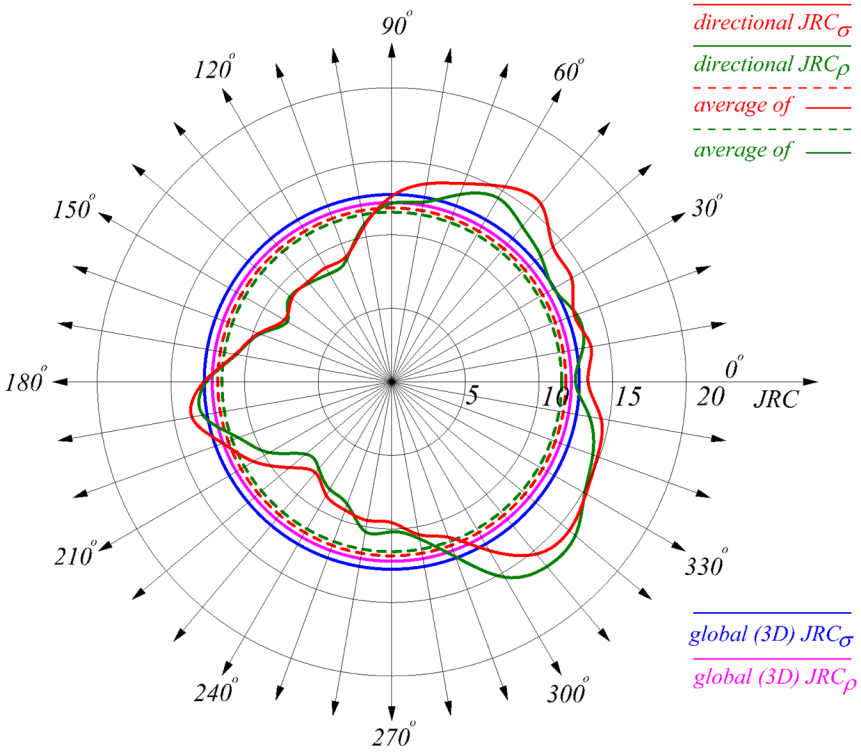

Figure 18. Directional JRC_σ and JRC_ρ, average of directional JRC_σ and JRC_ρ, global (3*D*) JRC_σ and JRC_ρ of the sample *C*.

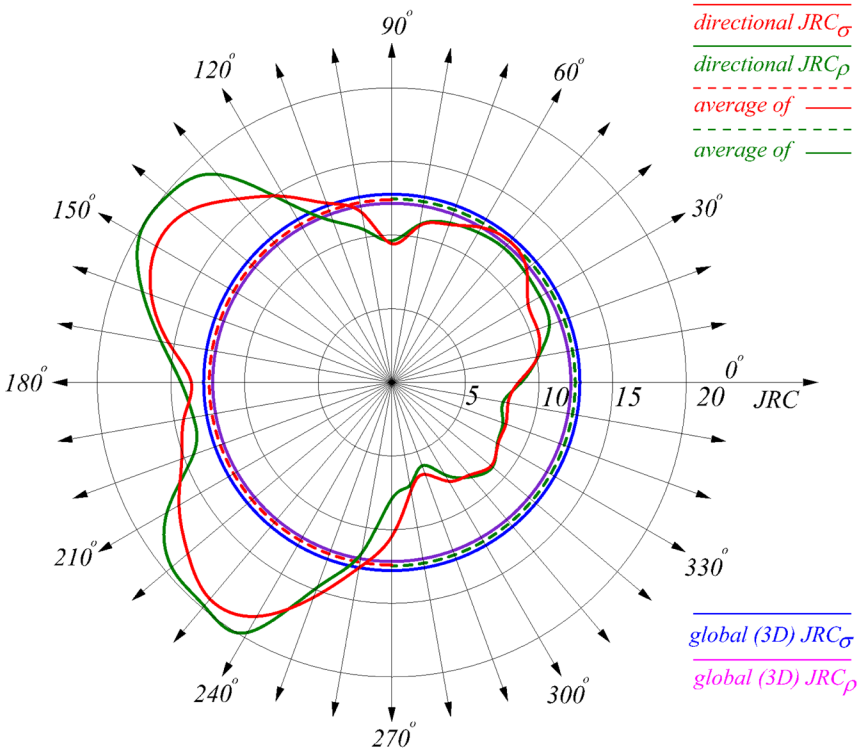

Figure 19. Directional JRC_σ and JRC_ρ, average of the directional JRC_σ and JRC_ρ, global (3*D*) JRC_σ and JRC_ρ of the sample *D*.

11. Conclusions

This article showed that the fractal dimension does not dependent on scaling. Therefore, there exists no direct relationship between the fractal dimension and *JRC*, any fractal dimension itself cannot be used for roughness modelling. *JRC* depends not only on the fractal dimension, but also on other variables. In this paper, statistical variability of the surface has been used. Increasing irregularities heights denote increasing of the *JRC* and conversely. Therefore, the standard deviation or average deviation must be placed to numerator of the *JRC* estimator.

The *JRC* estimator is designed to be able to determine the *JRC* in different topological dimensions, *i.e.* the *JRC* of fractal curves and the *JRC* of fractal surfaces as well. Therefore, Hurst exponent was used instead the fractal dimension. Increasing dimension denotes increasing roughness and decreasing Hurst exponent. Conversely-decreasing dimension denotes decreasing roughness and increasing Hurst exponent. For this reason, Hurst exponent must be placed to denominator of the *JRC* is estimator.

The estimator enables fully automatic estimation of the isotropic (global) joint roughness coefficient (this assumes independence on the direction) and also anisotropic (directional) joint roughness coefficient (which value depends on the direction). In case of the isotropic *JRC*, the estimator works with whole surface which is topologically two-dimensional, in case of the anisotropic *JRC*, the estimator works in chosen direction, *i.e.* with topologically one-dimensional profile. The average of the anisotropic *JRC* estimated for 360˚ with step 10˚ is approximately equal to the isotropic (global) *JRC*.

Acknowledgements

This work was supported by the Project LO1202 by financial means from the Ministry of Education, Youth and Sports under the National Sustainability Programme I.

The author thanks to prof. Tomáš Ficker from the Faculty of Civil Engineering of Brno University of Technology for the provided data.

References

[1] Barton, N. and Choubey, V. (1977): The Shear Strength of Rock Joints in Theory and Practice. *Rock Mechanics*, **10**, 1-65. https://doi.org/10.1007/BF01261801

[2] Tse, R. and Cruden, D.M. (1979) Estimating Joint Roughness Coefficients. *International Journal of Rock Mechanics and Mining Sciences*, **16**, 303-307. https://doi.org/10.1016/0148-9062(79)90241-9

[3] Maerz, N.H., Franklin, J.A., and Bennett, C.P. (1990) Joint Roughness Measurement Using Shadow Profilometry. *International Journal of Rock Mechanics and Mining Sciences*, **27**, 329-343. https://doi.org/10.1016/0148-9062(90)92708-M

[4] Hong, E.-S., Lee, I.-M. and Lee, J.-S. (2006) Measurement of Rock Joint Roughness by 3D Scanner. *Geotechnical Testing Journal*, **29**, 1-8.

[5] Hong, E.-S., Lee, I.-M. and Lee, J.-S. (2008) Underestimation of Roughness in

Rough Rock Joints. *International Journal for Numerical and Analytical Methods in Geomechanics*, **32**, 1385-1403. https://doi.org/10.1002/nag.678

[6] Fardin, N., Stephansson, O. and Jing, L. (2001) The Scale Dependence of Rock Joint Surface Roughness. *International Journal of Rock Mechanics and Mining Sciences*, **38**, 659-669. https://doi.org/10.1016/S1365-1609(01)00028-4

[7] Brown, S.R. and Scholz, C.H. (1985) Broad Band Width Study of the Topography of Natural Rock Surfaces. *Journal of Geophysics Research*, **90**, 12575-12582. https://doi.org/10.1029/JB090iB14p12575

[8] Miller, S.M., McWilliams, P.C. and Kerkering, J.C. (1990) Ambiguities in Estimating Fractal Dimensions of Rock Fracture Surfaces. In: Balkema, A.A., Ed., *Proceedings of the* 31*st U.S. Symposium, Colorado School of Mines*, Rotterdam, June 18-20 1990, 471-478.

[9] Power, W.L. and Tullis, T.E. (1991) Euclidean and Fractal Models for the Description of Rock Surface Roughness. *Journal of Geophysical Research*, **96**, 415-424. https://doi.org/10.1029/90JB02107

[10] Huang, S.L., Oelfke, S.M. and Speck, R.C. (1992) Applicability of Fractal Characterization and Modeling to Rock Joint Profiles. *International Journal of Rock Mechanics and Mining Science*, **29**, 89-98. https://doi.org/10.1016/0148-9062(92)92120-2

[11] Poon, C.Y., Sayles, R.S. and Jones, T.A. (1992) Surface Measurement and Fractal Characterization of Naturally Fractured Rocks. *Journal of Physics D: Applied Physics*, **25**, 1269-1275. https://doi.org/10.1088/0022-3727/25/8/019

[12] Odling, N.E. (1994) Natural Fracture Profiles, Fractal Dimension and Joint Roughness Coefficients. *Rock Mechanics*, **27**, 135-153. https://doi.org/10.1007/BF01020307

[13] Den Outer, A., Kaashoek, J.F. and Hack, H.R.G.K. (1995) Difficulties with Using Continuous Fractal Theory for Discontinuity Surfaces. *International Journal of Rock Mechanics and Mining Science*, **32**, 3-10. https://doi.org/10.1016/0148-9062(94)00025-X

[14] Ficker, T. (2016) Fractal Properties of Rock Joint Coefficients. *International Journal of Rock Mechanics & Mining Science*, **94**, 27-31. https://doi.org/10.1016/j.ijrmms.2017.02.014

[15] Lee, Y.H., Carr, J.R., Barr, D.J. and Haas, C.J. (1990) The Fractal Dimension as a Measure of the Roughness of Rock Discontinuity Profiles. *International Journal of Rock Mechanics and Mining Sciences*, **27**, 453-464. https://doi.org/10.1016/0148-9062(90)90998-H

[16] Li, Y. and Huang, R. (2015) Relationship between Joint Roughness Coefficient and Fractal Dimension of Rock Fracture Surfaces. *International Journal of Rock Mechanics and Mining Sciences*, **75**, 15-22. https://doi.org/10.1016/j.ijrmms.2015.01.007

[17] Sanei, M., Faramarzi, L., Goli, S., *et al.* (2015) Development of a New Equation for Joint Roughness Coefficient (JRC) with Fractal Dimension: A Case Study of Bakhtiary Dam Site in Iran. *Arabian Journal of Geosciencies*, **8**, 465-475. https://doi.org/10.1007/s12517-013-1147-3

[18] Li, Y., Oh, J., Mitra, R., *et al.* (2017) A Fractal Model for the Shear Behaviour of Large-Scale Opened Rock Joints. *Rock Mechanics and Rock Engineering*, **50**, 67-79. https://doi.org/10.1007/s00603-016-1088-8

[19] Gneiting, T. and Schlather, M. (2004) Stochastic Models Which Separate Fractal Dimension and Hurst Effect. Cornell University Library. *SIAM Review*, **46**, 269-282.

https://doi.org/10.1137/S0036144501394387

[20] Feder, J. (1988) Fractals. Plenum Press, New York.

[21] Maliverno, A. (1990) A Simple Method to Estimate Fractal Dimension of a Self-Affine Series. *Geophysical Research Letters*, **17**, 1953-1956. https://doi.org/10.1029/GL017i011p01953

[22] Bovil, C. (1996) Fractal Geometry in Architecture and Design. Birkhäuser, Boston. https://doi.org/10.1007/978-1-4612-0843-3

[23] Stamps, A.E. (2002) Fractals, Skylines, Nature and Beauty. *Landscape and Urban Planning*, **60**, 163-184. https://doi.org/10.1016/S0169-2046(02)00054-3

[24] Mandelbrot, B.B. (1967) How Long Is the Coast of Britain? Statistical Self-Similarity and Fractional Dimension. *Science*, **156**, 636-638. https://doi.org/10.1126/science.156.3775.636

[25] Hastings, H. and Sugihara, G. (1993) Fractals—A User's Guide for the Natural Sciences. Oxford University Press, Oxford.

[26] Martišek, D. and Druckmüllerová, H. (2014) Power-Function Method of Fractal Dimension Estimation. 20*th International Conference of Soft Computing Mendel* Brno, 26-27 June 2014, 147-152.

[27] Kulatilake, P.H.S.W., *et al.* (2006) Natural Rock Joint Roughness Quantification through Fractal Techniques. *Geotechnical and Geological Engineering*, **24**, 1181-1202. https://doi.org/10.1007/s10706-005-1219-6

[28] Power, W.L. and Tullis, T.E. (1991) Euclidean and Fractal Models for the Description of Rock Surface Roughness. *Journal of Geophysical Research*, **96**, 415-424. https://doi.org/10.1029/90JB02107

[29] Brown, S.R. (1987) A Note on the Description of Surface Roughness Using Fractal Dimension. *Geophysical Research Letters*, **14**, 1095-1098. https://doi.org/10.1029/GL014i011p01095

[30] Brown, S.R. (1995) Simple Mathematical Model of a Rough Fracture. *Journal of Geophysical Research*, **100**, 5941-5952. https://doi.org/10.1029/94JB03262

[31] Mandelborot, B. (1982) The Fractal Geometry of Nature. W. H. Freeman, San Francisco.

[32] Turcotte, D.L. (1992) Fractals and Chaos in Geology and Geophysics. Cambridge University Press, Cambridge.

[33] Martišek, D. (2002) The 2-D and 3-D Processing of Images Provided by Conventional Microscopes. *Scanning*, **24**, 284-296. https://doi.org/10.1029/94JB03262

[34] Martišek, D. and Druckmüllerová, H. (2014a) Multifocal Image Processing. *Mathematics for Applications*, **3**, 77-90. https://doi.org/10.13164/ma.2014.06

[35] Martišek, D., *et al.* (2015) High-Quality Three-Dimensional Reconstruction and Noise Reduction of Multifocal Images from Oversized Samples. *Journal of Electronic Imaging*, **24**, Article ID: 053029. https://doi.org/10.1117/1.JEI.24.5.053029

[36] Martišek, D. and Druckmüllerová, H. (2017) Registration of Partially Focused Images for 2D and 3D Reconstruction of Oversized Samples. *Scanning*, **2017**, Article ID: 8538215, 8 p.

MEASUREMENT SCIENCE REVIEW, **17**, (2017), No. 6, 273-281

DE GRUYTER OPEN

MEASUREMENT SCIENCE REVIEW

Journal homepage: http://www.degruyter.com/view/j/msr

ISSN 1335-8871

The Enhancement of 3D Scans Depth Resolution Obtained by Confocal Scanning of Porous Materials

Dalibor Martisek, Jana Prochazkova

Institute of Materials Science and Engineering, NETME center, Brno University of Technology, Czech Republic, martisek@fme.vutbr.cz, prochazkova.j@fme.vutbr.cz

The 3D reconstruction of simple structured materials using a confocal microscope is widely used in many different areas including civil engineering. Nonetheless, scans of porous materials such as concrete or cement paste are highly problematic. The well-known problem of these scans is low depth resolution in comparison to the horizontal and vertical resolution. The degradation of the image depth resolution is caused by systematic errors and especially by different random events. Our method is focused on the elimination of such random events, mainly the additive noise. We use an averaging method based on the Lindeberg–Lévy theorem that improves the final depth resolution to a level comparable with horizontal and vertical resolution. Moreover, using the least square method, we also precisely determine the limit value of a depth resolution. Therefore, we can continuously evaluate the difference between current resolution and the optimal one. This substantially simplifies the scanning process because the operator can easily determine the required number of scans.

Keywords: Noise reduction, porous materials, confocal microscope, 3D scans, 3D reconstruction.

1. INTRODUCTION

The 3D reconstruction based on laser scanning confocal microscopy is an indispensable tool for civil engineering. Particularly in civil engineering, many different porous materials must be analysed. Common examples include the micro fractures in the concrete or the cement paste. However, the depth resolution of these scans is substantially influenced by additive noise and other disturbing factors. The described work is a result of cooperation between the Faculty of Civil Engineering and the Faculty of Mechanical Engineering, BUT that is focused on the precise evaluation of the concrete material properties.

In this article, we propose a method that eliminates the vast majority of the additive noise without degradation of useful information. This allows enhancing the depth resolution of the scans to the order comparable with horizontal and vertical resolution. Firstly, we describe the mathematical apparatus of our method. Subsequently, we assess our method with statistical evaluation and compare our results with methods used in common software tools that are provided with the microscopes.

2. SUBJECT & METHODS

2.1. Material and current methods

Our method follows on the recently published work on morphological analysis of fracture surfaces [2], [3] and also, porous materials in [1]. The gist of our work is the improvement of *z*-resolution that determines the quality of the reconstruction. The overview of common approaches used for 3D reconstruction can be found in [6], [9].

The *z*-resolution, i.e. optical sectioning thickness, depends on many factors: the wavelength of the used light, pinhole size, numerical aperture of the objective lens, refractive index of components in the light path, and the assembly of the instrument. The degradation of the *z*-resolution is often caused by systematic errors and by random events. Systematic errors, for example imperfections of the lens, light diffraction, are not random so that they cannot be detected and eliminated by existing methods that work only with random events. For example, the authors [5] use the weighted window function to reduce the Poisson noise in confocal scanning. Also, our previous article [7] describes the methods to eliminate noise. But the systematic errors are not random so these methods are not able to eliminate it.

Especially, additive noise is added to original values during the making, transfer or reproduction of an image.

In our work, we deal with the random events reduction, especially additive noise, to improve *z*-resolution.

During measurement, we scan the same point of the sample twice with the same conditions. In the case of noiseless measurements, we would get two identical results. Nevertheless, different values indicate the presence of noise. From the mathematical point of view, we consider everything what causes this difference as the noise (typically heat vibrations, also measurement errors, mechanical oscillations, etc.)

DOI: 10.1515/msr-2017-0034

Let us mention some methods for reducing additive noise – Richardson-Lusy algorithm (*RLA*), Maximum Likelihood Estimation (*MLE*), and Iterative Constrained Tikhonov-Miller (*ICTM*) algorithm [4]. However, these methods are limited by the additional assumptions, e.g. Poisson distribution of noise [5]. Low-pass filters are commonly used to reduce the additive noise as well [9]. The key purpose of these filters is the reduction of high spatial frequencies in the signal in the sense of the Fourier transform. Nevertheless, these filters are not able to differentiate whether the high-frequency information is caused by noise or by high contrast in the image. Therefore, loss of information necessarily ensues.

Our recent work [7] presents the method based on the Lindeberg-Lévy theorem as the pre-processing tool for single 2D images. In this paper, we introduce the application of this approach in confocal scanning to eliminate the random events (additive noise) and improve the *z*-resolution to the same values as the *xy*-resolution. We perform a statistical comparison of our results with the standard commercial software solution (Olympus software, version 6). The results are summarised in Section 3 and in Appendix, Table 4. and Table 5.

Table 4. shows that the average of seven or eight following measurements gives the results comparable with a low-pass filtered surface. The accuracy is higher with the increasing number of measurements and the correlation reaches the approximate value 0.999872 for K=25.

All sample measurements were made with confocal microscope Olympus LEXT OLS 3100. This microscope includes a confocal mode which collects the data to the Comma Separated Values (CSV) file with step 0.62 μm in the *z*-axis. This value may lead to the conviction that the measured surface has the same accuracy. Nevertheless, this confidence is quite false in the case of porous materials as is shown in Section 3. We use the confocal mode with the field of vision 2560× 1920 μm at a pixel resolution of 1024×768 pixels. It follows that the xy-resolution was 2.5 μm.

We work with the sample of fracture surface of hydrated Portland cement paste. For illustrative purposes, several specimens consisting of hydrated cement pastes were selected from a set of one-year old specimens. Ordinary Portland cement was used for their preparation. The specimens were mixed with the water-to-cement ratio equal to 0.4, and the fresh paste was cast in moulds of the size 2x2x10 cm^3. The paste was cured at a temperature of 20±2°C, and relative humidity of 100 % for three months. The specimens were then fractured in the three-point bending arrangement and sectioned into small cubes 2x2x2 cm^3. The rest of the time the cubes were stored under normal laboratory conditions (20±2 C, 101 325 kPa, 60±10 % RH).

2.2. Statistical evaluation

This section describes the statistical evaluation that is used in other sections to evaluate the results. We use these parameters: root mean square error, (relative) average difference, and Pearson's correlation coefficient.

Denote P, Q results of two different scans of the same profile, P_{ij}, Q_{ij} values of pixel $[i, j]$ in profiles P, Q, W, and H width and height of profile matrices of P, Q. Then the root mean square error is defined as:

$$RMSE = \sqrt{\frac{1}{W \cdot H}\sum_{i=1}^{W}\sum_{j=1}^{H}\left(P_{ij} - Q_{ij}\right)^2}$$

The average difference:

$$AD = \frac{1}{W \cdot H}\sum_{i=1}^{W}\sum_{j=1}^{H}\left|P_{ij} - Q_{ij}\right|$$

the relative average difference:

$$RAD = \frac{AD}{\Delta z} = \frac{1}{\Delta z}\cdot\frac{1}{W \cdot H}\sum_{i=1}^{W}\sum_{j=1}^{H}\left|P_{ij} - Q_{ij}\right|$$

where $\Delta z = 0.62\ \mu m$ is the used step in the z-axis. The value RAD indicates how many times the real accuracy is less than the step in the z-axis. Finally, Pearson's correlation coefficient

$$CORR = \frac{\sum_{i=1}^{W}\sum_{j=1}^{H}\left(P_{ij} - \bar{P}\right)\left(Q_{ij} - \bar{Q}\right)}{\sqrt{\sum_{i=1}^{W}\sum_{j=1}^{H}\left(P_{ij} - \bar{P}\right)^2 \sum_{i=1}^{W}\sum_{j=1}^{H}\left(Q_{ij} - \bar{Q}\right)^2}}$$

where $\bar{P},\ \bar{Q}$ are arithmetic means of profiles $P;\ Q$.

2.3. Noise decreasing method

Proposed noise reduction method is based on the Lindeberg-Lévy Central Limit Theorem, which produces more accurate results in comparison with low-pass filters and can be used without any limitations, unlike *RLA*, *MLE* or *ICTM*.

Consider the noise as the realization of a random variable. Then we can say:

Theorem (Lindeberg-Lévy Central Limit Theorem). *Let $X_1; X_2; \ldots; X_K$ be random variables with arbitrary (but the same) distribution, the same mean value μ and the same (finite) variance σ^2. Then the mean of $X_1; X_2; \ldots; X_K$ for $K \to \infty$ converges to the normal distribution with the same mean value μ and variance $\acute{\sigma}^2 = \sigma^2/K$.*

The proof of this theorem can be found in [8] for example. Generally, the application of the theorem causes that the mean variance of K random variables is K-times lower. This will be described further.

Let P be the input profile that consists of the useful information U and the noise N. The noise N is the realization of a random variable with expected values equal to zero. We carry out the profile measurements K-times, therefore we obtain the series $\{P(k)\}$, $k = 1, 2, \ldots, K$. Let U_{ij} be the useful information and $N_{ij}(k)$ be the random noise in pixel $[i, j]$ in

profile $P(k)$. The arithmetic means in $[i,j]$-th pixel can be expressed as:

$$\overline{P_{ij}(K)} = \frac{1}{K}\cdot\sum_{k=1}^{K} P_{ij}(k) = \frac{1}{K}\cdot\sum_{k=1}^{K}\left(U_{ij} + N_{ij}(k)\right) = U_{ij} + \frac{1}{K}\cdot\sum_{k=1}^{K} N_{ij}(k) \tag{1}$$

The useful information U_{ij} (it is not random) is preserved and noise is:

$$N_{ij} = \frac{1}{K}\cdot\sum_{k=1}^{K} N_{ij}(k) \tag{2}$$

Equation (2) denotes that the mean is equal to zero and the variance is K-times lower.

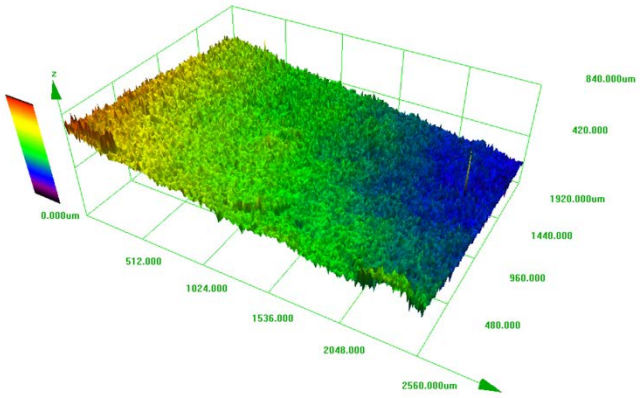

Fig.1. Non-filtered profile reconstructed with Olympus company software (step 0.62 μm in the *z*-axis) technology.

We use different statistical variables to compare our results. Let $\overline{P_{ij}(K)}$ be the arithmetic mean of K values in pixel $[i,j]$ in K scannings of the same profile. Let $\overline{Q_{ij}(K)}$ be the arithmetic mean of the following K values in pixel $[i,j]$ in the following K scannings of the same profile. Denote $RMSE(K)$, $AD(K)$; $RAD(K)$; $CORR(K)$ the root mean square error, average difference, relative average difference, and correlation of $\overline{P_{ij}(K)}$ and $\overline{Q_{ij}(K)}$, i.e.

$$RMSE(K) = \sqrt{\frac{1}{W\cdot H}\sum_{i=1}^{W}\sum_{j=1}^{H}\left(\overline{P_{ij}(K)} - \overline{Q_{ij}(K)}\right)^2}$$

where

$$\overline{P_{ij}(K)} = U_{ij}(K) + \frac{1}{K}\cdot\sum_{k=1}^{K} N_{ij}^{(P)}(k)$$

$$\overline{Q_{ij}(K)} = U_{ij}(K) + \frac{1}{K}\cdot\sum_{k=1}^{K} N_{ij}^{(Q)}(k)$$

It means

$$RMSE(K) = \frac{1}{K}\cdot\sqrt{\frac{1}{W\cdot H}\sum_{i=1}^{W}\sum_{j=1}^{H}\left(\sum_{k=1}^{K} N_{ij}^{(P)}(k) - \sum_{k=1}^{K} N_{ij}^{(Q)}(k)\right)^2} = \frac{1}{K}\cdot\sqrt{\frac{1}{W\cdot H}\sum_{i=1}^{W}\sum_{j=1}^{H}\left(\sum_{k=1}^{K}\left[N_{ij}^{(P)}(k) - N_{ij}^{(Q)}(k)\right]\right)^2} = \frac{1}{K}\cdot\sqrt{\frac{1}{W\cdot H}\sum_{i=1}^{W}\sum_{j=1}^{H}\left(\sum_{k=1}^{K} N_{ij}(k)\right)^2} \tag{3}$$

Similarly,

$$AD(K) = \frac{1}{K}\cdot\left[\frac{1}{W\cdot H}\sum_{i=1}^{W}\sum_{j=1}^{H}\left|\sum_{k=1}^{K} N_{ij}(k)\right|\right] \tag{4}$$

The expression $\sum_{k=1}^{K} N_{ij}(k)$ in (1), (2) describes the noise. Therefore, the expressions under the square root in (3) or whole expression in the square brackets (4) also determine the noise. This means that $RMSE(K)$ and $AD(K)$ are proportional to K inversely (where K denote the number of averaged scans).

Analogically, we can write:

$$RAD(K) = \frac{AD}{\Delta z} = \frac{1}{K}\cdot\frac{1}{\Delta z}\cdot\frac{1}{W\cdot H}\sum_{i=1}^{W}\sum_{j=1}^{H}\left|P_{ij}(K) - Q_{ij}(K)\right|$$

Correlation can be expressed as:

$$CORR(K) = \frac{\sum_{i=1}^{W}\sum_{j=1}^{H}\left(P_{ij}(K) - \overline{P(K)}\right)\left(Q_{ij}(K) - \overline{Q(K)}\right)}{\sqrt{\sum_{i=1}^{W}\sum_{j=1}^{H}\left(P_{ij}(K) - \overline{P(K)}\right)^2\sum_{i=1}^{W}\sum_{j=1}^{H}\left(Q_{ij}(K) - \overline{Q(K)}\right)^2}}$$

Note, that $0 < CORR,\ CORR < CORR(K), CORR(K) < 1$ and we can write $0 < CORR < CORR(K) < 1$.

3. Results and Discussion

As mentioned above, the Olympus LEXT OLS 3100 confocal microscope was used to acquire a CSV data file that describes the fracture surface of hydrated Portland cement paste (step 0.62 µm in the *z*-axis). For illustration, we show the surface reconstruction using Olympus company software in Fig.1. It confirms that reconstruction of porous materials is problematic and obviously, the image is also constructed with low resolution.

Fig.2. clearly shows that the reconstructed surface (by Olympus software) also contains a huge error. This error is clearly visible in Table 3. in Appendix where we compare the image section of two subsequent scans of the same area.

The differences covered the interval $-262\,\mu m$ to $+114\,\mu m$. Note that the z-step is $0.62\,\mu m$. For comparison,

we make the reconstruction of the same data using our proposed visualization software Micro3D.

We make five pairs $P^{(k)}; Q^{(k)}; \ k = 1,2,\dots,5$ of same sample measurements. We compute the statistical characteristics $RMSE^{(k)}; \ AD^{(k)}; \ RAD^{(k)} \ CORR^{(k)}; \ k = 1,2,\dots,5$ for each pair of these measurements. For each k, $P^{(k)}$ and $Q^{(k)}$ are measurements of the same profile, i.e. for each $k = 1,2,\dots,5$ the ideal values are: $RMSE^{(k)} = 0;$ $AD^{(k)} = 0; RAD^{(k)} = 0\ \%; CORR^{(k)} = 100\ \%$. As we can see from Table 1., the average difference AD is approximately $23.5\ \mu m$, the measurement error is therefore approximately 38 times higher than the used step $0.62\ \mu m$. The correlation reaches the value 97 %.

Moreover, we filtered this data using Olympus company low-pass filter, and Table 2. presents the same characteristics as Table 1. The values of statistical parameters are significantly better. However, these filters are not able to differentiate whether the high-frequency information is a useful signal or the noise.

Therefore, low-pass filters decrease additive noise but also degrade the reconstructed surface. We can see this fact on the visualization. The surface reconstructed by Olympus Company software is presented in Fig.3. It is evident that low-pass filters are not suitable for porous materials because of the visible surface degradation.

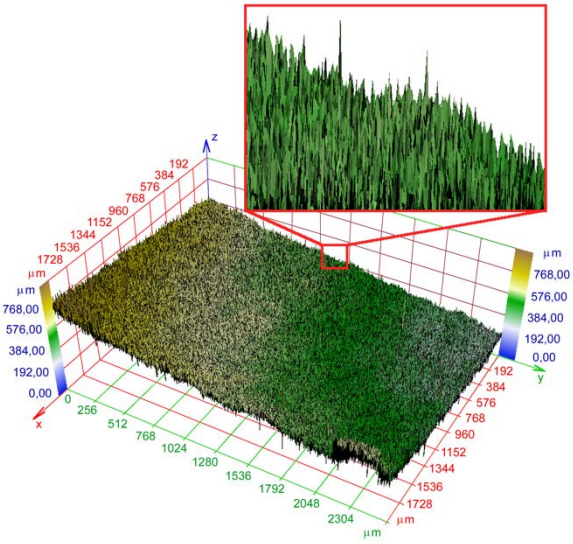

Fig.2. Non-filtered profile reconstructed with Micro3D software (same data as in Fig.1.)

Table 1. Comparison of five pairs of the same surface scans, non-filtered. (z-step 0.62 μm).

k	RMSE	AD	RAD	CORR
1	29.9229	23.4072	37.75	0.971787
2	29.944	23.4163	37.77	0.971762
3	29.9208	23.3903	37.73	0.971791
4	29.9884	23.4303	37.79	0.971667
5	30.0563	23.5059	37.91	0.971549

Table 2. The comparison of five pairs of the same surface scans filtered using Olympus company low-pass filter. (z-step 0.62 μm).

k	RMSE	AD	RAD	CORR
1	6.0940	4.5698	7.37	0.998676
2	6.1739	4.1664	6.72	0.998642
3	6.2504	4.6749	7.54	0.998610
4	6.3048	4.7052	7.59	0.998585
5	6.4391	4.7829	7.71	0.998529

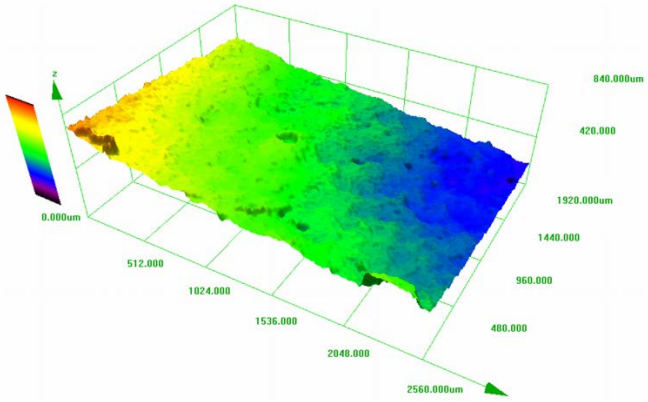

Fig.3. Profile from Fig.1. filtered by a common low-pass filter (Olympus company software).

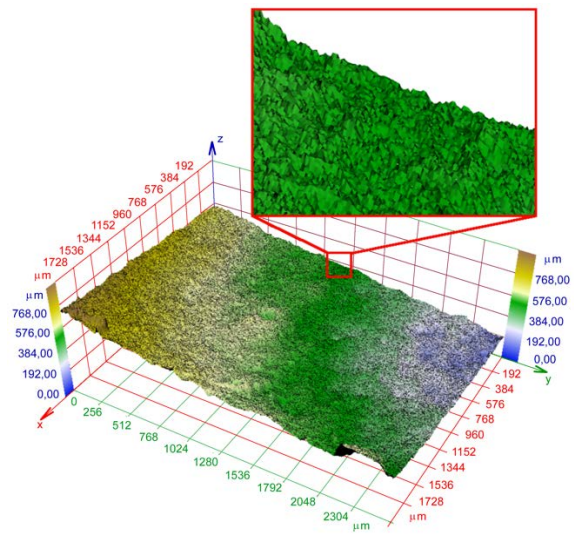

Fig.4. The surface composed of average values given by 25 scans - sample S_1 (Micro3D software).

The following part presents the advantage of the proposed noise reduction method using different statistical evaluation.

We make sequence of 25 pairs $P^{(k)}; Q^{(k)}; k = 1,2,\dots,25$ of the sample S_1 measurements. Consequently, we calculated 25 pairs of averages of K profiles.

$$\overline{P(K)} = \frac{1}{K}\sum_{k=1}^{K} P^{(k)}; \qquad \overline{Q(K)} = \frac{1}{K}\sum_{k=1}^{K} Q^{(k)}; \qquad K = 1, 2, \ldots, 25 \tag{5}$$

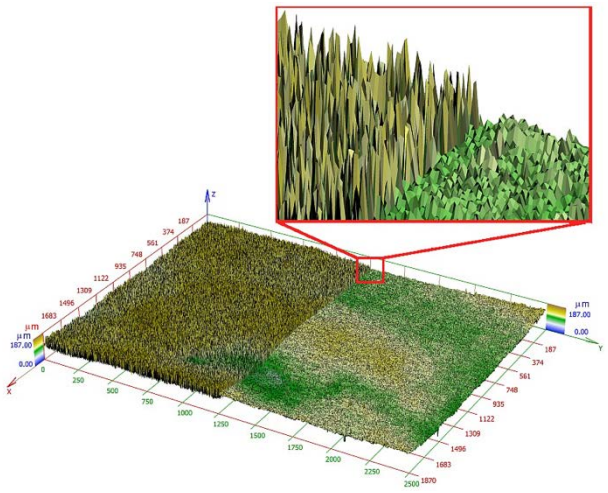

Fig.5. The surface composed of average values given by 25 scans - sample S_2 (Micro3D software).

For example, $\overline{P(10)}$ is the profile matrix calculated as the arithmetic mean of ten measurements $P^{(1)}$; $P^{(2)}$,..., $P^{(10)}$ of the same profile and $\overline{Q(10)}$ is the profile matrix calculated as the arithmetic mean of other ten measurements $Q^{(1)}$, $Q^{(2)}$,...;, $Q^{(10)}$ of the same profile. We compute the statistical characteristics between $\overline{P(K)}$ and $\overline{Q(K)}$ in dependence on the value of *K*.

Due to the Lindeberg-Lévy Central Limit Theorem, we eliminate the noise using (1), (2). Following computation of the statistical characteristics $RMSE(K)$, $AD(K)$, $RAD(K)$, and $CORR(K)$ between $\overline{P(K)}$ and $\overline{Q(K)}$ proves that the method improves the *z*-resolution significantly. The results in Table 4. show that the average of seven or eight following measurements *(K=7, 8)* gives the results comparable with a low-pass filtered surface. The accuracy is higher with the increasing number of measurements. The correlation reaches the approximate value 0.999872 for *K=25*. The surface composed of average values given by 25 scans is presented in Fig.4.

We make the measurement and the same computations as described in previous part for the second sample S_2 (profile of hydrated Portland cement paste). The analogy data to Table 4. are in Table 5., and the resulting surface is in Fig.5. (analogical to Fig.4.).

Due to the inverse proportion of $RMSE(K)$ and $AD(K)$ predicted in Section 2., measured data was fitted with a function $f(K) = \frac{a}{K} + b$ by the least squares method.

We obtain for the first sample data these equations:

$$RMSE(K) = \frac{a}{K} + b \approx \frac{27{,}32}{K} + 2.63 \tag{6}$$

$$AD(K) = \frac{c}{K} + d \approx \frac{22{,}15}{K} + 1.82 \tag{7}$$

The functions (6) and (7) are drawn in Fig.6. The noise variance gives the numerators in these equations. The additive constant *d* in (7) describes the difference from a supposed inverse proportion. This difference is probably caused by some non-random measurement error of the microscope. The additive constant depicts that even in the case of perfect additive noise reduction ($K \to \infty$) it is not possible to reconstruct the profile exactly. The limit precision is $\pm\frac{d}{2} \approx \pm 0{,}9\ \mu m$.

The sample S_2 values of a, b, c, d in (6), (7) are equal to $a = 27.04$; $b = 2.78$; $c = 21.92$; $d = 2.06$ and corresponding functions are in Fig.7.

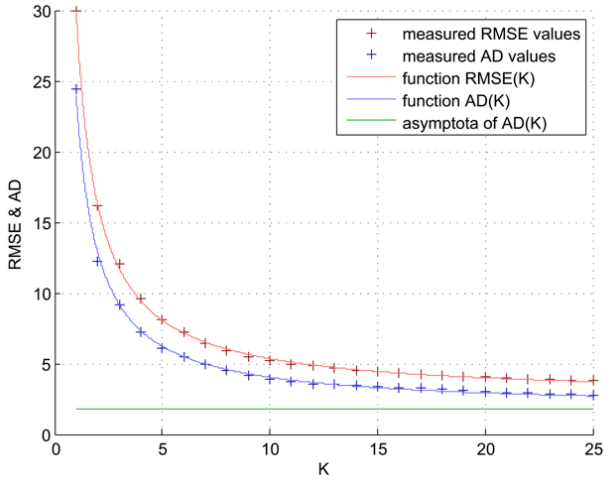

Fig.6. Functions *RMSE* and *AD* for sample S_1 – reliance of Root Mean Square Error and Average Difference on the number of averaged scans.

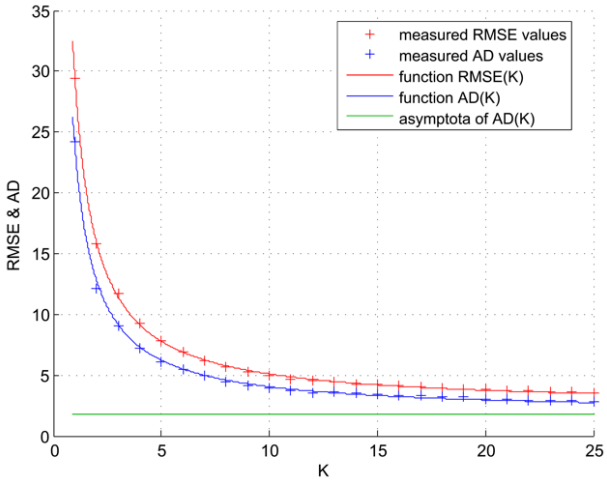

Fig.7. Functions *RMSE* and *AD* for sample S_1 – reliance of Root Mean Square Error and Average Difference on the number of averaged scans.

4. CONCLUSIONS

We have used the field of vision 2560× 1920 μm, a pixel resolution of 1024×768 pixels so that the xy-resolution was 2.5 μm. In our case, the z-resolution of input data was 0.62 μm. The course of the function $AD(K)$ indicates that we can improve the resolution even with low-quality data using 4-6 subsequent scans. The usage of 25 scans causes the improvement of z-axis resolution on the level comparable to the xy-resolution. Theoretically, due to additive constant d, maximal additive noise reduction ($K \to \infty$) means that the maximal resolution for tested samples is $\pm\frac{d}{2} \approx \pm 0.9\ \mu m$, and $\pm\frac{d}{2} \approx \pm 1.0\ \mu m$, i.e. three and 2.5 times higher resolution in comparison with xy-resolution. This method based on the Lindeberg–Lévy theorem is able to set the optimal number of measurements to get the required depth precision.

ACKNOWLEDGMENT

The authors acknowledge support from Project LO1202 by financial means from the Ministry of Education, Youth and Sports, the National Sustainability Programme I. The authors thank prof. Tomas Ficker from the Faculty of Civil Engineering of Brno University of Technology for the provided data.

REFERENCES

[1] Ficker, T., Len, A., Chmelík, R., Lovicar, L., Martišek, D., Němec, P. (2007). Fracture surfaces of porous materials. *Europhysics Letters*, 80 (6), 1600-1604.

[2] Ficker, T., Martišek, D., Jennings, H.M. (2010). Roughness of fracture surfaces and compressive strength of hydrated cement pastes. *Cement and Concrete Research*, 40 (6), 947-955.

[3] Ficker, T., Martišek, D. (2012). Digital fracture surfaces and their roughness analysis: Applications to cement-based materials. *Cement and Concrete Research*, 42 (6), 827-833.

[4] Van Kempen, G.M.P., Van Vliet, L.J., Verveer, P.J., Van Der Voort, H.T.M. (1997). A quantitative comparison of image restoration methods for confocal microscopy. *Journal of Microscopy*, 185, 354-365.

[5] Kervrann, C., Trubuil, A. (2004). An adaptive window approach for Poisson noise reduction and structure preserving in confocal microscopy. In *2nd IEEE International Symposium on Biomedical Imaging: Nano to Macro*, Arlington, VA, USA. IEEE, 788-791.

[6] Sheppard C.J.R., Shotton D.M. (1997) *Confocal Laser Scanning Microscopy*. Springer.

[7] Martisek, D., Prochazkova, J., Ficker, T. (2015). High-quality three-dimensional reconstruction and noise reduction of multifocal images from oversized samples. *Journal of Electronic Engineering*, 24 (5).

[8] Montgomery, D.C., Runger, G.C. (2003). *Applied Statistics and Probability for Engineers*, 3rd ed. John Wiley & Sons.

[9] Yio, M.H.N., Mac, M.J., Wong, H.S., Buenfeld, N.R. (2015). 3D imaging of cement-based materials at submicron resolution by combining laser scanning confocal microscopy with serial sectioning. *Journal of Microscopy*, 258 (2), 151-169.

Received May 19, 2017.
Accepted November 13, 2017.

APPENDIX

Table 3. Two submatrices of heights of the same sample points acquired by two subsequent scans (z-step 0.62 μm) and their differences (all in micrometers).

First scanning

542.85	562.70	556.07	566.79	553.22	545.08	274.90	554.55	576.03	506.31	518.87	523.18	556.51
538.57	568.27	560.31	576.65	509.64	516.04	526.16	550.84	543.13	596.15	539.87	570.22	588.08
588.11	570.42	559.23	558.35	572.98	563.72	541.97	571.48	550.09	492.95	551.80	555.34	571.24
560.49	577.91	599.61	573.03	586.78	564.28	563.84	587.45	554.41	577.02	577.18	559.52	554.95
563.75	559.75	624.12	573.59	552.75	521.04	531.06	601.79	574.48	571.30	560.83	560.34	585.82
552.68	540.69	547.04	563.95	552.87	558.38	568.50	549.32	539.15	559.13	559.33	557.79	536.69
567.29	580.02	569.31	569.65	553.17	538.72	489.03	519.95	544.29	570.86	573.38	554.37	569.80

Second scanning

580.01	531.17	580.64	529.34	545.78	539.43	536.89	603.34	537.14	554.97	548.45	565.95	555.79
555.20	557.44	556.71	574.78	559.01	571.09	564.41	560.34	582.43	572.75	507.05	538.50	544.71
519.34	548.63	552.61	559.06	567.07	584.37	559.08	557.77	554.29	569.76	538.78	557.55	542.16
531.10	577.58	529.96	550.27	575.13	568.18	552.65	533.79	537.70	548.60	566.12	488.60	508.98
568.32	558.87	510.08	563.84	566.87	573.43	564.06	517.01	514.14	586.94	542.68	515.10	529.12
545.59	570.74	582.44	581.88	559.33	537.92	565.95	564.70	557.55	580.76	555.95	487.07	561.33
576.52	564.66	545.22	581.80	525.63	576.65	577.54	563.64	546.92	541.52	529.59	568.95	581.74

Differences

-37.16	31.53	-24.57	37.45	7.45	5.64	**-261.98**	-48.79	38.89	-48.66	-29.58	-42.77	0.73
-16.63	10.84	3.60	1.86	-49.36	-55.05	-38.25	-9.49	-39.30	23.39	32.82	31.72	43.37
68.77	21.78	6.62	-0.71	5.91	-20.65	-17.11	13.71	-4.20	-76.80	13.02	-2.21	29.08
29.39	0.32	69.65	22.76	11.65	-3.89	11.19	53.66	16.72	28.42	11.06	70.92	45.96
-4.56	0.88	**114.04**	9.76	-14.13	-52.39	-33.00	84.78	60.34	-15.64	18.14	45.23	56.70
7.08	-30.04	-35.41	-17.93	-6.45	20.45	2.55	-15.39	-18.40	-21.63	3.37	70.71	-24.64
-9.23	15.36	24.09	-12.15	27.54	-37.93	-88.51	-43.69	-2.63	29.34	43.79	-14.57	-11.94

Table 4. Comparison of twenty-five pairs of the same surface measurements. Each measurement in each pair is the average of $K = 1, 2\ldots, 25$ scannings (Sample S_1).

K	RMSE(K)	AD(K)	RAD(K)	CORR(K)
1	29.9206	24.3918	39.34	0.976197
2	16.1997	12.2270	19.72	0.991638
3	12.0631	9.1397	14.74	0.995344
4	9.5787	7.2473	11.69	0.997058
5	8.0759	6.0922	9.83	0.997907
6	7.2181	5.4557	8.80	0.998326
7	6.4875	4.9875	8.04	0.998647
8	5.9424	4.4872	7.24	0.998864
9	5.4966	4.1483	6.69	0.999028
10	5.2196	3.8716	6.24	0.999156
11	4.9286	3.7250	6.01	0.999260
12	4.8247	3.5197	5.68	0.999340
13	4.7255	3.5833	5.78	0.999422
14	4.4789	3.4893	5.63	0.999498
15	4.4706	3.4192	5.51	0.999562
16	4.3470	3.3203	5.36	0.999604
17	4.2757	3.2708	5.28	0.999649
18	4.1745	3.1889	5.14	0.999682
19	4.1218	3.1536	5.09	0.999715
20	4.0364	3.0038	4.84	0.999749
21	3.9972	2.9587	4.77	0.999783
22	3.9334	2.9078	4.69	0.999806
23	3.8863	2.8604	4.61	0.999828
24	3.8373	2.8461	4.59	0.999851
25	3.7989	2.8046	4.52	0.999872

Table 5. Comparison of twenty-five pairs of the same surface measurements. Each measurement in each pair is the average of $K = 1, 2\ldots, 25$ scannings (Sample S_2).

K	RMSE(K)	AD(K)	RAD(K)	CORR(K)
1	29.4196	24.2045	39.65	0.976385
2	15.8359	12.1613	19.83	0.991685
3	11.7407	9.1049	14.80	0.995363
4	9.2811	7.2314	11.72	0.997066
5	7.7933	6.0879	9.84	0.997909
6	6.9441	5.4578	8.80	0.998326
7	6.2208	4.9942	8.03	0.998645
8	5.6812	4.4989	7.23	0.998862
9	5.2398	4.1634	6.67	0.999025
10	4.9656	3.8895	6.22	0.999153
11	4.6775	3.7444	5.98	0.999256
12	4.5746	3.5411	5.65	0.999337
13	4.4764	3.6041	5.75	0.999419
14	4.2323	3.5110	5.60	0.999495
15	4.2241	3.4416	5.48	0.999560
16	4.1017	3.3437	5.33	0.999602
17	4.0311	3.2947	5.25	0.999647
18	3.9309	3.2136	5.11	0.999680
19	3.8788	3.1787	5.05	0.999713
20	3.7942	3.0304	4.80	0.999747
21	3.7554	2.9857	4.73	0.999781
22	3.6923	2.9353	4.65	0.999804
23	3.6456	2.8884	4.57	0.999827
24	3.5971	2.8743	4.55	0.999850
25	3.5591	2.8332	4.48	0.999871

Hindawi
Scanning
Volume 2017, Article ID 8538215, 8 pages
https://doi.org/10.1155/2017/8538215

WILEY | Hindawi

Research Article

Registration of Partially Focused Images for 2D and 3D Reconstruction of Oversized Samples

Dalibor Martišek and Hana Druckmüllerová

Faculty of Mechanical Engineering, Institute of Mathematics, Brno University of Technology, Technická 2, 616 69 Brno, Czech Republic

Correspondence should be addressed to Dalibor Martišek; martisek@fme.vutbr.cz

Received 28 April 2016; Accepted 2 August 2016; Published 10 August 2017

Academic Editor: Brandon Weeks

Methods of fracture surface 3D reconstruction from a series of partially focused images acquired in a small field of view (e.g., by confocal microscope or CCD camera) are well known. In this case, projection rays can be considered parallel and recorded images do not differ in any geometrical transformation from each other. In the case of larger samples (oversized for microscope or CCD camera), it is necessary to use a wider viewing field (e.g., standard cameras); taken images primarily differ in scaling but may also differ in shifting and rotation. These images cannot be used for reconstruction directly; they must be registered; that is, we must determine all transformations in which the images differ and eliminate their effects. There are several ways to do this. This paper deals with the registration based on phase correlation.

1. Introduction

This paper follows up recent published works [1, 2] about 3D reconstruction methods for images acquired by confocal and nonconfocal microscopes. Confocal microscopes are actually optical microscopes which are distinguished from other optical microscopes by two unique properties. They have a very small depth of optical field and their advanced hardware is capable of removing nonsharp points from images. The points of objects very near to the focal plane are visible as sharp points and are depicted as light areas in our optical sections (see Figure 1(a)) whereas those parts lying above or beneath the focal plane are invisible and are represented by black regions. Analogous regions can be observed by using conventional microscopes fitted with the same lens (see Figure 1(b)). Both the confocal and nonconfocal snapshots (optical sections) show sharp regions of very similar shapes. The only difference concerns nonsharp regions that manifest themselves as blurred regions in the nonconfocal sections, whereas in the confocal sections they are missing (black regions). However, the shapes of confocal and nonconfocal out-of-focus regions are very similar.

To create a sharp image (2D reconstruction), it is necessary to obtain a series of images of the same object, each of them with different focusing and each point on the object focused in one of the images (in the ideal case). The sharp parts are identified and composed in a new image. There is also a simple method for constructing a rough 3D model of the object where all sharp points belonging to the same image have the same height.

There are two principal problems in this 2D and 3D reconstruction. The work [3] deals with methods that detect focused and blurred parts in images taken in nonconfocal mode and are able to assign the corresponding focus plane for each surface point. In this way, construction of 3D stair-approximation of the studied surface is possible (see Figure 2). However, this approximation is not sufficient in many applications. It is necessary to specify the height of each point between two focal planes and construct a smooth approximation (see Figure 3).

The projection used is the second problem. In the case of the confocal microscope, we can assume that the field of view is small and the used projection is parallel. The paper [4] and many other works [3, 5–11] presume this projection

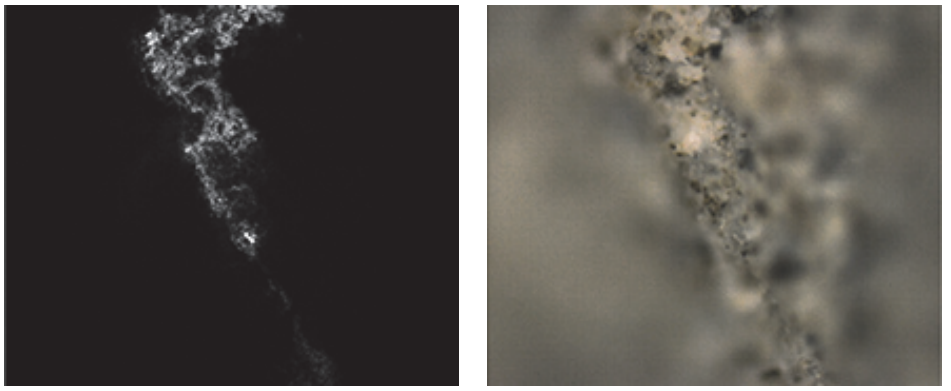

(a) (b)

Figure 1: Fracture surface of cement paste. The image was acquired by confocal microscope in confocal mode (a) and nonconfocal mode (b).

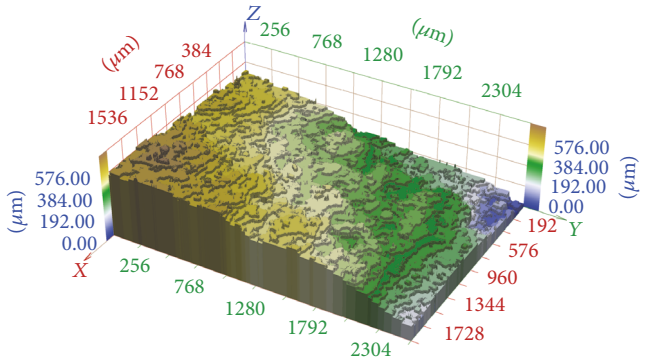

Figure 2: 3D stair-approximation of fracture surface of hydrated cement paste.

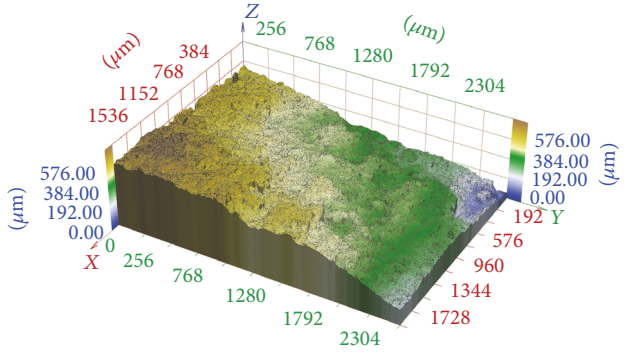

Figure 3: Smooth-approximation of fracture surface from Figure 2.

property. In parallel projection, all images are provided in the field of view with the same size. In Figure 4, there is the first image (a) and the thirtieth image (b) in a series of fifty-two photos of the fracture surface of hydrated cement paste acquired by the confocal microscope Olympus LEXT 3100. Corresponding pixels have the same coordinates in separate partial focused images (compare the crosses and arrows in Figure 4). However, this assumption is not valid in the case of larger samples; the angle of the projection lines is not negligible and the view fields are different. In Figure 5, we can see the first image (a) and the forty-third image (b) in a series of seventy photos of a sandstone sample (locality Brno-Hády, Czech Republic) taken with a Canon DSLR camera. The used projection is central and the fields of view (i.e., also coordinates of corresponding pixels) of individual images are clearly different (see crosses in Figure 5).

Therefore, we set two goals in the conclusion of the work [1]: firstly, to specify the height of each point between two sharpness planes and construct a smooth approximation. This goal has already been met in [2]; for the result of this new reconstruction see Figure 3. Some other works [3, 8, 10] also deal with this problem.

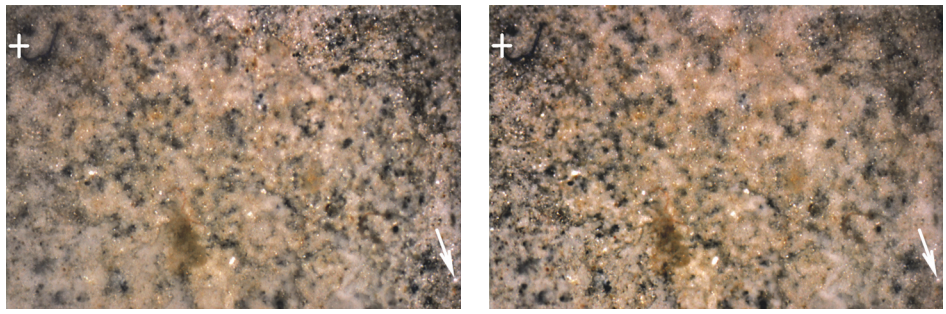

(a) (b)

Figure 4: The first image (a) and the thirtieth image (b) in the series of photos of the fracture surface of hydrated cement paste acquired by confocal microscope Olympus LEXT 3100. The projection used is parallel and the fields of view are the same size (compare the position of the marked points).

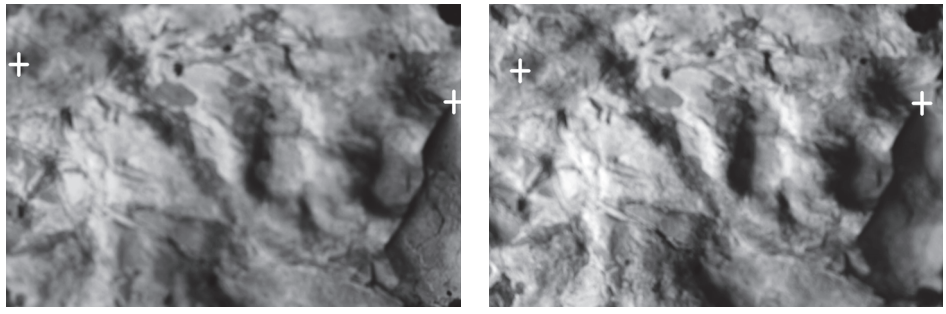

(a) (b)

Figure 5: The first image (a) and the forty-third image (b) in the series of photos of sandstone sample (locality Brno-Hády, Czech Rep.) taken with a Canon DSLR camera. The projection used is central and the fields of view are clearly different (compare the position of the marked points).

The second goal, solution of different sizes of the field of view, is discussed in this paper.

2. Materials and Methods

2.1. Materials and Equipment. The methods discussed in this article are suitable for 2D and 3D processing of samples which are oversized for confocal microscopes. These samples may have a size from a few centimetres (e.g., geological samples). Data may be taken by a CCD camera or conventional digital camera with a narrow sharpness zone. This scanning device must be connected with a stepping device that allows changing the distance between the camera and the scanning sample and thus the position of the camera sharpness zone.

Data used in this paper was acquired by special hardware designed and assembled by professor Tomáš Ficker from the Faculty of Civil Engineering of our University. The hardware consists of a Canon EOS 600D photographic camera augmented by EF 100 mm f/2.8 Macro USM lens. The photographic camera is mounted on a motorized tough stand which enables movement in the vertical direction. The vertical stepping movement is governed by software running on a PC. See [12] for more details.

Separate images are taken by central projection; that is, they differ at least in the scale used. The various scale of images could be solved using only elementary mathematics; the image size is proportional to the camera shifting in this case (see Figure 6 on the left).

However, the practical situation is more complicated. The images differ not only in the scale used but also in the content displayed (different parts are focused in different images). Due to mechanical errors, the step in the z-axis may be not fully constant; the images can also be mutually shifted in the x- or y-axis and even rotated. Image registration is also complicated by the nonplanarity of samples (see Figure 6 on the right). In Figure 5, we can see the first image (on the left) and the forty-third image (on the right) in a series of photos of a sandstone sample (locality Brno-Hády, Czech Republic) taken with a Canon DSLR camera. The projection used is central, the fields of view are clearly different.

In this paper we describe the preprocessing of a series of such images for 2D and 3D reconstruction. A suitable tool for this preprocessing is the Fourier transform.

2.2. Fourier Transform. This is an integral transform that transforms a function of one or more variables (in spatial domain) to another function (in frequency domain) of the same number of variables [3, 13, 14]. Since the Fourier transform of a function is in general a function with a complex image and since a digital image is a function of

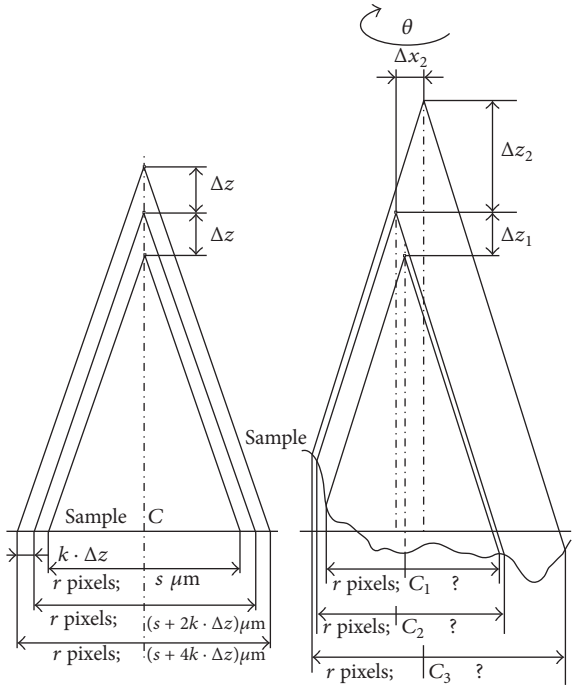

Figure 6: The central projection of an oversized sample, ideal case on the left, real case on the right.

two spatial variables, we will deal here for simplicity with functions $f : \mathbb{R}^2 \to \mathbb{C}$.

Digital images are rectangles; for simplicity we deal here with square images only. All computations that use the Fourier transform are performed using the discrete Fourier transform (or more precisely by special algorithms that speed up the discrete Fourier transform, such as the Fast Fourier Transform (FFT)). However, some derivations of image processing methods are better performed with the Fourier transform of functions with the domain $\mathbb{R}^2$ since operations such as rotation and rescaling are easily modeled on these functions.

The standard definition of the Fourier transform of a function of two variables is as follows [15].

Definition 1 (Fourier transform). Let $f(x; y) : \mathbb{R}^2 \to \mathbb{C}$ be a function such that

$$\iint_{\mathbb{R}^2} \left| f(x; y) \right| \mathrm{d}x \, \mathrm{d}y \tag{1}$$

exists and is finite. The *Fourier transform* of f is

$$F(\xi; \eta) = \iint_{\mathbb{R}^2} f(x; y) \exp\left(-i\left(x\xi + y\eta\right)\right) \mathrm{d}x \, \mathrm{d}y. \tag{2}$$

Function $F(\xi; \eta)$ is also called the Fourier spectrum of function f. Function $A(\xi; \eta) = |F(\xi; \eta)|$ is called amplitude spectrum of $f(x; y)$.

Definition 2 (inverse Fourier transform). Let $F(\xi; \eta) : \mathbb{R}^2 \to \mathbb{C}$ be a function such that

$$\iint_{\mathbb{R}^2} \left| F(\xi; \eta) \right| \mathrm{d}\xi \, \mathrm{d}\eta \tag{3}$$

exists and is finite. The *inverse Fourier transform* of function F is function

$$\mathscr{F}^{-1}\left\{F(x; y)\right\}(x; y) = f(x; y) : \mathbb{R}^2 \longrightarrow \mathbb{C} \tag{4}$$

defined as

$$f(x; y) = \frac{1}{4\pi^2} \iint_{\mathbb{R}^2} F(\xi; \eta) \exp\left(i\left(x\xi + y\eta\right)\right) \mathrm{d}\xi \, \mathrm{d}\eta. \tag{5}$$

2.3. Phase Correlation. For processing and analyzing the images it is necessary to transform the images so that the studied structures are at the same position in all the images. This is the task of image registration, to find the transformation. In some applications we assume that images were shifted only; in others we allow shift, rotation and scale change (i.e., similarity), general linear transformation, or even general transformations.

The methods used for registration depend on the expected transformation and on the structures in the image. Some methods use corresponding structures or points in the images and then find a global transformation using the measurements of positions of the structures or points [16–18]. These methods require these structures to be clearly visible. Other methods are based on correlation and work with the image as a whole. The phase correlation proved to be a powerful tool (not only) for registration of partially focused images. For functions f_1; f_2 it is defined as

$$P_{f_1;f_2}(x; y) = \mathscr{F}^{-1}\left\{\frac{F_1(\xi; \eta) \cdot \overline{F}_2(\xi; \eta)}{\left|F_1(\xi; \eta) \cdot F_2(\xi; \eta)\right|}\right\} \tag{6}$$

and its modification as

$$P_{f_1;f_2;p;q}(x; y) = \mathscr{F}^{-1}\left\{H(\xi; \eta) \cdot \frac{F_1(\xi; \eta) \cdot \overline{F}_2(\xi; \eta)}{\left(\left|F_1(\xi; \eta)\right| + p\right) \cdot \left(\left|F_2(\xi; \eta)\right| + q\right)}\right\}, \tag{7}$$

where bar means complex conjugation and $H(\xi; \eta)$ is a bounded real function such that $H(\xi; \eta) = H(-\xi; -\eta)$ and $p; q > 0$ are arbitrary constants. It can be proved that for real functions f_1; f_2 the phase correlation function is real [14]. This is of great value, since it enables us to search for extremes of the phase correlation function.

2.4. Shifted Images. The phase correlation function can be also used for estimation of image shift. The method was first published by Kuglin and Hines [19].

It is clearly seen that the phase correlation function of a function with itself is the δ-distribution, that is,

$$\begin{aligned} P_{f;f}(x; y) &= \mathscr{F}^{-1}\left\{\frac{F(\xi; \eta) \cdot \overline{F}(\xi; \eta)}{\left|F(\xi; \eta) \cdot F(\xi; \eta)\right|}\right\} = \mathscr{F}^{-1}\{1\} \\ &= \delta(x; y) \end{aligned} \tag{8}$$

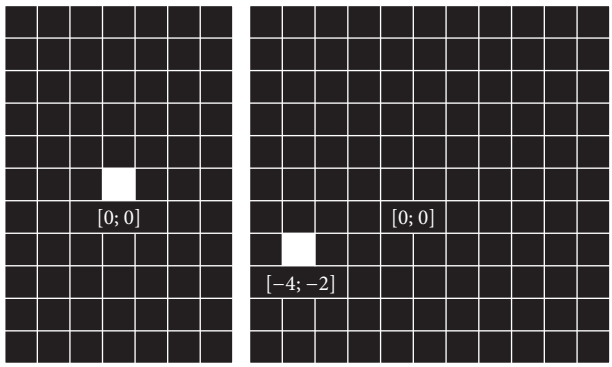

Figure 7: The main idea of phase correlation: on the left: the phase correlation of the function with itself, the δ-distribution $\delta(x; y)$. On the right: the phase correlation of the functions $f(x; y)$ and $f(x-4; y-2)$, δ-distribution $\delta(x+4; y+2)$. It is necessary to shift the function $f(x-4; y-2)$ by vector $(-4; -2)$ for further image processing and reconstruction.

δ-distribution is a generalized function for which

$$\delta(x; y) = \begin{cases} \infty; & [x; y] = [0; 0] \\ 0; & [x; y] \neq [0; 0], \end{cases} \qquad \iint_{\mathbb{R}^2} \delta(x; y)\, \mathrm{d}x\, \mathrm{d}y = 1. \tag{9}$$

In an illustration of the δ-distribution, maximum pixel value is used instead of infinity. The illustration of the phase correlation of a function with itself can be seen in Figure 7 on the left.

If two functions are shifted in arguments, that is, $f_2(x; y) = f_1(x - x_0; y - y_0)$, their Fourier transforms are shifted in phase; that is,

$$F_2(\xi; \eta) = F_1(\xi; \eta) \cdot \exp(-i(\xi x_0 + \eta y_0)) \tag{10}$$

and their phase correlation function is the δ-distribution shifted in arguments by the opposite shift vector

$$P_{f_1; f_2}(x; y) = \mathcal{F}^{-1}\{\exp(i(\xi x_0 + \eta y_0))\} = \delta(x + x_0; y + y_0). \tag{11}$$

The illustration of phase correlation of shifted but otherwise identical images can be seen in Figure 7 on the right.

This is the main idea of phase correlation. The task to find a shift between two images is converted by the phase correlation to the task of finding the only nonzero point in a matrix (computation using the discrete Fourier transform). If the images are not identical (up to a shift), that is, if the images are not ideal, the phase correlation function is more complicated, but it still has a global maximum at the coordinates corresponding to the shift vector. To keep this maximum global, (6) can be modified with possibilities suggested in (7) or modifying directly the original images and the parameters of these modifications can be optimized.

2.5. Rotated Images. The phase correlation function can be also used for estimation of image rotation and rescale. The method was first published by Reddy and Chatterji [20]. Let f_2 be function f_1 rotated and shifted in arguments; that is,

$$f_2(x; y) = f_1(x\cos\theta - y\sin\theta - x_0; x\sin\theta + y\cos\theta - y_0). \tag{12}$$

Their Fourier spectra and amplitude spectra are related as follows:

$$F_2(\xi; \eta) = \exp(-i(\xi x_0 + \eta y_0)) \cdot F_1(\xi\cos\theta - \eta\sin\theta; \xi\sin\theta + \eta\cos\theta), \qquad A_2(\xi; \eta) = A_1(\xi\cos\theta - \eta\sin\theta; \xi\sin\theta + \eta\cos\theta). \tag{13}$$

The shift results in a phase shift and the spectra are rotated in the same way as the original functions. A crucial step here is transformation of the amplitude spectra into the polar coordinate system to obtain functions $A_1^p; A_2^p : \mathbb{R}_0^+ \times \langle 0; 2\pi) \to \mathbb{R}_0^+$ such that $A_1^p(\rho; \varphi) = A_2^p(\rho; \varphi + \theta)$. The rotation around an unknown centre of rotation was transformed to a shift. This shift is estimated with the standard phase correlation, Section 2.4.; after rotating back by the measured angle, the shift $(x_0; y_0)$ is measured with another computation of the phase correlation.

2.6. Scaled Images. Let f_2 be function f_1 rotated, shifted, and scaled in arguments; that is,

$$f_2(x; y) = f_1(\alpha(x\cos\theta - y\sin\theta) - x_0; \alpha(x\sin\theta + y\cos\theta) - y_0). \tag{14}$$

Their Fourier spectra and amplitude spectra are related as follows:

$$F_2(\xi; \eta) = \frac{1}{\alpha^2}\exp(-i(\xi x_0 + \eta y_0)) \cdot F_1\left(\frac{1}{\alpha}(\xi\cos\theta - \eta\sin\theta); \frac{1}{\alpha}(\xi\sin\theta + \eta\cos\theta)\right), \qquad A_2(\xi; \eta) = \frac{1}{\alpha^2} \cdot A_1\left(\frac{1}{\alpha}(\xi\cos\theta - \eta\sin\theta); \frac{1}{\alpha}(\xi\sin\theta + \eta\cos\theta)\right). \tag{15}$$

The shift results in a phase shift; the spectra are rotated in the same way as the original functions and scaled with a reciprocal factor. A crucial step here is transformation of the amplitude spectra into the logarithmic-polar coordinate system

$$\exp\rho = \sqrt{x^2 + y^2}; \quad x = \exp\rho\cos\varphi; \quad y = \exp\rho\sin\varphi \tag{16}$$

to obtain $A_1^p; A_2^p : \mathbb{R}_0^+ \times \langle 0; 2\pi) \to \mathbb{R}_0^+$ such that $A_2^{1p}(\rho; \varphi) = A_2^{1p}(\rho - \ln\alpha; \varphi + \theta)$.

Both rotation and scale changes were transformed to a shift. The unknown angle θ and unknown factor α can be

estimated by means of the phase correlation applied on the amplitude spectra in the logarithmic-polar coordinate system $A_1^{1p}; A_2^{1p}$. After rotating function f_2 back by the estimated angle θ and scaling by factor α, the shift vector $(x_0; y_0)$ is estimated by means of the standard phase correlation, Section 2.4.

2.7. Practical Issues. Amplitude spectra of real functions are even functions $A(\xi; \eta) = A(-\xi; -\eta)$; therefore it is sufficient to use only a half of the domain of the spectra, for example, $\xi \geq 0$. If amplitude spectra (computed by means of the discrete Fourier transform) are transformed to polar coordinates, only a half of the domain on the angular axis is sufficient.

The amplitude spectra have very high values in $[0; 0]$ and its close neighbourhood compared to the rest of the domain; therefore instead of the values of the amplitude spectra it is better to use their logarithms $\ln(1 + A_1(\xi; \eta)); \ln(1 + A_2(\xi; \eta))$ to use the dynamic range of the amplitude spectra more effectively.

The discrete Fourier transform takes images as if they were periodic with period N on both axes. The image edges thus represent a jump in pixel values. Therefore, it is necessary to "remove" image edges, to smooth them out by multiplying them with so-called windowing functions. The most common are Gaussian and Hanning window functions. Most commonly they are applied radial-symmetrically. If there are important structures closer to image corners, they may also keep untouched a square or a rectangle and then decrease to zero.

Image pixel coordinates are integers but the scaling, rotation, and shift vector are obviously stated as not-integer values by registration. Therefore, values of pixels in the target image are calculated by various interpolation methods (nearest neighbour, bilinear or bicubic interpolation).

3. Results

The theory described in the previous section was applied to a series of 43 partially focused images of a sandstone sample (locality Brno-Hády, Czech Republic) which was acquired using a central projection in the viewing field 2,5 × 1,875 cm. The results are summarized in Table 1. We have identified mostly insignificant rotation (note that rotation of two hundred arc seconds around the centre means deviation of one-half pixel in the image with the resolution 1024 × 768); shift of the image centre is more significant.

The graph in Figure 8 illustrates the scaling for the individual image (relative to the first). It is not precisely linear in practice as was stated in Section 2.1 (see also Figure 6). In Figure 9 we can see the sum of four input images without registration (a) and the sum of the same images preprocessed using the registration method described in Section 3 (b).

The entire process of 2D and 3D processing of the series of the partially focused images acquired in central projection thus proceeds as follows:

(a) Preprocessing: registration of partially focused images using elementary mathematics (see Figure 6 on the left) simple but usually not precise enough method; or registration using the method proposed in Sections 2.2–2.7 in this paper.

(b) 2D reconstruction: Identification of sharp parts in separated images and composition of a new whole sharp 2D image (see [3, 4]).

Table 1: Scales, rotations, and shift vectors detected for the second to forty-third image (relative to the first).

Img. number	Scale	Angle (arc sec)	Shift vector (pixels)
2	0.99914	5.49	[−0.3; 0.5]
3	0.99757	14.77	[−0.1; 0.2]
4	0.99398	4.62	[0.3; 0.3]
5	0.99349	14.65	[0.5; 0.2]
6	0.99198	16.98	[0.6; 0.1]
7	0.98878	−6.44	[−1.6; 0.0]
8	0.98694	11.93	[1.7; 0.0]
9	0.98565	20.53	[0.5; 0.1]
10	0.98324	297.58	[0.4; 0.2]
11	0.98206	297.86	[0.4; 0.1]
12	0.97986	302.90	[0.3; 0.1]
13	0.97749	297.52	[0.3; 0.2]
14	0.97636	5.87	[0.1; 0.2]
15	0.97382	3.52	[0.1; 0.3]
16	0.97277	12.75	[0.1; 0.2]
17	0.97069	6.07	[0.0; 0.3]
18	0.96932	5.20	[−0.1; 0.4]
19	0.96716	4.13	[−0.2; 0.5]
20	0.96584	3.33	[−0.2; 0.6]
21	0.96372	3.10	[0.4; 0.7]
22	0.96156	−3.71	[−0.5; 0.7]
23	0.96036	−4.77	[0.2; 0.5]
24	0.95810	5.74	[0.1; 0.8]
25	0.95690	2.63	[0.0; 0.7]
26	0.95579	−14.45	[0.0; 0.5]
27	0.95358	4.72	[−2.3; 0.9]
28	0.95135	−9.62	[0.0; −0.9]
29	0.95020	−302.73	[−2.6; 0.5]
30	0.94808	3.41	[−1.0; 0.2]
31	0.94697	−13.04	[−1.1; 0.3]
32	0.94472	−6.45	[−1.1; 0.5]
33	0.94369	3.45	[−1.7; 0.5]
34	0.94134	4.95	[−1.6; 0.7]
35	0.94027	−4.22	[−1.1; 1.5]
36	0.93826	−4.97	[−1.3; 1.4]
37	0.93743	3.02	[−1.2; 1.5]
38	0.93669	−8.02	[−1.2; 1.5]
39	0.93419	9.59	[−1.3; 1.5]
40	0.93351	5.97	[−1.7; 1.0]
41	0.93093	11.41	[−1.3; 0.9]
42	0.93023	10.36	[1.3; 0.9]
43	0.92805	14.84	[−1.2; 0.7]

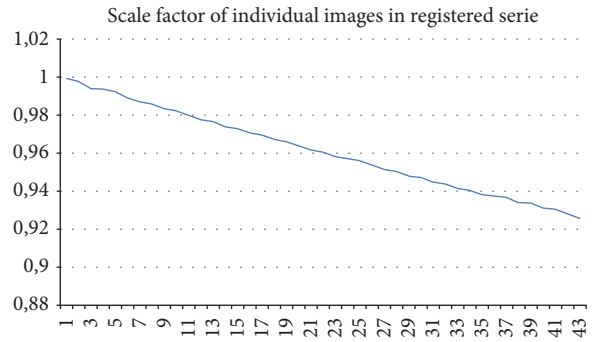

FIGURE 8: Scaling of individual images in processed serie, dependence is not precisely linear.

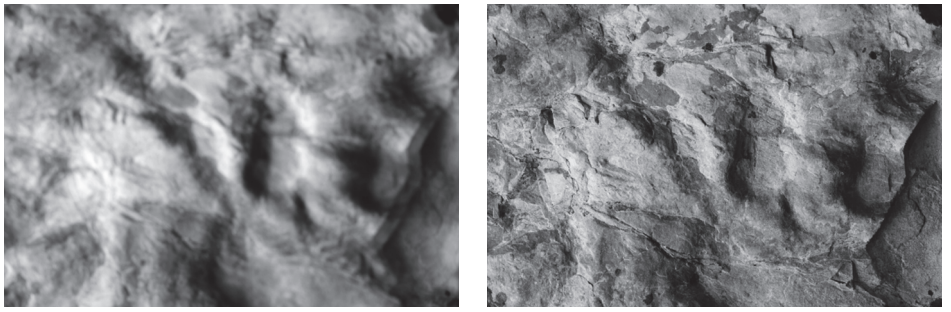

(a) (b)

FIGURE 9: Sum of first, tenth, twentieth, and fortieth partially focused photo of sandstone sample aquired in central projection: (a) no registration, (b) registration described in section 2 (first and forty-third image of this serie we can see in Figure 5).

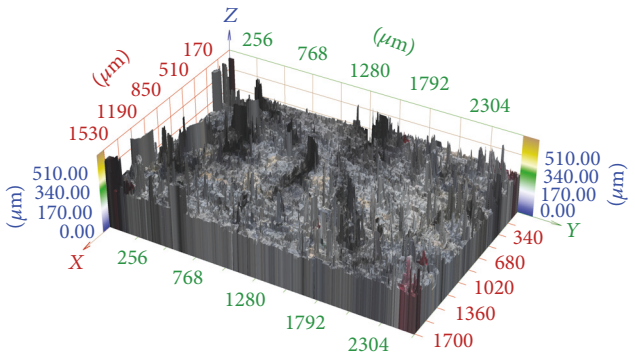

FIGURE 10: 3D reconstruction of image series aquired in central projection without any registration.

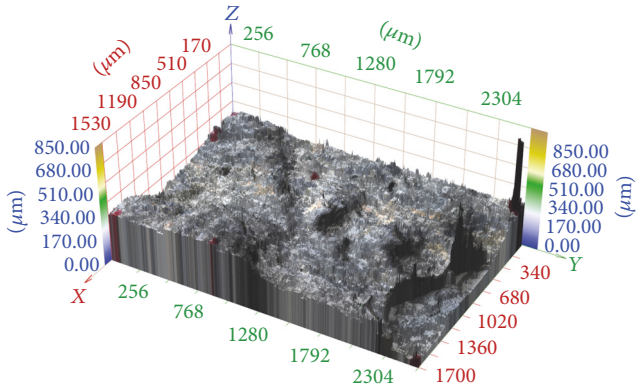

FIGURE 11: 3D reconstruction of image series aquired in central projection registered using elementary methods according to Figure 6 on the left.

(c) 3D reconstruction: Height is assigned to all the image points (see [1, 2, 4, 10]).

In Figure 10 we can see the 3D reconstruction of this series using the method described in [1, 2], that is, without any registration. The registration is not necessary in the case of confocal microscope images. However, images differ in scaling and rotation in the case of classic cameras and their 3D reconstruction without any registration is unusable.

In Figure 11, we can see the 3D reconstruction of the same series which was transformed using elementary mathematics according to Figure 6 on the left. The result is significantly better but artifacts are still evident.

In Figure 12, there is illustrated the 3D reconstruction of the same series which was registered using phase correlation described in Section 2. No artifacts are perspicuous in this reconstruction.

4. Conclusions

In the case of 3D reconstruction of a series of partially focused images of oversized surfaces, we usually cannot neglect the

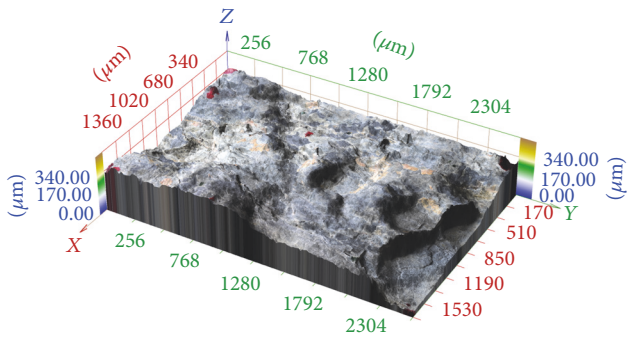

FIGURE 12: 3D reconstruction of image series aquired in central projection registered by phase correlation described in section 2.

angle between projection rays and therefore even the different scale of individual images. In the simplest case, we can assume that the scaling is linear and no other geometric transformations occur. This case can be solved using elementary methods but subsequent 3D reconstruction contains usually unwanted artifacts. In real devices, scaling is not linear and images can be shifted and even rotated with respect to each other. If accurate 3D reconstruction is required, precise image registration is necessary as preprocessing. Phase correlation is a suitable method for this preprocessing. It is able to detect the above-mentioned transformations with subpixel precision and we can neatly eliminate them.

Conflicts of Interest

There are no conflicts of interest related to this paper.

Acknowledgments

This work was supported by the Grant Agency of the Czech Republic under Contract no. 13-03403S. The authors acknowledge partial support from the Brno University of Technology, Specific Research Project no. FSI-S-14-2290 and Project LO1202 by financial means from the Ministry of Education, Youth and Sports under the National Sustainability Programme I. The authors thank Professor Tomáš Ficker from the Faculty of Civil Engineering of Brno University of Technology for the provided data.

References

[1] D. Martišek, J. Procházková, and T. Ficker, "High-quality three-dimensional reconstruction and noise reduction of multifocal images from oversized samples," *Journal of Electronic Imaging*, vol. 24, no. 5, Article ID 053029, 2015.

[2] T. Ficker and D. Martišek, "Three-dimensional reconstructions of solid surfaces using conventional microscopes," *Scanning*, vol. 38, no. 1, pp. 21–35, 2016.

[3] D. Martišek and H. Druckmüllerová, "Multifocal image processing," *Mathematics for Applications*, vol. 3, no. 1, pp. 77–90, 2014.

[4] D. Martišek, "The two-dimensional and three-dimensional processing of images provided by conventional microscopes," *Scanning*, vol. 24, no. 6, pp. 284–295, 2002.

[5] T. Ficker, D. Martišek, and H. M. Jennings, "Roughness of fracture surfaces and compressive strength of hydrated cement pastes," *Cement and Concrete Research*, vol. 40, no. 6, pp. 947–955, 2010.

[6] T. Ficker and D. Martišek, "Digital fracture surfaces and their roughness analysis: Applications to cement-based materials," *Cement and Concrete Research*, vol. 42, no. 6, pp. 827–833, 2012.

[7] Y. Ichikawa and J. Toriwaki, "Confocal microscope 3D visualizing method for fine surface characterization of microstructures," in *Proceedings of SPIE 2862, Flatness, Roughness, and Discrete Defect Characterization for Computer Disks, Wafers, and Flat Panel Displays*, pp. 96–101, Denver, Colo, USA.

[8] D. A. Lange, H. M. Jennings, and S. P. Shah, "Analysis of surface roughness using confocal microscopy," *Journal of Materials Science*, vol. 28, no. 14, pp. 3879–3884, 1993.

[9] K. Nadolny, "Confocal laser scanning microscopy for characterisation of surface microdiscontinuities of vitrified bonded abrasive tools," *International Journal of Mechanical Engineering and Robotics Research*, vol. 1, no. 1, pp. 14–29, 2012.

[10] M. Niederost, J. Niederöst, and J. Ščučka, "Automatic 3d reconstruction and visualization of microscopic objects from a macroscopic multificus image sequence," in *Proceedings of the International Archives of the Photogrammetry, Remote Sensing and spatial Information Sciences 34(5/W10)*, 2003.

[11] V. Thiéry and D. I. Green, "The multifocus imaging technique in petrology," *Computers and Geosciences*, vol. 45, pp. 131–138, 2012.

[12] T. Ficker and D. Martišek, "Computer Evaluation of Asperity Topology of Rock Joints," *Procedia Earth and Planetary Science*, vol. 15, pp. 125–132, 2015.

[13] J. K. Hunter and B. Nachtergaele, *Applied Analysis*, World Scientific Publishing Company, 1st edition, 2001.

[14] E. M. Stern and G. L. Weiss, *Introduction to Fourier Analysis on Euclidean Spaces*, Princeton University Press, Princeton, NJ, USA, 1975.

[15] H. Druckmüllerová, *Application of adaptive filters in processing of solar corona images [Ph.D. Thesis]*, Brno University of Technology, 2014.

[16] W. K. Pratt, *Digital Image Processing: PIKS Inside*, John Wiley & Sons, Inc., New York, USA, 3rd edition, 2001.

[17] B. Zitová and J. Flusser, "Image registration methods: a survey," *Image and Vision Computing*, vol. 21, no. 11, pp. 977–1000, 2003.

[18] M. V. Wyawahare, P. M. Patil, and H. K. Abhyankar, "Image registration techniques: an overview," *International Journal of Signal Processing, Image Processing and Pattern Recognition*, vol. 2, no. 3, 2009.

[19] C. D. Kuglin and D. C. Hines, "The phase correlation image alignment method," in *Proceeding of IEEE International Conference on Cybernetics and Society*, pp. 163–165, New York, NY, USA, 1975.

[20] B. S. Reddy and B. N. Chatterji, "An FFT-based technique for translation, rotation, and scale-invariant image registration," *IEEE Transactions on Image Processing*, vol. 5, no. 8, pp. 1266–1271, 1996.

3D Res (2016) 7:16
DOI 10.1007/s13319-016-0093-8

3DR EXPRESS

Elimination of Gibbs and Nyquist–Shannon Phenomena in 3D Image Reconstruction

Dalibor Martišek

Received: 15 January 2016 / Revised: 25 March 2016 / Accepted: 23 April 2016

Abstract Fracture surfaces are often modelled by Fourier two-dimensional (2D) series that can be converted into digital 3D reliefs mapping the morphology of solid surfaces. Such digital replicas may suffer from various artifacts when processed inappropriately. The Gibbs phenomenon and spatial aliasing are two of those artifacts that may devalue Fourier replicas. The Gibbs phenomenon involves the fact that Fourier sums overshoot at a jump discontinuity, and that this overshoot does not die out as the frequency increases. According to the Nyquist–Shannon sampling theorem spatial aliasing occurs when Fourier frequencies exceed the Nyquist critical frequency. In this paper it is shown how we can fully eliminate these unpleasant effects.

Graphical Abstract A new method for an approximation of fracture surfaces by a partial sum of the Fourier series which does not contain any Gibbs effects (a), any artefacts caused by convergence in the mean (b) and any alias (c). If number N of members of Fourier replica is equal to a resolution of a scanned original, the replica goes through the same points as the original. If it is higher, the original and replica differs in subpixel level only. Illustration (d) represents critical abrupt increases of aliasing artifacts in original 120×120 data matrix for sum of 480 members in case of standard Fourier series, case (e) is the sum of 480 members in the new series.

Electronic supplementary material The online version of this article (doi:10.1007/s13319-016-0093-8) contains supplementary material, which is available to authorized users.

D. Martišek (✉)
Faculty of Mechanical Engineering, Institute of Mathematics, Brno University of Technology, Technická 2, 616 69 Brno, Czech Republic
e-mail: martisek@fme.vutbr.cz

Published online: 11 May 2016

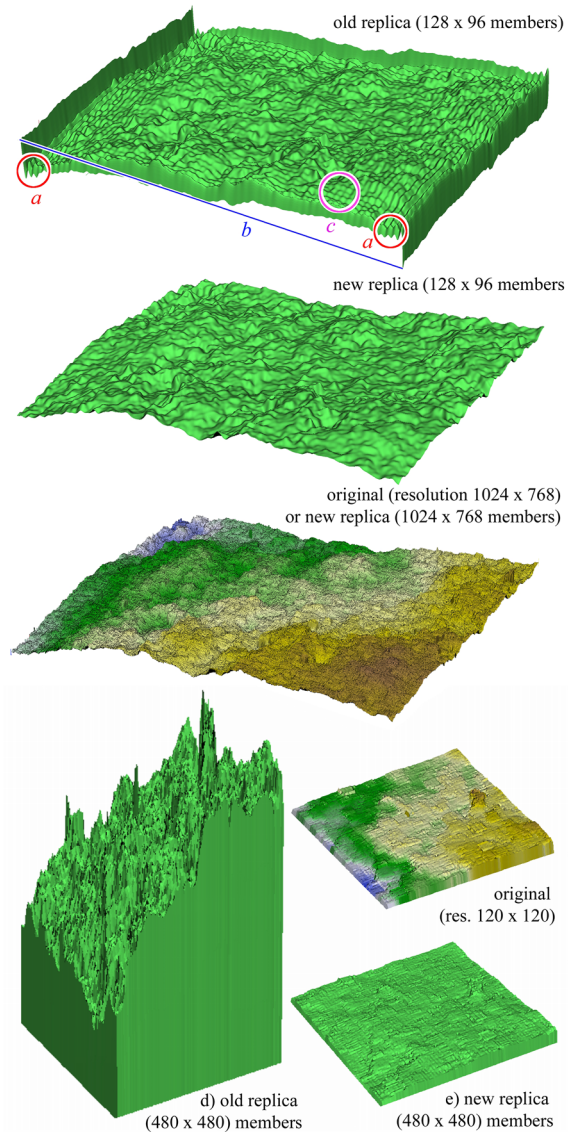

Keywords Gibbs phenomenon · Nyquist–Shannon theorem · Fourier 3D reconstructions · Spatial aliasing · 3D computations

1 Introduction

Gibbs oscillations [3, 7–10, 14, 16–18] and spatial aliasing [1, 4–6, 11, 12, 22–25] are some of possible drawbacks accompanying computations based on Fourier series. The Gibbs effect and aliasing are different phenomena but both have one thing in common: they both can very much degrade three-dimensional (3D) reconstruction using Fourier series.

It is known that the Fourier series $F(x)$ of a piecewise continuously differentiable function $f(x)$ on interval a, b converges to the arithmetic mean of left-hand and right-hand limits of $f(x)$ for $x \to x_0$ in point x_0. This convergence is called the piecewise convergence. The Gibbs phenomenon is caused by the fact that Fourier sums overshoot at a jump discontinuity, and that this overshoot does not die out as the frequency increases. At any jump point of a piecewise continuously differentiable function with a jump of a, the nth partial Fourier series will (for n very large) overshoot this jump by approximately $0.09 \cdot a$ at one end and undershoot it by the same amount at the other end; thus the "jump" in the partial Fourier series will also be about 9 % larger than the jump in the original function. At the location of the discontinuity itself, the partial Fourier series will converge to the midpoint of the jump (regardless of what the actual value of the original function is at this point). The quantity $g \approx 0.08949$ is sometimes known as the Wilbraham–Gibbs constant.

In this contribution, it is described how we can eliminate this phenomenon in conversion of a discretely scanned 3D surface relief into its continuous form.

Aliasing is an interesting artifact that deserves more attention since its action can be not only destructive but in some cases even useful when signal demodulation is to be performed. Spatial aliasing may occur as an unwanted effect when frequencies that are used during discrete 3D reconstructions exceed the value of the critical Nyquist frequency.

The classical interpretation of the Nyquist–Shannon theorem is related to the discretization (sampling) of continuous (analogue) signals. According to this theorem the discretization has to be performed with a sampling frequency v_S that is at least twice as high as the highest frequency (bandwidth) v_B of the analogue signal, i.e., $v_S \geq 2v_B$. The sampling frequency v_S of a sampling device (e.g., A/D converter) is usually called the Nyquist rate. It means that the sampling device with the Nyquist rate v_S is capable of correctly reproducing only those analogue signals whose bandwidths v_B are no more than one half of the Nyquist rate, i.e., $v_B \leq v_S/2$. The half of the Nyquist rate $v_S/2$ is usually called the Nyquist frequency. Analogue signals whose bandwidths exceed the Nyquist frequencies reportedly

cannot be successively converted into discrete forms [12].

However, there are opposite situations in which discrete signals are to be converted back into continuous forms (e.g., D/A converters). In these inverse procedures the sampling frequency of a discrete signal corresponds to the Nyquist rate and the reconstructed continuous form of the signal is therefore limited by one half of the sampling frequency of the discrete signal. The same rule holds also for other similar inverse procedures, e.g., when the discretely scanned 3D surface relief is to be converted into its continuous form using the 3D reconstruction procedure based on the Fourier 2D partial sum. In this case the highest frequency included in the Fourier partial sum has not to exceed one half of the sampling frequency of the scanned 3D relief. Exceeding this Nyquist frequency aliasing effects occur and, as a consequence, the Fourier replica will show flaws, as is explained in Ficker et al. [12] for example.

We will show that this classical interpretation is not quite right and a discrete signal can be converted to an arbitrary long Fourier series without Nyquist–Shannon aliasing.

2 Experimental Details

In fractography, the surfaces of fracture remnants are analyzed by various techniques, among which image recognition may serve as a useful source of morphological information. Fracture surfaces are usually scanned by a 3D technique. The confocal microscope Olympus Lext 3100 was used to create discrete digital 3D reliefs $f(x_i; y_j)$ in this case. This microscope works in two modes: confocal and normal (non-confocal). In the confocal mode, the microscope measures the height of single points using the reflection of the laser beam from the measured surface with the user-defined accuracy (step in z-axis). In the normal mode, the microscope works as a conventional optical device, e.g., a CCD camera or classic microscope.

The normal mode of the Olympus Lext 3100 was used and discrete digital 3D reliefs were constructed by our original software [20]. All the following outputs including Excel graphs were constructed in this software (Excel was used as an output device only).

The segments of digital confocal images were used with resolutions 120 × 120, 228 × 228 and 1024 × 764 pixels. The spatial resolution of these digital images was 1 μm or 2.5 μm per pixel, respectively.

Small pieces of fracture surfaces of hydrated Portland cement paste were used as tested species but any other fractured solid materials could be suitable for the study of aliasing effects manifested in the 3D digital images.

3 Current State of Knowledge

To enable Fourier analysis of fracture surfaces, the scanned reliefs $f(x_i, y_j)$; for $i = 0, 1,\ldots,W-1$ and $j = 0, 1,\ldots, H-1$ are possible to expand into Fourier partial sums SF_N (**S**tandard **F**ourier sum) combining both the sine and cosine harmonics

$$f(x_i, y_j) \approx SF_N(x_i, y_j) = \sum_{k,n=0}^{N-1} \lambda_{kn}\left(a_{kn}\cos\frac{k\pi x_i}{p}\cos\frac{n\pi y_i}{q} + b_{kn}\sin\frac{k\pi x_i}{p}\cos\frac{n\pi y_i}{q} + c_{kn}\cos\frac{k\pi x_i}{p}\sin\frac{n\pi y_i}{q} + d_{kn}\sin\frac{k\pi x_i}{p}\sin\frac{n\pi y_i}{q}\right), \tag{1}$$

where

$$\lambda = \begin{cases} 1 & k,\ n > 0, \\ 1/2 & k\cdot n = 0,\ k+n \neq 0, \\ 1/4 & k = n = 0, \end{cases}$$

$$a_{k,n} = \frac{1}{pq}\iint_{\Omega} f(x,\ y)\cos\frac{k\pi x}{p}\cos\frac{n\pi y}{q}\,\mathrm{d}x\mathrm{d}y,$$

$$b_{k,n} = \frac{1}{pq}\iint_{\Omega} f(x,\ y)\sin\frac{k\pi x}{p}\cos\frac{n\pi y}{q}\,\mathrm{d}x\mathrm{d}y,$$

$$c_{k,n} = \frac{1}{pq}\iint_{\Omega} f(x,\ y)\cos\frac{k\pi x}{p}\sin\frac{n\pi y}{q}\,\mathrm{d}x\mathrm{d}y,$$

$$d_{k,n} = \frac{1}{pq}\iint_{\Omega} f(x,\ y)\sin\frac{k\pi x}{p}\cos\frac{n\pi y}{q}\,\mathrm{d}x\mathrm{d}y, \tag{2}$$

and

$$\Omega = (-p,\ p)\times(-q,\ q), \tag{3}$$

is a ground plan of the scanned relief, or CF_N (**C**osine **F**ourier sum): Fourier partial sums in cosine base

$$f(x_i, y_j) \approx CF_N(x_i, y_j) = \sum_{k,n=0}^{N-1} \lambda_{kn}a_{kn}\cos\frac{k\pi x_i}{p}\cos\frac{n\pi y_j}{q}, \tag{4}$$

$$\lambda_{kn} = \begin{cases} 4 & k,\ n > 0, \\ 2 & k \cdot n = 0,\ k + n \neq 0, \\ 1 & k = n = 0, \end{cases} \tag{5}$$

$$a_{kn} = \frac{1}{pq} \iint_{\Omega} f(x,\ y) \cos\frac{k\pi x}{p} \cos\frac{n\pi y}{q} \mathrm{d}x\mathrm{d}y, \tag{6}$$

where

$$\Omega = (0,\ p) \times (0,\ q), \tag{7}$$

is a ground plan of the scanned relief [13].

For an analysis of aliasing artifacts manifested in Fourier replicas it is not sufficient to perform a visual inspection. Therefore, two height characteristics of the 3D profiles are introduced as numerical indicators of spatial aliasing in the present study:

$$H_a(N) = \frac{1}{pq} \sum_{i=0}^{K-1} \sum_{j=0}^{N-1} \left| f(x_i,\ y_j) - F_N(x_i,\ y_j) \right|, \tag{8}$$

$$H_q(N) = \sqrt{\frac{1}{pq} \sum_{i=0}^{K-1} \sum_{j=0}^{N-1} \left[f(x_i,\ y_j) - F_N(x_i,\ y_j) \right]^2}, \tag{9}$$

where $f(x_i, y_j)$ are heights of the analysed surface and $F_N(x_i, y_j)$ means $SF_N(x_i, y_j)$ or $CF_N(x_i, y_j)$ according to the used Fourier base.

From a statistical point of view, expression (8) is the average distance of f and F_N, expression (9) is the standard deviation. From a functional analysis point of view, these expressions are the distances of these surfaces in Manhattan (8) or Euclidean (9) metrics.

For the study of these distances, a so-called characteristic matrix

$$M_N(k,\ n) = \lambda_{kn} \sqrt{a_{kn}^2 + b_{kn}^2 + c_{kn}^2 + d_{kn}^2}, \tag{10}$$

was constructed in Ficker et al. [12].

In Fig. 1 on the left we can see a sample of fracture surface with the resolution of 228 × 228. On the right, there is the reconstruction by (1) with $N = 100$. For convergence it is necessary that $M_N(k, n) \to 0$ for k, $n \to \infty$ as is illustrated in Fig. 2, where a graph of $M_N(k, n)$ values was constructed. In the case of convergence, both parameters $H_a(N)$, $H_q(N)$ must go to zero for $N \to \infty$. This fact is illustrated in Table 1.

For calculating (2), (5), numerical integration is obviously used, 2D version of rectangle rule

$$\iint_{(-p,\ p)\times(-q,\ q)} g(x,\ y)\mathrm{d}x\mathrm{d}y \approx \sum_{i=0}^{W-1} \sum_{j=0}^{H-1} g(x_i,\ y_i), \tag{11}$$

was used in previous research [13, 20].

Let us study some results of this method. Take a sample with the resolution of 120 × 120 and let us compute SF_{90} and series $H_a(N)$, $H_q(N)$ for $N = 5$, 10,…,90 (see Table 2; Fig. 3). As is shown, parameters $H_a(N)$, $H_q(N)$ do not go to zero. They have a clear minimum for $N = 60$; their values are worsened by alias for higher N. It is totally in harmony with the sampling theorem.

Take the same sample and compute $H_a(N)$. $H_q(N)$ for higher N: $N = 10$, 20,….,480. We will discover "higher critical" and "resonance" frequencies $M_N\left(a \cdot \frac{v_S}{2},\ b \cdot \frac{v_S}{2}\right)$; $a, b = 0, 1, 2,\ldots$ where M_N is the characteristic matrix: see (10). In Fig. 4, we can see the graph of $M_{500}(k, n)$, for SF_{500}, for a surface scanned with resolution 120 × 120; where the resonance frequencies are very clear.

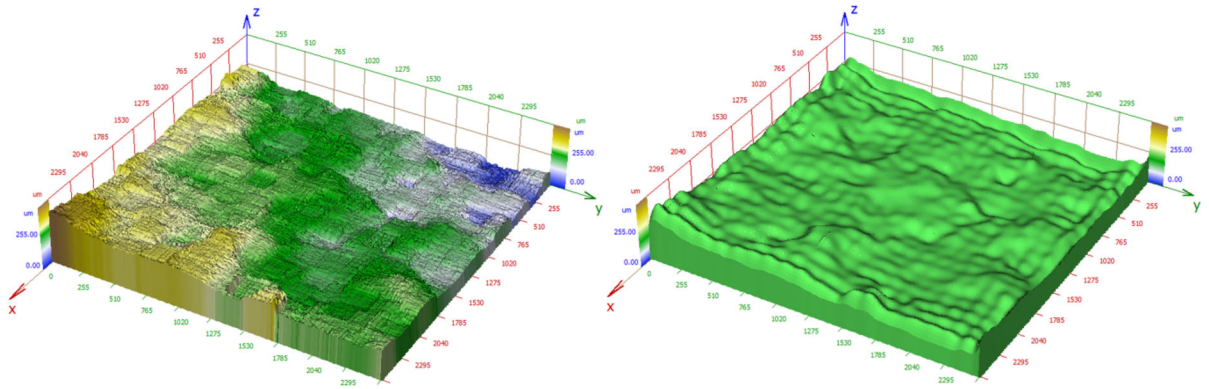

Fig. 1 Profile with resolution of 228 × 228 (on the *left*), its SF_N for $N = 20$ (on the *right*)

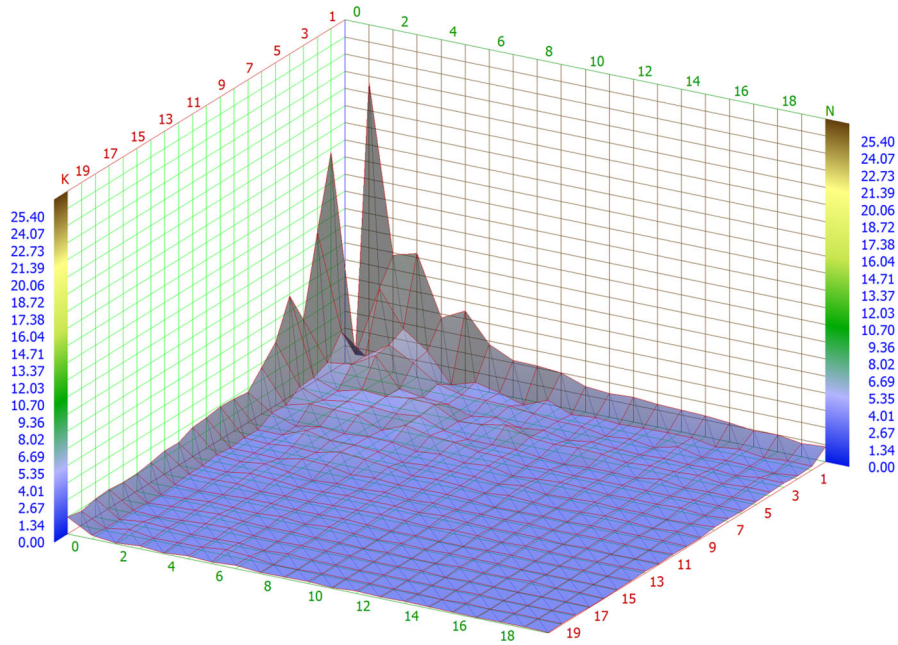

Fig. 2 Graph of $M_N(k, n)$ for SF_N from Fig. 1 [$M_N(0, 0)$ is skipped for its height]

Table 1 Values of $M_N(k, n)$ from Fig. 2 drop for growing n and k (illustrative submatrix)

	k = 0	k = 1	k = 2	k = 3	k = 4	k = 5	k = 6	k = 7	k = 8	k = 9
n = 0	172.803	41.476	28.763	16.783	13.506	10.480	8.985	5.675	4.039	5.797
n = 1	17.225	40.057	27.969	13.167	6.131	8.053	6.615	4.672	2.873	3.663
n = 2	2.533	13.762	9.720	2.544	2.731	5.665	3.634	1.666	2.470	1.029
n = 3	7.861	9.639	7.134	3.038	2.610	5.535	1.797	1.508	2.032	0.919
n = 4	4.028	5.631	4.092	2.351	1.815	2.476	3.171	1.525	3.116	1.753
n = 5	4.187	5.345	6.980	2.555	1.732	0.983	1.550	1.467	0.464	1.445
n = 6	3.409	2.362	3.484	2.215	0.527	2.394	1.184	1.942	0.824	1.160
n = 7	3.773	2.722	3.978	2.275	1.544	1.359	1.564	0.890	0.545	1.136
n = 8	2.634	3.147	2.797	1.311	1.023	0.713	1.041	0.798	0.913	0.426
n = 9	2.844	2.576	3.356	0.942	1.517	0.970	0.657	1.286	0.905	0.434

In Tables 3 and 4, we can see values of the $M_N(k, n)$ matrix for a surface scanned at the resolution 120 × 120; where $N > 180$. There is $\frac{v_S}{2} = 60$. Frequencies $\left(a \cdot \frac{v_S}{2}, b \cdot \frac{v_S}{2}\right)$, where at least one of the numbers a, b is odd, are critical, the other one means the resonance. First resonance, value $M_N(0, 0) = 172, 803$, is the arithmetic mean of surface heights in μm. The values $M\left(a \cdot \frac{v_S}{2}, b \cdot \frac{v_S}{2}\right)$ in higher critical frequencies $\left(a \cdot \frac{v_S}{2}, b \cdot \frac{v_S}{2}\right)$ where both of a, b are not even, are marked in bright yellow in Table 3. Resonance frequencies, i.e., $\left(a \cdot \frac{v_S}{2}, b \cdot \frac{v_S}{2}\right)$ where both of a, b are even, are marked in dark blue in Table 4.

Consequence of the sampling resonances, $H_a(N)$, $H_q(N)$ show abrupt 'jumps' at specific points $N = 120$, 240, 360, 480,… (see Fig. 5) and the same jumps we can see in heights of SCF_N in the same points (see Fig. 6).

Many papers deal with decreasing the Gibbs phenomenon [7, 15] and Shannon–Nyquist aliasing [1, 2, 4, 5, 19, 21, 23, 25]. We will show that it is possible to fully eliminate these unpleasant effects in the case of conversion of the discretely scanned surfaces into their continuous form.

Table 2 Values of series $H_a(N)$, $H_q(N)$, for SF_N, $N = 5, 10,\ldots,90$ (surface was scanned with resolution 120 × 120)

N	5	10	15	20	25	30	35	40	45
Ha	22.95	14.89	11.95	10.36	9.12	8.46	7.73	6.96	5.27
Hq	35.49	24.90	20.73	17.94	16.17	14.16	12.68	11.36	7.81
N	50	55	60	65	70	75	80	85	90
Ha	2.20	1.67	0.61	1.88	2.50	3.07	3.61	4.12	4.69
Hq	3.25	2.50	0.79	2.58	3.65	4.71	5.49	6.41	7.59

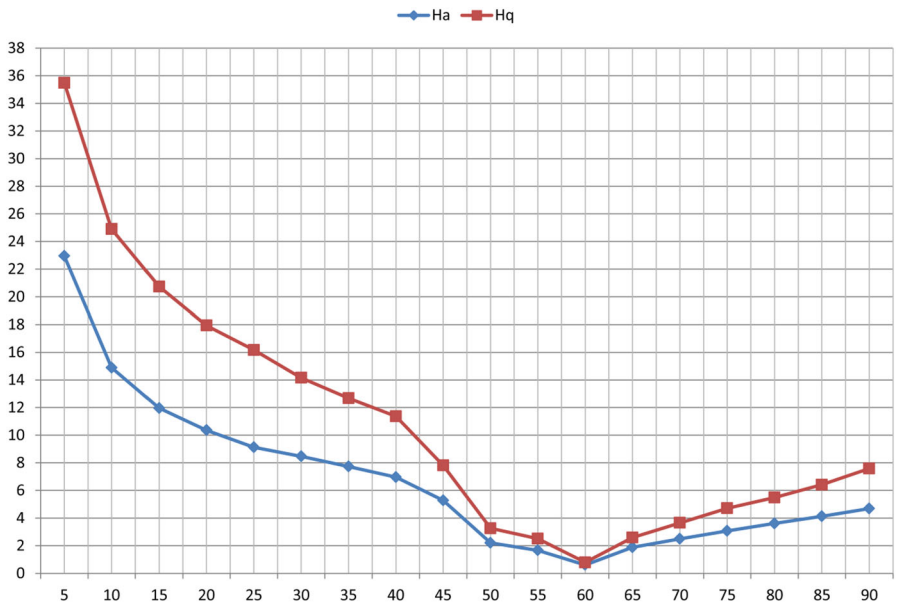

Fig. 3 Graph of series $H_a(N)$, $H_q(N)$, for SF_N, $N = 5, 10,\ldots,90$ (surface was scanned at the resolution 120 × 120)

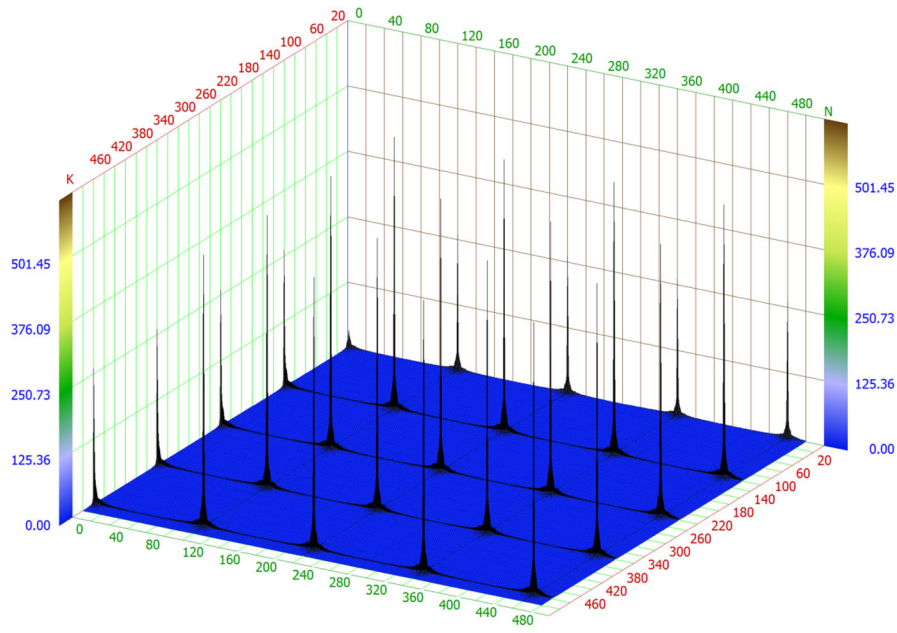

Fig. 4 Graph of $M_{500}(k, n)$, for SF_{500} (surface was scanned at the resolution 120 × 120)

Table 3 Frequencies for surface scanned at the resolution 120 × 120 and expanded to SF_N for $N > 180$

	k=0	k=1	k=2	....	k=58	k=59	k=60	k=61	k=62	....	k=178	k=179	k=180	k=181	k=182
n=0	172,803	41,476	28,763	....	1,153	1,299	1,167	1,299	1,153	....	1,153	1,299	1,167	1,299	1,153
n=1	17,225	40,057	27,969	....	0,814	0,798	1,287	0,798	0,814	....	0,814	0,798	1,287	0,798	0,814
n=2	2,533	13,762	9,720	....	0,492	0,684	0,341	0,684	0,492	....	0,492	0,684	0,341	0,684	0,492
....	....	....	....	....	....	....	....	....	....	....	....	....	....	....	....
n=58	0,447	0,555	0,651	....	0,108	0,048	0,169	0,048	0,108	....	0,108	0,048	0,169	0,048	0,108
n=59	0,565	0,543	0,463	....	0,107	0,138	0,091	0,138	0,107	....	0,107	0,138	0,091	0,138	0,107
n=60	0,010	0,701	0,764	....	0,076	0,057	0,159	0,057	0,076	....	0,076	0,057	0,159	0,057	0,076
n=61	0,565	0,543	0,463	....	0,107	0,138	0,091	0,138	0,107	....	0,107	0,138	0,091	0,138	0,107
n=62	0,447	0,555	0,651	....	0,108	0,048	0,169	0,048	0,108	....	0,108	0,048	0,169	0,048	0,108
....	....	....	....	....	....	....	....	....	....	....	....	....	....	....	....
n=178	0,447	0,555	0,651	....	0,108	0,048	0,169	0,048	0,108	....	0,108	0,048	0,169	0,048	0,108
n=179	0,565	0,543	0,463	....	0,107	0,138	0,091	0,138	0,107	....	0,107	0,138	0,091	0,138	0,107
n=180	0,010	0,701	0,764	....	0,076	0,057	0,159	0,057	0,076	....	0,076	0,057	0,159	0,057	0,076
n=181	0,565	0,543	0,463	....	0,107	0,138	0,091	0,138	0,107	....	0,107	0,138	0,091	0,138	0,107
n=182	0,447	0,555	0,651	....	0,108	0,048	0,169	0,048	0,108	....	0,108	0,048	0,169	0,048	0,108

Higher critical values in the matrix $M_N(k, n)$ are marked inbright yellow

Table 4 Resonance frequencies for surface scanned at the resolution 120 × 120 and expanded to SF_N for $N > 180$ resonance values in the matrix $M_N(k, n)$ for $N > 180$ are marked in dark blue

	k=0	k=1	k=2	....	k=118	k=119	k=120	k=121	k=122	....	k=238	k=239	k=240	k=241	k=242
n=0	172,803	41,476	28,763	....	28,763	41,476	345,607	41,476	28,763	....	28,763	41,476	345,607	41,476	28,763
n=1	17,225	40,057	27,969	....	27,969	40,057	34,449	40,057	27,969	....	27,969	40,057	34,449	40,057	27,969
n=2	2,533	13,762	9,720	....	9,720	13,762	5,066	13,762	9,720	....	9,720	13,762	5,066	13,762	9,720
....	....	....	....	....	....	....	....	....	....	....	....	....	....	....	....
n=118	2,533	13,762	9,720	....	9,720	13,762	5,066	13,762	9,720	....	9,720	13,762	5,066	13,762	9,720
n=119	17,225	40,057	27,969	....	27,969	40,057	34,449	40,057	27,969	....	27,969	40,057	34,449	40,057	27,969
n=120	345,607	82,952	57,526	....	57,526	82,952	691,214	82,952	57,526	....	57,526	82,952	691,214	82,952	57,526
n=121	17,225	40,057	27,969	....	27,969	40,057	34,449	40,057	27,969	....	27,969	40,057	34,449	40,057	27,969
n=122	2,533	13,762	9,720	....	9,720	13,762	5,066	13,762	9,720	....	9,720	13,762	5,066	13,762	9,720
....	....	....	....	....	....	....	....	....	....	....	....	....	....	....	....
n=238	2,533	13,762	9,720	....	9,720	13,762	5,066	13,762	9,720	....	9,720	13,762	5,066	13,762	9,720
n=239	17,225	40,057	27,969	....	27,969	40,057	34,449	40,057	27,969	....	27,969	40,057	34,449	40,057	27,969
n=240	345,607	82,952	57,526	....	57,526	82,952	691,214	82,952	57,526	....	57,526	82,952	691,214	82,952	57,526
n=241	17,225	40,057	27,969	....	27,969	40,057	34,449	40,057	27,969	....	27,969	40,057	34,449	40,057	27,969
n=242	2,533	13,762	9,720	....	9,720	13,762	5,066	13,762	9,720	....	9,720	13,762	5,066	13,762	9,720

4 Imperfections of Current Methods and Their Elimination

4.1 Ground Plan of Samples

Partial Fourier sums (1), (4) are suitably used in the case of samples with a squared ground plan, i.e., in the case of $p = q$—see conditions (3) and (7). If the ground plan is not squared ($p \neq q$) then the "density" of Fourier frequencies is different on its sides and reconstruction by sum (1) or (4) is destroyed by artificial waves (not by alias or Gibbs effect) unnecessarily. This fact is illustrated in Fig. 7. The profile to be reconstructed is modelled as the function $f(x, y) = \exp(-x^2 - y^2)$ which is defined on $(-16, 16) \times (-4, 4)$—see Fig. 7 on the left.

This surface was reconstructed by SF_N for $K = N = 10$—see Fig. 7 in the middle. For lack of frequencies along the longer side we can see clear artificial waves. This phenomenon can be decreased very simply when in place of expression (1) (SF_N) or expression (4) (CF_N) expressions

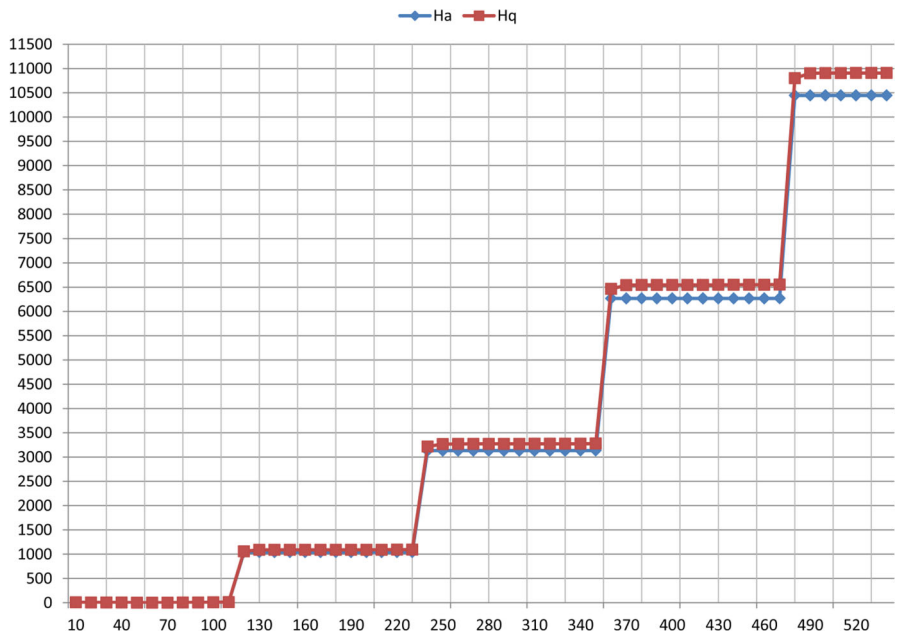

Fig. 5 Jumps of $H_a(N)$, $H_q(N)$ for SF_N for $N = 10, 20,\ldots,540$ for surface scanned at the resolution 120×120 in resonance frequencies $\left(a \cdot \frac{v_s}{2},\ b \cdot \frac{v_s}{2}\right)$; for $a = b = 2, 4,\ldots$

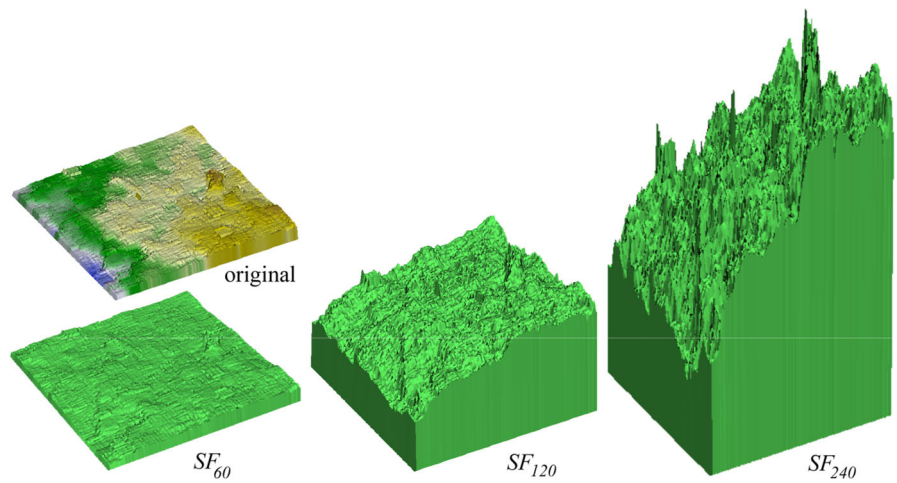

Fig. 6 Original fracture surface scanned at the resolution 120×120 and its SF_N. SF_{60} has a correct height, heights of SF_{120}, SF_{240}, SF_{380},... are multiplied because of sampling resonances

$$f(x_i;y_j) \approx SF_{KN}(x_i;y_j) = \sum_{k=0}^{K-1}\sum_{n=0}^{N-1}\lambda_{kn} \times \left(a_{kn}\cos\frac{k\pi x_i}{p}\cos\frac{n\pi y_j}{q} + b_{kn}\sin\frac{k\pi x_i}{p}\cos\frac{n\pi y_j}{q} + c_{kn}\cos\frac{k\pi x_i}{p}\sin\frac{n\pi y_j}{q} + d_{kn}\sin\frac{k\pi x_i}{p}\sin\frac{n\pi y_j}{q}\right), \quad (12)$$

$$f(x_i,\ y_j) \approx CF_{KN}(x_i,\ y_j) = \sum_{k=0}^{K-1}\sum_{n=0}^{N-1}\lambda_{kn}a_{kn}\cos\frac{k\pi x_i}{p}\cos\frac{n\pi y_j}{q}, \quad (13)$$

are used. It is necessary to meet the condition $K/N = p/q$. In Fig. 7 on the right we can see the result of SF_{KN} application for $K = 20$, $N = 5$. The total number of added members is equal to the previous case (100 addends) but the result is significantly better.

In the case of SF_N, it is possible to achieve the same quality for $N \geq 20$ (i.e., for min. 400 addends) only.

4.2 Convergence of Fourier Series

Research of SF_N is often preferred at present. In many cases, CF_N is used as a supplementary method only,

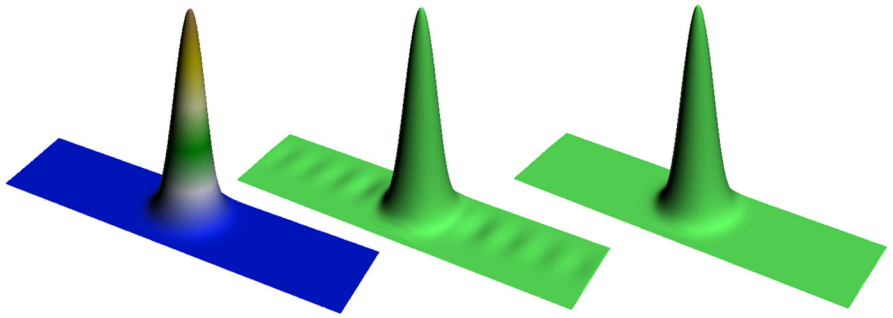

Fig. 7 Artificial waves caused by application of (1) to a surface with a *rectangular* ground plan. On the *left* the original surface, in the middle SF_{10}. On the *right* SF_{KN} for $K = 20$, $N = 5$. Total number of added members is equal to SF_{10}, the result is significantly better

because CF_N allegedly also suffers from the Gibbs effect [12]. However, this assertion is quite false. We use Dirichlet's theorem to disprove this opinion.

Theorem (Dirichlet) *The Fourier series $F(x)$ of a piecewise continuous function $f(x)$ on interval a, b converges to the arithmetic mean of left-hand and right-hand limits of $f(x)$ for $x \to x_0$; i.e.,*

$$F(x_0) = \frac{1}{2}\left[\lim_{x\to x_0^-} f(x) + \lim_{x\to x_0^+} f(x)\right]. \tag{14}$$

If $f(x)$ is discontinuous in x_0 then $\lim_{x\to x_0^-} f(x) \neq \lim_{x\to x_0^+} f(x)$ and $F(x)$ converges to the arithmetic mean of these limits (convergence in the mean). If $f(x)$ is continuous in x_0 then $\lim_{x\to x_0^-} f(x) = \lim_{x\to x_0^+} f(x)$ and $F(x)$ converges to the $f(x_0)$ in x_0. In the case of 2D by analogy.

The Fourier series converges in the same way to periodic extension of $f(x)$ on $(-\infty, \infty)$. The periodic extension of continuous fracture surface which is expanded to SF_{KN} (odd extension) is generally not continuous. In Fig. 8 on the left, we can see the periodic extension of function $f(x) = x \cdot y$ defined on $\Omega = (-p, p) \times (-q, q)$. Due discontinuities on the surface boundary, SF_{KN} does not converge to surface points here, but to the arithmetic mean of opposite boundary points (so-called convergence in the mean). Therefore, for parameters $H_a(N)$, $H_q(N)$ and arbitrary finite N is

$$H_a(N) \geq \frac{1}{K}\sum_{i=0}^{K-1} |f(x_i,\ 0) - f(x_i,\ p)| + \frac{1}{N}\sum_{j=0}^{N-1} |f(0,\ y_j) - f(q,\ y_j)|,$$

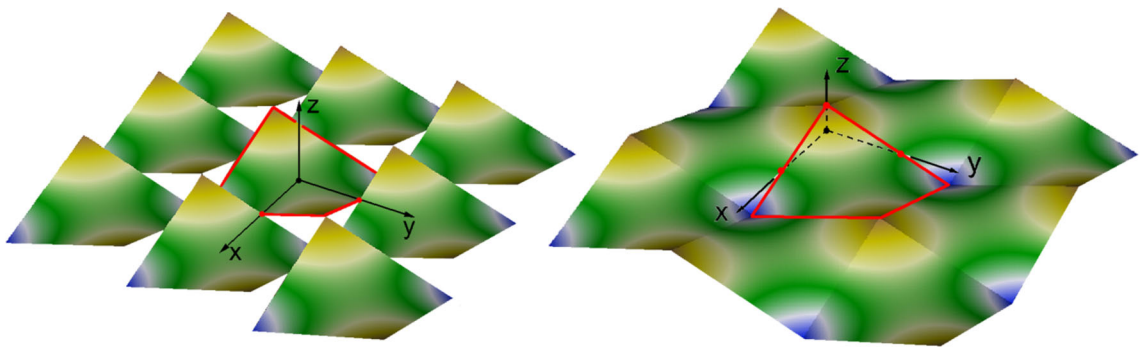

Fig. 8 Different periodic extensions of the profile to be expanded (*red perimeter*). On the *left* discontinuous odd extension by SF_{KN}, on the *right* continuous even extension by CF_{KN}

$$H_q(N) \geq \frac{1}{\sqrt{KN}} \sqrt{\sum_{i=0}^{K-1}[f(x_i, 0) - f(x_i, p)]^2 + \sum_{j=0}^{N-1}[f(0, y_j) - f(q, y_j)]^2}.$$

These values are $H_a(N) \geq 0.61$ and $H_q(N) \geq 0.79$ for our surface scanned at the resolution 120 × 120—see Table 2 and Fig. 3. These values may be equal to zero only and if only when for all x_i, y_j is $f(x_i, 0) = f(x_i, p)$ and $f(0, y_j) = f(q, y_j)$. These conditions are realisable in theoretical cases only. In practice, SF_{KN} is discontinuous and therefore suffers from the Gibbs effect.

Periodic extension of continuous fracture surface which is expanded to CF_{KN} is always continuous. Therefore, CF_{KN} cannot suffer from the Gibbs effect. Note the function $f(x) = x \cdot y$ defined on $\Omega = (-p, p) \times (-q, q)$ must be transformed to function $g(x) = (x - p/2) \cdot (y - q/2)$ defined on $\Omega = (0, p) \times (0, q)$ for this extension.

In Fig. 9 we can visually compare the convergence of discontinuous SF_{KN} and continuous CF_{KN} for the same profile. $K = N = 25$ in both cases. On the left we can clearly see the convergence in the mean (zeroed boundaries) and the Gibbs effect with its artifacts. On the right CF_{KN} converges in each point $[x_i, y_i]$ to $g(x_i, y_i)$. Therefore, CF_{KN} does no suffer from the Gibbs effect and does not have its artifacts.

In Table 5 we can see the values of $H_a(N)$, $H_q(N)$ for CF_{KN} expansions where $K = N = 10, 20, \ldots, 180$ for the same surface as in Table 2 and Fig. 3.

In Fig. 10, a graph is constructed of the series $H_a(N)$, $H_q(N)$, $N = 10, 20, \ldots, 180$ for CF_{120}. We can compare Table 5 and Fig. 10 with the corresponding Table 2 and Fig. 3 for SF_{60}—values of corresponding $H_a(N)$, $H_q(N)$ for CF_{120} are significantly smaller than for SF_{60}. Values of the parameters H_a, H_q for the SF are the minimum 0.61 or 0.79, respectively for $N = 60$. This means that the SF does not go through given points either in $N = 60$ (the sampling frequency for the resolution 120 × 120), nor anywhere else. This is a consequence of Gibbs phenomenon and the alias.

For the CF, the Nyquist frequency is given by $N = 120$ in the case of 120 × 120 sample resolution. It is twice as high as for SF but it is right—a wave length of the first SF_N member is equal to the sample side, the wave length of first CF_N member is twice as long, i.e., CF_N needs two times more members to reach

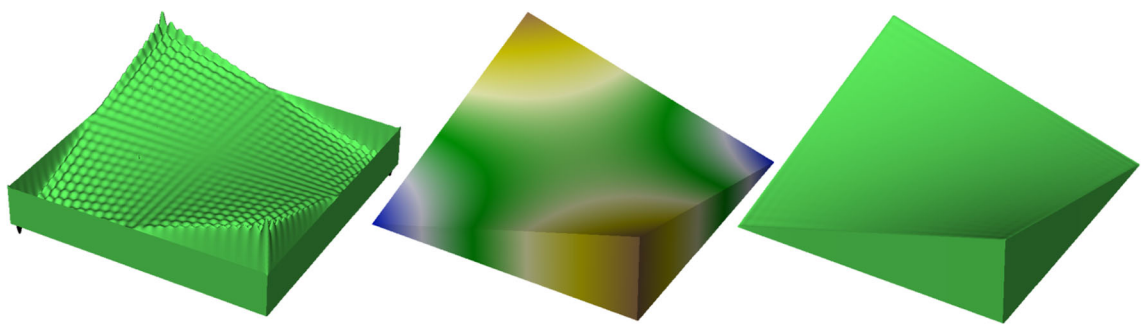

Fig. 9 "Original profile" modelled by the function $f(x, y) = x \cdot y$ (in the *middle*) was expanded by SF_{KN} (on the *left*) and by CF_{KN} (on the *right*). $K = N = 25$ in both cases

Table 5 Values of series $H_a(N)$, $H_q(N)$, $N = 10, 20, \ldots, 180$ for CF_{120}

N	10	20	30	40	50	60	70	80	90
Ha	13.54	9.07	7.79	7.13	6.42	5.96	5.56	5.08	4.43
Hq	18.43	12.78	11.18	10.27	9.34	8.71	8.03	7.25	6.24
N	100	110	120	130	140	150	160	170	180
Ha	3.67	2.72	0.00	3.04	4.35	5.59	6.71	7.81	8.77
Hq	5.05	3.65	0.00	4.12	6.01	7.94	9.70	11.52	13.10

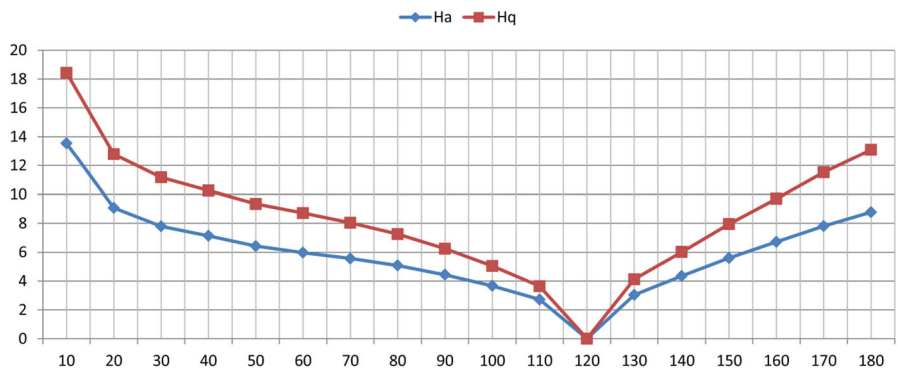

Fig. 10 Graph of series $H_a(N)$, $H_q(N)$, $N = 10, 20,\ldots,180$ for CF_{120}

Table 6 Frequencies for surface scanned at the resolution 120 × 120 and expanded to CF_N for $N > 240$

	k=0	k=1	k=2	....	k=118	k=119	k=120	k=121	k=122	....	k=238	k=239	k=240	k=241	k=242
n=0	172,803	57,289	3,972	....	0,077	0,063	0,000	0,063	0,077	....	0,077	0,063	0,000	0,063	0,077
n=2	12,820	50,220	9,053	....	0,298	0,126	0,000	0,126	0,298	....	0,298	0,126	0,000	0,126	0,298
n=3	15,070	9,627	12,416	....	0,345	0,434	0,000	0,434	0,345	....	0,345	0,434	0,000	0,434	0,345
....	....	....	....	....	....	....	....	....	....	....	....	....	....	....	....
n=118	0,053	0,066	0,374	....	0,012	0,007	0,000	0,007	0,012	....	0,012	0,007	0,000	0,007	0,012
n=119	0,314	0,039	0,159	....	0,005	0,066	0,000	0,066	0,005	....	0,005	0,066	0,000	0,066	0,005
n=120	0,000	0,000	0,000	....	0,000	0,000	0,000	0,000	0,000	....	0,000	0,000	0,000	0,000	0,000
n=121	0,314	0,039	0,159	....	0,005	0,066	0,000	0,066	0,005	....	0,005	0,066	0,000	0,066	0,005
n=122	0,053	0,066	0,374	....	0,012	0,007	0,000	0,007	0,012	....	0,012	0,007	0,000	0,007	0,012
....	....	....	....	....	....	....	....	....	....	....	....	....	....	....	....
n=358	0,053	0,066	0,374	....	0,012	0,007	0,000	0,007	0,012	....	0,012	0,007	0,000	0,007	0,012
n=359	0,314	0,039	0,159	....	0,005	0,066	0,000	0,066	0,005	....	0,005	0,066	0,000	0,066	0,005
n=360	0,000	0,000	0,000	....	0,000	0,000	0,000	0,000	0,000	....	0,000	0,000	0,000	0,000	0,000
n=361	0,314	0,039	0,159	....	0,005	0,066	0,000	0,066	0,005	....	0,005	0,066	0,000	0,066	0,005
n=362	0,053	0,066	0,374	....	0,012	0,007	0,000	0,007	0,012	....	0,012	0,007	0,000	0,007	0,012

Higher critical values in the matrix $M_N(k, n)$ are marked in bright yellow. They are equal to zero in opposite to SF_N (compare with Table 3)

the Nyquist frequency. Values of the parameters H_a, H_q for the CF are the minima equal to zero for $N = 120$. This means that CF_{120} goes exactly through the given point.

In Table 6, values of $M_N(k, n)$ for CF_N, $N > 240$ with the higher Nyquist frequencies $(a \cdot 120, b \cdot 120)$, $a, b = 1, 3$ are shown. Their frequencies are equal to zero in opposite to SF (compare Tables 3, 6).

In Table 7, values of $M_N(k, n)$ for $N > 240$ with the higher Nyquist frequencies $(a \cdot 120,\ b \cdot 120)$, $a, b = 1, 3$ are shown. They are the same values as the corresponding resonances in SF (compare Tables 4, 7).

All the facts prove that CF_N does not suffer from the Gibbs effect. However, parameters $H_a(N)$, $H_q(N)$ do not reach zero as is shown in Fig. 10. They have a minimum for $N = 60$, their values are worsened by alias for higher N as in the case of SF_N.

4.3 Gibbs Effect and Pseudo-Gibbs Effect

We explained that CF does no suffer from the Gibbs effect and does not have its artifacts. This statement may seem incorrect. Let us take an "original profile" which is scanned in the resolution 1000 × 1000 pixels and its values are given by the function

$$f(x,\ y) = \begin{cases} 500 - \dfrac{y}{2} & for\ [x,\ y] \in \langle 350,\ 650\rangle^2, \\ 200 - \dfrac{y}{2} & for\ [x,\ y] \notin \langle 350,\ 650\rangle^2, \end{cases} \tag{15}$$

whose domain is the set $\langle 0,\ 999^2\rangle \cap\ \mathrm{N}^2$.. This profile which is given by this function we can see in Fig. 11. It is characterized by a parallelepiped with sharp edges and large steep walls. In Fig. 12 there is constructed its

Table 7 Frequencies for surface scanned at the resolution 120 × 120 and expanded to CF_N for N > 240

	k=0	k=1	k=2	....	k=238	k=239	k=240	k=241	k=242	....	k=478	k=479	k=480	k=481	k=482
n=0	**172,803**	57,289	3,972	....	3,972	57,289	**345,607**	57,289	3,972	....	3,972	57,289	**345,607**	57,289	3,972
n=1	12,820	50,220	9,053	....	9,053	50,220	25,639	50,220	9,053	....	9,053	50,220	25,639	50,220	9,053
n=2	15,070	9,627	12,416	....	12,416	9,627	30,141	9,627	12,416	....	12,416	9,627	30,141	9,627	12,416
....	....	....	....	....	....	....	....	....	....	....	....	....	....	....	....
n=238	15,070	9,627	12,416	....	12,416	9,627	30,141	9,627	12,416	....	12,416	9,627	30,141	9,627	12,416
n=239	12,820	50,220	9,053	....	9,053	50,220	25,639	50,220	9,053	....	9,053	50,220	25,639	50,220	9,053
n=240	**345,607**	114,578	7,943	....	7,943	114,578	**691,214**	114,578	7,943	....	7,943	114,578	**691,214**	114,578	7,943
n=241	12,820	50,220	9,053	....	9,053	50,220	25,639	50,220	9,053	....	9,053	50,220	25,639	50,220	9,053
n=242	15,070	9,627	12,416	....	12,416	9,627	30,141	9,627	12,416	....	12,416	9,627	30,141	9,627	12,416
....	....	....	....	....	....	....	....	....	....	....	....	....	....	....	....
n=478	15,070	9,627	12,416	....	12,416	9,627	30,141	9,627	12,416	....	12,416	9,627	30,141	9,627	12,416
n=479	12,820	50,220	9,053	....	9,053	50,220	25,639	50,220	9,053	....	9,053	50,220	25,639	50,220	9,053
n=480	**345,607**	114,578	7,943	....	7,943	114,578	**691,214**	114,578	7,943	....	7,943	114,578	**691,214**	114,578	7,943
n=481	12,820	50,220	9,053	....	9,053	50,220	25,639	50,220	9,053	....	9,053	50,220	25,639	50,220	9,053
n=482	15,070	9,627	12,416	....	12,416	9,627	30,141	9,627	12,416	....	12,416	9,627	30,141	9,627	12,416

Higher resonance values in the matrix $M_N(k, n)$ are marked in dark blue. They are the same values as the corresponding resonances in SF_N (compare Tables 4, 7)

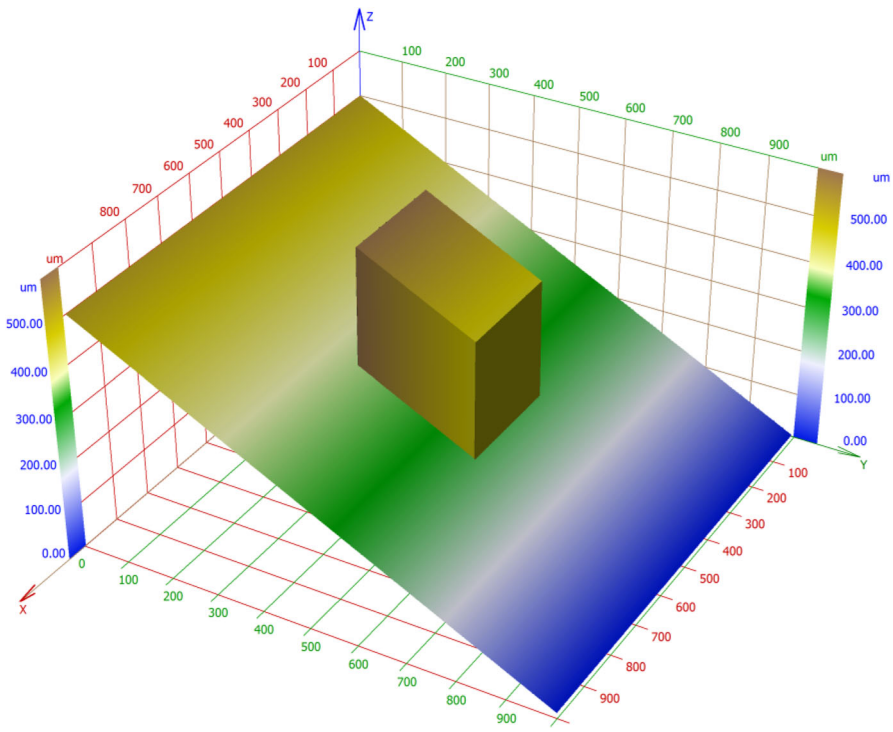

Fig. 11 "Original profile" modelled by the function $f(x, y)$: see (15). The function $f(x, y)$ is a set of isolated *points* but the modelled profile is continuous

SF_{25} (on the left) and corresponding CF_{50} (on the right). In SF_{25} we can see a clear Gibbs effect (a) which on CF_{50} does not exist. On the left we can see two clear artefacts (b) caused by the convergence to the mean (see Dirichlet's theorem in the previous chapter) which on CF_{50} does not exist.

However, we can see also clear artefacts (c) that exist in both cases. They look like the Gibbs effect but it is not Gibbs effect. As was said in the Introduction, the Gibbs effect is caused by the fact that Fourier sums overshoot at a jump discontinuity. There are Gibbs effects on the border of *SF* because

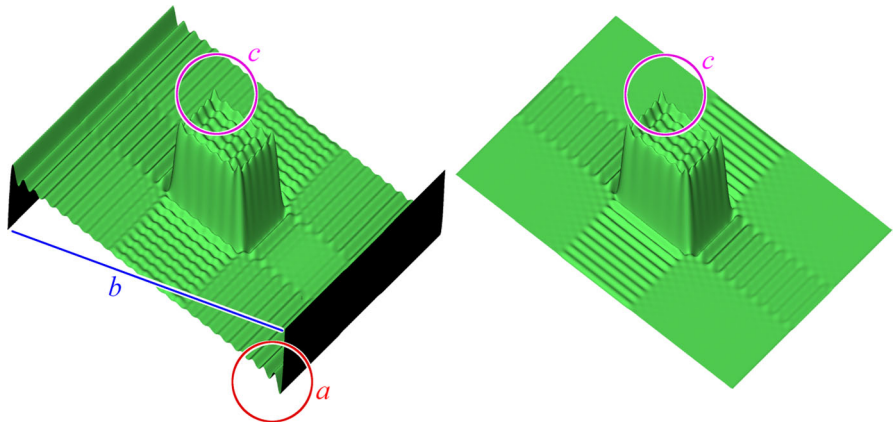

Fig. 12 Replicas of the profile from Fig. 11. On the *left* the standard replica (SF_N) for $N = 25$, on the *right* corresponding cosine replica (CF_N) for $N = 50$

SF means the odd extension of the profile and this extension is discontinuous (see Fig. 8 on the left). There are no Gibbs effects on the border of *CF* because *CF* means the even extension of the profile and this extension is continuous (see Fig. 8 on the right). Inside our profile there are no discontinuities, neither on the odd extension (*SF*) nor on the even extension (*CF*). Therefore no Gibbs effect exists here. Neither on *SF* nor on *CF*.

As was said in the Sect. 1, the Gibbs overshoot does not die out as the frequency increases but conversely it increases to the value of the Wilbraham–Gibbs constant. We can be sure of that if we construct SF_N and CF_N for higher N (see Fig. 13). The artifact (c) resembles the Gibbs phenomenon, however, unlike it, it is decreased by increasing N. We can therefore call it a "pseudo-Gibbs" effect.

Note that the *SF* suffers even one artifact due to discontinuous periodic extension—convergence in the mean. This artifact is marked by (b) and is clearly visible in Figs. 12 and 13 on the left.

4.4 Alias and the Resonance Frequencies

In previous research, *SF* and *CF* suffer from alias; it causes resonance frequencies in both cases. In our problem, alias is given by the rectangle rule (11) for calculation of integrals (2) and (6). We explain this fact for the case of cosine base in one variable. Let us compute the integral (6) for the profile $\{h_i\}_{i=0}^{L-1}$ with length L and resonance frequency $2L$ using the formula (11). We obtain

$$a_{2L} = \frac{1}{L}\int_0^L h_i \cos\frac{2L\pi x}{L}\,\mathrm{d}x = \frac{1}{L}\sum_{i=0}^{L-1}\int_i^{i+1} h_i \cos 2\pi x\,\mathrm{d}x$$
$$\approx \frac{1}{L}\sum_{i=0}^{L-1} h_i \cos 2\pi i = \frac{1}{L}\sum_{i=0}^{L-1} h_i. \qquad (16)$$

It is the average height of the profile $\{h_i\}$. However, analytic calculation gives

$$a_{2L} = \frac{1}{L}\int_0^L h_i \cos\frac{2L\pi x}{L}\,\mathrm{d}x = \frac{1}{L}\sum_{i=0}^{L-1}\int_i^{i+1} h_i \cos 2\pi x\,\mathrm{d}x$$
$$= \frac{1}{L}\sum_{i=0}^{L-1}\frac{h_i}{2\pi}\left[\sin 2\pi x\right]_i^{i+1} = 0. \qquad (17)$$

Therefore, each addition of the two to a or b in resonance frequencies $M\left(a\cdot\frac{v_S}{2},\ b\cdot\frac{v_S}{2}\right)$ increases the profile height by its original value approximately. Therefore, the correct height of SF_{60} was increased approximately 8 times to SF_{120} and approx. 16 times to SF_{120} in Fig. 6 (count the resonance frequencies in Table 4). $H_a(N)$, and $H_q(N)$ jump by analogy (see Fig. 5).

Alias or resonance is caused by the sampling of two or more frequencies. Alias and resonance which is described in Sect. 3, i.e., alias or resonance which arises when the discretely scanned 3D surface relief is converted into its continuous form is created unnecessarily. The rectangle rule of integration (11) is the reason of this unpleasant effect. It adds the samples

$$g(x_i y_i) = f(x_i,\ y_i)\cos\varphi(x_i)\cos\psi(y_i), \qquad (18)$$

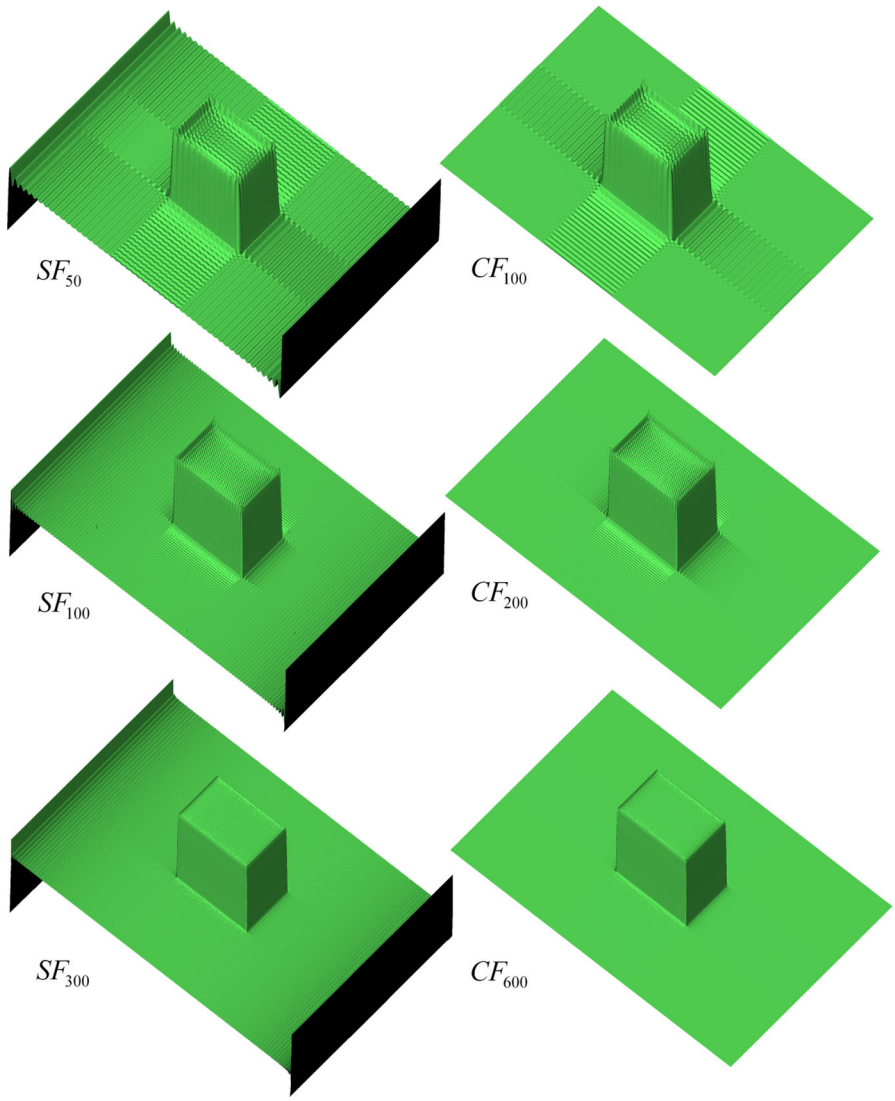

Fig. 13 Gibbs effect on the border of discontinuous odd extension by SF_N (on the *left*). Its overshoots increased for increased N and it converges to the Wilbraham–Gibbs constant for $N \to \infty$. Pseudo-Gibbs effect on sharp edges inside of surfaces decreased for increased N and it converges to zero for $N \to \infty$ in both cases (odd and even extension)

of function $g(x, y)$ in the case of CF_{KN} (in case of SF_{KN} by analogy). Alias reason is an interaction of three different frequencies here—frequency of profile scanning and two frequencies with the numerical integration samples of two trigonometric functions.

4.5 What Do We Want to Solve?

Higher Nyquist and resonance frequencies described in the previous text are interesting phenomena but in practice they may be a result of the unclarity of the problem only. Before the Fourier expansion we must answer a fundamental question: What is the purpose of this expansion? The fracture surface may be expanded for two basic reasons:

(a) We want to replace the given profile with a continuous function which exactly goes through the given points. This problem is known as an interpolation in mathematics.
(b) Given points are discrete samples of (at least piecewise) continuous function and we will expand this (at least piecewise) continuous function. The expansion does not exactly go to the given points. This problem is known as an approximation in mathematics.

The case of (a) is relatively simple. Trigonometric polynomials (1) or (4) work as a function which approximate given points by the method of least squares see [13] for example. If we have the sample scanned with resolution $W \times H$ (width $\times$ height) we use the CF_{KN} (not SF_{KN}) for $K = W$, $N = H$ (see Sects. 4.1 and 4.2). It goes exactly across the given points (see first critical frequencies in Table 6). Our profile and calculated CF_{WH} is one and the same. Therefore, any study of higher frequencies does not have any practical meaning in this case.

The case of (b) is more difficult. We want to study higher frequencies. We must add next assumptions about function behaviour outside given points and solve not a discrete but a (at least piecewise) continuous problem, i.e., we construct any (at worst piecewise) continuous function from the input data. In this case, there exist infinitely many high frequencies in Fourier expansion.

As an example let us introduce the problem where each pixel is not a dimensionless point but a square with the constant height h_{ij} where h_{ij} is a measured height in pixel $[i, j]$.

We find an expansion of function $f(x, y)$ to the infinite cosine series

$$f(x,\ y) = \sum_{k=0}^{\infty}\sum_{n=0}^{\infty} \lambda_{kn} a_{kn} \cos\frac{k\pi x}{W}\cos\frac{n\pi y}{H}, \tag{19}$$

where λ_{kn} is given by (5), a_{kn} by (6) and for all pixels

$$\Omega_{ij} = \langle i,\ i+1\rangle \times \langle j,\ j+1\rangle, \quad i = 0,\ 1, \ldots, W-1,\\ j = 0,\ 1, \ldots, H-1,$$

is

$$[x,\ y] \in \Omega_{ij} \Rightarrow f(x,\ y) = f(i,\ j) = h_{ij}.$$

We obtain

$$a_{00} = \frac{1}{W\cdot H}\iint_{\Omega} f(x,\ y)\cos\frac{k\pi x}{W}\cos\frac{n\pi y}{H}\mathrm{d}x\mathrm{d}y \\ = \frac{1}{W\cdot H}\sum_{i=0}^{W-1}\sum_{j=0}^{H-1} h_{ij} \tag{20}$$

$$a_{k0} = \frac{1}{W\cdot H}\sum_{i=0}^{W-1}\sum_{j=0}^{H-1}\iint_{\Omega_{ij}} f(x,\ y)\cos\frac{k\pi x}{W}\mathrm{d}x\mathrm{d}y, \tag{21}$$

$$a_{k0} = \frac{2}{k\pi H}\sin\frac{k\pi}{2W}\sum_{i=0}^{W-1}\left[\cos\frac{k\pi(2i+1)}{2W}\sum_{j=0}^{H-1} h_{ij}\right], \tag{22}$$

$$a_{0n} = \frac{1}{W\cdot H}\sum_{i=0}^{W-1}\sum_{j=0}^{H-1}\iint_{\Omega_{ij}} f(x,\ y)\cos\frac{n\pi x}{H}\mathrm{d}x\mathrm{d}y,$$

$$a_{0n} = \frac{2}{n\pi W}\sin\frac{n\pi}{2H}\sum_{j=0}^{H-1}\left[\cos\frac{n\pi(2j+1)}{2H}\sum_{i=0}^{W-1} h_{ij}\right], \tag{23}$$

$$a_{kn} = \frac{1}{W\cdot H}\sum_{i=0}^{W-1}\sum_{j=0}^{H-1}\iint_{\Omega_{ij}} f(x,\ y)\cos\frac{k\pi x}{W}\cos\frac{n\pi y}{H}\mathrm{d}x\mathrm{d}y,$$

$$a_{kn} = \frac{4}{nk\pi^2}\sin\frac{k\pi}{2W}\sin\frac{n\pi}{2H}\sum_{i=0}^{W-1}\left[\cos\frac{k\pi(2i+1)}{2W}\right.\\ \left.\sum_{j=0}^{H-1} h_{ij}\cos\frac{n\pi(2j+1)}{2H}\right]. \tag{24}$$

We could derive also expressions for standard series but (as was shown in Sect. 4.3) it suffers from the Gibbs effect and by convergence to the mean, therefore, we skip these calculations.

For analysis of the convergence, we cannot use (8) and (9), because they are discrete metrices. It is necessary to use their continuous forms:

$$H_a^{(KN)} = \iint_{\Omega}\frac{1}{WH}|f(x,\ y) - CF_{KN}(x,\ y)|\mathrm{d}x\mathrm{d}y, \tag{25}$$

i.e., the "distance" of $f(x, y)$, $CF_{KN}(x, y)$ in the so-called L_1 metrics, or

$$H_q^{(KN)} = \sqrt{\frac{1}{WH}\iint_{\Omega}[f(x,\ y) - CF_{KN}(x,\ y)]^2\mathrm{d}x\mathrm{d}y}, \tag{26}$$

i.e., the "distance" of $f(x, y)$, $CF_{KN}(x, y)$ in the so-called L_2 metrics.

Direct calculation of these integrals would be very difficult but we can use one result of functional analysis for the calculation of $H_q^{(KN)}$:

Theorem (Bessel) *Let $\boldsymbol{f} \in H$ be an element of a Hilbert space H; and*

$$\boldsymbol{s}_{kn} = \sum_{k=0}^{K}\sum_{n=0}^{N} c_{kn}\varphi_{kn},$$

its partial Fourier sum in orthogonal base $\{\varphi_{kn}\}$. *Then*

$$\|\boldsymbol{f} - \boldsymbol{s}_{kn}\|^2 = \|\boldsymbol{f}\|^2 - \sum_{k=0}^{K}\sum_{n=0}^{N} c_{kn}^2\|\varphi_{kn}\|^2. \tag{27}$$

In our case, H is the functional space $L_2\langle 0,\ W\rangle \times L_2\langle 0,\ H\rangle$, $\boldsymbol{f}$ is the scanned profile, $\boldsymbol{s}_{kn}$ is its partial sum, i.e., CF_{KN}.

Our Fourier coefficients are

$$c_{kn} = \lambda_{kn}a_{kn},$$

where λ_{kn} is given by (5), a_{kn} by (20)–(24) and orthogonal base is

$$\{\varphi_{kn}\} = \lambda_{kn}\left\{\cos\frac{k\pi x}{W}\cos\frac{n\pi y}{H}\right\}, \quad k = 0,\ 1,\ldots,K,$$
$$n = 0,\ 1,\ldots,N. \tag{28}$$

Norms of these functions are

$$\|\varphi_{00}\| = \sqrt{\int_0^W\int_0^H \cos^2\frac{0\pi x}{W}\cos^2\frac{0\pi y}{W}\mathrm{d}x\mathrm{d}y}$$
$$= \sqrt{\int_0^W\int_0^H 1\mathrm{d}x\mathrm{d}y} = \sqrt{W\cdot H},$$

$$\|\varphi_{k0}\| = \sqrt{\int_0^W\int_0^H \cos^2\frac{k\pi x}{W}\cos^2\frac{0\pi y}{W}\mathrm{d}x\mathrm{d}y}$$
$$= \sqrt{\int_0^W\int_0^H \cos^2\frac{k\pi x}{W}\mathrm{d}x\mathrm{d}y} = \sqrt{H\int_0^W \cos^2\frac{k\pi x}{W}\mathrm{d}x}$$
$$= \sqrt{\frac{H}{2}\int_0^W\left(1+\cos\frac{2k\pi x}{W}\right)\mathrm{d}x}$$
$$= \sqrt{\frac{H}{2}\left(\left[\frac{x}{2}\right]_0^W + \frac{1}{4k\pi}\left[\sin\frac{2k\pi x}{W}\right]_0^W\right)} = \sqrt{\frac{WH}{4}},$$

$$\|\varphi_{0n}\| = \sqrt{\frac{WH}{2}},$$

$$\|\varphi_{kn}\| = \sqrt{\int_0^W\int_0^H \cos^2\frac{k\pi x}{W}\cos^2\frac{n\pi y}{W}\mathrm{d}x\mathrm{d}y} = \frac{\sqrt{WH}}{2}.$$

Therefore, according to (26) is

$$H_q^{(KN)} = \sqrt{\frac{1}{WH}\left(\sum_{i=0}^{W-1}\sum_{j=0}^{H-1} f_{ij}^2 - \sum_{k=0}^{K}\sum_{n=0}^{N}\lambda_{kn}^2 a_{kn}^2\|\varphi_{kn}\|^2\right)},$$

where λ_{kn} are given by (5), a_{kn} by (20)–(24) and φ_{kn} by (28).

5 Results and Discussion

In Fig. 14, we can see the graph of $M_{1000}(k, n)$, with a_{kn} calculated using (20)–(24) for CF_{1000} (surface scanned at the resolution 120 × 120). In contrast with Fig. 4., there are not any acicular resonance frequencies. In Table 8, there are shown the frequencies of $M(k, n)$ with the same a_{kn}. "Resonance" frequencies ($k, n = 240, 480$) are equal to zero according to (17). Of course, other frequencies are non-zero in general because we calculate the Fourier series of piecewise constant function. This series has infinitely many members that are given by

$$CF(x,\ y) = \sum_{k=0}^{\infty} a_k\cos\frac{k\pi x}{L}$$

(in the 1D case for simplicity) where L is the length of our sample in pixels and

$$|a_k| = \left|\frac{1}{L}\int_0^L \cos\frac{k\pi x}{L}\mathrm{d}x\right| = \frac{1}{L}\sum_{i=0}^{L-1}\left|h_i\cdot\int_i^{i+1}\cos\frac{k\pi x}{L}\mathrm{d}x\right|, \tag{29}$$

are amplitudes of our frequencies. It is evident that all these integrals are equal to zero whenever k is equal to the integer multiple of L and they are non-zero in other cases.

All alias effects were also eliminated in this way. As stated above, alias is caused by the sampling of two or more frequencies but our profile is sampled only in (29). All integrals of trigonometric functions are theoretically exact numbers without any frequence and any sampling in (29).

In Fig. 15, there is constructed the graph of $H_q(N)$ for CF_N for $N = 20, 60,\ldots,1000$ for surface scanned at

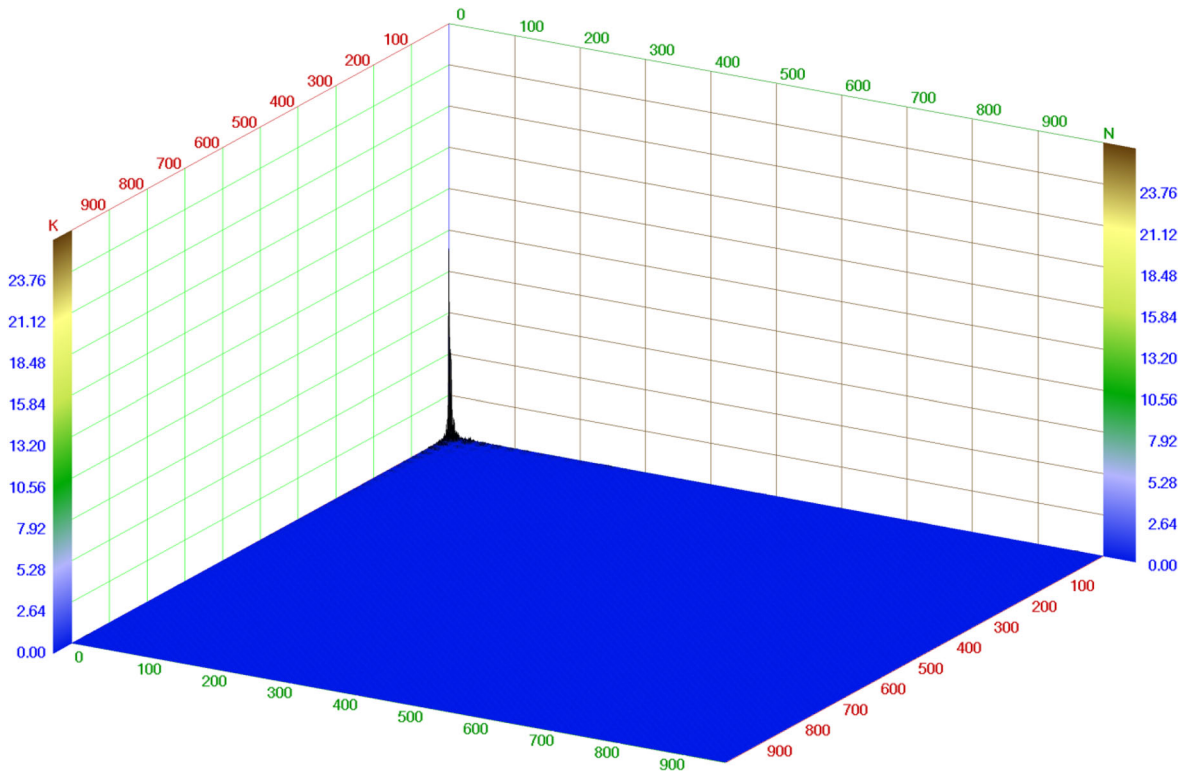

Fig. 14 Graph of $M_{1000}(k, n)$, for CF_{1000}, for surface scanned at the resolution 120 × 120), a_{kn} calculated using (20)–(24). We cannot see any resonance frequencies (compare with Fig. 4)

Table 8 Frequencies of $M(k, n)$, a_{kn} calculated using (20)–(24)

	k=0	k=1	k=2	....	k=238	k=239	k=240	k=241	k=242	....	k=478	k=479	k=480	k=481	k=482
n=0	172,803	60,6263	7,25574	....	0,06097	0,25367	6E-18	0,25156	0,05996	....	0,03036	0,12657	6E-18	0,12604	0,03011
n=1	15,206	56,3004	7,21149	....	0,0606	0,23557	5,2E-19	0,23361	0,0596	....	0,03017	0,11754	5,2E-19	0,11705	0,02992
n=2	15,5989	12,723	6,85561	....	0,05761	0,05323	5,4E-19	0,05279	0,05666	....	0,02868	0,02656	5,4E-19	0,02645	0,02845
....	....	....	....	....	....	....	....	....	....	....	....	....	....	....	....
n=238	0,13108	0,10692	0,05761	....	0,00048	0,00045	4,5E-21	0,00044	0,00048	....	0,00024	0,00022	4,5E-21	0,00022	0,00024
n=239	0,06362	0,23557	0,03017	....	0,00025	0,00099	2,2E-21	0,00098	0,00025	....	0,00013	0,00049	2,2E-21	0,00049	0,00013
n=240	6E-18	2,1E-18	2,5E-19	....	2,1E-21	8,8E-21	2,1E-37	8,7E-21	2,1E-21	....	1E-21	4,4E-21	2,1E-37	4,3E-21	1E-21
n=241	0,0631	0,23361	0,02992	....	0,00025	0,00098	2,2E-21	0,00097	0,00025	....	0,00013	0,00049	2,2E-21	0,00049	0,00012
n=242	0,12892	0,10515	0,05666	....	0,00048	0,00044	4,4E-21	0,00044	0,00047	....	0,00024	0,00022	4,4E-21	0,00022	0,00024
....	....	....	....	....	....	....	....	....	....	....	....	....	....	....	....
n=478	0,06527	0,05323	0,02868	....	0,00024	0,00022	2,3E-21	0,00022	0,00024	....	0,00012	0,00011	2,3E-21	0,00011	0,00012
n=479	0,03175	0,11754	0,01506	....	0,00013	0,00049	1,1E-21	0,00049	0,00012	....	6,3E-05	0,00025	1,1E-21	0,00024	6,2E-05
n=480	6E-18	2,1E-18	2,5E-19	....	2,1E-21	8,8E-21	2,1E-37	8,7E-21	2,1E-21	....	1E-21	4,4E-21	2,1E-37	4,3E-21	1E-21
n=481	0,03161	0,11705	0,01499	....	0,00013	0,00049	1,1E-21	0,00049	0,00012	....	6,3E-05	0,00024	1,1E-21	0,00024	6,2E-05
n=482	0,06473	0,05279	0,02845	....	0,00024	0,00022	2,2E-21	0,00022	0,00024	....	0,00012	0,00011	2,2E-21	0,00011	0,00012

Dark blue "resonance" frequencies (k, n = 240, 480) are equal to zero according to (17)

the resolution 120 × 120, a_{kn} are calculated using (20)–(24). We cannot see any "jumps" in resonance frequencies $\left(a \cdot \frac{v_S}{2}, b \cdot \frac{v_S}{2}\right)$; for $a = b = 2, 4, \ldots$ It is evident that $H_q(N) \to 0$ for $N \to \infty$ (compare with Fig. 5).

In Fig. 16, there is an original sample of fracture surface scanned at the resolution 120 × 120 and its CF_N for N = 120, 240, 480, 720, 980 calculated according to Sect. 4.3. (b) They do not suffer from sampling resonances and differ from the original and

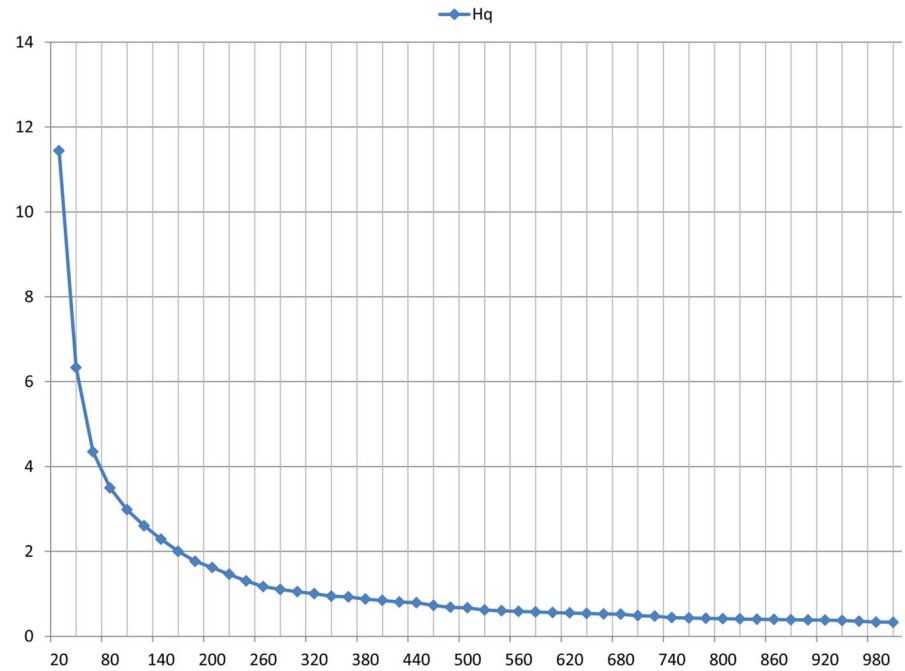

Fig. 15 Graph of $H_q(N)$ for CF_N for $N = 20, 60,\ldots,1000$ for surface scanned at the resolution 120×120, a_{kn} are calculated using (20)–(24). We can not see any "jumps" in resonance frequencies $\left(a \cdot \frac{v_S}{2},\ b \cdot \frac{v_S}{2}\right)$; for $a = b = 2, 4,\ldots$ It is evident that $H_q(N) \to 0$ for $N \to \infty$

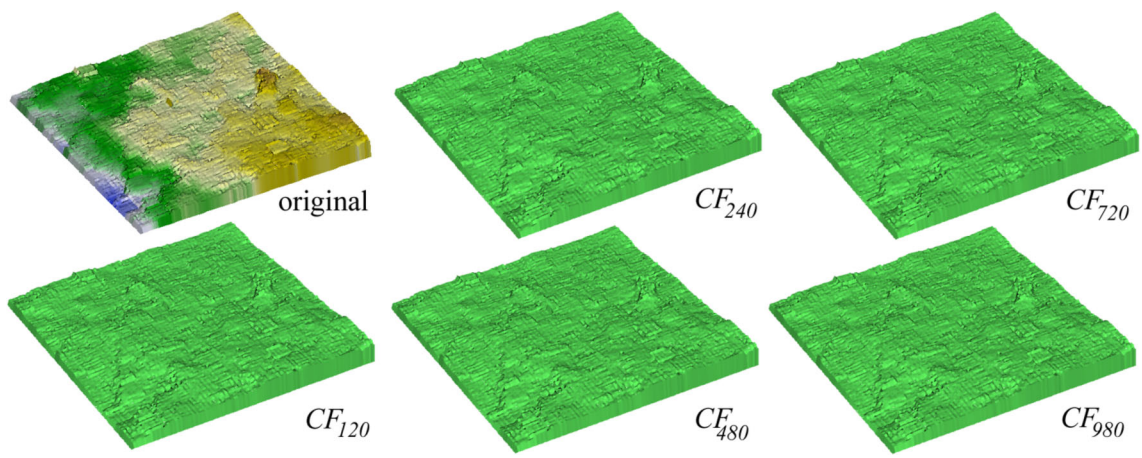

Fig. 16 Original sample fracture surface scanned at the resolution 120×120 and its CF_N for $N = 120, 240, 480, 720, 980$. They do not suffer from sampling resonances and differ from the original and each other on subpixel levels only (compare with Fig. 6)

each other on subpixel levels only (compare with Fig. 6).

In Fig. 17, there is shown the SF_{KN} for $K = 64$, $N = 48$ of fracture surface of Portland cement paste scanned at the resolution 1024×768. The Gibbs phenomenon in part (a), convergence to the arithmetic mean of boundary values according to (14) in part (b) and alias artifacts in part (c) are evident on this approximation.

In Fig. 18, there is constructed the $CF_{2K,2N}$ for $K = 64$, $N = 48$ (i.e., $CF_{128,96}$) of the same fracture surface as that in Fig. 17. The expression (12) has four members for one pair k, n, i.e., total number of members for SF_{KN} is $4 \cdot K \cdot N$. The expression (13) has one member for one pair k, n only, i.e., total number of members for $CF_{2K,2N}$ is also $2K \cdot 2N = 4 \cdot K \cdot N$. Therefore, computing demands are equal but the result is significantly better. We

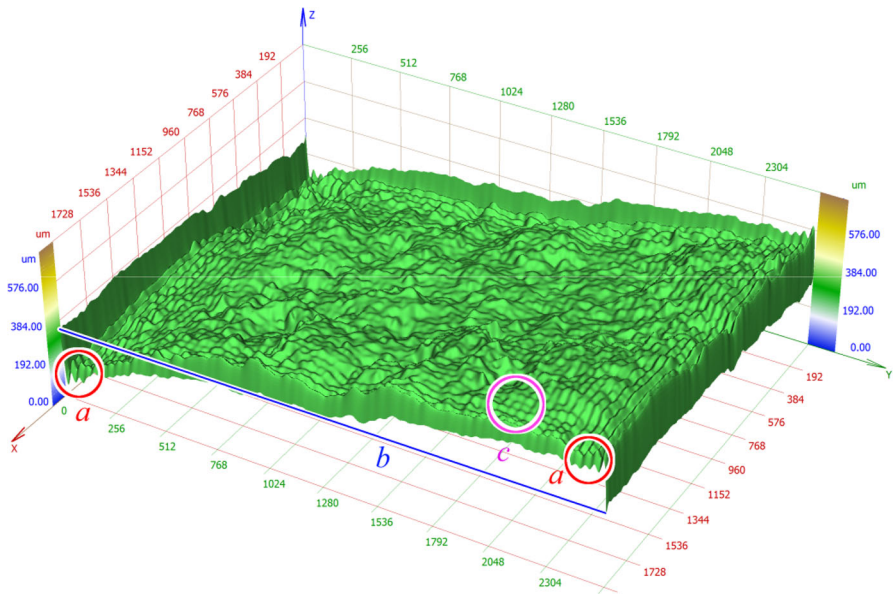

Fig. 17 The SF_{KN} for $K = 64$, $N = 48$ of fracture surface of Portland cement paste scanned at the resolution 1024×768. The Gibbs phenomenon (*a*), convergence to the arithmetic mean of boundary values (*b*) and alias artifacts (*c*) are evident on this approximation

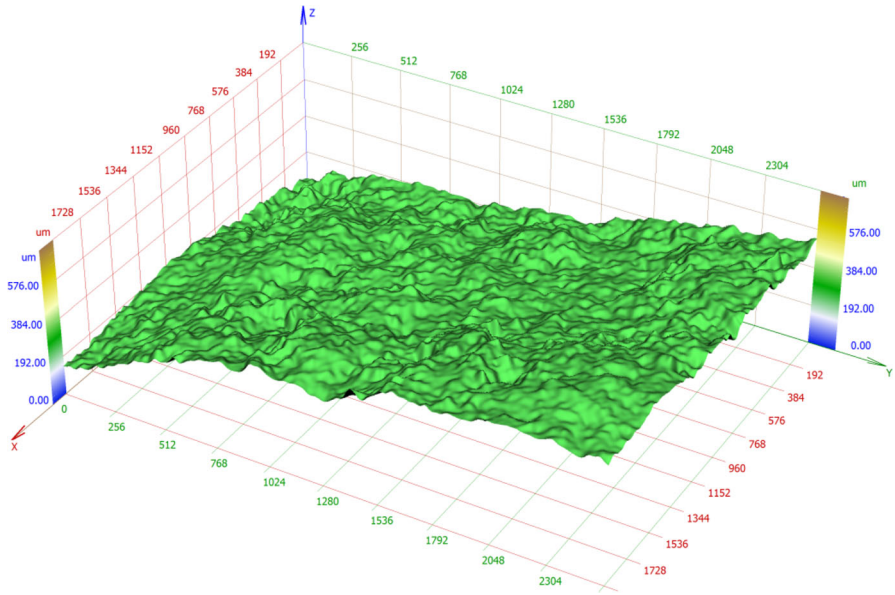

Fig. 18 The CF_{KN} for $K = 128$, $N = 96$ of fracture surface of Portland cement paste scanned at the resolution 1024×768. We cannot see any Gibbs phenomenon; any convergence to the arithmetic mean of boundary values or any alias artifacts

cannot see any Gibbs effect, any raised or decreased boundaries or any artifacts caused by alias.

We can see two surfaces in Fig. 19. The first one is the original fracture surface of cement paste scanned at the resolution 1024×768 pixels, the second is its CF_{KN} for $K = 1024$, $N = 768$ coloured by the same height palette. Coefficients a_{kn} were calculated by the numerical integration formula (10). Heights of all pixels are precisely equal.

6 Conclusions

Approximation and interpolation of fracture surface by Fourier series or its partial sums is an interesting possibility of its 3D reconstruction. The *SF* expansion combining sine and cosine harmonics is not suitable for this use because it suffers from the Gibbs effect and from the effect of convergence in the mean.

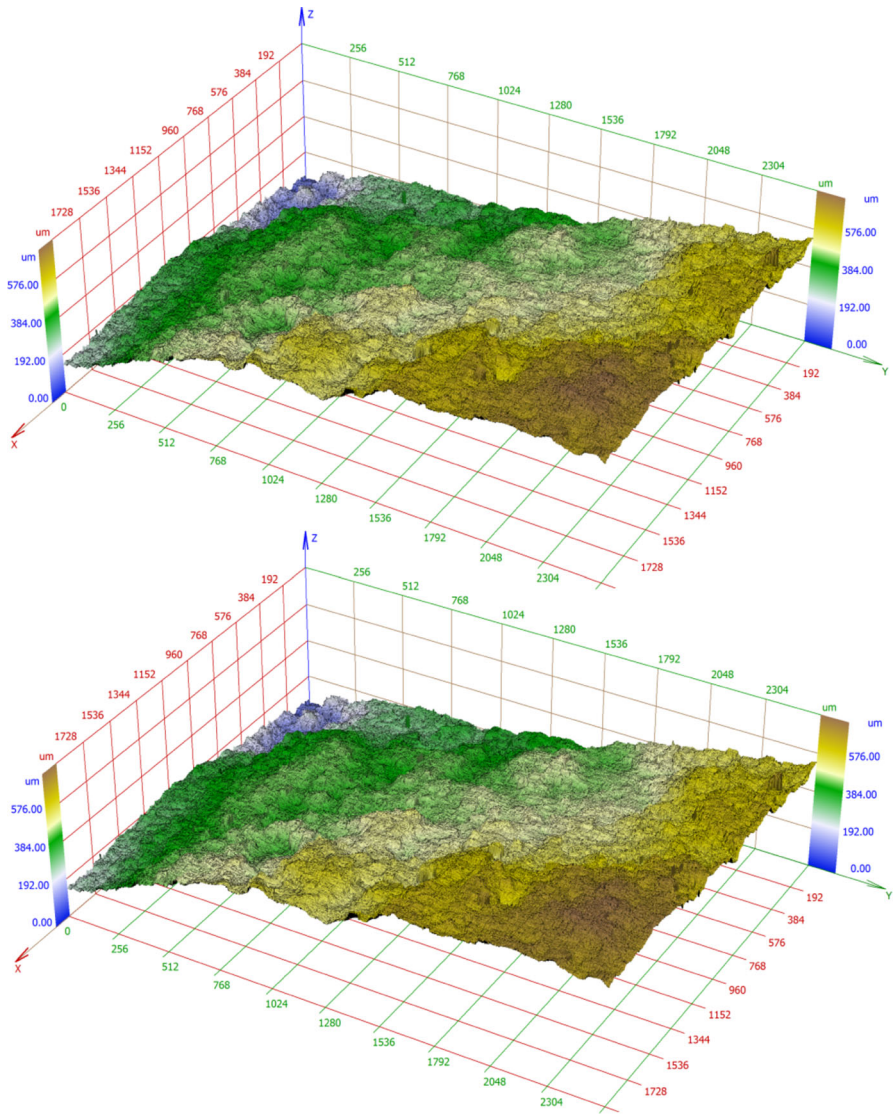

Fig. 19 First surface is the original fracture surface of cement paste scanned at the resolution 1024 × 768 pixels, the second is its CF_{KN} for $K = 1024$, $N = 768$ *coloured* by the same height palette. Heights of all pixels are precisely equal

These unpleasant phenomena may be eliminated by expansion to the *CF* series. It does not suffer either convergence in the mean or the Gibbs effect. The profile to be reconstructed is continuous. Its cosine replica constructed according to Sect. 5 is also continuous. This means that it does not know the Gibbs phenomenon (it is defined only for discontinuous functions). In cosine expansion, the pseudo-Gibbs effect may occur in the case of great and steep walls in the profile to be reconstructed. These artifacts resemble the Gibbs effect but (as opposed to it) decrease with the increasing number of trigonometric polynomial members and may be eliminated by arbitrary precision (they converge to zero for $N \to \infty$).

The alias is the next unpleasant effect. It can occur in the case of use of a non-suitable integration method. In the case of numeric integration with a step which is equal to the profile sampling, it is possible to construct a trigonometric polynomial which goes exactly through the measured values (so-called profile interpolation) but alias will appear in the case of a smaller step (see graph in Fig. 10). Alias grows with a decreasing step of numeric integration and leads to the resonance with profile sampling and to jumps of

reconstruction heights in higher resonance frequencies (see Figs. 5, 6).

These effects can be prevented if the profile is approximated (at least piecewise) continuous function and this function is subsequently expanded to the *CF* series according to Sect. 4.4, case (b).

Acknowledgments The author acknowledges partial support from Brno University of Technology, Specific Research Project No. FSI-S-142290 and Project LO1202 by financial means from the Ministry of Education, Youth and Sports National Sustainability Programme I. The author thanks Prof. Tomáš Ficker from the Faculty of Civil Engineering of Brno University of Technology for the provided data.

References

1. Ben Hagai, I., Fazi, F. M., & Rafaely, B. (2012). Generalized sampling expansion for functions on the sphere. *IEEE Transactions on Signal Processing, 60*(11), 5870–5879.
2. Boev, A., Bregovic, R., Damyanov, D., & Gotchev, A. (2009). Anti-aliasing filtering of 2D images for multi-view auto-stereoscopic displays. In *International workshop on local and non/local approximation in image processing* (pp. 97–97).
3. Boyd, J. P. (2002). A comparison of numerical algorithms for Fourier extension of the first, second, and third kinds. *Journal of Computational Physics, 178*(1), 118–160.
4. Cary, P. W. (1999). Genraized sampling and "beyond Nyquist" imaging. *CREWES Research Report*, *11*, 1–23.
5. Coulange, B., & Moisan, L. (2010). An aliasing detection algorithm based on suspicious colocalization of Fourier coefficients. In *Proceedings of IEEE 17th international conference on image processing*, Hong Kong (pp. 2012–2016).
6. Crow, F. C. (1977). Aliasing problem in computer-generated shaded images. *Communications of the ACM, 20*(11), 799–805.
7. Driscoll, T. A., & Fornberg, B. (2001). A Pade-based algorithm for overcoming the Gibbs phenomenon. *Numerical Algorithms, 26*(1), 77–92.
8. Eckhoff, K. S. (1993). Accurate and efficient reconstruction of discontinuous functions from truncated series expansions. *Mathematics of Computation, 61*(204), 745–763.
9. Eckhoff, K. S. (1995). Accurate reconstruction of functions of finite regularity from truncated Fourier series expansions. *Mathematics of Computation, 64*(210), 671–690.
10. Eckhoff, K. S. (1998). On a high order numerical method for functions with singularities. *Mathematics of Computation, 67*(223), 1063–1087.
11. Farsiu, S., Robinson, D., Elad, M., & Milanfar, P. (2004). Advances and challenges in super-resolution. *International Journal of Imaging System and Technology, 14*(2), 47–57.
12. Ficker, T., & Martišek, D. (2015). 3D image reconstructions and the Nyquist–Shannon theorem. *3D Research*, *6*(3), 1–18. doi:10.1007/s13319-015-0057-4.
13. Ficker, T., & Martišek, D. (2012). Digital fracture surfaces and their roughness analysis: Applications to cement-based materials. *Cement and Concrete Research, 42*, 827–833.
14. Gelb, A., & Tanner, J. (2006). Robust reprojection methods for the resolution of the Gibbs phenomenon. *Applied and Computational Harmonic Analysis, 20*(1), 3–25.
15. Gottlieb, D., Shu, C. W., Solomonoff, A., & Vandeven, H. (1992). On the Fourier partial sum of a nonperiodic analytic function. *Journal of Applied Mathematics and Computing, 43*(1–2), 91–98.
16. Gottlieb, D., & Shu, C. W. (1997). On the Gibbs phenomenon and its resolution. *SIAM Review*, *39*, 644–668.
17. Huybrechs, D. (2010). On the Fourier extension of nonperiodic functions. *SIAM Journal on Numerical Analysis, 47*(6), 4326–4355.
18. Jung, J.-H., & Shizgal, B. D. (2004). Generalization of the inverse polynomial reconstruction method in the resolution of the Gibbs phenomenon. *Journal of Computational and Applied Mathematics, 172*(1), 131–151.
19. Longhurt, P., Debattista, K., Gillibrand, R., & Chalmers, A. (2005). Analytic antialiasing for selective high fidelity rendering. In *Proceedings of the XVIII Brazilian symposium on computer graphics and image processing* (pp. 359–366).
20. Martišek, D., Procházková, J., & Ficker, T. (2015). High-quality 3D reconstruction and noise reduction of multifocal images from oversized samples. *Journal of Electronic Imaging, 24*(5), 053029. doi:10.1117/1.JEI.24.5.053029.
21. Nakamae, E., Ischiyaki, T., Nishita, T., & Takita, S. (1989). Composing 3D images with antialiasing and various shading effects. *IEEE Computer Graphics and Applications, 9*, 21–29.
22. Robinson, M. D., Toth, C. A., Lo, J. Y., & Farsiu, S. (2010). Efficient Fourier-wavelet super-resolution. *IEEE Transaction on Image Processing, 19*(10), 2669–2681.
23. Shekarforoush, H., Berthold, M., & Zerubia, J. (1995). 3D super-resolution using generalized sampling expansion. In *International conference on image processing* (Vol. 2, pp. 300–303). ISBN 0-8186-7310-9.
24. Vaidyanathan, P. P. (2001). Generalizations of the sampling theorem: Seven decades after Nyquist. *IEEE Transactions on Circuits and Systems, I: Fundamental Theory and Applications, 48*(9), 1094–1109.
25. Vandewalle, P., Sbaiz, L., Vandewalle, J., & Vetterli, M. (2004). How to take advantage of aliasing in bandlimited signals. In *Proceedings of international conference on acoustics, speech, and signal. Proceedings: Image and multidimensional signal processing special sessions* (Vol. III, pp. 948–951).

Journal of Electronic Imaging 24(0), ( )

High-quality three-dimensional reconstruction and noise reduction of multifocal images from oversized samples

Dalibor Martišek,[a] Jana Procházková,[a,*] and Tomáš Ficker[b]
[a]Brno University of Technology, Faculty of Mechanical Engineering, Department of Mathematics, Technická 2, Brno 616 69, Czech Republic
[b]Brno University of Technology, Faculty of Civil Engineering, Department of Physics, Veverí 95, Brno 602 00, Czech Republic

Abstract. Three-dimensional (3-D) reconstruction is an indispensable tool in the areas such as biology, chemistry, medicine, material sciences, etc. The sample can be reconstructed using confocal or nonconfocal mode of a microscope. The limitation of the confocal approach is the sample size. Currently used devices work mostly with sample surface area up to 1 cm^2. We suggest a three-step method that creates 3-D reconstruction from multifocal images in nonconfocal mode that is qualitatively comparable to the confocal results. Our method, thus, takes advantages of both microscope modes—high-quality results without sample size limitation. The preprocessing step eliminates the additive noise with Linderberg-Lévy theorem. The main focus criterion is based on adjusted Fourier transform. In the final step, we eliminate the defective clusters using the adaptive pixel neighborhood algorithm. We proved the effectiveness of our noise reduction and 3-D reconstruction method by the statistical comparisons; the correlation coefficients average 0.987 for all types of Fourier transforms. [DOI: 10.1117/1.JEI.24.XX.XXXXXX]

Keywords: noise reduction; three-dimensional reconstruction; multifocal image; Fourier transform.

Paper 15422 received Jun. 5, 2015; accepted for publication Sep. 21, 2015.

1 Introduction

The three-dimensional (3-D) reconstruction of general surfaces plays an important role in many branches, e.g., the morphological analysis of fracture surfaces reveals information on construction materials mechanical properties.[1,2] In technical practice, the confocal microscope is used as a standard tool for imaging three-dimensional surfaces.[3–6] However, our preprocessing, processing, and postprocessing mathematical methods are proposed generally, so that an optical (conventional) microscope can be used as well. The advantage of our approach is that our algorithms are able to work with larger objects (e.g., building materials) with sizes up to dozens of centimeters.

In our contribution, the confocal microscope Olympus LEXT OLS 3100 is used in confocal and nonconfocal modes. We work with images of the same scene taken from the identical viewpoint under different focal settings. The sharp image can be obtained in either the optical or computational way as clearly described.[7] These known methods cover the averaging of gray levels,[8] statistical characteristics (variance, range),[9–11] cosine transform,[12,13] wavelets,[14,15] or genetic algorithms.[16] There is also a simple method to construct a rough 3-D model with a constant height of the corresponding focus zones. This method is called the method of constant height cuts and is described in Ref. 9.

Our approach follows up on our recent work[9,17] that deals with amplitude spectra of the standard Fourier transform. The precision of these methods depends on the weighting of spatial frequencies in amplitude spectra. This method is clearly described in Sec. 3.2.

*Address all correspondence to: Jana Procházková, E-mail: prochazkova.j@fme.vutbr.cz

As mentioned in Ref. 7, the problem of the noise is important in the computational approach; therefore, our noise reduction method based on Linderberg-Lévy theorem is discussed in Sec. 3.1. Section 3.3 deals with adaptive neighborhood method for detection and correction of defective clusters.

We also present the objective comparison of recently used methods with our criteria and the results are summarized in Sec. 4.

2 Materials and Methods

The 3-D reconstruction methods should insist on image focusing. The object should be placed precisely in the camera or conventional microscope focal plane. However, this condition cannot be fulfilled because the focal plane intersects the 3-D object only in a contour line. The points of this contour line are displayed with maximum possible sharpness. Due to the wave properties of light and due to the finite resolution of the output device, the image can be considered sharp not only on this contour line but also in a certain interval of height, the zone of sharpness. The image of the zone of sharpness is called the optical cut. In Fig. 1, we can see a fracture surface of porous cement paste taken at different focal planes where the focused parts of the image are well discernible.

To create a sharp two-dimensional image, it is necessary to obtain a series of images of the same object, each of them with different focusing and each point of the object focused in at least one of the images. The optical cuts are identified and the sharp parts are assembled into a new image.

The confocal microscope Olympus LEXT OLS 3100 was used for testing. This microscope works in two modes: confocal and normal (nonconfocal). In the confocal mode, the microscope measures the height of single points using the

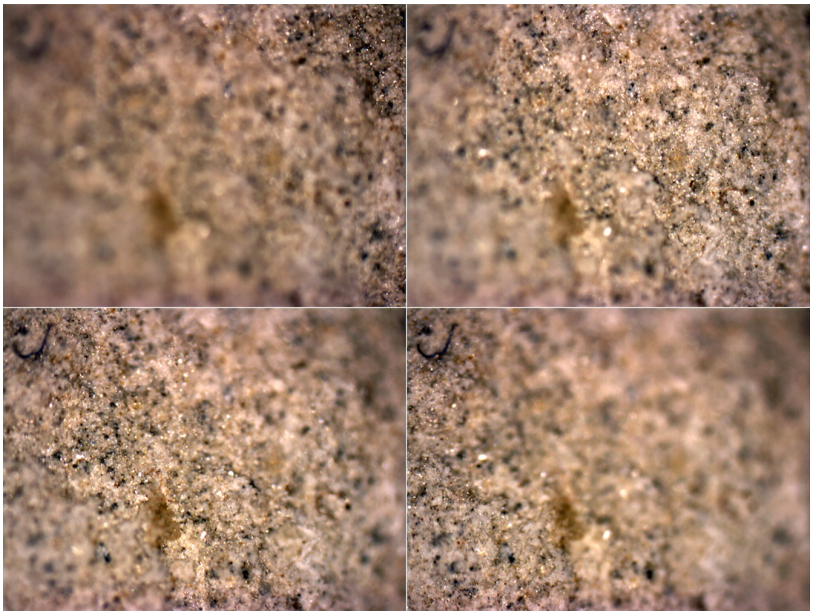

Fig. 1 Fracture surface of cement paste in different focal planes.

reflection of the laser beam from the measured surface with the user-defined accuracy (step in z axis). In the normal mode, the microscope works as a conventional optical device, e.g., a CCD camera or classic microscope.

The same fracture surface of the cement paste sample was scanned in both modes in resolution $W \times H = 1024 \times 768$ (field of view 1000×750 μm) with the step 12.5 μm. The data file *.csv with measured heights was obtained in the confocal mode using step 0.62 μm in z axis. The nonconfocal mode produced a series of 52 images.

The Olympus software is able to visualize the 3-D reconstruction of the samples in confocal mode only. Moreover, a reconstruction precision is low in our opinion, so that we use our own software to visualize the results for confocal and nonconfocal data. In confocal mode, the software visualizes the .csv file containing measured 3-D profile (Fig. 10). For data in nonconfocal mode, we implemented all known algorithms (low-pass filter, Fourier transform) and our own methods described in the following sections. The resulting 3-D reconstructions in Figs. 3, 4, and 11 are also computed and visualized using our software.

The preprocessing, processing, and postprocessing methods (additional noise reduction, focus image, impulse noise reduction, and 3-D reconstruction) are presented in Sec. 3. The known methods are briefly summarized in Sec. 2.1.

2.1 *Focusing Methods—Overview*

In this part, we describe some known focusing criteria that are used for $[i, j]$-pixel settings with the best focus in k'th image I_k, $k = 1,2,\ldots,K$.

Let $S_{i,j}$ be a square neighborhood of pixel $[i, j]$ with side sizes $2s + 1$ pixels. Let $x^{(k)}_{i+m,j+n}$ be $[i + m, j + n]$'th pixel value, $m, n = -s, -s + 1, \ldots, s - 1$ in k'th image. Then

$$M^{(k)}_{i,j} = \max\{x^{(k)}_{i+m,j+n}\} - \min\{x^{(k)}_{i+m,j+n}\} \tag{1}$$

is called range criterion,[9] and

$$V^{(k)}_{i,j} = \frac{1}{s^2}\sum_{m=-s}^{s}\sum_{n=-s}^{s} V^2_{m,n},$$

$$V_{m,n} = x^{(k)}_{i+m,j+n} - \frac{1}{s^2}\sum_{m=i-s}^{i+s}\sum_{n=j-s}^{j+s} x^{(k)}_{i+m,j+n} \tag{2}$$

is called variance criterion.[9]

Two other criteria are based on the Fourier transform. Let

$$\mathrm{D}: \{x^{(k)}_{i+m,j+n}\} \to \{X^{(k)}_{i+m,j+n}\}$$

$$m, n = -s, -s + 1, \ldots, s - 1$$

be discrete Fourier transform in pixel square neighborhood $\{x^{(k)}_{i+m,j+n}\}$ on k'th image and $\{|X^{(k)}_{i+m,j+n}|\}$ be an amplitude spectrum of Fourier image $\{X^{(k)}_{i+m,j+n}\}$. The expression

$${}_aF^{(k)}_{i;j} = \sum_{m=-s}^{s-1}\sum_{n=-s}^{s-1}[(|m| + |n|)|X^{(k)}_{i+m;j+n}|] \tag{3}$$

is called frequency criterion in Ref. 9.

The last criterion based on the Fourier transform (see Ref. 17) is

$${}_bF^{(k)}_{i,j} = \frac{1}{S(A_{i,j})}\sum_{[m,n]\in A_{i,j}} |X^{(k)}_{m,n}|, \tag{4}$$

where $A_{i,j}$ is a suitable annulus with the center in the amplitude spectrum center (in coordinates [0,0]) and $S(A_{i,j})$ is its area.

Methods described by Eqs. (1) and (2) are based on a square neighborhood with its center in the processing pixel; therefore, the pixel size of the square's side is an odd number. However, the Fourier transform in Eqs. (3) and (4) is computed with the fast Fourier transform (FFT) algorithm where the neighborhood of side size 2^n, $n \in \mathbf{N}$, is required. We used

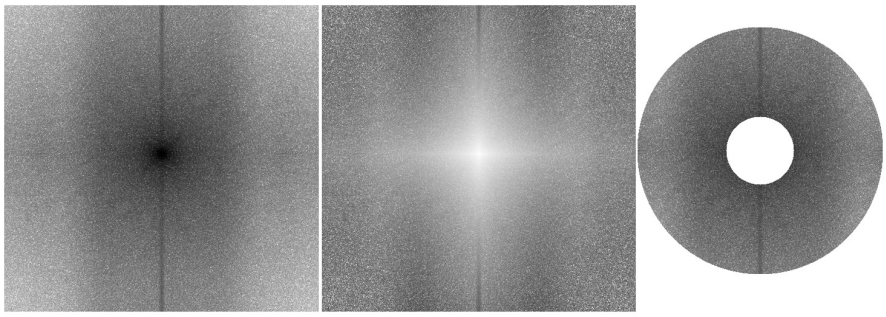

Fig. 2 Amplitude spectra of pixel neighborhood (negative, resolution 512×512): (a) original amplitude spectrum, (b) amplitude spectrum modified by criterion 3, and (c) amplitude spectrum modified by criterion 4.

the neighborhood centering to correct the size to the suitable odd number $2^n - 1$ so that the neighborhood is centrally symmetric.

In Fig. 2, we can see amplitude spectra of the neighborhood of the processed pixel modified by Eqs. (3) and (4). The size of the pixel neighborhood is only 512 because of the illustration. The real used sizes are 8, 16, or 32.

2.2 *Noise in the Images*

The 3-D reconstruction accuracy is substantially dependent on the noise. The influence of the input data noise on the 3-D reconstruction quality is not covered in the literature in detail. Just Ref. 10, as well as several others, provides brief notes about final adjustment of a 3-D profile using selected filters without further explanation of the methods used.

The noise can be categorized by many criteria. From the 3-D reconstruction point of view, additive and impulsive noise ratios are the most important.

The additive noise is added to every pixel value by each device used during creation, transfer, or reproduction of an image. It is typically caused by heat vibration. Low-pass filters are commonly used to reduce the additive noise (see, e.g., Ref. 18). But these filters are not able to differentiate whether high-frequency information is caused by noise or by small details of useful information. Therefore, loss of information ensues.

The impulse noise is not added to pixel values and it is caused by local problems of the device used, e.g., by dead pixels, dust grains, etc. The elimination of impulse noise pixel sets caused by these reasons can be done with simple median filters.[19,20] Nevertheless, real data commonly contains relatively big pixel clusters with the same value due to, e.g., overexposing. These clusters represent noise in 3-D reconstruction algorithms because the space frequencies are missing. The detection and correction of these pixels is difficult and sophisticated adaptive filters are used. In Sec. 3.3, we propose a filter based on the adaptive pixel neighborhood to eliminate these incorrect values.

3 Image Reconstruction Methods

3.1 *Additive Noise Reduction*

The 3-D reconstruction methods based on focusing criteria [Eqs. (1)–(4)] are very sensitive to input data noise. This noise has to be removed, but two important questions occurred: Should noise be reduced in input data directly or in the final sharp image? What type of the noise reduction method should be used?

Low-pass filters are commonly used to reduce the additive noise. The application of the Gaussian low-pass filter is illustrated in Figs. 3 and 4. Its principle is to reduce signals with high spatial frequencies. But these filters are not able to differentiate if high-frequency information is a useful signal or the noise. As a consequence, some details are missing, or unfocused parts appear in the final image. These filters are used in the company Olympus confocal microscope software, too.

Instead of low-pass filter methods, we preprocess data with the more correct method based on the Linderberg-Lévi theorem. Consider the noise as the realization of a random variable. Then we can write:

Theorem 1. Let $X_1, X_2, \ldots, X_P$ be random variables with arbitrary (but the same) distribution, the same mean value μ, and the same (finite) variance σ^2. Then the mean of $X_1, X_2, \ldots, X_P$ converges to the normal distribution with the same mean value μ and variance $\bar{\sigma}^2 = \sigma^2/P$.

The decreasing of the additive noise is realized as preprocessing, i.e., before the focusing criteria application.

Let the input noise image I consist of useful information U and noise N, which realizes a certain random variable. Every image I_k, $k = 1,2,\ldots,K$, is done p times, $p = 1,2,\ldots,P$. We compose the sequence of images

$$I_{k,p}, \quad k = 1,2,\ldots,K, \quad p = 1,2,\ldots,P,$$

where every p-tuplet $I_{k,1}, I_{k,2}, \ldots, I_{k,P}$ contains the same useful information U_k and different random noises $N_{k,p}$. For every k, we compute the arithmetic mean

$$\bar{I}_k = \frac{1}{P}\sum_{p=1}^{P}(U_k + N_{k;p}) = U_k + \frac{1}{P}\sum_{p=1}^{P} N_{k;p}. \tag{5}$$

Equation (5) preserves the useful information U_k (it is not random) and the variance of the noise

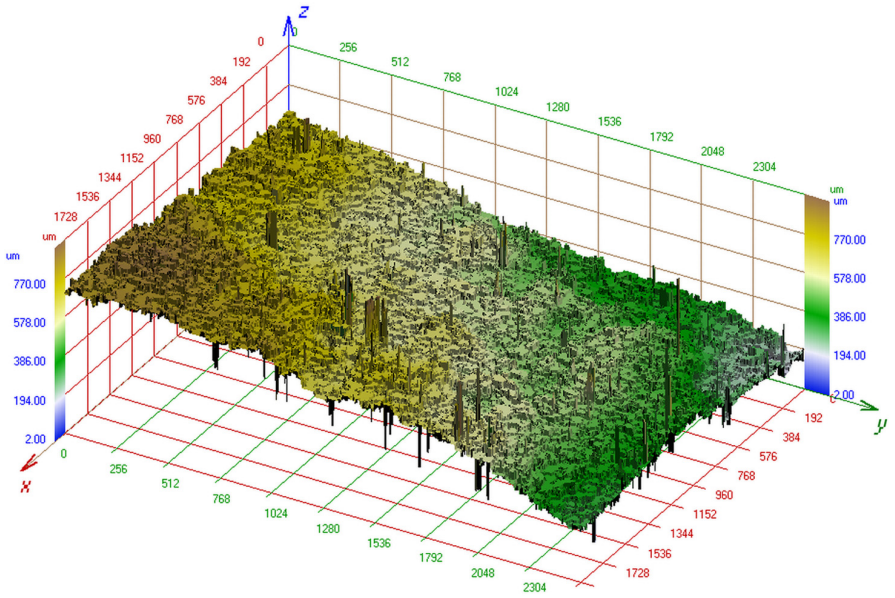

Fig. 3 Surface reconstruction using criterion 4 and visualization (without noise reduction, 52 images acquired by Olympus LEXT OLS 3100 in nonconfocal mode).

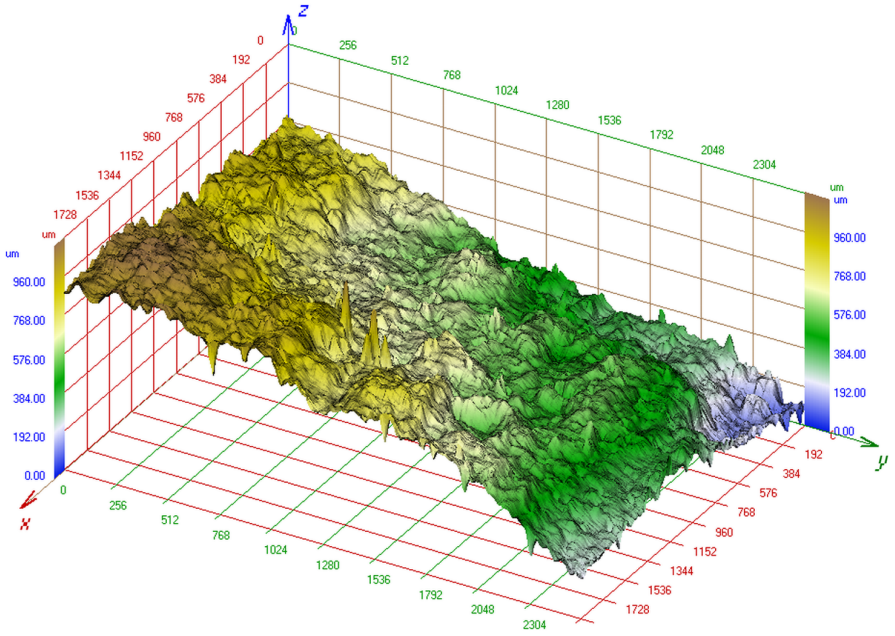

Fig. 4 Surface reconstruction using criterion 4 and visualization (with noise reduction by Gaussian low-pass filter, 52 images acquired by Olympus LEXT OLS 3100 in nonconfocal mode).

$$\bar{N}_k = \frac{1}{P}\sum_{p=1}^{P} N_{k,p} \tag{6}$$

will be P times lower.

The application of the Linderberg-Lévi theorem [Eq. (6)] with the focusing criterion [Eq. (4)] is illustrated in Fig. 5. The graph describes the dependence of one pixel value in image sequence I_k, $k = 1,2,\ldots,52$. The blue line shows the dependence if all images in k-tuplet are only once. Value fluctuations caused by noise are clearly visible in the neighborhood of maximum. The red line represents the Linderberg-Lévi theorem usage with 100 images in every k-tuplet. The smoothness of the red line indicates that the additive noise is significantly reduced and high spatial frequencies of useful information are preserved.

3.2 *Focusing Criteria*

The criteria [Eqs. (3) and (4)] are based on the standard Fourier transform. Let us note some of its disadvantages.

The criterion [Eq. (3)] adds weights to all frequencies including the low one, which indicated defocusing. On the other hand, this criterion enhances the high spatial frequencies that can be caused by noise. The criterion [Eq. (3)] cuts boundary frequencies too sharply. We propose a criterion that can eliminate all of these disadvantages.

$$ {}_cF_{i;j}^{(k)} = \sum_{m=-s}^{s-1} \sum_{n=-s}^{s-1} \left[|X_{i+m;j+n}^{(k)}| \sin^2 \pi \frac{\sqrt{m^2+n^2}}{s} \right]. \tag{7} $$

As it is known, edge effect occurs in the Fourier transform that can decrease focusing criteria based on this transform. Therefore, the following condition is added in Eqs. (3), (4), and (7):

If

$$ \mathrm{Re}(X_{i,j}^{(k)}) = 0 \quad \text{or} \quad \mathrm{Im}(X_{i,j}^{(k)}) = 0 $$

then we define

$$ |X_{i,j}^{(k)}| = 0. \tag{8} $$

Figure 6 shows the comparison of the modified Eqs. (3), (4), and (7). The resolution of the image is 512×512 because of the illustration. The 3-D reconstruction accuracy depends on the neighborhood size significantly. Small neighborhood sizes are extremely sensitive to noise because of the data deficiency. On the other hand, it is not appropriate to select big neighborhoods because the focusing is strictly a local property of the image.

Equations (3), (4), and (7) can be used in cosine Fourier transform, too. Reference 12 recommends the usage of Fourier cosine transform (DFT algorithm) instead of standard Fourier transform (FFT algorithm) so that we include DFT in our comparison. Corresponding expressions are formally identical, but $\{|X_{i;j}^{(k)}|\}$ means an amplitude spectrum of cosine Fourier transform of neighborhood of pixel $[i, j]$ on k'th image. The edge effect does not affect cosine transform so that the edge frequencies need not be zeroed.

Amplitude spectra of cosine transform $|X_{i;j}^{(k)}|$ with Eqs. (3), (4), and (7) are illustrated in Fig. 7.

3.3 *Detection and Correction of Defective Clusters*

The images often contain relatively large pixel clusters with the same values as mentioned in Sec. 2.2. The focusing criteria lack the correct information about space frequencies here. These monochromatic areas are the most visible on the focused image and defocusing makes them lighter. Near the focused image there is placed a curve minimum on the contrary (Fig. 5) and defocusing causes an increasing trend to two maximal values of the criteria (Fig. 8). In this case, the focusing criterion determines a bad pixel as correct and it causes the occurrence of relatively large defective clusters.

Note that the local minimum may be caused by additive noise (situation in Fig. 5); therefore, the reduction of additive noise is necessary in preprocessing as described in the previous section.

This two-step algorithm provides the correction of these defective clusters.

1. Detection—use statistical hypothesis testing to determine whether the pixel is correct.
2. Correction—compute correct values of incorrect pixels from the previous step.

The first step consists of the detection of incorrect pixels. This detection is usually based on the differences between the current pixel and its neighborhood (see, e.g., Refs. 21

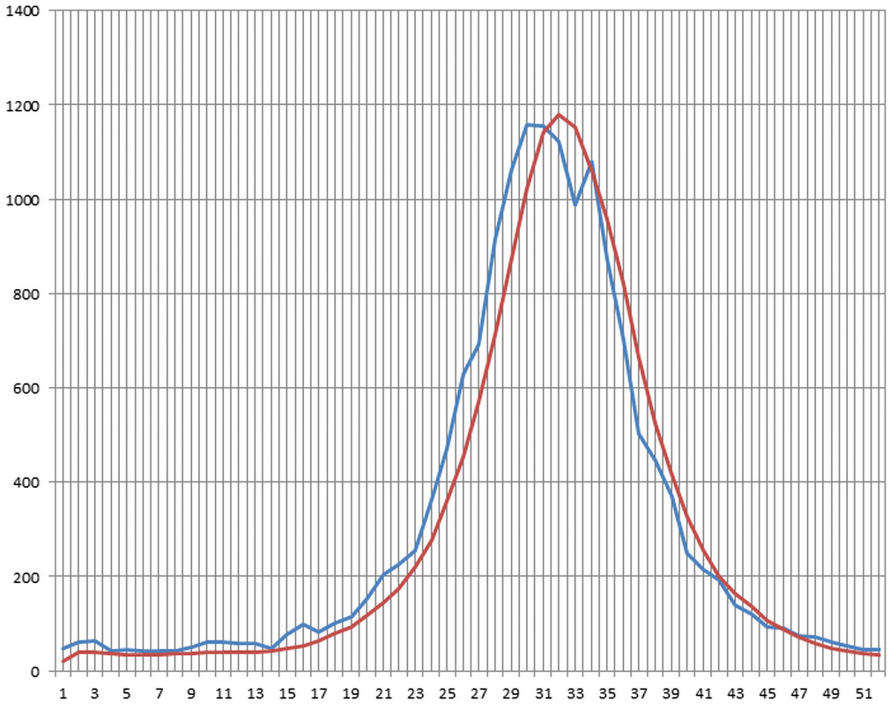

Fig. 5 Illustration of one noise reduction by Linderberg-Lévi theorem.

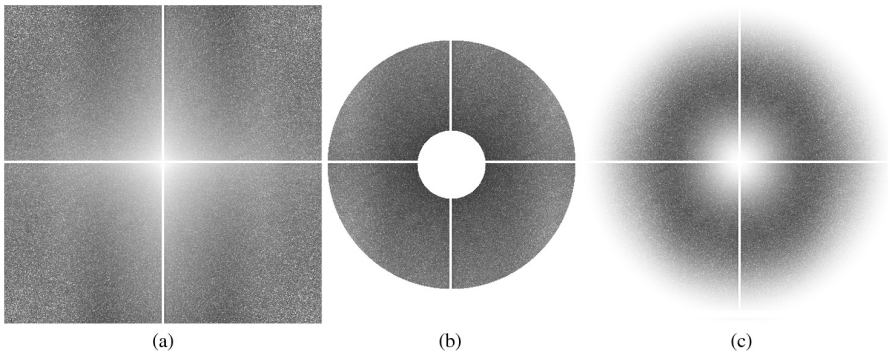

Fig. 6 Modified amplitude spectra based on standard Fourier transform: (a) criterion 3, (b) criterion 4, and (c) criterion 7.

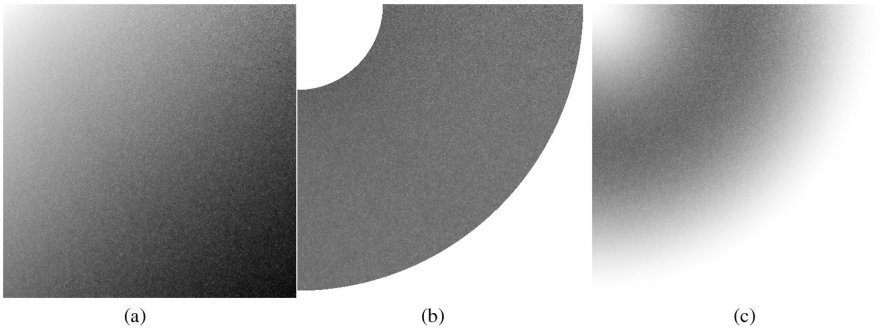

Fig. 7 Modified amplitude spectra based on cosine Fourier transform: (a) criterion 3, (b) criterion 4, and (c) criterion 7.

and 22). We can use the fact that pixel values through all optical cuts contain two local maxims (see Fig. 8). In the second step, we correct these clusters using the statistical function median. Standard filters are not appropriate to remove pixel clusters so that the adaptive approach is suitable with respect to size and shape of clusters. In our method, we use the adaptive pixel neighborhood, which can be defined as follows:

Let $A_{w,k}[i,j]$ be the pixel set that

1. has k members,
2. is a subset of a square neighborhood $S_w[i,j]$ with side size w, and pixel $[i,j]$ is the center of it,
3. the expression

$$\sum_{[i,j]\in V} |f_{m,n} - f_{i,j}|$$

takes the minimum for $V = A_{w,k}[i,j]$ ($f_{m,n}$ is the value of the pixel $[m,n]$ and $f_{i,j}$ is the value of the pixel $[i,j]$).

Then the pixel set $A_{w,k}[i,j]$ is called the adaptive neighborhood of the pixel $[i,j]$.

The adaptive neighborhood of the pixel $[i,j]$ contains k near pixel values. Note that the set V in definition of the adaptive neighborhood is not uniquely determined. Nevertheless, the choice of the set V is arbitrary—pixel values are the same for every set, only their positions differ.

Our procedure produces adaptive neighborhood $A_{w,k}[i,j]$ for every wrong pixel and the original value $[i,j]$ is replaced with median of $A_{w,k}[i,j]$ neighborhood.

3.3.1 *Filtering algorithm*

The main principle of the filter is illustrated in Fig. 9. Let us presume that a cluster (brown colored pixels in Fig. 9) is the biggest in reconstructed surface. We set the following parameters:

m ... maximal horizontal or vertical size ($m = 9$)
n ... maximal number of pixels in the cluster ($n = 19$)
k ... $k = 2n + 1 = 49$
w ... $w > m$, $w^2 > k$ ($w = 19$)

Then, in this way the highest value 438, which is marked in Fig. 9, will be replaced by value 312.

4 Results

The methods were tested on the fracture surface of porous cement paste. We measured this surface with the confocal microscope in the confocal mode using z step of 12.5 μm.

Consequently, we prepared a set of 52 images of the same surface in the nonconfocal mode (z-step was 12.5 μm) as described in Sec. 2. After that we made a series of computations using the range [Eq. (1)] and variance [Eq. (2)] methods. The neighborhood size was 15×15 pixels. Also, the standard Fourier transform modified by Eqs. (3), (4), and (7) was computed—these methods are denoted by FFT1, FFT2, and FFT3 in Table 1 and the cosine Fourier transform modified by the same way (denoted by DCT1, DCT2, and DCT3). The neighborhood size was 16×16 pixels due to FFT and DFT, respectively; the neighborhood 16×16 pixels was processed in amplitude spectra. The input data were

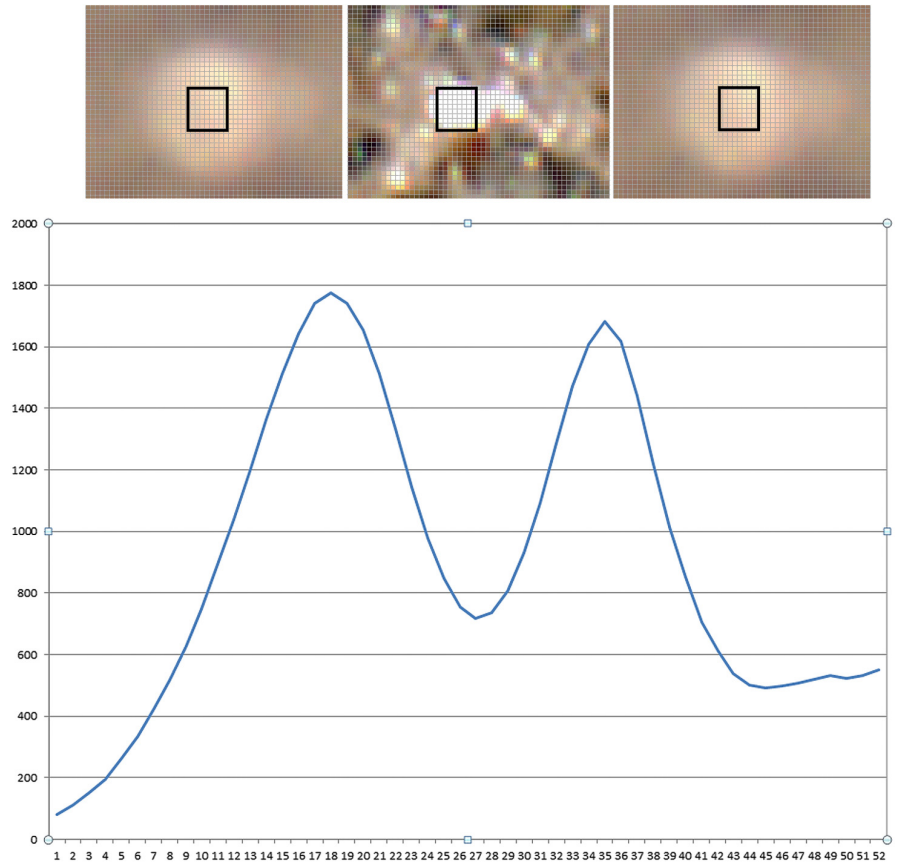

Fig. 8 Detection of wrong clusters—graph with two local maxima.

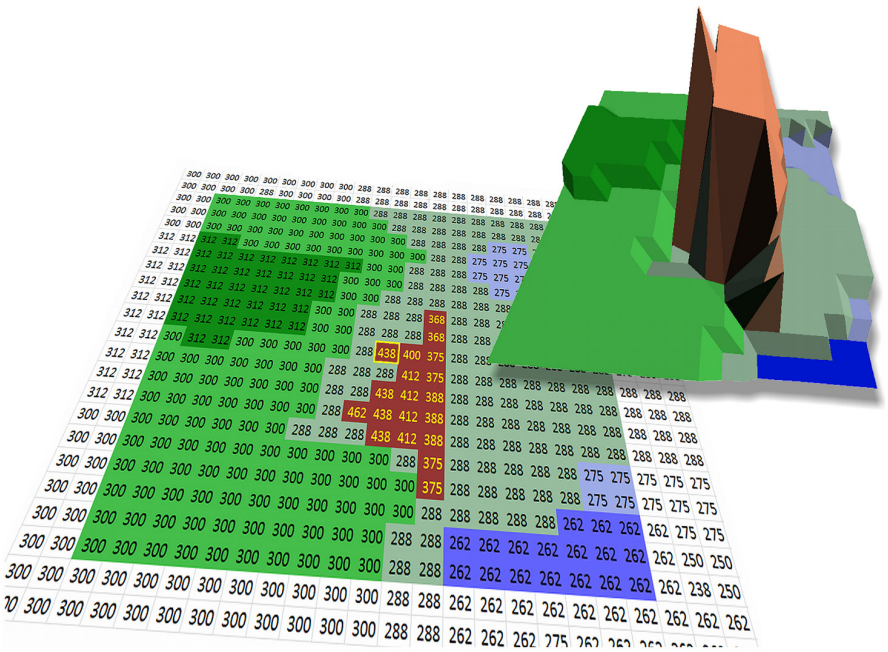

Fig. 9 Correction of clusters with adaptive median filter with adaptive neighborhood.

Table 1 Comparison of optical cuts three-dimensional reconstruction of fracture surface using methods described in Secs. 2 and 3 (z-step 12.5 μm), and the scanning of the same surface in confocal mode (z-step 12.5 μm).

Methods	RMSD abs.	RMSD rel.	AMD abs.	AMD rel.	CORR	IED
Surface constructed from noise data						
Range	26.05	2.0840	18.93	1.5144	0.9812	17.4786
Variance	25.81	2.0648	17.94	1.4352	0.9816	17.3469
FFT1	23.41	1.8728	17.03	1.3624	0.9849	17.4802
FFT2	22.59	1.8072	16.51	1.3208	0.9860	17.4827
FFT3	22.51	1.8008	16.49	1.3192	0.9861	17.4213
DCT1	25.40	2.0320	19.11	1.5288	0.9865	17.5119
DCT2	25.54	2.0432	19.26	1.5408	0.9865	17.5107
DCT3	25.64	2.0512	19.37	1.5496	0.9865	17.4780
Decreased additive noise (via theorem 1)						
Range	24.48	1.9584	17.81	1.4248	0.9834	17.3469
Variance	24.27	1.9416	16.76	1.3408	0.9838	17.3446
FFT1	21.70	1.7360	15.86	1.2688	0.9870	17.3472
FFT2	21.61	1.7288	15.81	1.2648	0.9871	17.3482
FFT3	21.56	1.7248	15.76	1.2608	0.9872	17.3454
DCT1	21.75	1.7400	15.98	1.2784	0.9870	17.3479
DCT2	21.15	1.6920	15.98	1.2784	0.9870	17.3462
DCT3	21.67	1.7336	15.90	1.2720	0.9871	17.3453
Decreased additive and impulse noise (defective pixel clusters)						
Range	23.24	1.8592	16.21	1.2968	0.9864	17.3442
Variance	22.01	1.7608	16.11	1.2888	0.9866	17.3436
FFT1	21.44	1.7152	15.75	1.2600	0.9873	17.3448
FFT2	21.50	1.7200	15.77	1.2616	0.9873	17.3451
FFT3	21.40	1.7120	15.69	1.2552	0.9874	17.3439
DCT1	21.75	1.7400	15.98	1.2784	0.9870	17.3478
DCT2	21.15	1.6920	15.98	1.2784	0.9870	17.3461
DCT3	21.65	1.7320	15.89	1.2712	0.9871	17.3450

RMSD, root mean square deviation; AMD, arithmetic mean of differences; CORR, correlation; IED, information entropy of differences; FFT, fast Fourier transform.

Table 2 Confocal scanning (z-step 0.62 μm) and the same scanning filtered with Olympus company low-pass filter—results for five pairs of these surfaces.

Methods	RMSD abs.	RMSD rel.	AMD abs.	AMD rel.	CORR	IED
Pair 1	21.43	34.8871	15.85	25.5645	0.9602	18.7061
Pair 2	22.14	36.0430	16.03	25.8548	0.9584	18.7095
Pair 3	22.35	36.3848	16.15	26.0484	0.9576	18.7080
Pair 4	21.93	35.7011	15.92	25.6774	0.9594	18.7059
Pair 5	21.82	35.5220	15.88	25.6129	0.9597	18.7054

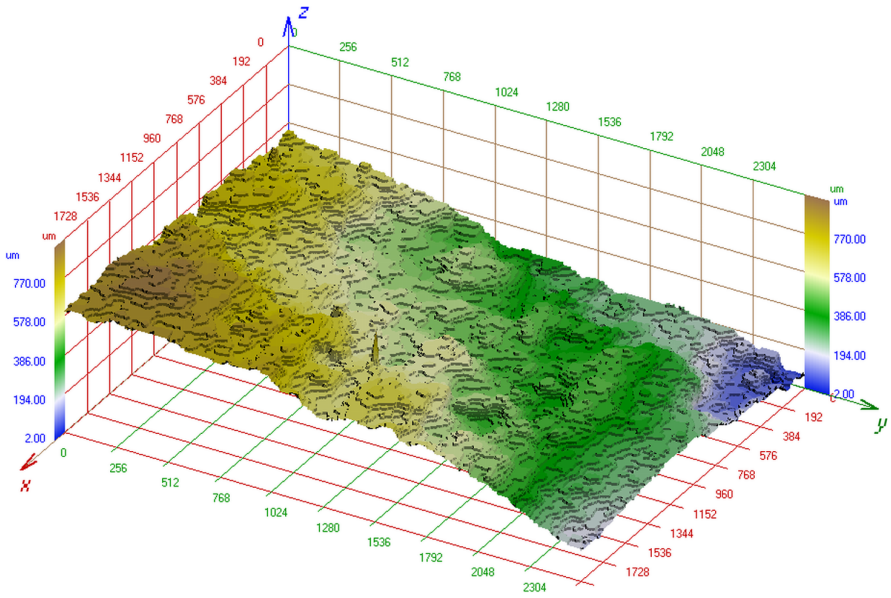

Fig. 10 Three-dimensional (3-D) visualization of fracture surface of cement paste (data: Olympus LEXT OLS 3100, 3-D profile in .csv format by Olympus company software, confocal mode).

1. with all noise
2. with additive noise, which was reduced using the Linderberg-Lévy theorem—see Sec. 3.1
3. with additive noise reduced according to point 2 and impulse noise, which was reduced by the adaptive median filter with adaptive neighborhood—see Sec. 3.3

The input data were compared with the same nonfiltered surface that was acquired in the confocal mode using the minimal z step (12.5 μm) namely in the following ways.

Let F_{ij} be the confocal microscope profile and $\bar{F}$ its arithmetic mean. Let f_{ij} be the 3-D reconstruction results (using all mentioned methods) and $\bar{f}$ its mean. Then

$$\mathrm{RMSD} = \sqrt{\frac{1}{WH} \cdot \sum_{i=0}^{W-1} \sum_{j=0}^{H-1} (F_{ij} - f_{ij})^2} \tag{9}$$

is the root mean square deviation of both profiles, and

$$\mathrm{AMD} = \frac{1}{WH} \cdot \sum_{i=0}^{W-1} \sum_{j=0}^{H-1} |F_{ij} - f_{ij}| \tag{10}$$

is the arithmetic mean of differences, and correlation CORR is defined as

$$\mathrm{CORR} = \frac{\sum_{i=0}^{W-1} \sum_{j=0}^{H-1} (F_{ij} - \bar{F})(f_{ij} - \bar{f})}{\sqrt{\sum_{i=0}^{W-1} \sum_{j=0}^{H-1} (F_{ij} - \bar{F})^2 \sum_{i=0}^{W-1} \sum_{j=0}^{H-1} (f_{ij} - \bar{f})^2}}.$$

The information (Shannon) entropy IE can be used as an indicator of the surfaces similitude (used, e.g., in Ref. 23).

$$\mathrm{IE} = -\sum_{i=0}^{n} p_i \log_2 p_i, \tag{11}$$

where $0 < p_i < 1$ for every p_i and $\Sigma p_1 = 1$. Equation (11) indicates the degree of chaoticness of a probability distribution p_i.

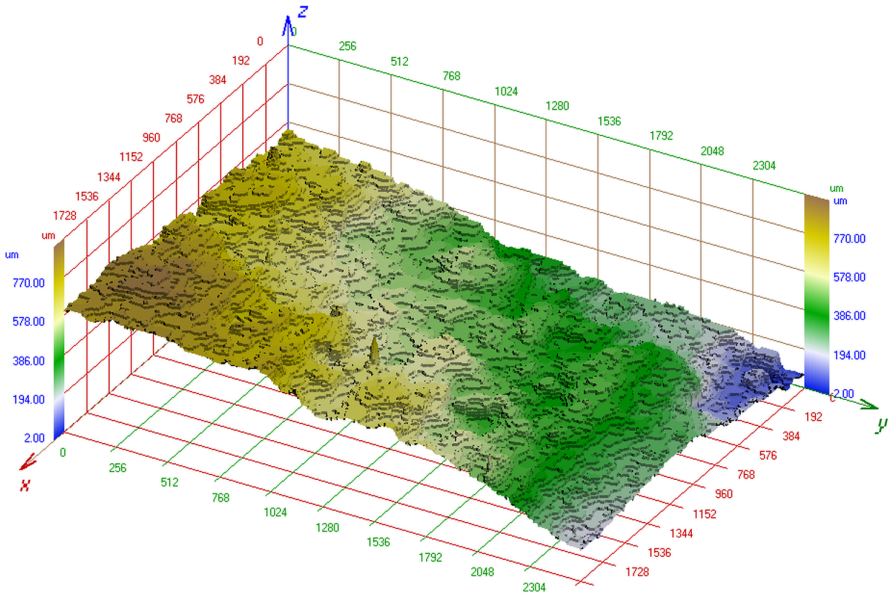

Fig. 11 3-D reconstruction of fracture surface of cement paste using Linderberg-Lévi theorem additive noise reduction as preprocessing and adaptive median filter as postprocessing described in Sec. 3 (data: Olympus LEXT OLS 3100, nonconfocal mode).

Table 3 The comparison of the execution time (s), the notations 8×8, respectively 16×16 mean used pixel neighborhood size.

	Range	Variance	FFTa	FFTb	FFTc	DCTa	DCTb	DCTc
PC1 8×8	33	61	796	801	800	440	442	441
PC2 8×8	58	82	1099	1104	1102	832	839	837
PC1 16×16	81	208	3634	3580	3588	1714	1745	1732
PC2 16×16	116	298	4708	4636	4693	3521	3542	3533

Table 4 The RSM comparison of the surfaces constructed using the proposed methods.

	Range	Variance	FFTa	FFTb	FFTc	DCTa	DCTb	DCTc
Range	0.0000	0.7723	0.6650	0.7165	0.6532	0.6921	0.6878	0.6820
Variance		0.0000	0.7298	0.7869	0.7214	0.7736	0.7677	0.7574
FFTa			0.0000	0.3526	0.3243	0.4993	0.4674	0.4648
FFTb				0.0000	0.4594	0.5458	0.5532	0.5524
FFTc					0.0000	0.4283	0.3979	0.3811
DCTa						0.0000	0.2873	0.3161
DCTb							0.0000	0.2167
DCTc								0.0000

Table 5 The CORR comparison of the surfaces constructed using the proposed methods.

	Range	Variance	FFTa	FFTb	FFTc	DCTa	DCTb	DCTc
Range	100.000	99.7321	99.8006	99.7787	99.8079	99.7841	99.7870	99.7905
Variance		100.000	99.7609	99.7226	99.7658	99.7318	99.7356	99.7418
FFTa			100.000	99.9438	99.9528	99.9004	99.9012	99.9026
FFTb				100.000	99.9054	99.8750	99.8619	99.8627
FFTc					100.000	99.9177	99.9258	99.9343
DCTa						100.000	99.9630	99.9955
DCTb							100.000	99.9963
DCTc								100.000

Table 6 The IED comparison of the surfaces constructed using the proposed methods.

	Range	Variance	FFTa	FFTb	FFTc	DCTa	DCTb	DCTc
Range	0.000	17.9724	18.0557	18.1449	18.0320	18.1229	18.1230	18.1044
Variance		0.000	17.5754	17.8468	17.4536	17.6993	17.6449	17.5989
FFTa			0.000	16.6688	16.1688	17.0771	17.0478	17.0392
FFTb				0.000	17.0461	17.3733	17.4047	17.4074
FFTc					0.000	15.9722	16.7270	16.6024
DCTa						0.000	15.9722	16.2471
DCTb							0.000	15.1585
DCTc								0.000

Further, let

$$p_{ij} = \frac{F_{ij} - f_{ij}}{\sum_{m=0}^{W-1} \sum_{n=0}^{H-1} |F_{mn} - f_{mn}|} \tag{12}$$

be the information entropy of the differences (IED). We define $p_{ij} = 0$ in case $F_{ij} = f_{ij}$.

The results are summarized in Table 1. There are stated quadratic and arithmetic means of differences between the optical cuts of 3-D reconstruction of the fracture surface using the methods described in Secs. 2 and 3 (z step of 12.5 μm), and the scanning of the same surface in the confocal mode (with the same z step of 12.5 μm). These values are stated in micrometers in absolute columns, and they are divided by the used z step in relative columns.

The same comparison is provided for the surface that we obtained in the confocal mode using a z step of 0.62 μm and the same surface that was filtered with the Olympus company low-pass filter. The results are visible in Table 2.

We can visually compare the fracture surface obtained in the confocal mode by z step of 12.5 μm (Fig. 10) and 3-D reconstruction of the same surface constructed from optical cuts acquired with the same step in the nonconfocal mode (Fig. 11).

Table 3 shows the time comparison of the proposed methods. The computations were tested on computers: PC1: Intel Core i7-2600CPU @ 3.74 GHz 3.70 GHz, RAM 8 GB, W7, 64 bit, PC2: Intel Core i7-2670QM CPU @ 2.20 GHz 2.20 GHz, RAM 3 GB useable, W7, 32 bit.

5 Conclusion

1. The difference between all surfaces constructed by the proposed methods and the confocal nonfiltered surface is comparable with the difference between the nonfiltered and filtered confocal surface, i.e., all proposed methods for 3-D reconstruction from the series of optical cuts are also useful for 3-D reconstruction of porous materials in cases when the confocal microscope is unusable.
2. Decreasing additive noise according to Sec. 3.1 improves the results of all methods described in Secs. 2 and 3.2.

3. The proposed method of noisy clusters elimination in Sec. 3.3 improves the results of all methods.
4. Table 3 shows the processing time of the methods. The range method and variance method are significantly faster than Fourier transform methods; however, their results are worse in all indicators RSMD, CORR, and IED. It is presented in Tables 4–6. The DCT methods are faster than the FFT methods because they do not use the imaginary part of the transform. DCT methods also provide better results in comparison with FFD methods.
5. Our future research deals with the images (mainly scale changed) of larger samples. In this paper, we solve surfaces with discrete levels of the height, but we solve the problem of the automatic image registration and intensively smooth output surfaces.

Acknowledgments

This work was supported by the Grant Agency of the Czech Republic under contract no. 13-03403S. The second author acknowledges partial support from the Brno University of Technology, Specific Research Project no. FSI-S-14-2290 and Project LO1202 by financial means from the Ministry of Education, Youth and Sports under the National Sustainability Programme I.

References

1. T. Ficker, D. Martisek, and H. Jennings, "Roughness of fracture surfaces and compressive strength of hydrated cement pastes," *Cem. Concr. Res.* **40**(6), 947–955 (2010).
2. T. Ficker and D. Martisek, "Digital fracture surfaces and their roughness analysis: applications to cement-based materials," *Cem. Concr. Res.* **42**(6), 827–833 (2012).
3. V. Thiry and D. Green, "The multifocus imaging technique in petrology," *Comput. Geosci.* **45**, 131–138 (2012).
4. Y. Ichikawa and J. I. Toriwaki, "Confocal microscope 3D visualizing method for fine surface characterization of microstructures," *Proc. SPIE* **2862**, 96–101 (1996).
5. K. Nadolny, "Confocal laser scanning microscopy for characterisation of surface microdiscontinuities of vitrified bonded abrasive tools," *Int. J. Mech. Eng. Rob. Res.* **1**(1), 14–29 (2012).
6. D. Lange, H. Jennings, and S. Shah, "Analysis of surface roughness using confocal microscopy," *J. Mater. Sci.* **28**(14), 3879–3884 (1993).
7. V. Aslantas and R. Kurban, "Fusion of multi-focus images using differential evolution algorithm," *Expert Syst. Appl.* **37**(12), 8861–8870 (2010).
8. Z. Zhang and R. Blum, "A categorization of multiscale-decomposition-based image fusion schemes with a performance study for a digital camera application," *Expert Syst. Appl.* **87**(8), 1315–1326 (2010).
9. D. Martisek, "The 2-D and 3-D processing of images provided by conventional microscopes," *Scanning* **24**(6), 284–296 (2002).
10. M. Niederost, J. Niederost, and J. Scucka, "Automatic 3D reconstruction and visualization of microscopic objects from a monoscopic multifocus image sequence," 2003, http://www.isprs.org/proceedings/XXXIV/5-W10/papers/niederoe.pdf (24 September 2015).
11. N. Chern, P. A. Neow, and M. Ang, "Practical issues in pixel-based autofocusing for machine vision," in *IEEE International Conference on Robotics and Automation*, pp. 2791–2796, IEEE (2001).
12. T. Kristan et al., "A Bayes-spectral-entropy-based measure of camera focus using a discrete cosine transform," *Pattern Recognit. Lett.* **27**(13), 1431–1439 (2006).
13. R. Minhas, A. Mohammed, and Q. Wu, "Shape from focus using fast discrete curvelet transform," *Comput. Geosci.* **44**(4), 839–853 (2011).
14. J. Kautsky et al., "A new wavelet-based measure of image focus," *Pattern Recognit. Lett.* **23**(14), 1785–1794 (2002).
15. C. Yuan, Z. Peng, and X. Yan, "Surface characterization using wavelet theory and confocal laser scanning microscopy," *J. Tribol.* **127**(2), 394–404 (2005).
16. M. Mahmood, A. Majid, and T. Choi, "Optimal depth estimation by combining focus measures using genetic programming," *Inf. Sci.* **181**(7), 1249–1263 (2011).
17. D. Martisek and H. Druckmullerova, "Multifocal image processing," *Math. Appl.* **3**(1), 77–90 (2014).
18. S. Dong-Mo et al., "Experimental demonstration of a low-pass spatial filter based on a one-dimensional photonic crystal with a defect layer," *Chin. Phys. Lett.* **30**(4) (2013).
19. I. A. Shaik et al., "Impulse noise detection and filtering based on adaptive weighted median filter," *Res. Inventy: Int. J. Eng. Sci.* **1**(8), 49–54 (2012).
20. N. Petrojevic and V. Crnojevic, "Universal impulse noise filter based on genetic programming," *IEEE Trans. Image Process.* **17**(7), 1109–1120 (2008).
21. Y. Dong and S. Xu, "A new directional weighted median filter for removal of random-valued impulse noise," *IEEE Signal Process. Lett.* **14**, 193–196 (2007).
22. S. Akkoul et al., "A new adaptive switching median filter," *IEEE Signal Process. Lett.* **17**, 587–590 (2010).
23. J. A. Munoz-Rodriguez, "Computational cryptography based on trigonometric algorithms and intensity superposition," *Imaging Sci. J.* **58**(2), 61–80 (2010).

Dalibor Martišek is an associate professor at Brno University of Technology. He received his PhD in mathematical engineering from the Institute of Mathematics in 2000. He is the author of 13 journal papers and has written a monograph about computer graphics. His current research interests include computer graphics and image analysis.

Jana Procházková is an assistant professor at Brno University of Technology. She received her MS degree in mathematics and geometry from Masaryk University in 2004 and her PhD in applied mathematics from Brno University of Technology in 2007. She is a young researcher and is the author of five journal papers. Her current research interests cover the area of computer graphics, modeling, and three-dimensional reconstructions.

Tomáš Ficker is a professor at Brno University of Technology. He is the author of more than 50 journal papers and the holder of 4 patents. His current research interests include confocal microscopy, cement and concrete research.

SCANNING VOL. 00, 1–11 (2012)

Direct Volume Rendering Methods for Cell Structures

DALIBOR MARTIŠEK* AND KAREL MARTIŠEK

Department of Computer Geometry and Graphics, Institute of Mathematics, Faculty of Mechanical Engineering, Brno University of Technology, Brno, Czech Republic

Summary: The study of the complicated architecture of cell space structures is an important problem in biology and medical research. Optical cuts of cells produced by confocal microscopes enable two-dimensional (2D) and three-dimensional (3D) reconstructions of observed cells. This paper discuses new possibilities for direct volume rendering of these data. We often encounter 16 or more bit images in confocal microscopy of cells. Most of the information contained in these images is unsubstantial for the human vision. Therefore, it is necessary to use mathematical algorithms for visualization of such images. Present software tools as OpenGL or DirectX run quickly in graphic station with special graphic cards, run very unsatisfactory on PC without these cards and outputs are usually poor for real data. These tools are black boxes for a common user and make it impossible to correct and improve them. With the method proposed, more parameters of the environment can be set, making it possible to apply 3D filters to set the output image sharpness in relation to the noise. The quality of the output is incomparable to the earlier described methods and is worth increasing the computing time. We would like to offer mathematical methods of 3D scalar data visualization describing new algorithms that run on standard PCs very well. SCANNING 00: 1–11, 2012. © 2012 Wiley Periodicals, Inc.

Key words: DVR algorithm, Bresenham's algorithm, voxel, integer arithmetic, fast 3D filters, illumination model

Contract grant sponsor: Center of Quality and Reliability; Contract grant number: 1M06047; Contract grant sponsor: Brno University; Contract grant number: FSI-J-10-76.

Address for reprints: Dalibor Martišek, Department of Computer Geometry and Graphics, Institute of Mathematics, Faculty of Mechanical Engineering, Brno University of Technology, Technicka 2, Brno 616 69, Czech Republic
E-mail: martisek@fme.vutbr.cz

Received 8 December 2011; Accepted with revision 1 February 2012

DOI 10.1002/sca.21019
Published online in Wiley Online Library (wileyonlinelibrary.com)

Introduction

Algorithms that process three-dimensional (3D) data can be classified into two groups: surface-fitting algorithms (SF algorithms) and direct volume rendering algorithms (DVR algorithms). SF algorithms construct a geometric surface representation of the scalar field to be displayed, and then construct this surface. DVR algorithms display the scalar field directly without surface representation.

An original SF algorithm of conventional microscope outputs processing was presented in Martišek (2002). It is used for the study of the mechanical properties of inorganic materials—see Ficker *et al*. (2007), Ficker *et al*. (2010), Ficker *et al*. (2011). Our first results of SF algorithms for confocal microscopes applied on cell structures was published in Martišek (2002) and DVR algorithms for the same use in Martišek (2007).

A confocal microscope output is formed by a series of (usually a few tens of) optical cuts through an examined object and our ambition is to reconstruct the object on the basis of these cuts: two-dimensionally and especially three-dimensionally. Biology and medical research use the fact that confocal microscopy is basically a noninvasive and nondestructive kind of study of the space structure of cells and tissues.

For study of the complicated architecture of space structure of cells, we have more and more quality instruments available but the needed software support falls behind slightly. Most of the programs provided with these instruments are not able to master the 3D object reconstruction at an appropriate level and, if they are, companies do not publish any applied methods or algorithms for commercial reasons. Therefore very little information can be found on these methods. This paper tries to fill all these gaps at least partially.

Materials and Methods

Primary Data

The primary data used in this paper have been provided by the Olympus Fluoview II fluorescent

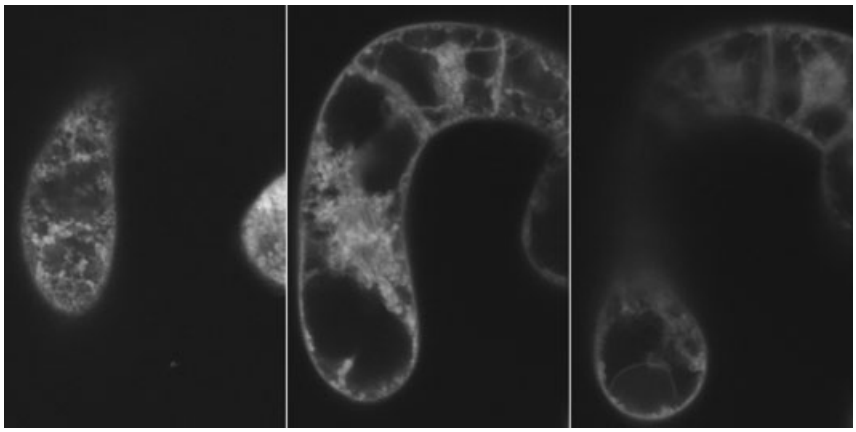

Fig 1. Optical cuts of *Tobacco* cell, RGB true color, original resolution 1,024 × 768 pixels, 10th, 40th, and 80th from 99 cuts are chosen as an example.

scan confocal microscope by Prof. Roman Janisch of the Department of Biology, Faculty of Medicine, Masaryk University, Brno, Czech Republic and Prof. Zdenek Opatrny of the Institute of Plant Physiology, Faculty of Science, Charles University in Prague, Czech Republic. We can see optical cuts of *Tobacco* cell in Figure 1 (true RGB color and resolution of 1,024 × 768 pixels of each cut in original data). The 10th, 40th, and 80th from 99 cuts are chosen as an example. In Figure 2, there are shown optical cuts of *Euplotes patela* cell—red (nucleus) and green (other structures) separate optical cuts, color depth 16 bits, resolution of 450 × 460 pixels of each cut in original data. The 1st, 10th, 19th, and 28th from 28 cuts are chosen as example (red cuts—upper part of the image, green cuts—lower part of the image).

Principle of Recent Methods

The basic principle of recent DVR algorithms is the so called ray casting. The method tracks the viewing ray and calculates values of the scalar field.

The optical cuts create a 3D data grid for space reconstruction of cell structures. Finding the intersections of a projection line with a data grid is an important problem (see Fig. 3). Strictly speaking: it is not too difficult to find them, but we have to find these intersections quickly and efficiently. It is necessary to realize that this procedure will be repeated for each pixel of an output bitmap, that is, for several hundreds of thousands or even several millions of lines with a few thousands of intersections lying on each of them. This is a serious burden even for the best

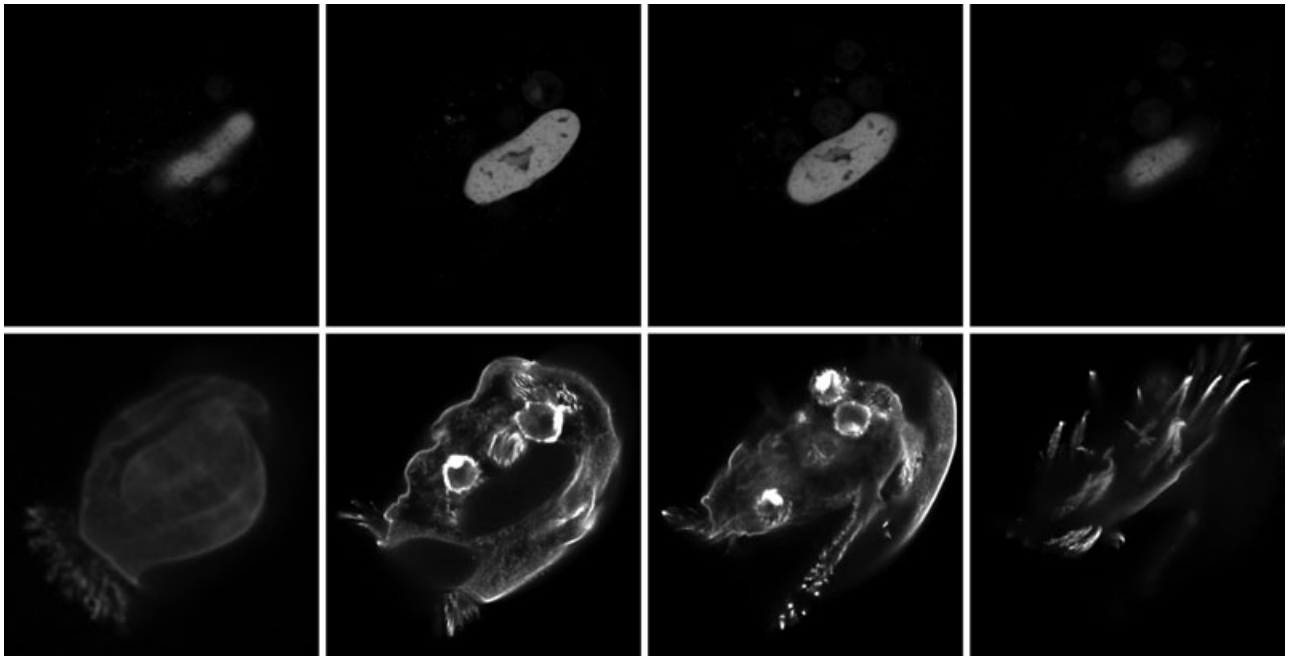

Fig 2. Optical cuts of *Euplotes patela* cell, 16 bits per pixel, original resolution 453 × 464 pixels, 2 × 28 cuts (red, green), the 1st, 10th, 19th, and 28th are chosen as example.

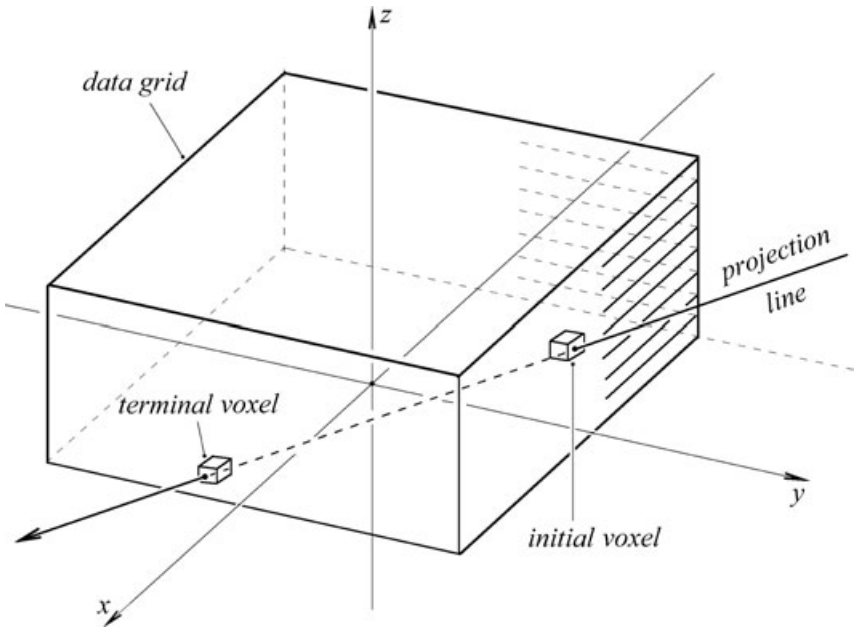

Fig 3. 3D data grid created by optical cuts and passage of a projection line through it as the base for 3D line voxelization and space reconstruction.

computers. It is necessary to find out which voxels lie on the line segment bounded by the initial and terminal voxel.

A fast graphic algorithm for two-dimensional (2D) line construction comes from Bresenham—see Bresenham ('65) or Foley *et al*. ('90). It works with integer arithmetic only and is therefore fundamentally faster. We have two points with integer coordinates. Our task is to construct a line segment connecting these two points or—very intuitively—to decide "which pixels of an output device will be processed." In literature, this procedure is often called rasterization of a line segment. The straight line on which our line segment lies has the equation $y = k \cdot x + q$, where (with respect to the integer coordinates of the limiting points) $k = \frac{\Delta y}{\Delta x} \in \mathrm{Q}$; $q \in \mathrm{Z}$. We must decide which pixel (A or B—see Fig. 4) will be processed.

For using the integer arithmetic, it is necessary to generate a "predictor" sequence $\{p_i\}_{i=1}^{b_1-a_1+1}$,

$$p_i = (r_i - s_i)\Delta x. \tag{1}$$

Bresenham proved that

$$\begin{aligned} & p_1 = 2\Delta y - \Delta x \\ p_i > 0 \Rightarrow\ & p_{i+1} = p_i + 2\Delta y - \Delta x \\ p_i \le 0 \Rightarrow\ & p_{i+1} = p_i + 2\Delta y. \end{aligned}$$

Thus, the ith step of Bresenham's algorithm is as follows:

If $p_i > 0$ then the pixel with the coordinates $[x_i + 1; y_i + 1]$ is processed.

If $p_i \le 0$ then the pixel with the coordinates $[x_i; y_i]$ is processed.

The algorithm described above works with the tangent k lying in the interval (0;1). We work by analogy in other cases.

The classical Bresenham's algorithm works in 2D, but some its generalizations for the 3D space are known as well—see Mokrzycki ('88), Cohen and Kaufman ('97) or Chikit and Woo (2011), for example.

We use double Bresenham's algorithm—its principle is shown in Figure 5. The procedure is as follows:

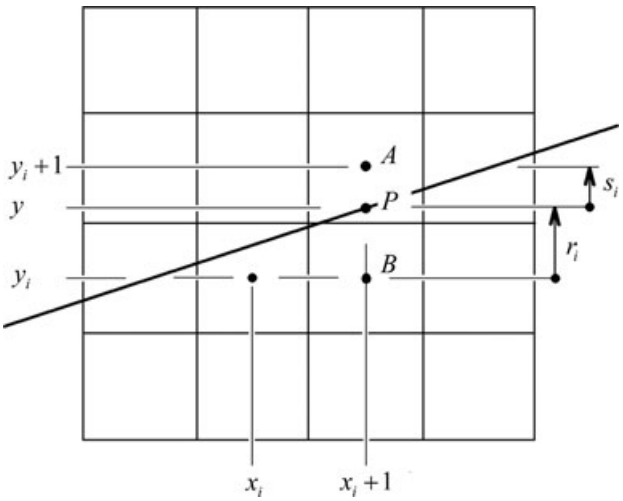

Fig 4. Principle of Bresenham's algorithm—the task is to decide which pixel will be colored. Only integer arithmetic is used.

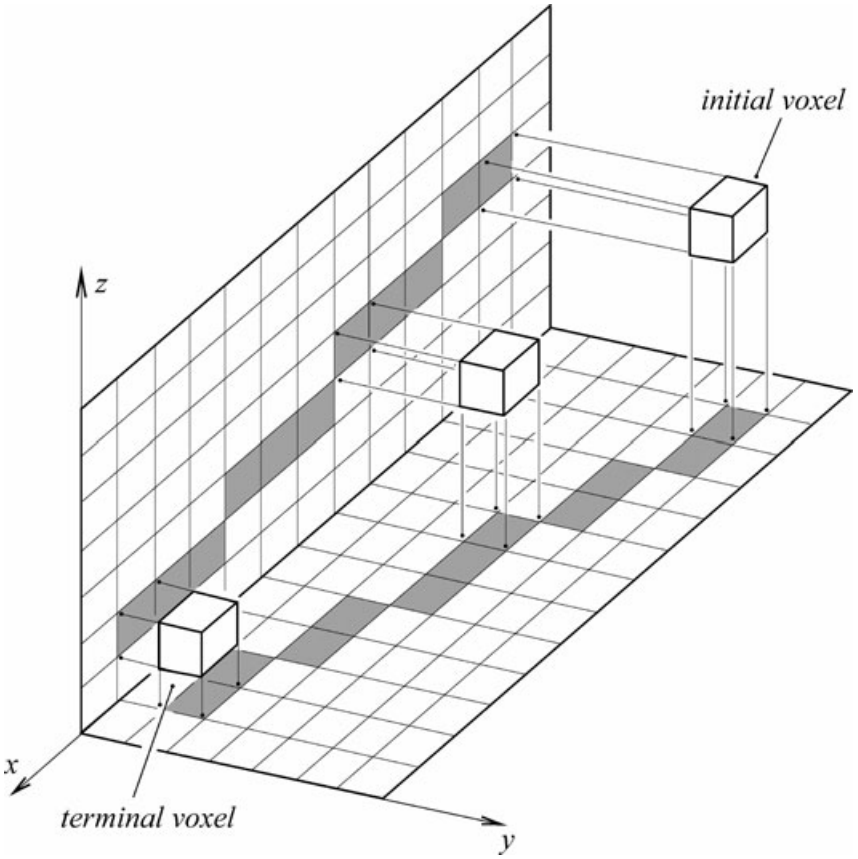

Fig 5. Principle of 3D generalization of Bresenham's algorithm: we use the classical 2D Bresenham's algorithm in planes xy and xz to generate a series of 3D voxels for projection line.

using the coordinates of the input and output voxels, we find out on which axis appears the biggest difference between the original and the terminal coordinates. Let, for example, the axis x be this axis (see Fig. 5). Now let us project the initial and the terminal voxels into the plane xy and let us use Bresenham's algorithm for the first time. It will proceed along the axis x and generate the y-coordinates of pixels approaching the line segment connecting the original and the terminal pixels. Now let us project the initial and the terminal voxels into the plane xz and let us use Bresenham's algorithm for the second time (array of x-coordinates may be generated only once).

The voxelized line is processed in following ways:

First intensity projection algorithm displays the first nonzero intensity along the projection line only.

Maximum intensity projection algorithm (MIP) displays the maximum intensity along the projection line.

Summed intensity projection algorithm (SIP) displays the sum intensity along the projection line.

Average intensity projection algorithm (AIP) displays the arithmetic mean of intensity along the projection line.

Back-to-Front algorithm (BtF) or Front-to-Back algorithm (FtB) displays a value

$$v = I_0 \cdot \prod_{i=1}^{m} t_i + \sum_{i=1}^{m} v_i \prod_{j=i+1}^{m} t_j \,(\text{BtF});$$
$$v = I_0 \cdot \prod_{i=1}^{m} t_i + \sum_{i=1}^{m} v_i \prod_{j=1}^{i} t_j \,(\text{FtB}). \qquad (2)$$

These algorithms are able to simulate a transparency of an object—v_i are values of processed voxels, t_i their transparencies, and I_0 is the intensity of ambient light.

It is recommended to apply some illumination models for improving these outputs. There must be given a norm of surface point for calculating, a so called illumination model of an object to be displayed. But there exists no surface in a scalar field; the norm is therefore replaced by the gradient of this field. It is defined as

$$\mathbf{n}_A \approx \text{grad} G_A = \left(\frac{\partial G_A}{\partial x}; \frac{\partial G_A}{\partial y}; \frac{\partial G_A}{\partial z} \right)$$

for a differentiation able function of three variables (G_A is the value of the scalar field in point A)—see Levoy ('88) or Cohen and Kaufman ('90), for example. In the case of discrete data, this expression must be replaced by a vector of first central differentials

$$\mathbf{n}_A \approx \mathrm{grad} G_A \approx \left(\Delta_x^1 G_A; \Delta_y^1 G_A; \Delta_z^1 G_A\right). \tag{3}$$

However, these methods are not suitable for huge and complicated volume data.

Some improvements were proposed—see Glassner ('84), Kaufman and Shimony ('86), Kaufman ('87), Max ('95) and Nielson ('96), for example.

Value Interpolation and Rendering in Integer Arithmetic

The value interpolation and shading of a constant volume grid is a self-reliant problem.

We have generated the sequence $\{{}_yp_i\}$ according to the formula (1) in the plane xy. For all ${}_yp_i$ is

$$2\Delta x_y s_i = \Delta x - {}_yp_i, \tag{4}$$

where ${}_ys_i$ is the distance between the projection ${}_yA$ of the processed voxel A and the projection ${}_yP$ of point P into the plane xy.Because

$$\frac{{}_yd_A}{{}_ys_i} = \frac{\Delta x}{\sqrt{(\Delta x)^2 + (\Delta y)^2}}$$

where ${}_yd_A$ is the distance between the projection ${}_yA$ of the processed voxel A and the projection ${}_yl$ of the projection line l into the plane xy (see Fig. 6), is

$$4{}_yd_A^2[(\Delta x)^2 + (\Delta y)^2] = (2\Delta x_y s_i)^2 \overset{\text{see(5)}}{=} (\Delta x - {}_yp_i)^2.$$

Because

$$\begin{aligned} 2\Delta x_y r_i &= 2\Delta x - 2\Delta x_y s_i \overset{\text{see(4)}}{=} 2\Delta x - (\Delta x - {}_yp_i) \\ &= \Delta x + {}_yp_i, \end{aligned} \tag{5}$$

is by analogy

$$\frac{{}_yd_B}{{}_yr_i} = \frac{\Delta x}{\sqrt{(\Delta x)^2 + (\Delta y)^2}}$$

$$4{}_yd_B^2[(\Delta x)^2 + (\Delta y)^2] = (2\Delta x_y r_i)^2 \overset{\text{see(4)}}{=} (\Delta x + {}_yp_i)^2.$$

If we generate the sequence $\{{}_zp_i\}$ according to formula (1) in the plane xz, it is

$$4{}_zd_A^2[(\Delta x)^2 + (\Delta y)^2] = (\Delta x - {}_zp_i)^2$$

$$4{}_zd_B^2[(\Delta x)^2 + (\Delta y)^2] = (\Delta x + {}_zp_i)^2.$$

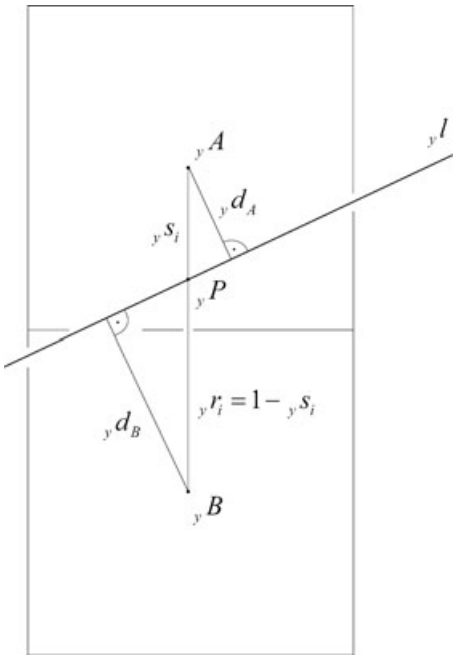

Fig 6. Principle of data value interpolation in integer arithmetic.

In 3D space, there is

$$\begin{aligned} &4[(\Delta x)^2 + (\Delta y)^2] \cdot d_A^2 \\ &\quad = 4[(\Delta x)^2 + (\Delta y)^2] \cdot \left({}_yd_A^2 + {}_zd_A^2\right) \\ &\quad = (\Delta x - {}_yp_i)^2 + (\Delta x - {}_zp_i)^2 \end{aligned} \tag{6}$$

$$\begin{aligned} &4[(\Delta x)^2 + (\Delta y)^2] \cdot d_B^2 \\ &\quad = 4[(\Delta x)^2 + (\Delta y)^2] \cdot ({}_yd_B^2 + {}_zd_B^2) \\ &\quad = (\Delta x + {}_yp_i)^2 + (\Delta x + {}_zp_i)^2 \end{aligned} \tag{7}$$

where d_A; (d_B) is the distance between the voxel A (B) and the projection line l in 3D. The intensity of physical fields is inversely related to the square of its distance from its source. For the value (or density) v_i which is necessary to assign to point$P$ may be therefore

$$v_i = k \cdot \frac{v_A}{d_A^2} + k \cdot \frac{v_B}{d_B^2} \Rightarrow d_A^2 d_B^2 v_i = k \cdot d_B^2 v_A + k \cdot d_A^2 v_B$$

where v_A; v_B are known values (or densities) of voxels A; B and k is any constant. This "strictly physical method" is not applicable—for $d_A \to 0$ or $d_B \to 0$ (it means $P \to A$ or $P \to B$) is $v_i \to \infty$. Therefore, we let

$$\begin{aligned} v_i &= k \cdot d_A^2 \cdot v_B + k \cdot d_B^2 \cdot v_A \\ &= [(\Delta x - {}_yp_i)^2 + (\Delta x - {}_zp_i)^2] \cdot v_B \\ &\quad + [(\Delta x + {}_yp_i)^2 + (\Delta x + {}_zp_i)^2] \cdot v_A. \end{aligned} \tag{8}$$

Values v_i can be calculated during Bresenham line construction for all voxels and we use integer arithmetic only. For $d_A \to 0$ is $v_i \to d_B^2 \cdot v_A = \frac{(\Delta x)^2}{(\Delta x)^2+(\Delta y)^2} \cdot v_A$ and for $d_B \to 0$ is $v_i \to d_A^2 \cdot v_B = \frac{(\Delta x)^2}{(\Delta x)^2+(\Delta y)^2} \cdot v_B$, therefore it is necessary to divide by $\frac{(\Delta x)^2}{(\Delta x)^2+(\Delta y)^2}$, but it is possible to execute it only once for the whole projection line (after the processing of all voxels on the projection line) in MIP, SIP, AIP. Expression (2) for BtF and FtB can be theoretically processed in integer arithmetic too—transparencies t_i can be given as integer per cent for example—but this way leads obviously to integer overflow and we must use the real arithmetic as the last step in application of these algorithms. Nevertheless, interpolation of each v_i in integer arithmetic means an important acceleration of BtF and FtB.

The "normal vector" $\mathbf{n}_A$ for the processed voxel A (see formula (3) which is necessary for calculation of illumination model can be calculated in integer arithmetic too. The projection line, unfortunately, does not go through processed voxels and this vector must be calculated for a real point in this ray. In spite of it, normal $\mathbf{n}_i$ for real coordinates of the point P (see Fig. 4) can be calculated using integer arithmetic.

Let $\mathbf{n}_A; \mathbf{n}_B$ be vectors given by formula (3) for voxels $A; B$. These voxels have integer coordinates; vectors $\mathbf{n}_A; \mathbf{n}_B$ are therefore countable in integer arithmetic therefore. We can solve this problem by analogy to previous techniques and we get

$$\begin{aligned}\mathbf{n}_i &= d_A^2 \cdot \mathbf{n}_B + d_B^2 \cdot \mathbf{n}_A \\ &= [(\Delta x - {}_y p_i)^2 + (\Delta x - {}_z p_i)^2] \cdot \mathbf{n}_B \\ &\quad + [(\Delta x + {}_y p_i)^2 + (\Delta x + {}_z p_i)^2] \cdot \mathbf{n}_A. \end{aligned} \tag{9}$$

These vectors must be normalized for using any illumination model, but interpolation of each $\mathbf{n}_i$ in integer arithmetic results in (as in the case of v_i) important shading acceleration.

Fast 3D Filters

In Image processing, so called linear filters are defined, which replace the value of each pixel with a value of convolution of an image with a convolution matrix. If we denote the image O and the convolution matrix $\mathbf{C}$, then the value of convolution is given by the expression

$$\begin{aligned}\mathbf{C}(A_{ij}) \otimes O(A_{ij}) &= \sum_{m=-\varepsilon}^{\varepsilon} \sum_{n=-\varepsilon}^{\varepsilon} \mathbf{C}(A_{mn}) O(A_{i-m;\, j-n}) \\ &= \sum_{m=-\varepsilon}^{\varepsilon} \sum_{n=-\varepsilon}^{\varepsilon} \mathbf{C}(m;\, n) O(i-m;\, j-n).\end{aligned}$$

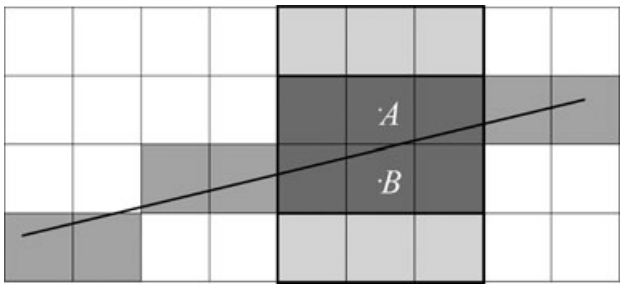

Fig 7. Using of a classic filter (2D illustration). Voxel surroundings overlap, most of voxels are processed several times therefore.

Properties of linear image filters depend on the convolution matrix. We can work with low-pass filters or high-pass filters for example. It is possible to generalize all these filters for an "$n - D$ image," for a 3D data grid in particular

$$\begin{aligned}&\mathbf{C}(A_{ijk}) \otimes G(A_{ijk}) \\ &\quad = \sum_{m=-\varepsilon}^{\varepsilon} \sum_{n=-\varepsilon}^{\varepsilon} \sum_{p=-\varepsilon}^{\varepsilon} \mathbf{C}(A_{mnp}) G(A_{i-m;\, j-n;\, k-p}) \\ &\quad = \sum_{m=-\varepsilon}^{\varepsilon} \sum_{n=-\varepsilon}^{\varepsilon} \sum_{p=-\varepsilon}^{\varepsilon} \mathbf{C}(m;\, n;\, p) G(i-m;\, j-n;\, k-p).\end{aligned} \tag{10}$$

In a 3D data grid, the additional noise is disturbing especially for normal vector calculation. Therefore, it is necessary to apply a 3D low-pass filter. We can do it in several ways. It is possible to use a constant convolution matrix (we replace the value of each voxel by the arithmetic mean of neighboring voxels). The whole filtering is feasible in integer arithmetic in this case—we calculate sums only, dividing by number of surrounding voxels is possible to do at the end for the whole projection line. This approach has several disadvantages—most of voxels are processed several times—voxel surroundings overlap (this fact is illustrated in Fig. 7), we cannot take into consideration the line distance of each voxel.

The principle of a more sophisticated method is shown in Figure 8 (we illustrate it in the plane xy).

We processed a column of the height of $2n$ for each voxel. Voxels $A; B$ add the value ${}^{AB}v_i$ to the value or density of the processed point according to formula (8) and to the normal vector according to formula (9). For voxels $C; D$ (the second pair of voxels) is ${}_y^{CD}s_i = {}_y^{AB}s_i + 1$, therefore

$$\begin{aligned}2\Delta x\, {}_y^{CD}s_i &= 2\Delta x\, {}_y^{AB}s_i + 2\Delta x \overset{\text{see(4)}}{=} (\Delta x - {}_y p_i) + 2\Delta x \\ &= 3\Delta x - {}_y p_i\end{aligned} \tag{11}$$

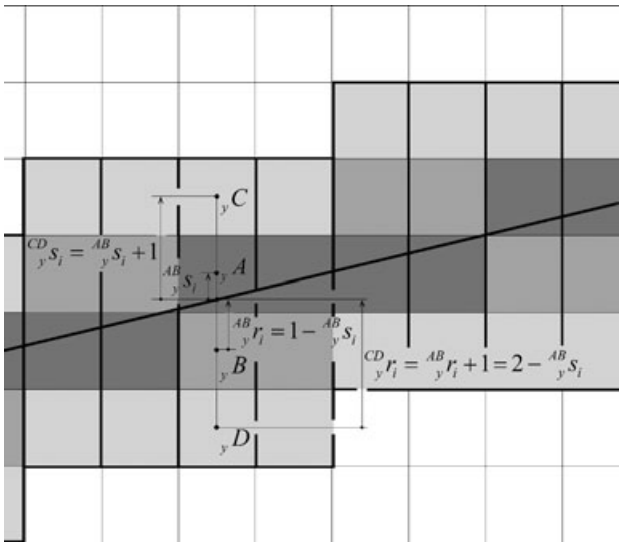

Fig 8. Fast low-pass filter (2D illustration). For given projection line, each voxel from a column is processed once only.

and ${}^{CD}_{y}r_i = 2 - {}^{AB}_{y}s_i$, therefore

$$2\Delta x^{CD}_{y}r_i = 4\Delta x - 2\Delta x^{AB}_{y}s_i \overset{\text{see(4)}}{=} 4\Delta x - (\Delta x - {}_yp_i) = 3\Delta x + {}_yp_i. \tag{12}$$

Because

$$\frac{{}_yd_C}{{}^{CD}_{y}s_i} = \frac{\Delta x}{\sqrt{(\Delta x)^2 + (\Delta y)^2}}$$

is

$$4{}_yd_C^2[(\Delta x)^2 + (\Delta y)^2] = \left(2\Delta x^{CD}_{y}s_i\right)^2 \overset{\text{see(11)}}{=} (3\Delta x - {}_yp_i)^2. \tag{13}$$

Because

$$\frac{{}_yd_D}{{}^{CD}_{y}r_i} = \frac{\Delta x}{\sqrt{(\Delta x)^2 + (\Delta y)^2}}$$

is

$$4{}_yd_D^2[(\Delta x)^2 + (\Delta y)^2] = \left(2\Delta x^{CD}_{y}r_i\right)^2 \overset{\text{see(12)}}{=} \left(3\Delta x + {}_yp_i\right)^2 \tag{14}$$

(in the plane yz by analogy). In 3D space, there is therefore

$$4[(\Delta x)^2 + (\Delta y)^2]\cdot d_C^2 = 4[(\Delta x)^2 + (\Delta y)^2]\cdot({}_yd_C^2 + {}_zd_C^2) \overset{\text{see(13)}}{=} (3\Delta x - {}_yp_i)^2 + (3\Delta x - {}_zp_i)^2$$

$$4[(\Delta x)^2 + (\Delta y)^2]\cdot d_D^2 = 4[(\Delta x)^2 + (\Delta y)^2]\cdot({}_yd_D^2 + {}_zd_D^2) \overset{\text{see(14)}}{=} (3\Delta x + {}_yp_i)^2 + (3\Delta x + {}_zp_i)^2$$

and

$${}^{CD}v_i = d_C^2\cdot v_D + d_D^2\cdot v_C = [(3\Delta x - {}_yp_i)^2 + (3\Delta x - {}_zp_i)^2]\cdot v_D + [(3\Delta x + {}_yp_i)^2 + (3\Delta x + {}_zp_i)^2]\cdot v_C$$

$${}^{CD}\mathbf{n}_i = d_C^2\cdot \mathbf{n}_D + d_D^2\cdot \mathbf{n}_C = [(3\Delta x - {}_yp_i)^2 + (3\Delta x - {}_zp_i)^2]\cdot \mathbf{n}_D + [(3\Delta x + {}_yp_i)^2 + (3\Delta x + {}_zp_i)^2]\cdot \mathbf{n}_C$$

For a kth pair A_k; B_k of these voxels, it is generally

$$4[(\Delta x)^2 + (\Delta y)^2]\cdot d_{A_k}^2 = [(2k-1)\cdot\Delta x - {}_yp_i]^2 + [(2k-1)\cdot\Delta x - {}_zp_i]^2$$

$$4[(\Delta x)^2 + (\Delta y)^2]\cdot d_{B_k}^2 = [(2k-1)\cdot\Delta x + {}_yp_i]^2 + [(2k-1)\cdot\Delta x + {}_zp_i]^2.$$

The kth pair A_k; B_k adds to the value or density of a processed point by analogy to (8)

$${}^{k}v_i = d_{A_k}^2\cdot v_{B_k} + d_{B_k}^2\cdot v_{A_k} = \{[(2k-1)\Delta x - {}_yp_i]^2 + [(2k-1)\Delta x - {}_zp_i]^2\}\cdot v_{B_k} + \{[(2k-1)\Delta x + {}_yp_i]^2 + [(2k-1)\Delta x + {}_zp_i]^2\}\cdot v_{A_k}. \tag{15}$$

The total density value v_i is obtained as a weighted sum of ${}^{k}v_i$. Partial densities ${}^{k}v_i$ calculated according to 14 increase proportionally to the square of distance $|A_kB_k| = 2k-1$, if $v_{A_k} = v_{A_1}$ and $v_{B_k} = v_{B_1}$, it is ${}^{k}v_i = (2k-1)^2\cdot {}^{1}v_i$ instead of ${}^{k}v_i = \frac{{}^{1}v_i}{(2k-1)^2}$. Therefore, we

Fig 9. Image with high contrast and sharpness (on the left) and the same image with low contrast and sharpness (on the right).

must construct the weighted sum as

$$\begin{aligned} v_i &= [2n-1]^4 \cdot {}^1v_i + [2(n-1)-1]^4 \cdot {}^2v_i + \ldots \\ &\quad + [2(n-k)-1]^4 \cdot {}^kv_i + \ldots + {}^nv_i \\ &= \sum_{k=1}^{n} [2(n-k+1)-1]^4 \cdot {}^kv_i. \end{aligned} \tag{16}$$

According to (15), formula (16) is countable in integer arithmetic. Values v_i must be normalized by expression

$$\bar{v}_i = \frac{(\Delta x)^2 + (\Delta y)^2}{(\Delta x)^2} \cdot \frac{v_i}{\sum\limits_{k=1}^{n} [2(n-k+1)-1]^4}$$

for BtF and FtB. It is possible to execute it only once for a whole projection line in MIP, SIP, AIP.

Normal vectors are calculated by an analogous technique:

$$\begin{aligned} {}^k\mathbf{n}_i &= d_{A_k}^2 \cdot \mathbf{n}_{B_k} + d_{B_k}^2 \cdot \mathbf{n}_{A_k} = \{[(2k-1)\Delta x - {}_yp_i]^2 \\ &\quad + [(2k-1)\Delta x - {}_zp_i]^2\} \cdot \mathbf{n}_{B_k} \\ &\quad + \{[(2k-1)\Delta x + {}_yp_i]^2 \\ &\quad + [(2k-1)\Delta x + {}_zp_i]^2\} \cdot \mathbf{n}_{A_k} \end{aligned} \tag{17}$$

$$\begin{aligned} \mathbf{n}_i &= [2n-1]^4 \cdot {}^1\mathbf{n}_i + [2(n-1)-1]^4 \cdot {}^2\mathbf{n}_i \ldots \\ &\quad + [2(n-k)-1]^4 \cdot {}^k\mathbf{n}_i + \ldots + {}^n\mathbf{n}_i \\ &= \sum_{k=1}^{n} [2(n-k+1)-1]^4 \cdot {}^k\mathbf{n}_i. \end{aligned} \tag{18}$$

These vectors must be normalized for computation of a lighting model.

Expressions (16) and (18) yield significant acceleration of rendering methods and provide better results than classical low-pass filters.

Results and Applications

We have evaluated our outputs with respect to the quality of cells displaying and algorithm efficiency.

The quality of cell structure display is preeminently given by the image contrast and sharpness. These characteristics are given by high frequencies in the image amplitude spectrum obtained by the Fourier transform of the analyzed image. The amplitude spectrum of a discrete image is a matrix with the same resolution as the original image. Low frequencies are situated in the center; increase of the distance from the image center distance means increase of image frequencies. Image boundary itself represents high frequencies for the Fourier transform in most cases, its multiplication by so called Hanning function is used for its reduction.

In the left part of Figure 9, we can see a sharp and contrasty image (its resolution is 1,024 × 1,024 pixels). In the right part of Figure 9 is shown the same but highly blurred image with very small contrast. These images were multiplied by the Hanning function and transformed by the Fourier transform. Final amplitude spectra are constructed in Figure 10 (left part for the sharp image, right part for the blurred one). The sum through a felicitous annulus with the center in the center of the amplitude spectrum is a suitable criterion for image contrast and sharpness diagnostics. We use the characteristic

$$S = \frac{1}{m(A)} \sum_{[i,j] \in A} v_{ij} \tag{19}$$

where v_{ij} is the value of the pixel $[i, j]$ and $m(A)$ is the number of pixels $[i, j]$ in the annulus A (it is drawn by dark gray in Fig. 10). Circle radii are $r = 64$ pix

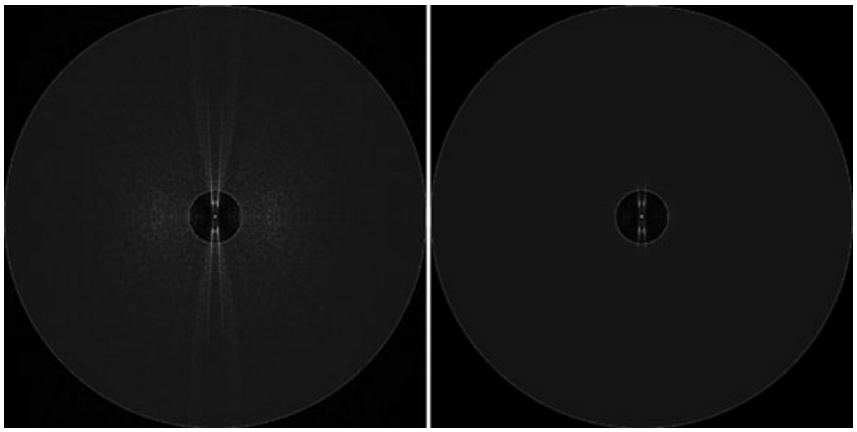

Fig 10. Amplitude Fourier spectra of images from Figure 9. Spectrum of high contrast and sharpness image (on the left) and low contrast and sharpness image (on the right).

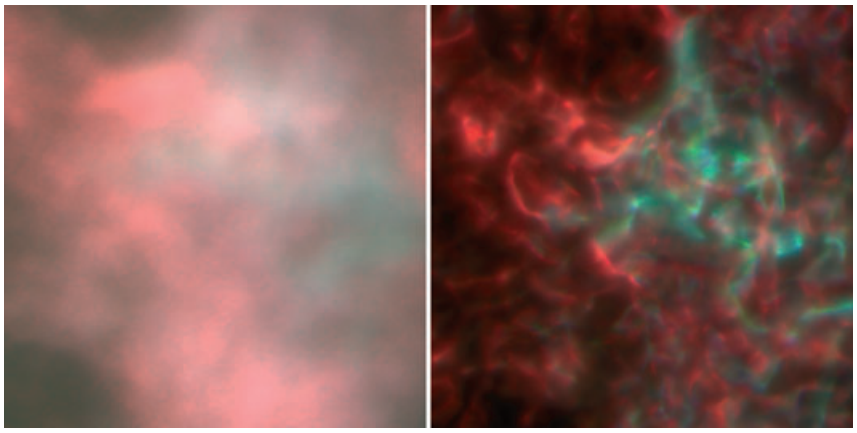

Fig 11. Detail of *Tobacco* cell 3D reconstruction (output resolution 1,024 ×1,024 pixels): AIP method on the left, BtF method calculated according to the Chapters 2.3 and 2.4 (original input data—see Fig. 1).

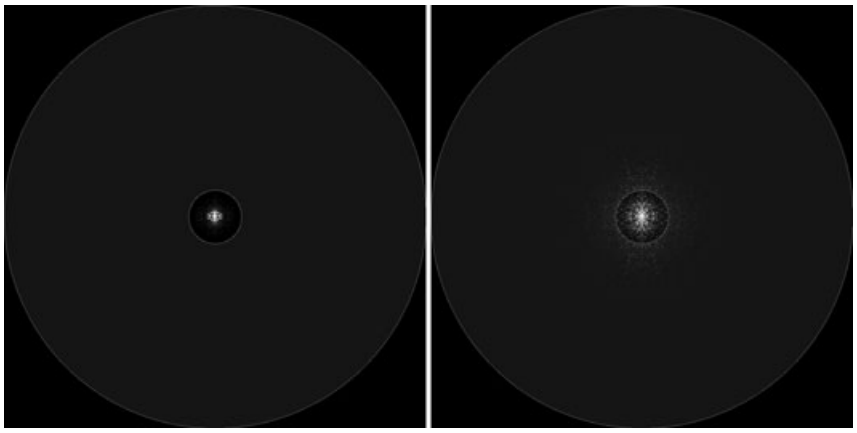

Fig 12. Amplitude Fourier spectra of images from Figure 11. BtF method calculated according to sections Value Interpolation and Rendering In Integer Arithmetic and Fast 3D Filters (spectrum on the right) provide higher contrast and sharpness than AIP (spectrum on the left).

and $R = 1,024$ pix, respectively. The Characteristic (19) is $S = 5.27297$ (left spectrum) and $S = 0.00613$ (right spectrum), respectively.

We can see a detail of *Tobacco* cell constructed on a common PC in Figure 11 (original input data—see Fig. 1, output resolution is 1,024 × 1,024 pixels). Left part of the figure was constructed by the classic AIP method. In the right part, the Btf method according to the formula (2) was used, $t_i = 0,6$ for each i. Values v_i along the projection lines were

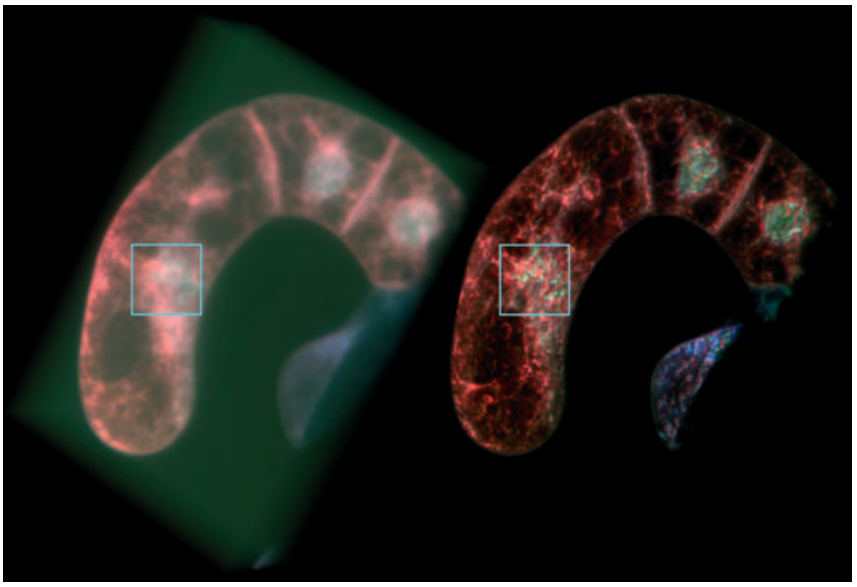

Fig 13. 3D reconstruction of complete *Tobacco* cell: recent AIP method on the left, BtF method calculated according to sections Value Interpolation and Rendering In Integer Arithmetic and Fast 3D Filters on the right (output resolution 2,400×1,800 pixels).

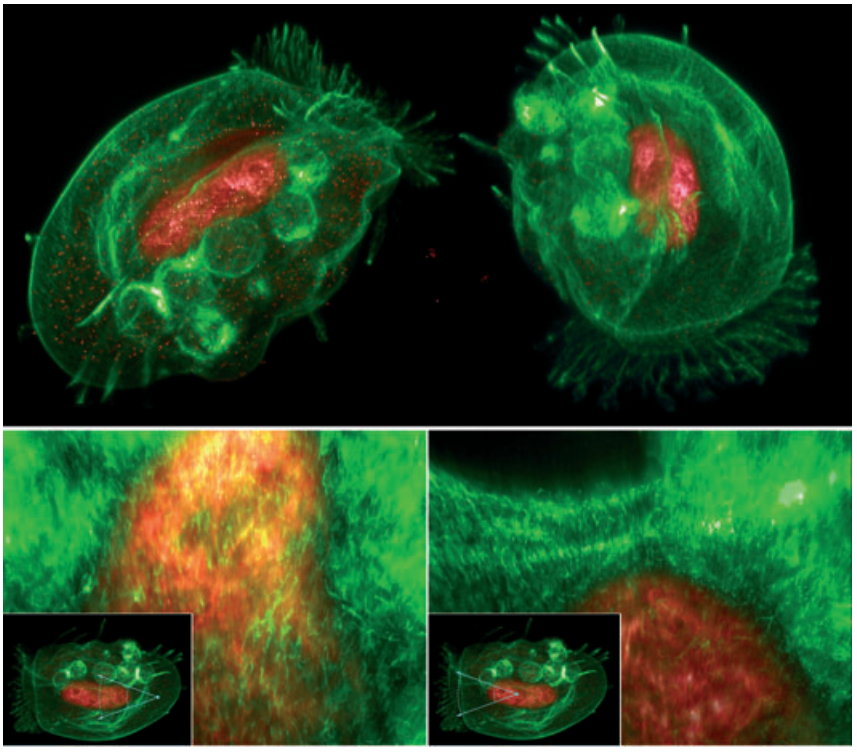

Fig 14. 3D reconstruction of *Euplotes patela* cell. Orthogonal projection (on top) and sights of virtual inner camera (down). Output resolution is 1,600×1,200 pixels).

processed by formulae (8) and (9). The noise of the scalar data was decreased by the 3D low-pass filters (15) and (16); vectors for rendering were calculated by expressions (17) and (18). Phong illumination model was used—see Phong ('75) or Wojdel *et al.* ('98), for example.

Amplitude spectra of these outputs are constructed in Figure 12 (left spectrum for classical AIP, right one for our method). The Characteristic (19) is $S = 0.00026$ (left spectrum) and $S = 0.55437$ (right spectrum), respectively. We can see a 3D reconstruction of the complete *Tobacco* cell in Figure 13. The AIP method is used on the left, BtF method calculated according to the Chapters 2.3 and 2.4 on the right. The part of the cell which is drawn in Figure 11 is bordered by a blue square here.

The run time for 100 optical cuts and resolution of 1,024 × 768 on a PC with 1 GHz CPU and 1 GB RAM is 20 s for $n = 1$, 2 min for $n = 2$. These methods enable us to reconstruct inner cell structures too. In Figure 14, we can see two views of a 3D reconstruction of *E. patela* cell and two virtual camera sights on its inner structures (original input data—see Fig. 2, output resolution is 1,600 × 1,200 pixels).

As you can see, 3D processing contributes to the quality of cells displaying significantly. On the other hand, let us note that an effective software implementation of these algorithms represents another difficult challenge because of their very high computational costs.

References

Bresenham J. 1965. Algorithm for computer control of a digital plotter. IBM Syst J 4:25–30.

Chikit A, Woo T. 2011. Three dimensional extension of Bresenham's Algorithm with Voronoi diagram. Comput Aided Des 43:417–426.

Cohen D, Kaufman A. 1990. Scan conversion algorithms for linear and quadratic objects. In: Kaufman A, editor. Volume visualization. Los Alamitos, CA: IEEE Computer Society Press. p 280–301.

Cohen D, Kaufman A. 1997. 3D line voxelization and connectivity control. IEEE Comput Graph Appl 17:80–87.

Ficker T, Martišek D, Chmelík R, Lovicar L, Němec P. 2007. Fracture surfaces of porous materials. Europhys Lett 80:1600–1604.

Ficker T, Martišek D, Jennings MH. 2010. Roughness of fracture surfaces and compressive strength of hydrated cement pastes. Cement Concrete Res 9(6):1440–1445.

Ficker T, Len A, Martišek D. 2011. A remark on nano-particle stability of cement C-S-H gel. Cent Eur J Phys 9:553–557.

Foley JD, Van Dam A, Feiner S, Hughes JF. 1990. Computer graphics: Principles and practice, 2nd edition. Reading, MA: Addison-Welsey.

Glassner AS. 1984. Space subdivision for fast ray tracing. IEEE Comput Graph Appl 4:15–22.

Kaufman A. 1987. An algorithm for 3D scan-conversion of polygons. Proc. EUROGRAPHICS'87, Amsterdam, the Netherlands. p 197–208.

Kaufman A, Shimony E. 1986. 3D scan-conversion algorithms for voxel-based graphics. Proc. ACM Workshop on Interactive 3D Graphics, Chapel Hill, NC. p 45–75.

Levoy M. 1988. Display of surfaces from volume data. IEEE Comput Graph Appl 8:29–37.

Martišek D. 2002. The 2D and 3D processing of images provided by conventional microscopes. Scanning 24:284–296.

Martišek D. 2002. Methods of detection of equipotential surfaces in cell structures. Proceedings of 4th Conference on Cell Biology, České Budějovice. p 47–54.

Martišek D, Martišek K, Procházková J. 2007. New methods for space reconstruction of inside cell structures. J Appl Biomed 5:151–156.

Martišek K. 2007. Numerical methods of multispectral confocal microscopy. Diploma Thesis, Brno University of Technology, Brno, Czech Republic. p 1–65.

Max N. 1995. Opical models for direct volume rendering. IEEE Trans Vis Comput Graph 1:99–108.

Mokrzycki W. 1988. Algorithms of discretization of algebraic spatial curves on homogeneous cubical grids. Comput Graph 12:477–487.

Nielson GM. 1996. The volume rendering equations. Scientific Data Visualization, Eurographics'93 Tutorial.

Phong BT. 1975. Illumination for computer generated images. Commun ACM 18:311–317.

Wojdel A, Petruszka M, Rothkrantz LJM. 1998. Simplifying settings of the parameters in the Phong Illumination Model. ASCI 98 and Fourth International Conference of the Advanced School for Computing and Imaging, Delft, Netherlands.

55 (2010) APPLICATIONS OF MATHEMATICS No. 5, 419–430

RELATION BETWEEN ALGEBRAIC AND GEOMETRIC VIEW ON NURBS TENSOR PRODUCT SURFACES*

DALIBOR MARTIŠEK, JANA PROCHÁZKOVÁ, Brno

(Received October 7, 2008)

Abstract. NURBS (Non-Uniform Rational B-Splines) belong to special approximation curves and surfaces which are described by control points with weights and B-spline basis functions. They are often used in modern areas of computer graphics as free-form modelling, modelling of processes. In literature, NURBS surfaces are often called tensor product surfaces. In this article we try to explain the relationship between the classic algebraic point of view and the practical geometrical application on NURBS.

Keywords: tensor product surface, bilinear form, B-spline, NURBS

MSC 2010: 53A05

1. INTRODUCTION

NURBS have become a standard type of mathematical approximation of surfaces in modern computer graphics. The general NURBS surface is described by a net of control points with weights and by two knot vectors. Theory of NURBS is summarized in [9], for example. NURBS objects are often used for free-form modelling because of their good modification possibilities (e.g. technic FFD—see [12]). The NURBS are used in different branches, for example robotics [5], film industry [13], reverse engineering [10], GIS [14], physical computing [11], etc.

The basic B-spline theory was proposed by Carl de Boor in [1], where the tensor product is schematically described. Tensor calculus is described in [2] and [6]. Non-tensor product NURBS surfaces using the smoothing cofactor-conformality method are constructed in [7].

* This work was supported by the project of MSMT of the Czech Republic No. 1M06047 Centre for Quality and Reliability of Production.

In this paper, we try to explain the algebraic point of view on tensor product surfaces and to establish the connection between this theory and the geometrical and practical use of NURBS.

Section 2 briefly outlines the basic tensor theory. In Section 3 the algebraic approach to B-spline functions and curves is discussed. Section 4 discusses the projective extension of NURBS curves and defines the abstract curve as a set of curves which are invariant with each other.

In Section 5 we deal with the NURBS surfaces. Analogously to Section 4, we introduce an abstract surface based on the characteristic form. In the last Section 6, we discuss some results and practical examples of our theory.

2. Tensor calculus

Let U, V be vector spaces over a field $\mathbb{T}$. A bilinear form ω on $U \times V$ is a function $\omega\colon\ U \times V \to T$ which satisfies the well-known axioms. The vector space of all bilinear forms between spaces U and V is called the tensor product. These mappings can be written as

$$\omega(\mathbf{u}, \mathbf{v}) = \sum_{i=0}^{m} \sum_{j=0}^{n} u_i v_j \omega(\mathbf{e}_i, \mathbf{f}_j) = \sum_{i=0}^{m} \sum_{j=0}^{n} u_i v_j a_{ij}, \quad a_{ij} = (e_i, f_j), \tag{2.1}$$

or in the matrix form

$$\omega(\mathbf{u}, \mathbf{v}) = (u_0, u_1, \ldots, u_m) \begin{pmatrix} a_{00} & a_{01} & \ldots & a_{0n} \\ a_{10} & a_{11} & \ldots & a_{1n} \\ \vdots & \vdots & \ddots & \vdots \\ a_{m0} & a_{m1} & \ldots & a_{mn} \end{pmatrix} \begin{pmatrix} v_0 \\ v_1 \\ \vdots \\ v_n, \end{pmatrix}, \tag{2.2}$$

where u_i, $i = 0, \ldots, m$, v_j, $j = 0, \ldots, n$ are the coordinates of the vectors $\mathbf{u} \in U$, $\mathbf{v} \in V$ with bases $\{\mathbf{e}_0, \mathbf{e}_1, \ldots, \mathbf{e}_m\}$, $\{\mathbf{f}_0, \mathbf{f}_1, \ldots, \mathbf{f}_n\}$.

A surface is described by a function of two parameters as a mapping of a plane area to Euclidean 3-dimensional space. Formally

$$S(s,t) = (x(s,t), y(s,t), z(s,t)) = \sum_{i=0}^{m} \sum_{j=0}^{n} f_i(u) g_j(v) b_{ij} \tag{2.3}$$

where $b_{ij} = (x_{ij}, y_{ij}, z_{ij})$, $0 \leqslant s, t \leqslant 1$, $m = 2$, $n = 2$.

Eq. (2.1) is formally similar to Eq. (2.3). Therefore, NURBS surface defined by Eq. (2.3) is often called as the tensor product surface (see [9]).

Eq. (2.3) defines a mapping of the set $D = \langle s1, s2\rangle \times \langle t1, t2\rangle$ (the set of ordered pairs $[s, t]$—the so called parameters area) to the Euclidean point space E_3. Therefore, the point $S = [x, y, z]$ of the surface $\mathcal{S}$ is a function of two real variables s, t.

3. B-SPLINE CURVES—ALGEBRAIC POINT OF VIEW

Definition 3.1. Let $\boldsymbol{t} = (t_0, t_1, \dots t_n)$ be a non-decreasing sequence of positive real numbers. The sequence t is called a knot vector. The B-spline function of degree p is defined as

$$N_i^0(t) = \begin{cases} 1, & t \in \langle t_i, t_{i+1}), \\ 0, & \text{otherwise}, \end{cases}$$

$$N_i^p(t) = \frac{t - t_i}{t_{i+p} - t_i} N_i^{p-1}(t) + \frac{t_{i+p+1} - t}{t_{i+p+1} - t_i} N_{i+1}^{p-1}(t), \tag{3.1}$$

where $p > 0$, $0 \leqslant i \leqslant n - p - 1$, $i \leqslant p \leqslant n - 1$, $\frac{0}{0} = 0$.

Example 3.1. The knot vector is $\mathbf{t} = (0, 0, 1, 1)$, the degree $p = 0, 1$, the basis functions are

$$N_0^0(t) = 0, \quad N_1^0(t) = 1, \quad N_2^0(t) = 0,$$
$$N_0^1(t) = 1 - t, \quad N_1^1(t) = t, \quad t \in \langle 0, 1).$$

Example 3.2. The knot vector is $\mathbf{t} = (0, 0, 0, 1, 1, 1)$, the degree $p = 0, 1, 2$, the basis functions are

$$N_i^0(t) = 0 \quad \text{for } i = 0, 1, 3, 4, \quad N_2^0(t) = 1,$$
$$N_0^1(t) = N_3^1(t) = 0, \quad N_1^1(t) = 1 - t, \quad N_2^1(t) = t,$$
$$N_0^2(t) = (1 - t)^2, \quad N_1^2(t) = 2t(1 - t), \quad N_2^2(t) = t^2, \quad t \in \langle 0, 1).$$

We can see that the polynomials of degree two correspond to the Bezier coefficients, because the Bezier curve is a subset of NURBS curves for a special knot vector (see e.g. [4]).

An arbitrary B-spline curve can be defined as

Definition 3.2. Let $\mathbf{t} = (t_0, t_1, \dots, t_n)$ be a knot vector, let $p \geqslant 1$ be the degree and $\mathbf{P}_i \in E^d$, $i = 0, 1, \dots, m$, the control points. The B-spline curve is defined by

$$C(t) = \sum_{i=0}^{m} \mathbf{P}_i N_i^p(t), \tag{3.2}$$

where N_i^p are the B-spline functions.

Eq. (3.2) can be written in the vector form as

$$\mathbf{c}(t) = \sum_{i=0}^{m} \mathbf{P}_i N_i^p(t), \tag{3.3}$$

where $\mathbf{c}(t)$ is the varying location vector of the curve points.

4. Explanation of weights of non-uniform B-spline (NURBS)—geometric point of view

NURBS curves are defined similarly to the B-spline. Every point $\mathbf{P}_i \in E^d$ has its real weight ω_i, $i = 0, 1, \ldots, m$. So an expression similar to (3.2) can be written as

$$C(t) = \frac{\sum_{i=0}^{m} \omega_i \mathbf{P}_i N_i^p(t)}{\sum_{i=0}^{m} \omega_i N_i^p(t)} \tag{4.1}$$

and one coordinate can be written as

$$c_k(t) = \frac{\sum_{i=0}^{m} \omega_i p_{ik} N_i^p(t)}{\sum_{i=0}^{m} \omega_i N_i^p(t)}, \quad k = 1, 2, \ldots, d. \tag{4.2}$$

More information about the influence of the weights on the form of the NURBS curve is available in [8].

Coordinates $c_k(t)$ in Eq. (4.2) are not linear combinations of basic functions, therefore they cannot be used for tensor product construction. We will show that these coordinates can be written as linear combinations of B-spline functions.

Let $\mathbf{P}_i = [p_{i1}, p_{i2}, \ldots, p_{id}] \in E^d$ be a d-dimensional point of the Euclidean space E^d. Eq. (3.2) can be written as

$$c_k(t) = \sum_{i=0}^{m} p_{ik} N_i^p(t), \quad k = 1, 2, \ldots, d, \tag{4.3}$$

where $\mathbf{C} = [c_1, c_2, \ldots, c_d] \in E^d$. In the projective extension $\overline{E}^d$ of the space E^d there is a correspondence between points $\mathbf{C}, \mathbf{P}_i \in E^d$ and $\overline{\mathbf{C}}, \overline{\mathbf{P}}_i \in \overline{E}^d$. These points can be written as

$$\overline{\mathbf{P}}_i = (\overline{p}_{i1}, \ldots, \overline{p}_{id}, \overline{p}_{id+1}) = \omega_i(p_{i1}, \ldots, p_{id}, 1) = (\omega_i p_{i1}, \ldots, \omega_i p_{id}, \omega_i), \tag{4.4}$$

$$\overline{\mathbf{C}} = (\overline{c}_1, \overline{c}_2, \ldots, \overline{c}_d, \overline{c}_{d+1}) = \omega(c_1, c_2, \ldots, c_d, 1) = (\omega c_1, \omega c_2, \ldots, \omega c_d, \omega), \tag{4.5}$$

where $\omega_i \neq 0$ ($\omega \neq 0$) generates the point $\overline{\mathbf{P}}_i$ or $\overline{\mathbf{C}}$ using its arithmetic representation $(p_{i1}, \ldots, p_{id}; 1)$ or $(c_1, \ldots, c_d; 1)$ respectively.

In the projective extension $\overline{E}^d$ of the space E^d, Eq. (4.3) can be written as

$$\bar{c}_k(t) = \sum_{i=0}^{m} \bar{p}_{ik} N_i^p(t) = \sum_{i=0}^{m} \omega_i p_{ik} N_i^p(t), \quad k = 1, 2, \ldots, d+1. \tag{4.6}$$

It is evident that the basis functions for the B-spline are the same as for NURBS. The difference between Eq. (4.2) and Eq. (4.6) is in the usage of non-homogeneous and homogeneous coordinates. An arbitrary point $\overline{C}$ is

$$\begin{aligned} \overline{C} &= (\bar{c}_1, \bar{c}_2, \ldots, \bar{c}_d, \bar{c}_{d+1}) \\ &= \left(\sum_{i=0}^{m} \omega_i p_{i1} N_i^p(t), \sum_{i=0}^{m} \omega_i p_{i2} N_i^p(t), \ldots, \sum_{i=0}^{m} \omega_i p_{id} N_i^p(t), \sum_{i=0}^{m} \omega_i N_i^p(t) \right). \end{aligned} \tag{4.7}$$

We have $\bar{c}_{d+1} \neq 0$ for proper points in (4.7). We get the Cartesian coordinates of the corresponding euclidean point by dividing by the last number:

$$\overline{C} = \left(\frac{\bar{c}_1}{\bar{c}_{d+1}}, \frac{\bar{c}_2}{\bar{c}_{d+1}}, \ldots, \frac{\bar{c}_d}{\bar{c}_{d+1}}, 1 \right) \Rightarrow C = \left(\frac{\bar{c}_1}{\bar{c}_{d+1}}, \frac{\bar{c}_2}{\bar{c}_{d+1}}, \ldots, \frac{\bar{c}_d}{\bar{c}_{d+1}} \right). \tag{4.8}$$

Eq. (4.8) corresponds to Eq. (4.1) of the rational expression of the NURBS curve.

Abstract curves

NURBS curves or surfaces are commonly used in various CAD/CAM systems. The work with weights is based on decreasing or increasing the number from the explicit value 1. It causes the different shape of the curve (surface). Weights are obviously interpreted as the weights of the control points. From the geometrical point of view, however, the situation is somewhat different.

Example 4.1. Let us have a NURBS curve with arbitrary three control points P_0, P_1, P_2, a knot vector $(0, 0, 0, 1, 1, 1)$ and a weight vector $(1, \omega_1, 1)$. The value of ω_1 changes the type of the curve:

- $\omega_1 < 1 \rightarrow$ ellipse,
- $\omega_1 = 1 \rightarrow$ parabola,
- $\omega_1 > 1 \rightarrow$ hyperbola.

We see that the position of the control points does not change the type of the curve. So the weights decide about the geometric behavior of the curve.

Definition 4.1. The set of all curves with the same weight vector $(\omega_0, \ldots, \omega_m)$ over the same knot vector is called an abstract NURBS curve. The expression of the last term in Eq. (4.7)

$$\bar{c}_{d+1} = \sum_{i=0}^{m} \omega_i N_i^p \tag{4.9}$$

is called the equation of the abstract curve.

Remark 4.1. Eq. (4.9) is not an equation of a concrete curve. A particular curve is determined by the control points chosen. In this way, a representation of the abstract curve is actually chosen.

Remark 4.2. The concrete curves in the same abstract curve have the same geometrical behavior. It means that one curve can be transformed to another by projective transformations.

For $m = 2$, Eq. (4.9) is the equation of an abstract conic section. It describes the set of all conic sections which are projectively invariant. With a special choice of the control points we get the classical conic sections, i.e. hyperbola, parabola, ellipse. For example, the characteristic equation

$$\bar{c}_{d+1} = N_0^2 + \frac{\sqrt{2}}{2} N_1^2 + N_2^2 \tag{4.10}$$

or the weight vector

$$\left(1, \tfrac{1}{2}\sqrt{2}, 1\right) \tag{4.11}$$

determine the elliptic arc defined by the so-called polar conjugate diameters. If the control points P_0, P_1, P_2 satisfy

$$\overrightarrow{P_0P_1} \perp \overrightarrow{P_1P_2},$$

these diameters are the axes of the ellipse. If, in addition,

$$|P_0P_1| = |P_1P_2| = r,$$

then the arc is a quadrant. The abstract curve defined by the vector (4.11) is illustrated in Fig. 1. Axis affinity as an important example of projective transform is used.

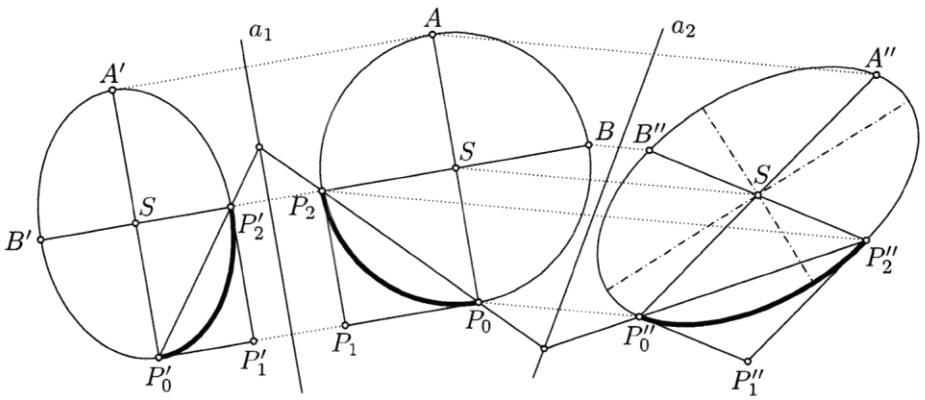

Figure 1. Different representants of abstract NURBs curve $(1, \sqrt{2}/2, 1)$.

Remark 4.3. By means of suitable control points, four representations may be selected in (4.11) to create an ellipse.

Remark 4.4. Substitute the vector $k\boldsymbol{\omega} = (k\omega_0, \ldots, k\omega_m)$, $k \neq 0$ for $\boldsymbol{\omega} = (\omega_0, \ldots, \omega_m)$ in (4.9). Then we get

$$\overline{C} = \Big(k\sum_{i=0}^{m} \omega_i p_{i1} N_i^p(t), k\sum_{i=0}^{m} \omega_i p_{i2} N_i^p(t), \ldots, k\sum_{i=0}^{m} \omega_i p_{id} N_i^p(t), k\sum_{i=0}^{m} \omega_i N_i^p(t) \Big). \tag{4.12}$$

Dividing by the last member we obtain the same homogeneous coordinates as for the vector $\boldsymbol{\omega} = (\omega_0, \ldots, \omega_m)$. It means that the weight vectors $\boldsymbol{\omega}, k\boldsymbol{\omega}$, $k \neq 0$, define the same abstract curve. This fact is used in particular for $k = -1$ in the next chapter.

5. NURBS SURFACE AS THE TENSOR PRODUCT OF NURBS CURVES

NURBS surface is defined on a regular net of control points $\mathbf{P}_{ij} \in E^d$, $i = 0, \ldots, m$; $j = 0, \ldots n$ with weights ω_{ij} and with two knot vectors $\mathbf{u} = (u_0, u_1, \ldots, u_{m+p+1})$ and $\mathbf{v} = (v_0, v_1, \ldots, v_{n+q+1})$.

The equation of the NURBS surface can be written as

$$C(u,v) = \frac{\sum_{i=0}^{m}\sum_{j=0}^{n} \omega_{ij}\mathbf{P}_{ij} N_i^p(u) N_j^q(v)}{\sum_{i=0}^{m}\sum_{j=0}^{n} N_i^p(u) N_j^q(v)}, \tag{5.1}$$

where $(u,v) \in \langle u_0, u_{m+p+1}) \times \langle v_0, v_{n+q+1})$.

The kth coordinate of a point on a NURBS surface is

$$c_k(u,v) = \frac{\sum_{i=0}^{m}\sum_{j=0}^{n} \omega_{ij} p_{ijk} N_i^p(u) N_j^q(v)}{\sum_{i=0}^{m}\sum_{j=0}^{n} N_i^p(u) N_j^q(v)}, \quad k = 0, 1, \ldots, d, \tag{5.2}$$

where p_{ijk} is the kth Cartesian coordinate of $\mathbf{P}_{ij}$.

In the projective extension $\overline{E}_d$ of the space E_d, NURBS surface has equations

$$\overline{c}_k(u,v) = \sum_{i=0}^{m}\sum_{j=0}^{n} \omega_{ij} \overline{p}_{ijk} N_i^p(u) N_j^q(v), \quad k = 0, 1, \ldots, d, \tag{5.3}$$

$$\overline{c}_{d+1}(u,v) = \sum_{i=0}^{m}\sum_{j=0}^{n} \omega_{ij} N_i^p(u) N_j^q(v), \tag{5.4}$$

where p_{ijk} is the kth projective coordinate of the corresponding $\overline{P}_{ij}$.

The matrix notation of Eqs. (5.3) and (5.4) is

$$\overline{c}_k = (N_0^p, N_1^p, \ldots, N_m^p) \begin{pmatrix} \omega_{00}p_{00k} & \omega_{01}p_{01k} & \cdots & \omega_{0n}p_{0nk} \\ \omega_{10}p_{10k} & \omega_{11}p_{11k} & \cdots & \omega_{1n}p_{1nk} \\ \vdots & \vdots & \ddots & \vdots \\ \omega_{m0}p_{m0k} & \omega_{m1}p_{m1k} & \cdots & \omega_{mn}p_{mnk} \end{pmatrix} \begin{pmatrix} N_0^q \\ N_1^q \\ \vdots \\ N_n^q \end{pmatrix} \tag{5.5}$$

and

$$\overline{c}_{d+1} = (N_0^p, N_1^p, \ldots, N_m^p) \begin{pmatrix} \omega_{00} & \omega_{01} & \cdots & \omega_{0n} \\ \omega_{10} & \omega_{11} & \cdots & \omega_{1n} \\ \vdots & \vdots & \ddots & \vdots \\ \omega_{m0} & \omega_{m1} & \cdots & \omega_{mn} \end{pmatrix} \begin{pmatrix} N_0^q \\ N_1^q \\ \vdots \\ N_n^q \end{pmatrix}. \tag{5.6}$$

Definition 5.1. The matrix of type $(m+1) \times (n+1)$ in (5.6) is called the weight matrix. The set of all NURBS surfaces with the same weight matrix is called an abstract NURBS surface. Equation (5.4) or (5.6) is called the equation of the abstract NURBS surface (compare with Def. 4.1).

Remarks 4.2 and 4.1 hold for abstract and concrete NURBS surfaces by analogy.

Assume $\omega_{ij} \neq 0$ for all $i = 0, 1, \ldots, m$, $j = 0, 1, \ldots, n$ and choose $r = 0, \ldots, m$ and $s = 0, \ldots, n$ arbitrary but constant indexes. Let

$$\overline{\omega}_{rs} = \pm\sqrt{|\omega_{rs}|}. \tag{5.7}$$

If $\overline{\omega}_{rs} > 0$, let

$$\overline{\omega}_{is} = \frac{\omega_{is}}{\overline{\omega}_{rs}}; \quad \overline{\omega}_{rj} = \frac{\omega_{rj}}{\overline{\omega}_{rs}}; \quad \overline{\omega}_{ij} = \frac{\omega_{ij}}{\overline{\omega}_{is}\overline{\omega}_{rj}}.$$

If $\overline{\omega}_{rs} < 0$, let

$$\overline{\omega}_{is} = -\frac{\omega_{is}}{\overline{\omega}_{rs}}; \quad \overline{\omega}_{rj} = \frac{\omega_{rj}}{\overline{\omega}_{rs}}; \quad \overline{\omega}_{ij} = \frac{\omega_{ij}}{\overline{\omega}_{is}\overline{\omega}_{rj}}.$$

Equations (5.5) and (5.6) are transformed to equations

$$\begin{aligned}(5.8)\qquad \overline{c}_k = {} & (\overline{\omega}_{0s}N_0^p, \ldots, \overline{\omega}_{rs}N_r^p, \ldots, \overline{\omega}_{ms}N_m^p) \\ & \times \begin{pmatrix} \overline{\omega}_{00}p_{00k} & \cdots & p_{0sk} & \cdots & \overline{\omega}_{0n}p_{0nk} \\ \vdots & \ddots & \vdots & \ddots & \vdots \\ p_{r0k} & \cdots & p_{rsk} & \cdots & p_{rnk} \\ \vdots & \ddots & \vdots & \ddots & \vdots \\ \overline{\omega}_{m0}p_{m0k} & \cdots & p_{msk} & \cdots & \overline{\omega}_{mn}p_{mnk} \end{pmatrix} \begin{pmatrix} \overline{\omega}_{r0}N_0^q \\ \vdots \\ \overline{\omega}_{rs}N_s^q \\ \vdots \\ \overline{\omega}_{rn}N_n^q \end{pmatrix}\end{aligned}$$

and

$$\begin{aligned}(5.9)\qquad \overline{c}_{d+1} = {} & (\overline{\omega}_{0s}N_0^p, \ldots, \overline{\omega}_{rs}N_r^p, \ldots, \overline{\omega}_{ms}N_m^p) \\ & \times \begin{pmatrix} \overline{\omega}_{00} & \cdots & 1 & \cdots & \overline{\omega}_{0n} \\ \vdots & \ddots & \vdots & \ddots & \vdots \\ 1 & \cdots & 1 & \cdots & 1 \\ \vdots & \ddots & \vdots & \ddots & \vdots \\ \overline{\omega}_{m0} & \cdots & 1 & \cdots & \overline{\omega}_{mn} \end{pmatrix} \begin{pmatrix} \overline{\omega}_{r0}N_0^q \\ \vdots \\ \overline{\omega}_{rs}N_s^q \\ \vdots \\ \overline{\omega}_{rn}N_n^q \end{pmatrix}\end{aligned}$$

by these substitutions.

To construct the tensor product surface, it is necessary to work with vector spaces $\mathbf{N}_m^p$ and $\mathbf{N}_n^q$ which are generated respectively by B-spline functions $[N_0^p, N_1^p, \ldots, N_m^p]$ and $[N_0^q, N_1^q, \ldots, N_n^q]$ with knot vectors $\mathbf{u}$ and $\mathbf{v}$.

The elements of these spaces are linear combinations of basis functions in the form (4.9)—sets of projective invariant curves (abstract curves). The coordinates of the abstract NURBS curve as a vector of the vector space N_m^p are the coordinates of its weight vector $(\omega_0, \omega_1, \ldots, \omega_m)$.

The tensor product $\mathbf{N}_m^p \otimes \mathbf{N}_n^q$ of vector spaces $\mathbf{N}_m^p$ and $\mathbf{N}_n^q$ (sets of abstract curves, i.e. projectively invariant NURBS curves) is a set of bilinear forms

$$\begin{aligned}(5.10)\qquad \omega(N_{\mathbf{u}}^p, N_{\mathbf{v}}^q) &= \overline{c}_{d+1} \\ &= (\overline{\omega}_{0s}, \ldots, \overline{\omega}_{rs}, \ldots, \overline{\omega}_{ms}) \begin{pmatrix} \overline{\omega}_{00} & \cdots & 1 & \cdots & \overline{\omega}_{0n} \\ \vdots & \ddots & \vdots & \ddots & \vdots \\ 1 & \cdots & 1 & \cdots & 1 \\ \vdots & \ddots & \vdots & \ddots & \vdots \\ \overline{\omega}_{m0} & \cdots & 1 & \cdots & \overline{\omega}_{mn} \end{pmatrix} \begin{pmatrix} \overline{\omega}_{r0} \\ \vdots \\ \overline{\omega}_{rs} \\ \vdots \\ \overline{\omega}_{rn} \end{pmatrix}.\end{aligned}$$

Definition 5.2. The set of all bilinear forms (5.10) is called the r, s-partial tensor product of abstract curves given by vectors $(\overline{\omega}_{0s}, \ldots, \overline{\omega}_{rs}, \ldots, \overline{\omega}_{ms})$ and $(\overline{\omega}_{r0}, \ldots, \overline{\omega}_{rs}, \ldots, \overline{\omega}_{rn})$. If in the weight matrix (5.10), $\overline{\omega}_{ij} = 1$ holds for all i, j; $i = 0, 1, \ldots, m$, $j = 0, 1, \ldots, n$ then (5.10) is called the total tensor product (or shortly the tensor product) of these curves. The bilinear form (5.10) is the weight form of the abstract surface.

A sign conversion of $\overline{\omega}_{rs}$ according to (5.7) results in the sign conversion of all ω_{is} or ω_{rj} in (5.8), (5.9), (5.10), i.e. in the sign conversion of the weight vectors of both the curves in the tensor product. However, the vectors $\overline{\omega}$ and $-\overline{\omega}$ define the same abstract curves (see Remark 4.4). The transform of the characteristic equation (5.6) to the r, s-partial tensor product (5.10) is unique.

The partial tensor product of abstract curves does not define the abstract surface uniquely. For example, all 0,0-partial products of the same NURBS abstract curves have identical two boundaries, but other rth and sth abstract curves may be different. The total tensor product defines the abstract surface uniquely which follows from the fact that all r-curves (s-curves) are identical.

6. Results and applications

The dimensions of the spaces $\mathbf{N}_m^p$ and $\mathbf{N}_n^q$ are $m+1$ or $n+1$ respectively. It means that they are isomorphic with linear spaces $\mathbb{R}^{m+1}$ and $\mathbb{R}^{n+1}$ respectively but the spaces $\mathbf{N}_m^p$ and $\mathbf{N}_n^q$ are more suitable for practical use.

Example 6.1. The weight form

$$\omega(N_2^2\, N_2^2) = \left(1, \frac{1}{2}, 1\right) \begin{pmatrix} 1 & 1 & 1 \\ 1 & \overline{\omega}_{11} & \overline{\omega}_{12} \\ 1 & \overline{\omega}_{21} & \overline{\omega}_{22} \end{pmatrix} \begin{pmatrix} 1 \\ 2 \\ 1 \end{pmatrix}$$

describes the surface which is created by the 0,0-partial tensor product of the ellipse $\left(1, \frac{1}{2}, 1\right)$ and the hyperbola $(1, 2, 1)$. These two abstract curves represent the adjoining curves of the surface boundary. The next boundary curves are specified by characteristic vectors $\left(1, \frac{1}{2}\overline{\omega}_{12}, \overline{\omega}_{22}\right)$ and $(1, 2\overline{\omega}_{21}, \overline{\omega}_{22})$. Other r-curves, s-curves are curves with characteristic vectors $\left(1, \frac{1}{2}\overline{\omega}_{11}, \overline{\omega}_{21}\right)$ and $(1, 2\overline{\omega}_{11}, \overline{\omega}_{12})$.

Example 6.2. Consider an abstract surface with the weight form

$$\omega(N_2^2\, N_2^2) = \left(1, \frac{1}{2}, 1\right) \begin{pmatrix} 1 & 1 & 1 \\ 1 & 2 & 1 \\ 1 & 1 & 1 \end{pmatrix} \begin{pmatrix} 1 \\ 2 \\ 1 \end{pmatrix}.$$

It is a partial tensor product of 0,0-type (or 0,2; 2,0; 2,2 types too) of the ellipse $\left(1, \frac{1}{2}, 1\right)$ and the hyperbola $(1, 2, 1)$. These curves form the boundary of the surface, the "central" curves are the parabola $(1, 1, 1)$ and the hyperbola $(1, 4, 1)$.

Example 6.3. The characteristic form of the total tensor product of a parabola and a line is

$$\omega(N_1^1\, N_2^2) = (1, 1) \begin{pmatrix} 1 & 1 & 1 \\ 1 & 1 & 1 \end{pmatrix} \begin{pmatrix} 1 \\ 1 \\ 1 \end{pmatrix}.$$

The resulting surface is a parabolic cylinder.

Example 6.4. The characteristic form of the total tensor product of an elliptic arc with a hyperbolic arc is a part of an elliptical hyperboloid

$$\omega(N_2^2\, N_2^2) = \left(1, \frac{\sqrt{2}}{2}, 1\right) \begin{pmatrix} 1 & 1 & 1 \\ 1 & 1 & 1 \\ 1 & 1 & 1 \end{pmatrix} \begin{pmatrix} 1 \\ \sqrt{2} \\ 1 \end{pmatrix}. \tag{6.1}$$

By using suitable control points, four representatives may be selected in (6.1) to create a unipartite elliptical hyperboloid (according to Remark 4.3).

7. Conclusion

In this paper, the relationship between the classical view on tensor product and application of NURBS surfaces was explained. Our idea is based on projective extension of surfaces and introducing the abstract curves and surfaces. These sets of projective invariant curves and surfaces demonstrate their projective properties clearly than the control points. Our approach was illustrated on some examples.

In our future work we are interested in studying abstract objects with singularities and their properties.

References

[1] *C. De Boor*: A Practical Guide to Splines. Springer, Berlin, 1978.

[2] *U. C. De, J. Sengupta, A. A. Shaikh*: Tensor Calculus. Alpha Science International, Oxford, 2005.

[3] *R. Goldman*: The ambient spaces of computer graphics and geometric modeling. IEEE Computer Graphics and Applications, Vol. 20. IEEE Computer Society Press, Los Alamitos, 2000, pp. 76–84.

[4] *W. T. Hewitt, Ying Liang Ma*: Point inversion and projection for NURBS curve: control polygon approach. Proc. Conf. Theory and Practice of Computer Graphics. IEEE, Las Vegas, 2003, pp. 113–120.

[5] *Chang-Soon Hwang, K. Sasaki*: Evaluation of robotic fingers based on kinematic analysis. Proc. Conf. Intelligent Robots and Systems (IROS 2003). IEEE/RSJ, 2003, pp. 3318–3324.
[6] *D. C. Kay*: Schaumm's Outline of Tensor Calculus. McGraw-Hill, New York, 1998.
[7] *Chong-Jun Li, Ren-Hong Wang*: Bivariate cubic spline space and bivariate cubic NURBS surface. Proc. Geometric Modeling and Processing 2004 (GHP 04). IEEE, Beijing, 2004, pp. 115–123.
[8] *L. Piegl*: Modifying the shape of rational B-splines. Part 1: Curves. Computer Aided Design *21* (1989), 509–518.
[9] *L. Piegl, W. Tiller*: NURBS Book. Springer, Berlin, 1995.
[10] *J. Procházková, J. Sedlák*: Direct B-spline interpolation from clouds of points. Engineering Technology, Brno *12* (2007), 24–28.
[11] *H. Qin, D. Terzopoulos*: D-NURBS: A physics-based framework for geometric design. IEEE Transaction of Visualisation and Computer Graphics *2* (1996), 85–96.
[12] *T. Sederberg, S. Parry*: Free-form deformation of solid geometric models. ACM SIGGRAPH Computer Graphics *20* (1986), 151–160.
[13] *Sy-sen Tang, Hong Yan, Alan Wee-Chung Liew*: A NURBS-based vector muscle model for generating human facial expressions. Proc. 4th Conf. Information, Communications and Signal Processing and 4th Pacific Rim Conf. on Multimedia. ICICS-PCM, Singapore, 2003, pp. 15–18.
[14] *J. Zheng, Y. Wang, H. S. Seah*: Adaptive T-spline surface fitting to Z-map models. Proc. 3rd Conf. Computer Graphics and Interactive Techniques in Australasia and South East Asia. ACM, New York, 2005, pp. 405–411.

Authors' address: *D. Martišek, J. Procházková*, Brno University of Technology, Faculty of Mechanical Engineering, Institute of Mathematics, Dept. of Computer Graphics and Geometry, Technická 2, 616 69 Brno, Czech Republic, e-mail: martisek@fme.vutbr.cz, prochazkova.j@fme.vutbr.cz.

Cement and Concrete Research 42 (2012) 827–833

Contents lists available at SciVerse ScienceDirect

Cement and Concrete Research

journal homepage: http://ees.elsevier.com/CEMCON/default.asp

Digital fracture surfaces and their roughness analysis: Applications to cement-based materials

Tomáš Ficker [a,*], Dalibor Martišek [b]

[a] Brno University of Technology, Faculty of Civil Engineering, Department of Physics, Veveří 95, 602 00 Brno, Czech Republic
[b] Brno University of Technology, Faculty of Mechanical Engineering, Department of Mathematics, Technická 2, 616 62 Brno, Czech Republic

ARTICLE INFO

Article history:
Received 26 October 2011
Accepted 13 March 2012

Keywords:
Roughness numbers (B)
Fracture surfaces (B)
Confocal microscopy (B)
Cement-based materials (D)
Fourier functions

ABSTRACT

Roughness numbers employed in morphological analyses characterize height irregularities of solid surfaces, which are also utilized in fractographic studies. In principle, roughness numbers are computed as height differences between the measured height profile and the reference level that has to be implemented into the profile. Positioning reference level is not an unambiguous computational operation and the result depends on the type of optimization procedure as well as the functional pattern used. A wrong position or an inconvenient pattern results in wrong roughness numbers, which devalue morphological analyses. The Fourier series has proved to be a reliable functional pattern capable of optimum positioning within the digitalized height profiles. The whole procedure is illustrated with fracture surfaces of hydrated cement pastes, whose fracture surfaces have been a subject of fractography analyses and morphological studies for several past decades.

1. Introduction

There are no doubts that fractographic studies represent fruitful tools for exploring fracture processes in solid materials [1–7]. Fracture surfaces which are a result of crack propagation bear valuable morphological information on that dynamic process. For example, in brittle materials when the speed of a crack exceeds a specific value, interesting surface morphological changes have been observed in the form of conical objects that decorated fracture surfaces of those materials [1–3].

In fractographic analyses the so-called roughness numbers are commonly used along with other surface parameters to quantify irregularities of fracture surfaces [4,5]. Roughness numbers were initially developed for the classification of surface finishing of sliding metallic surfaces used in some machinery parts but the fracture surfaces of very different materials such as cement-based composites require a special approach to the surface classification and a special application of roughness numbers. There is a large series of roughness numbers based on different definitions but in principle they all characterize surface irregularities, i.e. the height protrusions (peaks) and the depth depressions (valleys) of surfaces. Some of them are well correlated to such important quantities of cement-based materials as porosity, compressive strength or water-to-cement ratio [4–7]. This noteworthy property makes them attractive for further study.

The roughness parameters are computed either from two-dimensional (2D) profiles measured by contact/non-contact profilometers or from three-dimensional (3D) digital surface reliefs determined by a more advanced technique, e.g., laser scanning devices [8], including the laser scanning confocal microscopes [4–7,9,10].

By computing roughness numbers from digital 2D-profiles or 3D-surface reliefs a basic conceptual problem emerges whose solution inevitably influences the numerical values of roughness numbers and requires a special treatment if these numbers are to be properly used. The core of the problem consists in the fact that the values of roughness numbers strongly depend on the position and the analytical type of the so-called reference level that has to be introduced into the digital profile to compute those numbers. In addition, when the surface consists of a superposition of irregularities of various length-scales, the roughness numbers also show different values for different length-scales.

The goal of this paper is to tackle the mentioned obstacles and to find an acceptable way of solving the problems, especially in the case of fracture surfaces. Prior to the discussion of the studied problem in Sections 3 and 4, a short overview of the confocal surface reconstruction is presented in Section 2, while in Section 5 some applications to cement pastes illustrate and complement the topic. In concluding Section 6 the main results are summarized.

2. Confocal sections and digital surface reconstruction

Scanning confocal microscopes are optical microscopes with a very small depth of field which ensures that the confocal images show only those parts of objects that are very near to the focal

* Corresponding author. Tel.: +420 541 147 661.
E-mail address: ficker.t@fce.vutbr.cz (T. Ficker).

0008-8846/$ – see front matter © 2012 Elsevier Ltd. All rights reserved.
doi:10.1016/j.cemconres.2012.03.007

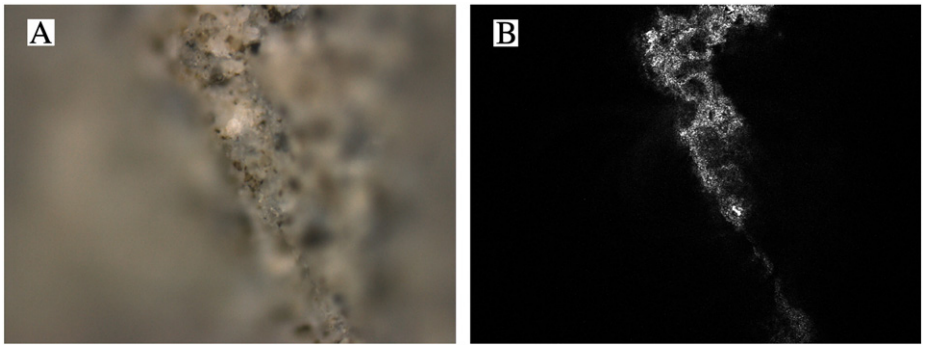

Fig. 1. Microscope images of fracture surfaces of cement paste: A) a non-confocal image with blurred margins; B) a confocal image with sharply visible points and removed blurred parts.

plane while other parts, farther from the focal plane, are invisible on the images. This is illustrated in Fig. 1. Part A of this figure shows non-confocal image with blurred left and right margins which represent points of the fracture surface that are out of the focal plane. In the central region of this image there are sharply imaged points localized in the focal plane. The points from the blurred regions are excluded from the confocal image Fig. 1B leaving only the sharp points from the central region. Fig. 1B is the so-called confocal optical section, which contains only sharply imaged points from the given position of the focal plane. Stepping the focal plane through a range of vertical positions provides a series of confocal optical sections from which the software reconstructs a 3D surface digital map (surface relief) illustrated in Fig. 2. The *z*-resolution, i.e. optical sectioning thickness, depends on a number of factors: the wavelength of the light used, pinhole size, numerical aperture of the objective lens, refractive index of components in the light path and the assembly of the instrument. The easiest and quickest estimation of convenient z-steps is to perform preliminary tests based on a series of probing optical *z*-sections. However, commercial confocal microscopes usually offer an automatic procedure for setting optimum input parameters.

Thanks to very shallow optical fields of confocal microscopes the final 3D surface reliefs contain only sharply imaged points of the fracture surface and their heights within the reliefs are determined from the positions of corresponding optical sections. As soon as the surface is digitally reconstructed, a discrete function f of the two variables x and y is available. It is the relief function $f(x, y)$ that analytically describes the fracture surface (Fig. 2).

3. Critical position of reference level in the digital surface relief

There are standard procedures for determining surface texture from measured profiles developed by machinery engineers and technologists [11,12]. In principle, these procedures comprise three main steps: fitting, filtering and analysis. Fitting raw data of a metallic surface means removing any unwanted geometry from the surface data such as global tilting or nominal curvature. This involves fitting the raw profile with a reference level in the form of a slanted straight line (i.e. first order polynomial) or arc (second order polynomial) or a polynomial of higher order. The fitting procedure results in the so-called primary profile, which is subjected to filtering. Filtering, as a second step in processing primary profiles, is usually based on passing a Gaussian, weighted average through the primary data to obtain the so-called waviness profile. The waviness profile is smoother than the primary profile. The stage of smoothing depends on the 'cutoff wavelength' used as a parameter within the Gaussian filter. The cutoff wavelength determines a border between the waviness and roughness profiles. The roughness profile comprises the slightest surface irregularities (peaks and valleys). It represents the finest scale of profile residues. Once all the profiles are separated, i.e. the primary, waviness and roughness profiles, the third step of the morphology

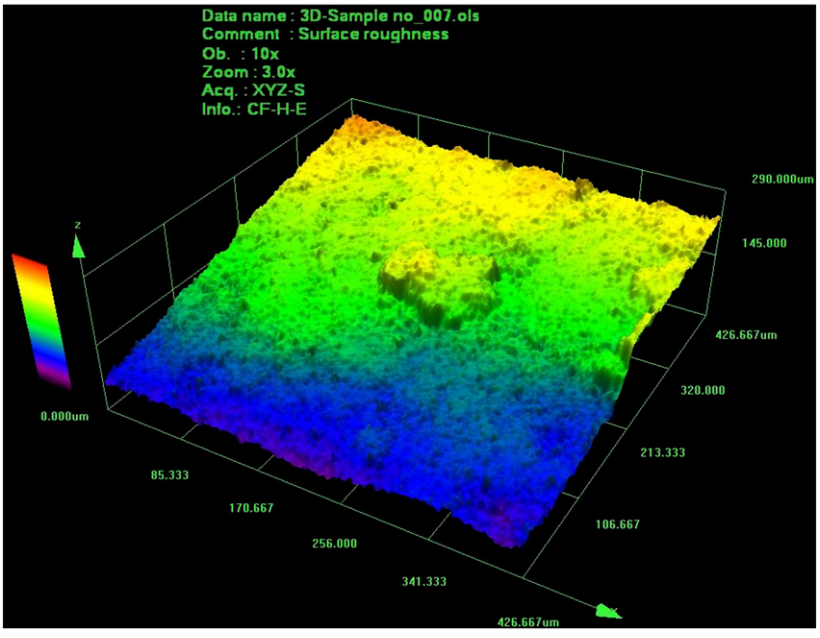

Fig. 2. Confocal reconstruction of fracture surface — digitally created 3D-profile.

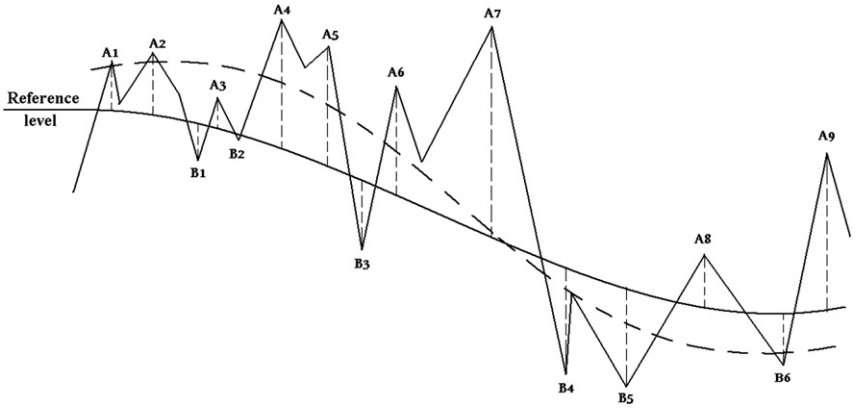

Fig. 3. A scheme of surface profile with marked central level.

analysis may start. The analysis of the irregularities within the roughness profile results in the so-called *R*-values, i.e. roughness numbers. Hundreds of different definitions of roughness number have been proposed, some of which are described in ISO standard 251787 [11]. The frequently used roughness parameters are the arithmetic average R_a and the root mean square (rms) R_q. It should be mentioned that the value of cutoff wavelength implemented within the Gaussian filter has a huge impact on the values of all the roughness numbers. Choosing a shorter cutoff wavelength will result in smaller roughness numbers. To prevent an arbitrary choice of the cutoff value and to encourage a consistent approach to this item, ISO standard 4288-1996 [12] presents a table of standard cutoff values along with selection recommendation.

The evaluation of surface irregularities described in the preceding paragraph concerned especially metallic surfaces that were processed to attain a required 'smoothness'. However, dealing with non-metallic materials and their fracture surfaces, whose profiles are not processed but are a result of natural fracture processes, requires an alternative approach. In the next paragraphs it will be shown that fitting and filtering procedures can be realized also within the Fourier analytical scheme in a quite natural way that respects the hierarchical structure of fracture surfaces. The Fourier fitting and filtering procedures are performed by using the partial Fourier sums with a variable number of terms. The number of terms in those sums has a similar meaning as the cutoff parameter within the Gaussian filter. A detailed description of this method is presented in Section 4.

As was mentioned in the introduction, numerical expressions of surface irregularities necessarily require positioning some reference level that ideally goes through the central parts of the digitalized profile, as is schematically indicated in Fig. 3. In the case of the 2D-profile it is the central curve and in the case of the 3D-profile it is the central 'surface', i.e. the central level. Unfortunately, there is no precise, general method for finding ideal positions for these central objects and, thus, in practice some type of fitting procedures has to be employed to reach a satisfactory result. Usually a polynomial is chosen as a fitting pattern for the central object but its order is set intuitively even though it has a considerable influence on the values of the resulting profile roughness numbers. The higher the order of the polynomial, the better it follows the contours of the digital profile and the smaller are the differences between the reference level and the profile and, as a consequence, lowering the roughness numbers appears. In such a case it is difficult to find an acceptable compromise.

Under these circumstances it should not be surprising that two independent computations of profile numbers may lead to different results due to the different polynomial orders. Treating such results without knowing properly under what conditions they were achieved results in a real risk of faulty conclusions and misinterpretation of otherwise reliable measurements. A comparison of two profile numbers which resulted from different processing conditions has no meaning. For all these reasons it is essential to specify properly the fitting pattern used and the type of fitting procedure.

4. Fourier scheme

To explore behavior of a more sophisticated central pattern, we implemented the Fourier series $F(x, y)$ as a functional object positioned in the 3D-profile $f(x, y)$

$$\begin{aligned} F(x,y) &= \lim_{N\to\infty} F_N(x,y) \\ &= \lim_{N\to\infty} \sum_{k,n=0}^{N-1} \lambda_{kn} \left(a_{kn} \cos\frac{k\pi x}{p} \cos\frac{n\pi y}{q} + b_{kn} \sin\frac{k\pi x}{p} \cos\frac{n\pi y}{q} + \right. \\ &\left. + c_{kn} \cos\frac{k\pi x}{p} \sin\frac{n\pi y}{q} + d_{kn} \sin\frac{k\pi x}{p} \sin\frac{n\pi y}{q} \right) \end{aligned} \tag{1}$$

where $2p$ and $2q$ specify the length and the width, respectively, of the investigated sample

$$\begin{aligned} &\Omega = \{x \in (-p,+p), y \in (-q,+q)\} \\ &a_{kn} = \frac{1}{pq} \iint_\Omega f(x,y) \cos\frac{k\pi x}{p} \cos\frac{n\pi y}{q} dxdy \\ &b_{kn} = \frac{1}{pq} \iint_\Omega f(x,y) \sin\frac{k\pi x}{p} \cos\frac{n\pi y}{q} dxdy \\ &c_{kn} = \frac{1}{pq} \iint_\Omega f(x,y) \cos\frac{k\pi x}{p} \sin\frac{n\pi y}{q} dxdy \\ &d_{kn} = \frac{1}{pq} \iint_\Omega f(x,y) \sin\frac{k\pi x}{p} \sin\frac{n\pi y}{q} dxdy \\ &\lambda_{kn} = \left\{ \begin{array}{ll} 1 & (k>0,\ n>0) \\ 1/2 & k=0,\ n>0 \quad or \quad k>0,\ n=0 \\ 1/4 & k=n=0 \end{array} \right\} \end{aligned} \tag{2}$$

At first sight it might seem that we do not perform any fitting procedure like e.g. the method of least squares but the integrations (Eq. (2)) included in the Fourier scheme in fact ensure such an optimization, which is analogous to the method of least squares. The main difference between the optimization of polynomials by the method of least squares and the Fourier integration method consists in the different bases they use. The method of least squares performed with polynomials employs a non-orthogonal basis, whereas Fourier integration is performed within the orthogonal basis of harmonic functions. An identical mathematical background of the least square method and the Fourier procedure is discussed and explained in Appendix A.

By increasing N in Eq. (1), we increase the number of terms (N^2) in the partial Fourier function $F_N(x, y)$,[1] which has the same effect as increasing the order of polynomials. Increasing the number of terms

[1] By 'term in the Fourier series' we understand the whole expression in the parentheses in Eq. (1).

makes the Fourier surface follow more closely the contours of the 3D-profiles and this decreases the values of roughness numbers because the absolute differences between the 3D-profile and the Fourier surface, i.e. $|f(x, y) - F(x, y)|$, become smaller. For this reason it is extremely important to specify clearly what number N has been chosen for the reference surface and this information must accompany the calculated profile numbers. Unfortunately, there is no exact quantitative measure determining the best value of N. This situation is analogous to that of the cutoff Gaussian wavelengths whose values were specified [12] on an empirical basis rather than from an exact theory. The choice of the particular reference level within the Fourier scheme will be discussed in the next section after the investigation of the capability of partial Fourier's functions (Eq. (1)) to converge on our measured 3D profiles.

Since the partial sums $F_N(x, y)$ of Fourier's series (Eq. (1)) do not always converge, it is necessary to investigate their convergence capability, i.e. to check the limiting behavior $\lim_{N\to\infty} F_N(x, y)$. This convergence behavior can be observed with the so-called delta function $\Delta(N)$, which may be expressed in the discrete form as follows:

$$\Delta(N) = \frac{1}{K \cdot L} \sum_{i=1}^{K} \sum_{j=1}^{L} \left[f\left(x_i, y_j\right) - F_N\left(x_i, y_j\right) \right] \tag{3}$$

where $K \cdot L$ is a pixel resolution of the used images. The delta function $\Delta(N)$ is a real function and may assume both the positive and negative values, i.e. $\Delta(N) \in (-\infty, +\infty)$. In case of convergence, i.e. $\lim_{N\to\infty} F_N(x, y) = f(x, y)$, the function $\Delta(N)$ will approach zero

$$\lim_{N\to\infty} \Delta(N) = 0 \tag{4}$$

This auxiliary criterion of convergence will be used in the next section as a testing tool investigating the convergence capability of partial Fourier's functions $F_N(x, y)$ within the present morphological study of the fracture surfaces of hydrated cement pastes.

Finally, to illustrate the behavior of profile numbers in practical applications, the following two profile/roughness numbers are introduced as probing tools:

$$H_a(N) = \frac{1}{K \cdot L} \sum_{i=1}^{K} \sum_{j=1}^{L} \left| f\left(x_i, y_j\right) - F_N\left(x_i, y_j\right) \right| \tag{5}$$

$$H_q(N) = \sqrt{\frac{1}{K \cdot L} \sum_{i=1}^{K} \sum_{j=1}^{L} \left[f\left(x_i, y_j\right) - F_N\left(x_i, y_j\right) \right]^2} \tag{6}$$

The roughness number H_a actually represents an average of absolute irregularities whereas H_q is a root mean square (rms) of those irregularities. Both these numbers are frequently used in surface roughness analyses of metallic materials and have been tested recently as indicators of mechanical quantities of hydrated cement materials [4–7]. They both show statistically reliable characteristics.

5. Applications to fracture surfaces of cement paste

As has been mentioned, we have recently studied morphology of the fracture surfaces of hydrated cement pastes by roughness numbers of different kinds [4–7] to investigate their correlation to porosity and other related volume quantities of cement-based materials. A confocal microscopy was employed in those studies to reconstruct 3D-profiles in the form of digital replicas. When computing roughness numbers from digital replicas, we encountered difficulties with an optimum position of reference surface and initiated an alternative procedure different from that used for industrially processed metallic surfaces. This procedure seems to be suitable for cementitious.

For illustrative purposes several specimens consisting of hydrated cement pastes were selected from a set of one-year old specimens. Ordinary Portland cement was used for their preparation. The specimens were mixed with the water-to-cement ratio equal to 0.4, and the fresh paste was cast in molds of a size $2 \times 2 \times 10$ cm^3. The paste was cured at a temperature of 20 ± 2 °C, and relative humidity of 100% for three months. Then, the specimens were fractured in the three-point bending arrangement and sectioned into small cubes $2 \times 2 \times 2$ cm^3. The rest of time the cubes were stored at normal laboratory conditions (20 ± 2 °C, ~101.325 kPa, 60 ± 10% RH). After 1 year some of those cubes were subjected to surface roughness analysis.

Fig. 4 shows the image of the 3D digital profile reconstructed from microscopic sections (magnification 20×, area of optical field 1 mm^2, pixel resolution 1024×1024). The Fourier series defined by Eq. (1) was implemented into the digitally reconstructed profile. The number of Fourier's terms was gradually increased starting from $N = 2$ (4 parenthesis terms) up to $N = 20$ or 50 (400 or 2500 parenthesis terms). The delta function $\Delta(N)$as an indicator of convergence was calculated according to Eq. (3) and can be seen in Fig. 5. Since the $\Delta(N)$approaches zero, in agreement with Eq. (4), a reliable convergence of the partial Fourier sums $F_N(x, y)$ may be anticipated.

The second step in our morphology analysis requires the selection of a reference level, i.e. a convenient number N that would specify a corresponding Fourier's function $F_N(x, y)$. There is no rule or convention for such a selection. This situation is analogous to that of metrology of metallic surfaces where the polynomials of the 'first' or higher orders are used. Since the machining metallic surfaces are rather plane, the polynomials of the first and second orders usually comply with their basic 'form geometry'. However, if the metallic surfaces were more wavy and rougher, or in the case of the fracture surfaces of cementitious materials or rocks, then a much higher order of polynomials would be necessary. It means that also within the Fourier's method a larger N-number should be anticipated in order to ensure a correct description of the 'basic geometry' of surfaces. The term 'basic geometry' reflects more or less the situation with metallic samples as they are usually nominally curved or tilted due to the machinery processing. However, fracture surfaces of cement-based materials result from the stochastic crack propagation and thus they often manifest unclear basic geometry that does not allow unambiguous placement of the reference surface (level). On the other hand, using a wider set of reference surfaces $F_N(x, y)$ with gradually increasing N, one can study the profile behavior by means of $H_a(N)$ and $H_q(N)$ on still finer length scales and in this way investigate the distribution of surface irregularities spanning over a broad band of texture and roughness formations.

For the sake of illustration, in the first row of Fig. 6 there are three images showing three different Fourier reference surfaces (levels) for $N = 2$, 7 and 20 (from the left to the right), which were derived from

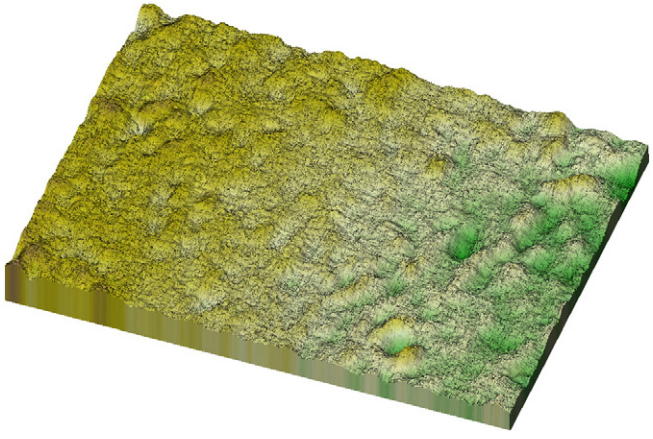

Fig. 4. 3D fracture surface of hydrated ordinary Portland cement paste.

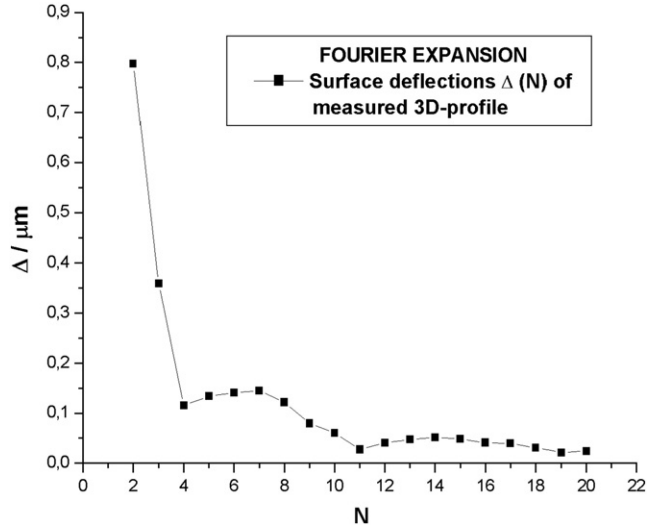

Fig. 5. The graph of delta function $\Delta(N)$ computed as differences between the 3D-profile and the Fourier reference level. The tendency $\lim_{N\to\infty}\Delta(N)\to 0$ confirms the right convergence behavior of the Fourier functions $F_N(x, y)$, which subsequently approach the measured 3D relief shown in Fig. 4.

the measured 3D-profile of the fracture relief displayed in Fig. 4. Comparing these three images it is obvious that for higher values of N the reference levels are wavier since they approach more closely the wavy shape of the real profile (Fig. 4). In the second row of Fig. 6 there are the same reference levels but augmented by the protrusions (marked in brown in the color images or by darker gray tones in the black-and-white images). The protrusions form roughness structures rising above the reference levels and when comparing these structures it can be seen that with higher N the roughness structures become finer and denser (a larger number of discrete peaks). In fact, the images in the second row of Fig. 6 do not show the complete peaks but only their sections with reference surface (see color islands). The third row of Fig. 6 also contains the reference levels for $N=2$, 7 and 20 but they are decorated by depressions (valleys) directed below the reference levels. The color of these depressions is blue in the color images or dark-gray in the black-and-white images. And again we can find finer and denser structures of those depressions when going from $N=2$ to $N=20$ (from the left to the right in the third row of Fig. 6).

From the structural changes presented in Fig. 6 it is possible to derive general conclusions concerning both protrusions and depressions, namely that at low values of N they both do not cover the reference areas too dense. Accordingly, the surfaces modeled with such low values of N are rather rough and thus yield large values of roughness numbers H_a and H_q (see Fig. 7). The largest values (7.5–11.5) μm of the functions in Fig. 7 can be observed at $N<5$ but then their values quickly decrease in the interval $N\in(5, 20)$ whereas for still larger values $N>20$ the decrease is only moderate.

Those structural and functional phenomena remind us of a great importance of selecting the reference level 'appropriately' because its position within the studied profile has a huge impact on roughness numbers $H_{a?}$ and $H_{q?}$. As already stated, there is no general rule for positioning the reference level; we can rely either on an intuitive way supported by empirical practice or adopt an 'artificial' rule, which would allow researchers to assume a unified approach to the selection procedure. For example, it would be possible to employ the delta function $\Delta(N)$ for this purpose. By normalizing the graph $|\Delta(N)|$ to unity, i.e. $|\Delta(1)|=1$ and fitting the graph with a smooth function $\Phi(N)>0$, we could find a number N_r of the reference level $F_{N_r}(x, y)$ by means of the equation $\Phi(N_r)=0.1$, whose right side represents one tenth of the initial value $\Phi(1)\approx 1$. Other rules are also possible but there is a question whether all those rules would be meaningful. It seems to us that a more reasonable concept would be to adopt the fact that the surface texture and the surface roughness are scale dependent properties of fracture surfaces and to treat them accordingly. A good alternative is to move the reference level $F_N(x, y)$ within the 3D profile by means of a sufficiently large interval of N-values and quantify those surface properties by using properly defined functions similar to those of $H_a(N)$ and $H_q(N)$. Introducing the reference levels with subsequently increasing N-values we actually change the length scale on which the surface texture/roughness is analyzed (the higher the N-value, the smaller the length scale). This means that on different length scales different texture/roughness

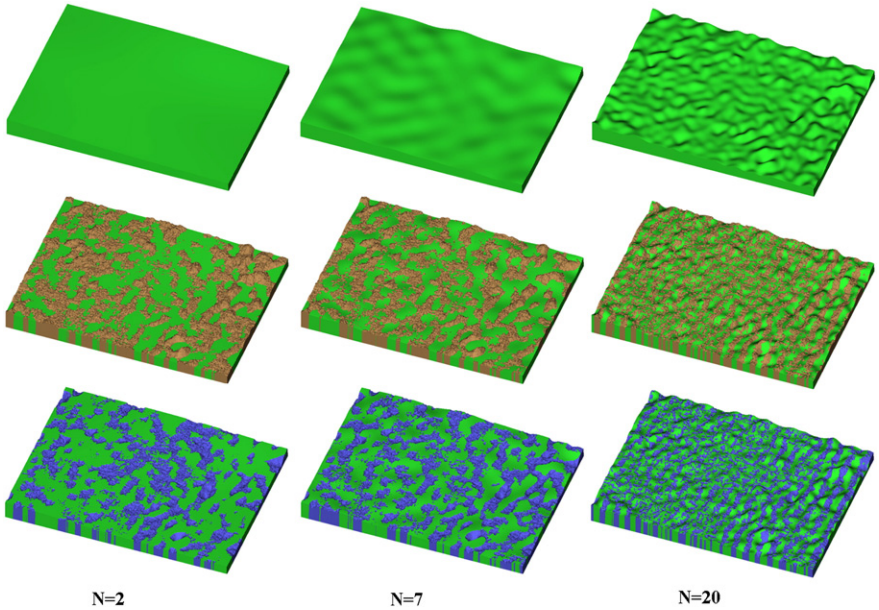

Fig. 6. Three different 3D Fourier's reference levels (green color) corresponding to $N=2$, 7 and 20 along with their modifications showing protrusions (brown color) and depressions (blue color). All the reference levels are derived from the measured 3D-profile presented in Fig. 4.

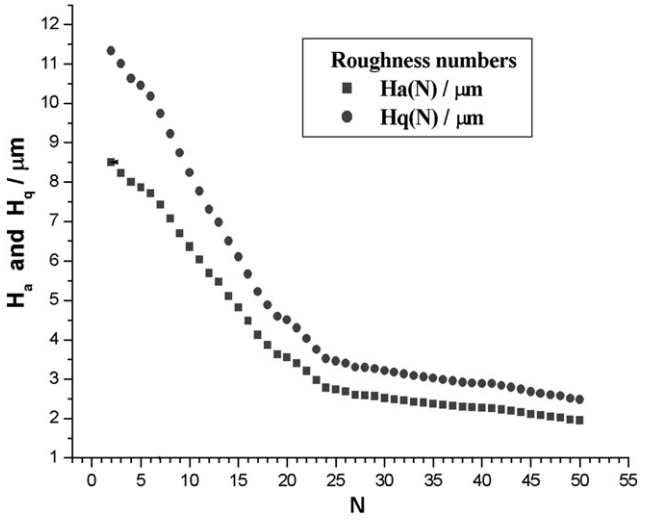

Fig. 7. The graphs of roughness numbers $H_a(N)$ and $H_q(N)$ illustrating their decreasing tendency caused by adding the terms in the Fourier series.

can be found and quantified. However, these quantities are valid only for a given scale and thus have only restricted (local) meaning. Looking for a global indicator of the 'overall' texture/roughness, one should analyze the surface functions like $H_a(N)$ and $H_q(N)$, and introduce a parameter or parameters characterizing their 'overall functional behavior'. To find such 'overall' indicators (if they exist) is not a straightforward matter and will require more research.

6. Conclusion

Finding an optimum reference levels within digital 3D surface profiles is a general problem that concerns all the calculation methods that could be used. The position as well as the shape of the reference level considerably influences the values of profile/roughness numbers computed from the 3D-profiles, and thus it would be important to specify conditions under which these values are determined.

The numerically processed data, which were originally measured on fracture surfaces of cement pastes, have indicated that fracture surfaces in contrast to industrially processed metallic materials have practically no 'basic geometry', and thus there is practically no aid for adequate positioning the reference level. In addition, the surface texture/roughness as a scale dependent property cannot be anchored to a single length-scale but requires analyzing all length scales present in the surface irregularities of the investigated samples. The multi-wave Fourier scheme proved to be a very convenient tool for this purpose. It allows quantifying the surface texture/roughness subsequently for different length scales by means of moving reference level and creating a broad spectrum of values of profile/roughness parameters. In this way an overview of the profile/roughness behavior in a wide range of length scales may be available and the corresponding quantitative output may be subjected to further analyses.

Acknowledgements

This work was supported by the Ministry of the Czech Republic under contract no. ME 09046 (Kontakt). Thanks are also due to Professor H. M. Jennings (Massachusetts Institute of Technology, USA) for his interest and support.

Appendix A. Equivalence between the method of least squares and Fourier's expansion

In this section we show that the method of least squares and the Fourier expansion method have the same mathematical background. First we formulate the general method of least squares and then on this basis we derive the Fourier expansion coefficients. For simplicity we discuss only one-dimensional case but the derivation in two dimensions would be analogous. The following derivation should not be considered as a rigorous mathematical proof but rather as a popular explanation which nevertheless contains a sound core. Such a popular explanation has been chosen to make it easier for the broadest class of readership.

Let us have a function $f(x)$ defined in the interval(α, β). It can be approximated by means of basis functions $\phi_o(x)$, $\phi_1(x)$, $\phi_2(x)$, ... $\phi_r(x)$ in the same interval as follows

$$f(x) = c_o\phi_o(x) + c_1\phi_1(x) + c_2\phi_2(x) + \ldots\ldots + c_p\phi_p(x) = \sum_{k=0}^{r} c_k\phi_k(x) \quad (7)$$

Let the function $f(x)$ be specified in a discrete form by a set of couples of points$\{f(x_i), x_i\}_{i=1}^{n}$. The expansion coefficients c_k may be optimized by the method of least squares to fit the set of the points (regression method). For this purpose a sum S of squares is introduced

$$S = \sum_{i=1}^{n}\left[f(x_i) - \sum_{k=0}^{r} c_k\phi_k(x_i)\right]^2 = \min \quad (8)$$

and its minimum is sought

$$\frac{\partial S}{\partial c_k} = 0, k = 0,\ 1,\ 2, \ldots\ldots r \quad (9)$$

which leads to a more straightforward algebraic expression

$$\frac{\partial S}{\partial c_k} = -2(a_k - c_1a_{k1} - c_2a_{k2} - \ldots\ldots - c_ra_{kr}) = 0 \quad (10)$$

where

$$a_k = \sum_{i=1}^{n} f(x_i)\phi_k(x_i), \quad a_{kh} = \sum_{i=1}^{n}\phi_k(x_i)\phi_h(x_i), \quad k,\ h = 0,\ 1,\ 2, \ldots\ldots ra \quad (11)$$

Eqs. (10) and (11) define a system of linear algebraic equations

$$\begin{aligned} &a_{00}c_0 + a_{01}c_1 + \ldots\ldots + a_{0r}c_r = a_0 \\ &a_{10}c_0 + a_{11}c_1 + \ldots\ldots + a_{1r}c_r = a_1 \\ &\ldots\ldots\ldots\ldots\ldots\ldots\ldots\ldots \\ &a_{r0}c_0 + a_{r1}c_1 + \ldots\ldots + a_{rr}c_r = a_r \end{aligned} \quad (12)$$

whose solution provides optimized expansion coefficients $\{c_k\}_{k=0}^{r}$ related to Eq. (7). This scheme is applicable with any arbitrary groups of basis functions $\phi_k(x)$. For example, if the polynomial regression of third order is to be performed, then the basis functions are defined as follows: $\phi_1(x) = 1$, $\phi_2(x) = x$, $\phi_3(x) = x^2$, $\phi_4(x) = x^3$ and Eq. (7) assumes the form of the polynomial of third order

$$f(x) = c_o + c_1x + c_2x^2 + c_2x^3 \quad (13)$$

The polynomial basis represents a non-orthogonal basis, since the off-diagonal terms a_{kh} of Eqs. (12) are non-zero, i.e. $a_{kh} = \sum_{i=1}^{n}\phi_k(x_i)\phi_h(x_i) \neq 0$, and as a consequence the full system of linear algebraic equations (12) has to be solved.

On the other hand, with an orthogonal basis the off-diagonal terms in system (12) are identically zero, i.e. $a_{kh} = \sum_{i=1}^{n}\phi_k(x_i)\phi_h(x_i) = 0$, and

system (12) is considerably simplified. In this case the expansion coefficients c_k may be computed straightforwardly as follows

$$c_k = \frac{a_k}{a_{kk}} = \frac{\sum_{i=1}^{n} f(x_i)\phi_k(x_i)}{\sum_{i=1}^{n} \phi_k(x_i)\phi_k(x_i)} \tag{14}$$

Now let us apply the procedure of least squares to Fourier's scheme. The Fourier set of trigonometric functions $\{1,\ \cos\frac{\pi x}{b},\ \sin\frac{\pi x}{b},\ \cos\frac{2\pi x}{b},\ \sin\frac{2\pi x}{b},\ \ldots\ldots\ \cos\frac{r\pi x}{b},\ \sin\frac{r\pi x}{b}(r\to\infty)\}$ represents an infinite orthogonal basis defined within a continuous interval $(-b,\ +b)$ so that the algebraic system (12) now contains an infinite number of equations and the members of that system should be investigated within the continuous representation. The transition from discrete to continuous representations can 'schematically' be realized by shortening the equidistant length Δx between points x_i to an infinitesimally small value, i.e. $\Delta x \to 0$. The off-diagonal elements then assume integral forms

$$a_{kh} = \lim_{\Delta x\to 0} \sum_{i=1}^{n} \phi_k(x_i)\phi_h(x_i)\Delta x = \int_{-b}^{+b} \phi_k(x)\phi_h(x)dx = \\ = \left\{ \begin{array}{l} \int_{-b}^{+b} \sin\left(\frac{k\pi x}{b}\right)\cos\left(\frac{h\pi x}{b}\right)dx = 0 \\ \int_{-b}^{+b} \sin\left(\frac{k\pi x}{b}\right)\sin\left(\frac{h\pi x}{b}\right)dx = 0 \\ \int_{-b}^{+b} \cos\left(\frac{k\pi x}{b}\right)\cos\left(\frac{h\pi x}{b}\right)dx = 0 \end{array} \right\} \quad \text{for } k \neq h \tag{15}$$

Provided $f(x)$ is a periodic function in the interval $(-b,\ +b)$ with the period $2b$, we can find the Fourier expansion coefficients by means of Eq. (14) as follows

A) For $k > 0$

$$c_k = \lim_{\Delta x\to 0} \frac{\sum_{i=1}^{n} f(x_i)\phi_k(x_i)\Delta x}{\sum_{i=1}^{n} \phi_k(x_i)\phi_k(x_i)\Delta x} = \frac{\int_{-b}^{+b} f(x)\phi_k(x)dx}{\int_{-b}^{+b} [\phi_k(x)]^2 dx} \\ = \frac{\int_{-b}^{+b} f(x)\phi_k(x)dx}{b} = \\ = \left\{ \begin{array}{l} \frac{1}{b}\int_{-b}^{+b} f(x)\cos\left(\frac{k\pi x}{b}\right)dx = c_k^{(c)} \\ \frac{1}{b}\int_{-b}^{+b} f(x)\sin\left(\frac{k\pi x}{b}\right)dx = c_k^{(s)} \end{array} \right\} \tag{16}$$

B) For $k = 0$

$$c_0 = \frac{1}{2b}\int_{-b}^{+b} f(x)dx = c_0^{(c)} = c_0^{(s)} \tag{17}$$

Inserting the expansion coefficients $c_k^{(c)}$ and $c_k^{(s)}$ from Eqs. (16) and (17) into Eq. (7), the usual Fourier series emerges

$$f(x) = \sum_{k=0}^{\infty} \left[c_k^{(c)} \cos\left(\frac{k\pi x}{b}\right) + c_k^{(s)} \sin\left(\frac{k\pi x}{b}\right) \right] \tag{18}$$

The foregoing derivation has confirmed that Eq. (18) can be viewed as a result of the optimizing procedure of least squares, in which an infinite and continuous basis of periodic trigonometric functions has been employed.

References

[1] K. Ravi-Chandar, W.G. Knauss, An experimental investigation into dynamic fracture: II microstructural aspects, Int. J. Fract. 26 (1984) 65–80.
[2] D. Dalmas, C. Guera, J. Scheibert, D. Bonany, Morphological aspects and deterministic reconstruction of dynamical fracture surfaces in brittle materials, EPJ Web Conf. 6 (2010), doi:10.1051/epjconf/20100639010 39010-p1–3910-p2.
[3] J. Scheibert, C. Guera, F. Célarié, D. Dalmas, D. Bonamy, Brittle–quasibrittle transition in dynamic fracture, Phys. Rev. Lett. 104 (2010) 045501-1–045501-4.
[4] T. Ficker, D. Martišek, H.M. Jennings, Roughness of fracture surfaces and compressive strength of hydrated cement pastes, Cem. Concr. Res. 40 (2010) 947–955.
[5] T. Ficker, D. Martišek, H.M. Jennings, Surface roughness and porosity of hydrated cement pastes, Acta Polytech. 51 (2011) 7–20.
[6] T. Ficker, Fracture surfaces and compressive strength of hydrated cement pastes, Constr. Build. Mater. 27 (1) (2012) 197–205.
[7] T. Ficker, D. Martišek, Roughness and fractality of fracture surfaces as indicators of mechanical quantities of porous solids, Cent. Eur. J. Phys. 9 (2011) 1440–1445, doi:10.2478/s11534-011-0061-0.0.
[8] K.-R. Wu, A. Yan, J. Liu, D. Zhang, W. Yao, Reconstruction and analysis of 3-D profile of fracture surface of concrete, Cem. Concr. Res. 30 (2000) 981–987.
[9] D.A. Lange, H.M. Jennings, S.P. Shah, Analysis of surface-roughness using confocal microscopy, J. Mater. Sci. 28 (14) (1993) 3879–3884.
[10] D.A. Lange, H.M. Jennings, S.P. Shah, Relationship between fracture surface roughness and fracture behavior of cement paste and mortar, J. Am. Ceram. Soc. 76 (3) (1993) 589–597.
[11] ISO 25178-2, Geometrical product specifications (GPS)—surface texture: areal—part 2: terms, definition and surface texture parameters (International Organization for Standardization, Geneva, 2012).
[12] ISO 4288-1996, Geometrical product specification (GPS)—surface texture: profile method—rules and procedures for the assessment of surface texture, (International Organization for Standardization, Geneva, 1996).

Journal of
APPLIED
BIOMEDICINE

J. Appl. Biomed.
5:151–156, 2007
ISSN 1214-0287

REVIEW

New methods for space reconstruction of inside cell structures

Dalibor Martišek, Karel Martišek, Jana Procházková

Institute of Mathematics, Faculty of Mechanical Engineering, Brno University of Technology, Czech Republic

Received 24th April 2007.
Revised 25th May 2007.
Published online 27th July 2007.

Summary
This paper discusses new methods for 3-D processing of confocal microscope outputs - single optical cuts through an explored object. The method can model cell illumination by an external light source and is a next important step in the realistic displaying of cells. The computer program based on these methods can be run on a common PC.

Keywords: confocal microscope – vector data – raster data – 3-D model – opacity - illumination

INTRODUCTION

The study of the complicated architecture of cell space structures is an important problem in biology and medical research. Optical cuts of cells produced by confocal microscopes enable 2-D and 3-D reconstructions of observed cells. The existing software tools used to reconstruct small objects usually do not employ all the features of the state-of-the-art hardware. Since the existing software is run on high-level computers, the efficiency of the algorithms is not the issue. Technologies such as OpenGL or DirectX can only be used on graphic stations with special graphic cards with graphics accelerators. These tools have extreme memory fact that these graphics cards are approximately forty times faster than computer processors. The software programmes recommended by the microscope manufacturers usually do not work on standard PCs. For example, the software system used to decode Olympus data halts because of insufficient global memory even on a PC with 2GB RAM. Data visualization based on OpenGL or DirectX does run on a PC, but only with great difficulties.

The main problem is the quality of output created by means of OpenGL and DirectX. With the method proposed, more parameters of the environment can be set, making it possible to apply 3D filters to set the output image sharpness in relation to the noise. The quality of the output is incomparable and is worth increasing the computing time.

We would like offer to the biomedical community mathematical methods of 3D scalar data visualization describing new algorithms that run on standard PCs very well.

Some publications (Druckmüller 2001, 2003, Martišek 2002a, 2002b) were some of the first attempts in this direction.

✉ Dalibor Martišek, Institute of Mathematics, Faculty of Mechanical Engineering, Brno University of Technology, Czech Republic
martisek@fme.vutbr.cz
☎ +420 541 142 713
🖷 +420 541 142 710

CURRENT COMMON PRINCIPLES OF 3-D DATA VISUALIZATION

Algorithms which process 3-D data can be classified into two groups: surface fitting algorithms (SF algorithms) and direct volume rendering algorithms (DVR algorithms). SF algorithms construct a geometric surface representation of the scalar field to be displayed, and then construct this surface. DVR algorithms display the scalar field directly without surface representation.

In computer graphics, either vector or raster data can be processed. In terms of graphic data, a vector is understood in the traditional sense being identified with an intuitively understood oriented line segment, i.e. one with base and end points. Vector data are usually processed by vector algorithms. We can relatively easily use a parallel projection method which simulates a long-distance camera, and centre projection methods to model a camera situated closer to the object. Determining for this projection is an angle called a viewing angle – see Fig. 1 on the left.

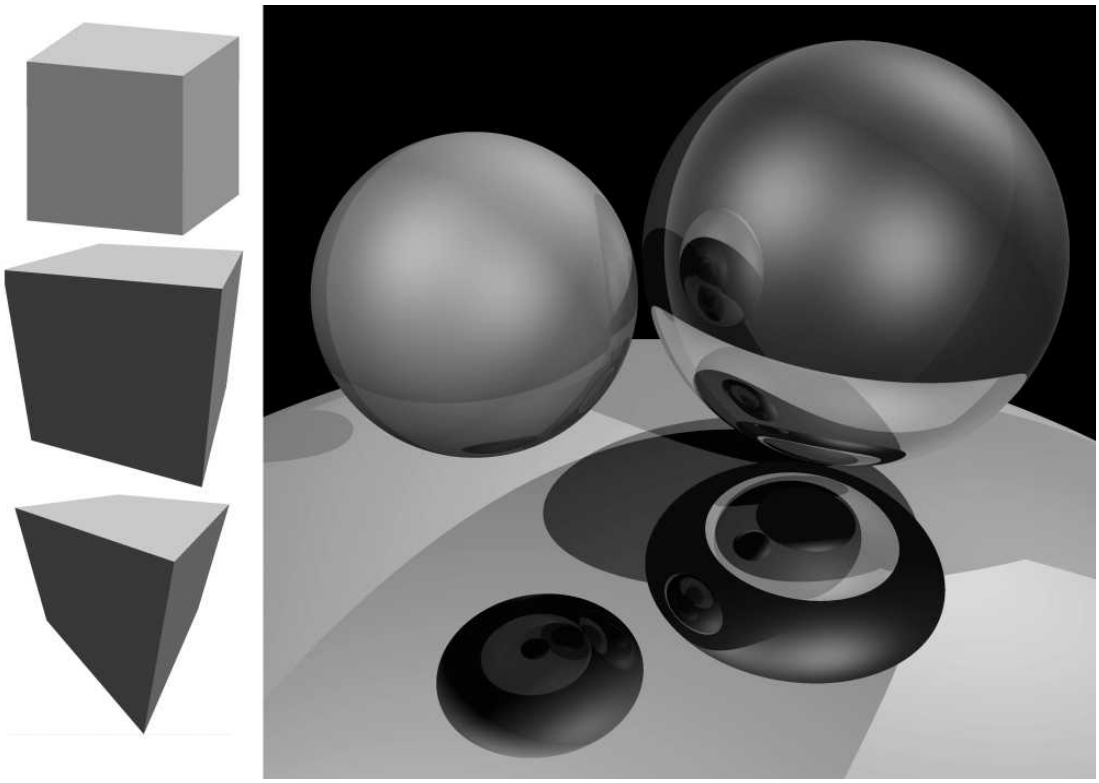

Fig 1. **3-D processing of vector data.** Parallel and central projection of a cube on the left - the cube was projected by a viewing angle of 0^o (parallel projection), 42^o (maximum of human viewing angle) and 70^o (wide-angle objective). Light and shadow of a scene on the right – the sphere on the left reflects virtually no light at all, and the lower sphere reflects almost all the light. Both of the coefficients (mirror component and diffuse component) are 50% for the sphere on the right. The ambient component is 30%. The scene is illuminated by three light sources.

While displaying vector data, we usually work with illumination as well. Light illuminates a scene (the space displayed) in a certain direction. If a planar optical interface had a microscopically ideal surface then both reflection and refraction would preserve parallelism. However, a real body does not have a totally smooth surface so both reflected and refracted beams have various directions. Asperities have a fractal character and the properties of reflected and refracted beams can be described only approximately. A function which tries to describe this character is called a reflection (refraction) function. An application of this function in a particular situation is then called an illuminant model.

Object lighting is important for space information processing realised by human vision. The interpretation of light reflection and refraction can be approached in two ways in the case of vector data. Physical models result from the physical laws of light propagation trying to describe the reflection from an uneven surface through the use of the energy propagation principle. These methods are very difficult, very time-consuming and are only

applicable to real calculations with serious difficulties. Empirical models do not have a direct relation to the physical principles of light propagation and trying to simulate the expected result in a simple way. They are far simpler, and applications based on them are considerably faster. The simplest empiric illuminant models result from the fact that the whole luminous intensity coming from a given point to an observer is given by the sum of the specular and the diffusive components. "A uniform contribution of ambient light" is mostly also added . This component inhibits areas reversed from light sources to be displayed as completely black ones. Hence, the total luminous intensity is given by the sum of these components. The simplest empiric illuminant model is called Phong's model. We can see an implementation of this model in Fig. 1 on the right.

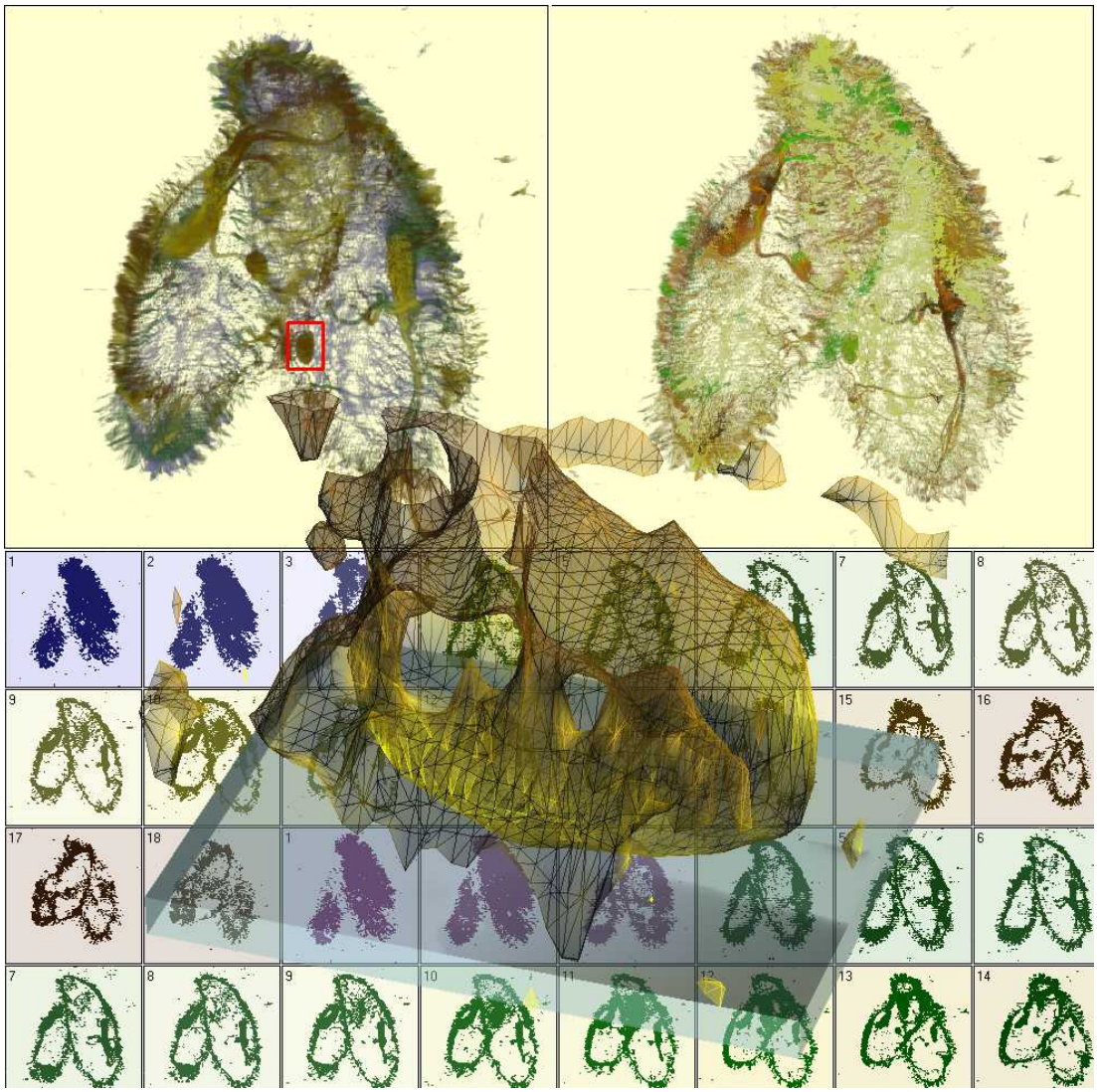

Fig 2. **3-D vector processing of raster data.** These algorithms are only suitable for visualising high-contrast structures. The central projection with a viewing angle of 25° and an illuminant model with one light source are used. Two infusorian cells *Paramecium caudatum* with overlapped anterior, detail (micronucleus) were chosen by the rectangle on the 2-D reconstruction.

Raster data do not contain any „vector" information on saved objects. From these data, it is not possible to find out in a simple way whether an image is composed of cubes, spheres or something else. A file contains information on the size of the image, on the way it may have been compressed and on the colour encoding used. The image itself is saved as a matrix and each element of this matrix represents one image pixel. Most of the displaying devices (monitors, printers, cameras etc.) work on this principle. The data provided by a confocal microscope are also raster.

NEW SURFACE FITTING METHODS FOR CELL RECONSTRUCTION

Vector visualisation algorithms are, by default, used for vector data, but they can be used for raster data as well (including confocal microscopes data). Raster data mostly contain tens of millions of values. It is usually impracticable to vectorize such amounts of data and therefore these algorithms are only used to visualise selected details of the data structures. Vectorisation works mostly on the principle of detection of an iso-surface, i.e. the surface passing through points of the same density value in a given scalar field. That is why these algorithms are only suitable for visualising high-contrast structures, which can be taken for objects with a strongly defined boundary representing this surface. Central projection and illuminant models can be applied in a relatively simple way. In Fig. 2, we can see the output of our software - two infusorian cells *Paramecium caudatum* with overlapped anteriors. In the background, there are 2-D reconstructions with different transparencies and reduced optical cuts. In front is a 3-D reconstruction of the micronucleus provided by the iso-area detection method. Pseudo-colours are used – called a topographical palette (the blue parts are lower than the brown ones). Another possible colour wheel is used for 2-D reconstruction on the right. The primary data have a grey-scale palette.

The isolated micronucleus from Fig. 2 can be seen in Fig. 3 with various viewing angles used.

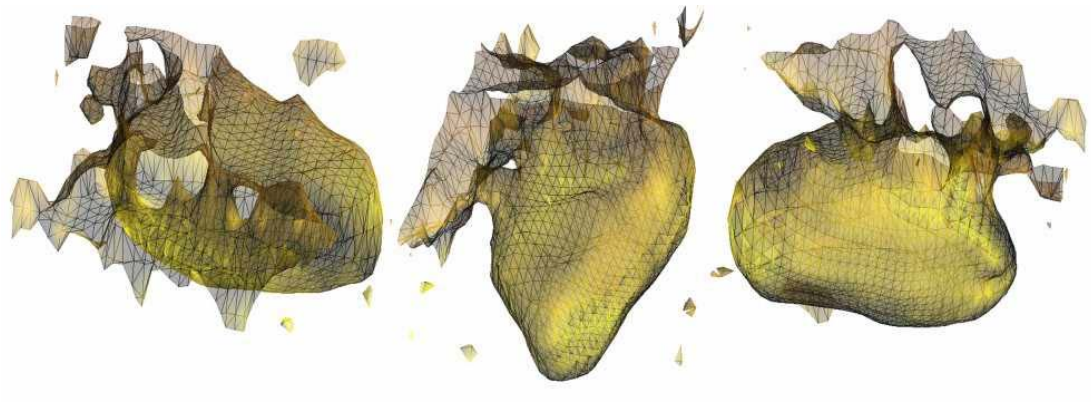

Fig.3. The isolated micronucleus from Fig.2 displayed at various viewing angles.

NEW RASTER METHODS FOR CELL RECONSTRUCTION

The basic principle of current DVR algorithms is called ray casting. The method tracks the viewing ray and calculates the values of the scalar field. The standard methods that work with 3-D raster data use 2-D methods for ray casting: a maximum intensity projection algorithm (MIP algorithm) displays the most intensive pixel. The Summed Intensity Projection algorithm (SIP algorithm) displays the sum of pixel intensity, the average intensity projection algorithm (AIP algorithm) displays the arithmetic mean of pixel intensity. (Levoy 1988). Other more precise methods have also been developed. These raster methods, however, consume an enormous volume of computer memory and require high-speed processing (Druckmüller 2001, 2003). Moreover, these methods can only be used for work with parallel projection, and not with centre projection. The cells observed by a conventional or a confocal microscope are often highly transparent, and, because of the lighting geometry, the structures inside the cell do not create visible shadows. The present methods cannot be used to solve this problem because they cannot apply an illuminant model.

Thus question arises: is it possible to find another method by means of which we will be able to abolish at least one of these insufficiencies? The response to this question appears to be positive. Moreover, it is possible to solve both these problems (fasting and shading) at once. The tool we are after is Bresenham's raster algorithm of 2-D line

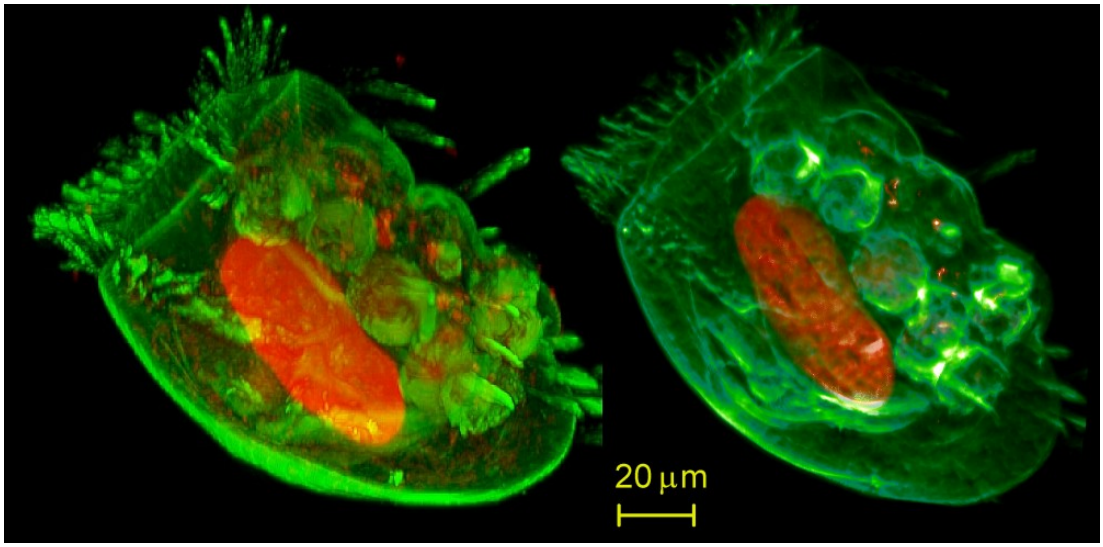

Fig 4. **Phong's illuminant model applied to raster data**. The cell opacity simulation on the left is taken from Druckmüller (2003). The illuminant model was modified for raster data on the right. The human eye analyses light and shade to obtain space information, therefore, space information is significantly better. Infusorian cell *Euplotes patella,* in green colour microtubules, red DNA of macronucleus.

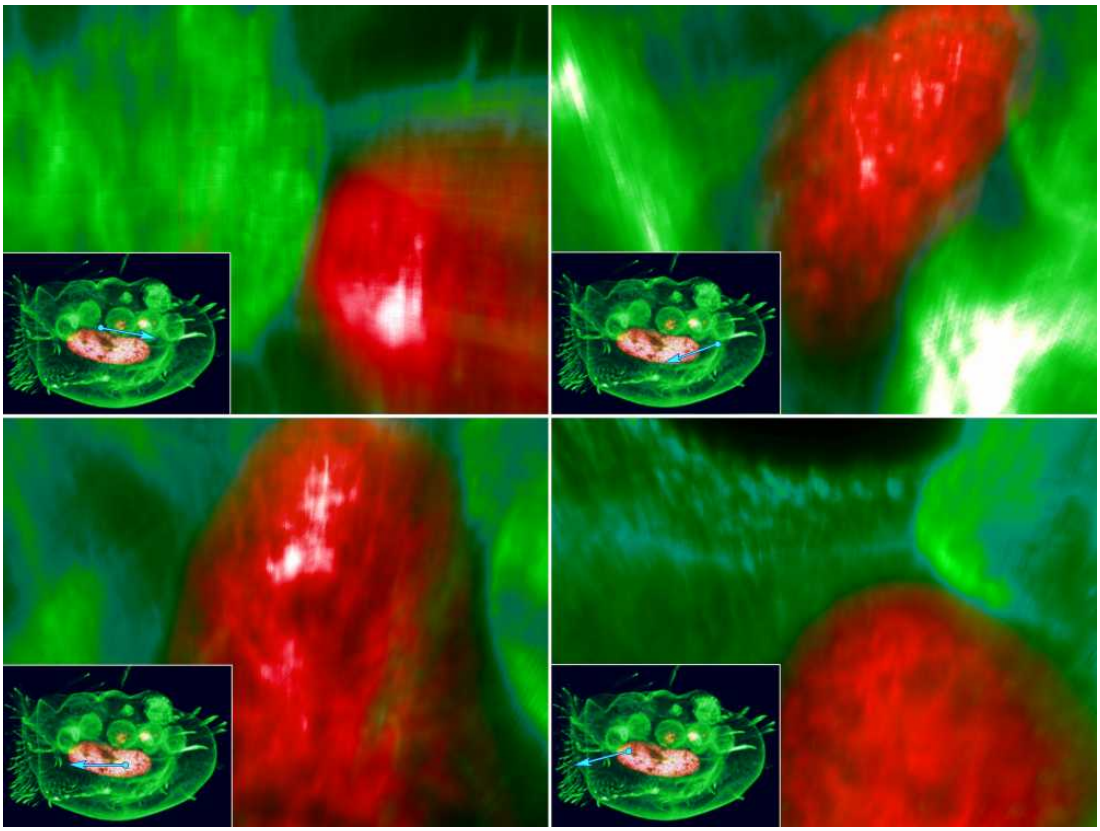

Fig 5. **Cell interior**. Methods of central projection and illuminant models are combined with the direct volume rendering method. We obtain a free camera which can be placed inside a cell. Two light sources were used, the transparency of each data element is 90%. Both the mirror and the diffuse components are 50%. The viewing angle is 35^{o} (Interior of *Euplotes patella* cell).

segment construction in integer arithmetic generalized for 3-D. This generalized algorithm can be called line segment voxelization. With the use of this generalization, the basic calculation time of one image drops from several minutes to approximately twenty seconds.

An illuminant model can be applied to raster data as well. After some modification, it is even possible to use models originally developed for Computer Aided Design (CAD) systems. These systems are usually used in mechanical engineering. Modified formulas of Phong's model were applied to each voxel of three-dimensional data processed (Fig. 4).

Our method makes it possible to use the centre projection not only for vector data, but also for raster data. It is the next important step for cell-realistic representation. Our new method can be characterised by what is called a "free camera". We can place the camera not only outside the cell but also inside the cell (Fig. 5).

The primary data was obtained by the Olympus Fluoview II fluorescent scan confocal microscope by Prof. R. Janisch (Department of Biology, Faculty of Medicine, Masaryk University, Brno, Czech Republic).

ACKNOWLEDGEMENT

This study was supported by the Ministry of Education, Youth and Sports of the Czech Republic, research plan MSM 0021630518 "Simulation modelling of mechatronic systems".

References

Druckmüller M: Adaptive Image Processing in Biology. In Berger J (ed.): Cells III, Kopp Publ., České Budějovice 2001, pp. 71–79.

Druckmüller M: Opacity simulation technique for confocal microscope image processing. J. Appl. Biomed. 1:71–75, 2003.

Martišek D: The Two-dimensional and three-dimensional processing of images provided by conventional microscopes. Scanning 24:284–295, 2002a.

Martišek D: Three-Dimensional Filters and their Use for Computer Modelling. Proceedings of the 1st International Conference Aplimat, February 7.–8., 2002, Bratislava 2002b, pp. 291–296.

SCANNING VOL. 24, 000–000 (2002)

Received: February 27, 2002
Accepted with revision: August 28, 2002

The Two-Dimensional and Three-Dimensional Processing of Images Provided by Conventional Microscopes

DALIBOR MARTIŠEK

Department of Mathematics, Faculty of Mechanical Engineering, Brno University of Technology, Brno, Czech Republic

Summary: In this paper, I present an interesting processing method of microscopic images. High-pass type filters are generally used for image focusing. They enhance the high spatial frequencies. They are, however, efficient only in cases when the picture is not sharp because of the low contrast on high frequencies (for example in a TV picture). These filters, are not appropriate if the lack of sharpness has been caused by other factors. In this case, it is not possible to construct a three-dimensional model of the observed object. Better results and a three-dimensional model can be obtained by applying the following theory. As part of this paper, an original program based on this theory is described.

Key words: graphic plane, physical pixel, multifocal image, Euclidean trace of point, focusing criterion

PACS: 07.60.Pb, 07.79.-v

1.0 Introduction

In computer graphics, data are stored as the coordinates of points. Points are viewed as nondimensional objects conforming to the traditional Euclidean geometry. The display surface of an output device is, however, a physical object and cannot display dimensionless points. For this reason, the notion of "pixel" rather than point is used, denoting the smallest viewable formation. In mathematical modelling, however, pixels in the logical sense have to be considered (i.e. the output device is thought of as a set of isolated Euclidean points) in contrast to the physical sense (where the output device is taken to represent a set of elementary small surfaces). In the present literature, these differences are often ignored. Nevertheless, even in cases where these notions are differentiated, their definitions are very vague and sometimes even false. To allow for all possible constructions, it is very important to give an exact definition of pixel.

In the following, we will provide a mathematical model of the entire situation.

2. Graphic Plane

2.1. Definition

Let $I = \langle i_1;i_2)$; $J = \langle j_1;j_2)$ be intervals. Further let $D_x = \{x_i\}_{i=0}^{m}$; $m > 1$ be an equidistant division of I, $D_y = \{y_i\}_{i=0}^{n}$; $n>1$ an equidistant division of J. The rectangle $\mathbf{F}_{ij} = \langle x_i;x_{i+1}) \times \langle y_j;y_{j+1})$; $i = 0,1,..,m-1$, $j = 0,1..,n-1$, will be called a physical pixel. The number $p_x = x_{i+1}-x_i$ or $p_y = y_{j+1}-y_j$ will be called the horizontal or the vertical dimension of the physical pixel $\mathbf{F}_{ij}$, respectively. The rectangle $I\times J$ together with divisions D_x, D_y is called a graphic plane, denoted by $\mathcal{G}_2$, or in detailed notation, $\mathcal{G}_2 = (I\times J,D_x,D_y)$. We will call the ordered pair $(m;n)$ the graphic plane resolution.

The theorem shown below follows directly from this definition:

2.2. Theorem

The set $\mathcal{F}_2 = \{\mathbf{F}_{ij} = \langle x_i;x_{i+1}) \times \langle y_j;y_{j+1}) \mid i \in \{0,..,m-1\}; j \in \{0,..,n-1\}\}$ of all physical pixels in the graphic plane $\mathcal{G}_2$ is a representation of $\mathcal{G}_2$.

By the definition, all the vertical and horizontal vertical sizes of the physical pixels $\mathbf{F}_{ij}$ in $\mathcal{G}_2$ are equal. This immediately proves the following theorem:

2.3. Theorem

Let $\mathcal{G}_2$ be an arbitrary graphic plane, $\mathcal{F}_2$ the set defined in 2.2. The relation ρ defined on $\mathcal{G}_2$ by $\rho(A,B) \Leftrightarrow (\exists \mathbf{F}_{ij} \in \mathcal{F}_2)[A \in \mathbf{F}_{ij} \wedge B \in \mathbf{F}_{ij}]$ is an equivalence on $\mathcal{G}_2$.

This project is supported by research design CEZ: J22/98:261100009 "Non-traditional methods for investigating complex and vague systems".

Address for reprints:

Dalibor Martišek
Department of Mathematics
Faculty of Mechanical Engineering
Brno University of Technology
Technicka 2
CZ-61669 Brno, Czech Republic
e-mail: martisek@mat.fme.vutbr.cz

2.4. Definition

Let $\mathcal{G}_2$ be a graphic plane. The factor set $\mathcal{F}_2 = \mathcal{G}_2/\rho$, where ρ is the equivalence from the previous theorem, is called the physical plane of $\mathcal{G}_2$. Under the resolution of the physical plane $\mathcal{F}_2$ we understand the resolution of the corresponding graphic plane $\mathcal{G}_2$.

To model a graphic plane we can use virtually any output device such as a monitor, printer, and so forth.

2.5. Definition

Let $\mathcal{F}_2$ be a physical plane, $\mathbf{F}_{ij}$ its physical pixels. The ordered pair $[i,j]$ is called the coordinates of $\mathbf{F}_{ij}$.

2.6. Definition

Let $\mathcal{F}_2$ be a physical plane and $C_r = \{c \in N;\ 0 \le c \le r;\ r > 1\}$. A mapping $O: \mathcal{F}_2 \to C_r$ is called an image matrix or short an image. The set C_r is called an r-chromatic set. If $O: \mathbf{F}_{ij} \to c$, c is called the value or colour of $\mathbf{F}_{ij}$. Under the resolution of the image we understand the resolution of the incident physical plane.

Next, it is obvious that the following theorem holds:

2.7. Theorem

Let $\mathcal{G}_2$ be a graphic plane, $\mathcal{F}_2$ its physical plane, $\mathbf{F}_{ij}$ its physical pixels. The mappings

$$^{(2)}\mathscr{E}_{\mathcal{F}} : \mathcal{F}_2 \times \mathcal{F}_2 \to \mathbf{R} \text{ such, that}$$
$$^{(2)}\mathscr{E}_{\mathcal{F}}(\mathbf{F}_{ij};\mathbf{F}_{kl}) = \sqrt{(k-i)^2 + (l-j)^2};$$

$$^{(2)}\mathscr{P}_{\mathcal{F}} : \mathcal{F}_2 \times \mathcal{F}_2 \to \mathbf{R} \text{ such, that}$$
$$^{(2)}\mathscr{P}_{\mathcal{F}}(\mathbf{F}_{ij};\mathbf{F}_{kl}) = |k-i| + |l-j|;$$

$$^{(2)}\mathscr{C}_{\mathcal{F}} : \mathcal{F}_2 \times \mathcal{F}_2 \to \mathbf{R} \text{ such, that}$$
$$^{(2)}\mathscr{C}_{\mathcal{F}}(\mathbf{F}_{ij};\mathbf{F}_{kl}) = \max\{|k-i|;|l-j|\};$$

are metrics on $\mathcal{F}_2$.

2.8. Definition

Let $\mathcal{G}_2$ be a graphic plane, $\mathcal{F}_2$ its physical plane, $\mathbf{F}_{ij}$ its physical pixel. The Mappings $^{(2)}\mathscr{E}_{\mathcal{F}}$; $^{(2)}\mathscr{P}_{\mathcal{F}}$; $^{(2)}\mathscr{C}_{\mathcal{F}}$ from Theorem 2.7. are called a Euclidean, postman, and square metric on $\mathcal{F}_2$, respectively.

For its computational simplicity, the square metric is used in image processing. For sophisticated graphic algorithms and other applications, mostly other metrics are used (e.g. for three-dimensional [3-D] reconstruction).

3. Mathematical Model of a Conventional Microscope

In geometrical optics, terms such as object space and image space are used. In the sequel, we will use a mapping that conforms to the postulates of geometrical optics and call it a geometrical projection. The mapping is implemented by direct rays that pass through the point P that is to be displayed. These rays are transformed by the optical system into conjugated rays that pass through the image space and meet at a point P'.

However, the mapping as implemented by a real conventional microscope does not conform exactly to the postulates of geometrical optics. The following is a list of some of the reasons for this:

The limited width of the beam of rays: The mapping of point P is carried out by a beam of rays. If we denote by $\mathcal{A}$ the set of the values assumed by the angles formed by the rays of the bunch, then $\sup \mathcal{A} = \pi$. Although the beam of rays that enter into the lens is very broad, since it must always carry enough light with a real microscope we have always $\sup \mathcal{A} < \pi$. Thus by S we shall denote the beam of rays that really goes through the optical microscope.

The wave nature of light: Geometric optics presumes, that light propagates along straight lines. This presumption, however, is valid only if light goes through a homogeneous and isotropic environment (which, in a microscope, can be presumed), and further if light passes obstacles that are larger than its wavelength by orders of magnitude. This, however, is not the case with microscopes. When a microscopic a microscopic preparation is observed, light is always inflected by a small obstacle—the preparation itself. The optical system of the microscope as such also produces flexural phenomena, namely, on the input pupil. Thus, to give a mathematical description of an optical microscope we must also take into account the wave nature of these phenomena. This means that the geometrical projection $\mathcal{G}: P_3 \to P_3'$ cannot be used and has to be replaced by a more general correspondence between the object and image space; strictly speaking between the sharpness plane ω and the ocular focal plane φ_2:

3.3. Definition

Let $\mathcal{M}_v \subset \omega \times \varphi_2$ be a relation such that $[P;Q] \in \mathcal{M}_v \Leftrightarrow Q \in \mathscr{S}_V^P = \left\{ X \in \varphi_2 \,\middle|\, |XP'| \le \frac{\lambda_0}{4A} \wedge P' = \mathcal{G}(P) \right\}$ $\mathcal{M}_v$ is called wave scanning. The set $\mathscr{S}_V^P$ is called the wave trace of the point P, the number $d(\mathscr{S}_V^P) = \sup_{X,Y \in \mathscr{S}_V^P} \{a \in R | a = |X;Y|\} = \frac{\lambda_0}{2A}$ is called its average. (A is the so-called numerical aperture of the microscope, λ_0 the wave length of light used.) The wave trace of the point is illustrated in Fig. 1.

Nonplanarity of the preparation: As indicated above, it follows that it is impossible to focus the microscope so that it displays the point as a point. When observing a nonpla-

nar preparation, further problems are encountered. As mentioned before, for an image of the preparation to be sharp, the preparation must be placed exactly in the plane to which the microscope is focussed. This plane is called a sharpness plane. However, in many cases, we cannot take the preparation to be a plane, and therefore these conditions cannot be fulfilled. The sharpness plane intersects the 3-D preparation in a contour line. The points of this contour line will be displayed with maximum possible sharpness. The points of the preparation that lie outside this plane cannot be displayed as points, even if we abstract from the wave nature of light and assume its straight propagation (see Fig. 2).

3.4. Definition

Let P_3 be the object space of a microscope, $\mathcal{G}$: $P_3 \to P_3'$ a geometrical projection. Further let $\bar{P} \in P_3$; $\mathcal{G}$: $\bar{P} \to \bar{P}'$; S be the homocentric bunch gone thorough the point $\bar{P}$ and $\mathcal{G}$: $S \to S'$. The relation $\mathcal{M}_E \subset P_3 \times \varphi_2 = \left\{ \left[\bar{P}; \bar{P}' \right] \middle| \exists \bar{p} \in S' : \bar{P}' \in \bar{p} \cap \varphi_2 \right\}$ is called Euclidean scanning. We will call the set $\mathcal{S}_E^P = \left\{ P' \in \varphi_2 \middle| [P; P'] \in \mathcal{M}_E \right\}$ the Euclidean trace of the point P, and the number $d\left(\mathcal{S}_E^P\right) = \sup\left\{ |X;Y|; X, Y \in \mathcal{S}_E^P \right\}$ its average.

If we view the image of point P from the object focal plane of the ocular, then the Euclidean scanning translates this point into its trace whose average is generally greater than zero, even if straight propagation of light is assumed (see Fig. 3).

Scanner resolution: In all the above considerations of the properties of an optical microscope, we assumed that all the

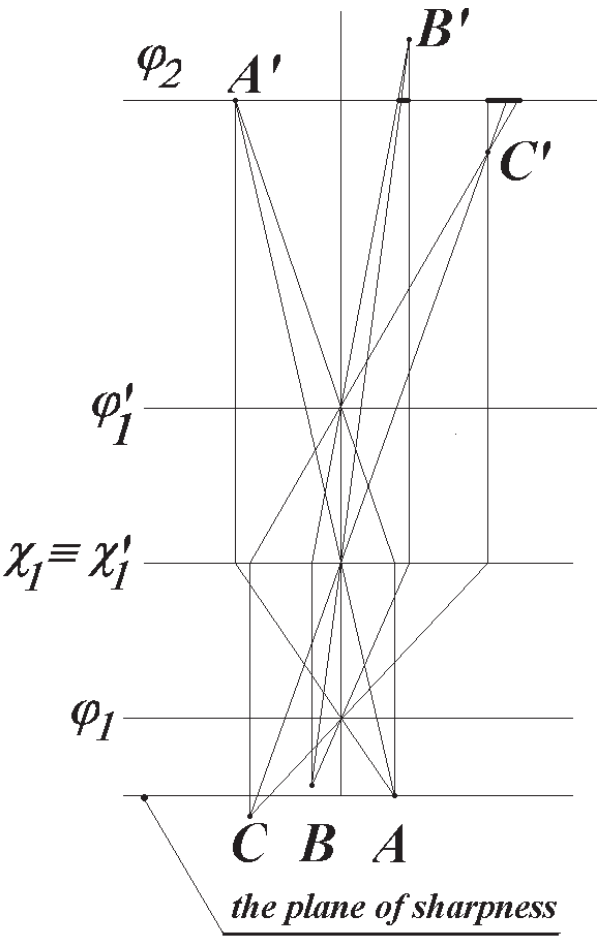

FIG. 2 Nonplanarity of the preparation.

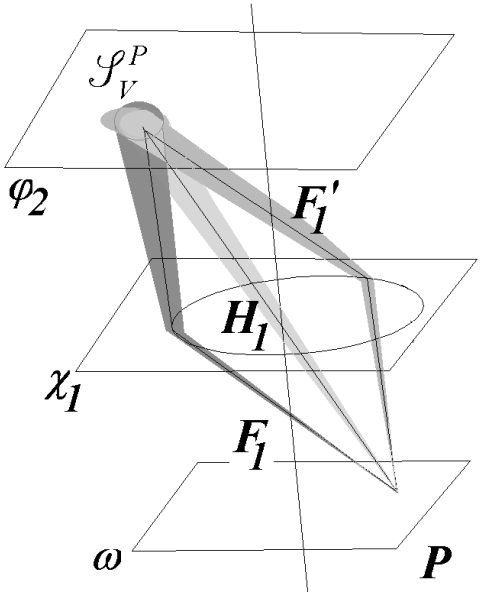

FIG. 1 Wave trace of the point.

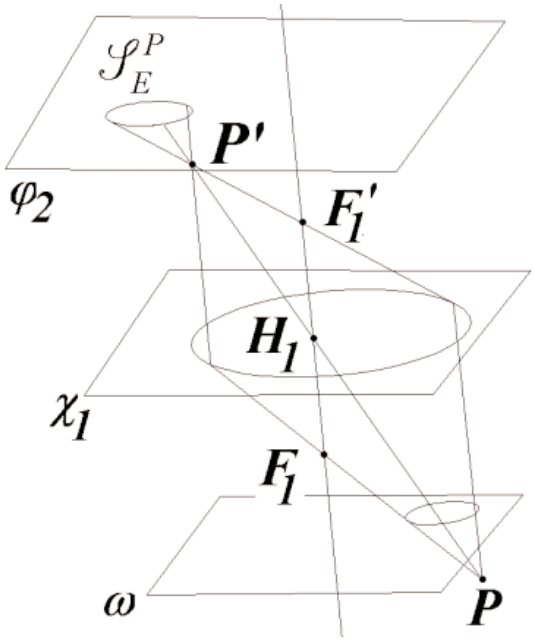

FIG. 3 Euclidean trace of the point.

deviations from the geometrical projection originate in the microscope during the projection itself. However, these deviations are also caused by the scanner. Assuming the straight propagation of light let the preparation being placed flush with the microscope sharpness plane, then the geometrical projection $\mathcal{G}$ takes every point $P \in \omega$ of the preparation to point $P' \in \varphi$. Despite this, this point cannot be mapped to a point. A scanner is a physical object and, therefore, it cannot represent the point as a dimensionless object. No matter on which principle the scanner works, it more or less meets the criteria of a graphic plane, as described in the definitions starting by 2.1. Every point is displayed as a physical pixel with nonzero dimensions, and its particular value depends on the size and resolution $(w;h)$ of the scanner.

The image acquired by a particular scanner from a particular microscope is the result of intricate interactions of the phenomena described above. An accurate mathematical description of these interactions would be extremely complicated. However, as will be demonstrated in the following, there are interesting possibilities of reconstructing real images.

4. Zone of Sharpness, Multifocal Image

In the previous chapter, we indicated that in a nonplanar preparation only the contour line, in which the preparation intersects the sharpness plane, is displayed sharply. However, in such a case, any nonplanar preparation would be virtually out of focus. On the other hand, in real images resulting from conventional microscopes, the parts that are in focus are perfectly sharp with only the rest out of focus (see Fig. 4), with microphotographs of an *Astrophy-*

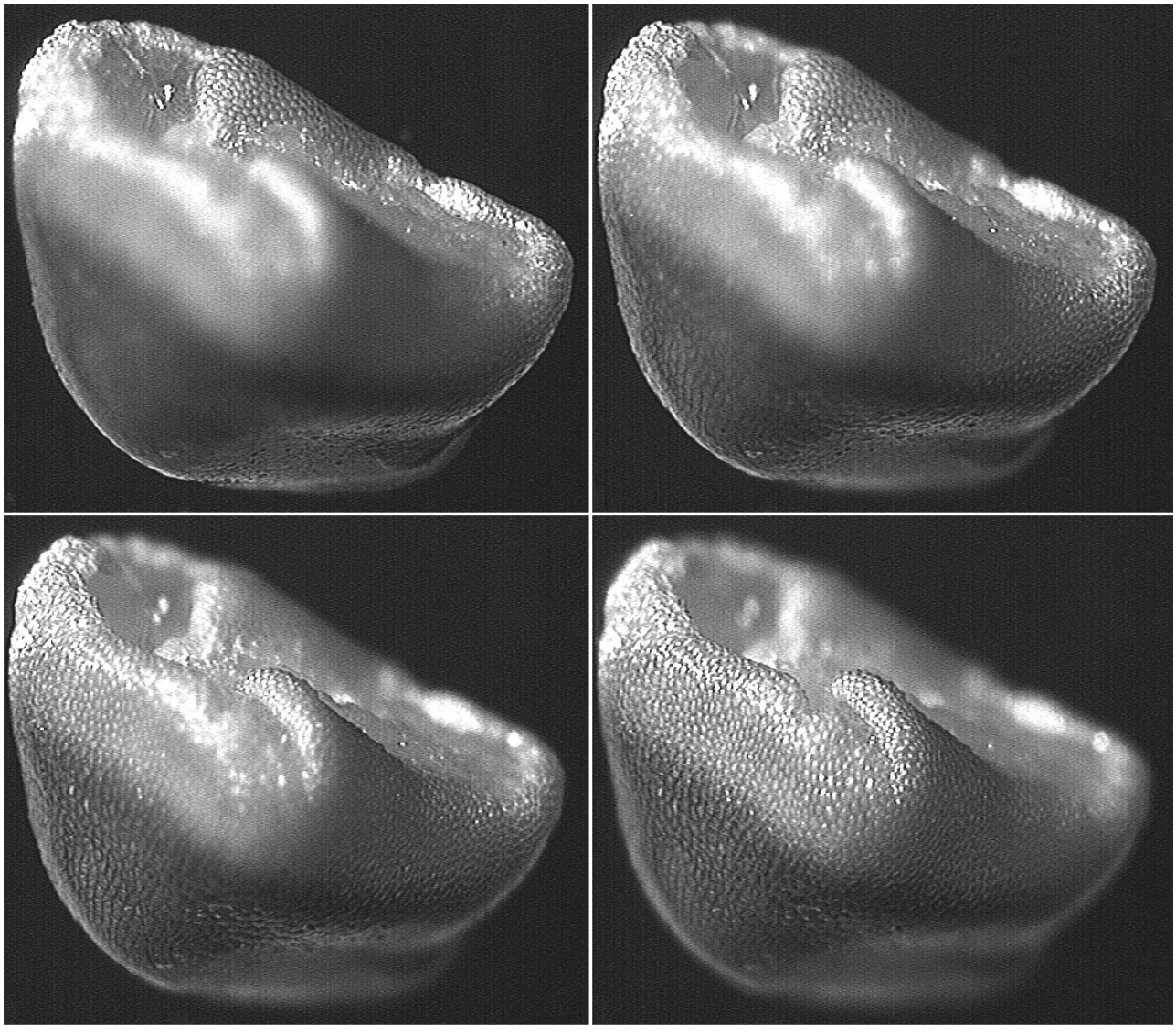

FIG. 4 Different optical cuts of the preparation.

tum Ornatum cactus seed taken at different focal planes where the focussed parts of the image are well discernible. The conclusions concerning the focalisation contour line are based on the assumption that the sharpness level and the focal plane are Euclidean planes, but this assumption is not valid.

If the point to be displayed lies outside the sharpness plane, it is displayed into its Euclidean trace, whose radius depends on the distance of the point from the plane. As the distance is increased, so is the radius. However, the dependence is not proportional. If it were possible to display Euclidean points in the plane, then every nonzero Euclidean trace would cause a defocussed image.

If the plane of a scanning device is a set of physical pixels, then the unsharpness is only demonstrated if $d(\mathscr{S}_E^P)>p$ where $p = \min\{p_x;p_y\}$. If $d(\mathscr{S}_E^P)\le p$, we can take the picture for sharp.

4.1. Definition:

Let $P \in P_3$ be a point of an objective space, $\mathscr{M}_E \subset P_3 \times \varphi$ an Euclidean scanning, $\mathcal{F}_2$ the physical plane of the focal plane φ, $p_x;p_y$ the dimension of its physical pixels, $d(\mathscr{S}_E^P)$ the diameter of the Euclidean trace of point P. We call the set ${}_{(O)}P_3 = \{P \in P_3 \mid d(\mathscr{S}_E^P) < p; p = \min\{p_x;p_y\}\}$ an open zone of sharpness. Its image ${}_{(O)}P_3'$ in the geometrical projection $\mathcal{G}:{}_{(o)}P_3 \to {}_{(O)}P_3'$ is called an optical cut.

It is evident that the result of a scanning depends not only on the preparation that is observed, but also on the microscope focalisation. The same preparation may be observed with different focalisations, that is, with different settings of the focal planes. If the number of these settings is generally n, we will get n different scannings and n different optical cuts ${}_{(O)}P_3'$ of the preparation. It is evident that it is only possible to obtain a sharp image by a single scanning, if the zone of sharpness is wider then the preparation height. If, however, it is smaller than the preparation height, part of the preparation is always out of focus (in Fig. 4. we can see different optical cuts of the *Astrophytum Ornatum* cactus seed). To construct a sharp picture in such a case, a multifocal image is required. This is a sequence of images whose zones of sharpness cover the whole preparation height.

4.2. Definition

Let $\{{}^{(k)}\mathscr{M}_E\}; k = 1,..,n$ be a sequence of Euclidean scanning of the same preparation $\mathscr{P}$, $\{{}^{(k)}_{(O)}\overline{P}^3\}; k = 1;..;n$ a sequence of its sharpness zones where $\mathscr{P} \subset \bigcup_{k=1}^{n} {}^{(k)}_{(O)}\overline{P}^3$. The sequence $\{{}^{(k)}O\}; k = 1,..,n$ of the scanning results is called a multifocal image (or, more precisely, an n-focal image).

The two-dimensional (2-D) processing of an n-focal image obviously involves constituting new image so that this new image consists of the optical cuts of the images $\{{}^{(k)}O\}; k = 1,..,n$.

5. Focussing Criteria

In the next step, we will fix criteria for assigning each pixel in the images $\{{}^{(k)}O\}; k = 1,..,n$ to an optical cut ${}_{(O)}P_3'$. Human eyes can see a part of the image sharply when the brightness of near points differs significantly. To identify the most focussed part and to construct a sharp image, it is necessary to analyse the magnitude dependent on these differences – the so-called focussing criteria. First, the focussing of a physical pixel has to be formally defined:

5.1. Theorem

Let $K_{ij} = (\mathbf{F}_{ij};r)$ be a circle in an arbitrary metric of the scanner physical plane $\mathcal{F}_2$, ${}^{(k)}P_{ij}:K_{ij} \to C_n$ a subimage of the image ${}^{(k)}O$ from the n-focal image $\{{}^{(k)}O\}$; $k = 1,..,n$, and $\mathscr{S}_{ij} = 2^{K_{ij}}$ be a set of all the subset of circle K_{ij}. Furthermore, let ${}^{(k)}C_{rs}$ be the value of the physical pixel $\mathbf{F}_{ij}$ in the image ${}^{(k)}O$ and let ${}^{(k)}C = \sum_{K_{rs}} {}^{(k)}C_{rs}$ be a sum over the values of K_{ij} in the image ${}^{(k)}O$. Let ${}^{(k)}P:\mathscr{S}_{ij}$ be a mapping, where

a) $${}^{(k)}P\left(\{\mathbf{F}_{rs}\}\right) = \frac{{}^{(k)}C_{rs}}{{}^{(k)}C}$$

b) $$A, B \in \mathscr{S}_{ij} \wedge A \cap B = \varnothing \Rightarrow {}^{(k)}P\left(\{A \cup B\}\right) = {}^{(k)}P\left(\{A\}\right) + {}^{(k)}P\left(\{B\}\right)$$

Then $(K_{ij};\mathscr{S}_{ij};{}^{(k)}P); k = 1,..,n$ are probability spaces and the mappings ${}^{(k)}X:K_{ij}\to\mathbf{R}$: ${}^{(k)}X\left(\{F_{rs}\}\right) = \frac{{}^{(k)}C_{rs}}{{}^{(k)}C}$ are discrete integrable random variables.

5.2. Definition

The mappings ${}^{(k)}X:K_{ij} \to \mathbf{R}$; $k=1,2,..,n$ in the previous theorem are called the focussings of the physical pixel $\mathbf{F}_{ij}$ in the image ${}^{(k)}O$.

Variation span, variance, high spatial frequency amount in the sense of the Fourier transformation can all be used as focussing criteria.

The mean values of the defined focussings are $E({}^{(k)}X) = \sum_{K_{ij}} \frac{{}^{(k)}C_{rs}}{{}^{(k)}C}$ and the value range is

$$v\left({}^{(k)}X\right) = \frac{1}{{}^{(k)}C}\left(\max_{\mathbf{F}_{rs}\in K_{ij}}\left\{{}^{(k)}C_{rs}\right\} - \min_{\mathbf{F}_{rs}\in K_{ij}}\left\{{}^{(k)}C_{rs}\right\}\right) \quad (1)$$

The mappings ${}^{(k)}Y = ({}^{(k)}X - E({}^{(k)}X))^2 : K_{ij}\to\mathbf{R}$, where

$${}^{(k)}Y\left(\mathbf{F}_{rs}\right) = \left(\frac{{}^{(k)}C_{rs}}{{}^{(k)}C} - \sum_{K_{ij}} \frac{{}^{(k)}C_{rs}}{{}^{(k)}C}\right)^2; k = 1,2,..,n,$$

are also discrete integrable random variables, and

$$D\left({}^{(k)}X\right)=\frac{1}{{}^{(k)}C}\sum_{K_y}\left(\frac{{}^{(k)}C_{rs}}{{}^{(k)}C}-\sum_{K_{ij}}\frac{{}^{(k)}C_{rs}}{{}^{(k)}C}\right)^2 \qquad (2)$$

are dispersions of random variables ${}^{(k)}X$ defined on circle K_{ij} in the scanner physical plane $\mathcal{F}_2$.

To construct the last criterion, we use a Fourier transform. If $\mathcal{D}: \{{}^{(k)}C_{rs}\} \rightarrow \{{}^{(k)}X_{mn}\}$ is a discrete Fourier transform where ${}^{(k)}C_{rs}$ is the value of the processed pixel $\mathbf{F}_{ij}$ in image k, ${}^{(k)}X_{mn} = {}^{(k)}U_{mn} + i^{(k)}V_{mn}$; $m,n = 0,1,..,2\varepsilon$, then the expressions $\left|{}^{(k)}X_{mn}\right| = \sqrt{{}^{(k)}U_{mn}^2 + {}^{(k)}V_{mn}^2}$ determine the amplitudes of the spatial frequencies that exist in the neighbourhood K_{ij} of the physical pixels $\mathbf{F}_{ij}$ in the particular images ${}^{(k)}O$, $k = 1,2,..,n$. Higher values of indices m,n mean higher spatial frequencies, which indicate a higher contrast of small details in the surveyed surrounding and thus also a better focussing. Therefore, as a focussing criterion, the expression containing the frequency $|{}^{(k)}X_{mn}|$ may be used, that assigns higher weight to higher indicies m,n. To identify the sharpness zone, we particularly used the expression

$${}^{(k)}T(X_{mn})=\sum_{m=0}^{H}\sum_{n=0}^{H}(m+n)\sqrt{{}^{(k)}U_{mn}^2+{}^{(k)}V_{mn}^2}; H \le \varepsilon \qquad (3)$$

I call this expression a frequency criterion.

The maxima of the Eqs. (1), (2), and (3), called a variation, dispersal, and frequency criterion, respectively, detect the pixels focussed at a maximum very well and thus may be used to compose a sharp picture.

Fig. 5a shows the sharpness zones detected by Eq. (1) for a multifocal image composed of four images (the first and the fourth can be seen in Fig. 4). A sharp image is constructed in 5b.

6. Logical Pixels, Mapping

A physical pixel can be thought of as the smallest object distinguished by the given equipment. The set of all the physical pixels is called a physical plane.

6.1. Definition

Let $\mathcal{G}_2$ be a graphic plane. The factor set $\mathcal{F}_2 = \mathcal{G}_2/\rho$ where the relation ρ is defined as $\rho(A,B) \Leftrightarrow (\exists F_{ij} \in \mathcal{F}_2)$ $\lfloor A \in F_{ij}\, B \in F_{ij} \rfloor$ is called the physical plane of $\mathcal{G}_2$.

In many graphical applications, a so-called logical plane and logical pixels have to be used. Sometimes it is important to which (Euclidean) point of the physical pixel we refer — its centre, vertex, and so forth. Thus, by a logical pixel L_{ij} we mean a representative of the physical pixel $\mathbf{F}_{ij}$, the logical plane $\mathcal{L}$ being the set of all the logical pixels $\mathcal{L}$:

6.2. Definition

Let $\mathcal{G}_2$ be a graphical plane, $\mathcal{F}_2$ its physical plane, p_x or p_y the dimensions of its physical pixels F_{ij} respectively. Let

$$\text{for } c \in \langle 0;1)\ {}_cW = \left\{r_i \in \mathbf{R} \middle| \forall i \in \{0,1,...,w-1\} : r_i \in \langle i; i+1) \wedge r_i - k = c\right\} \text{ and}$$

$$\text{for } d \in \langle 0;1)\ {}_dH = \left\{s_j \in \mathbf{R} \middle| \forall j \in \{0,1,...,h-1\} : s_j \in \langle j; j+1) \wedge s_j - k = d\right\},$$

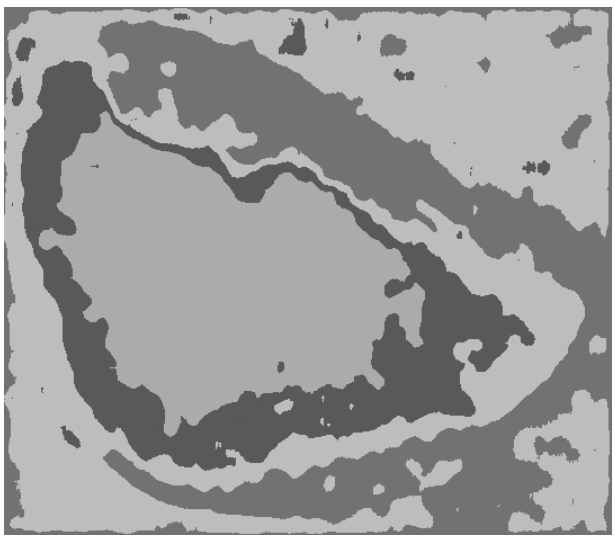

(a)

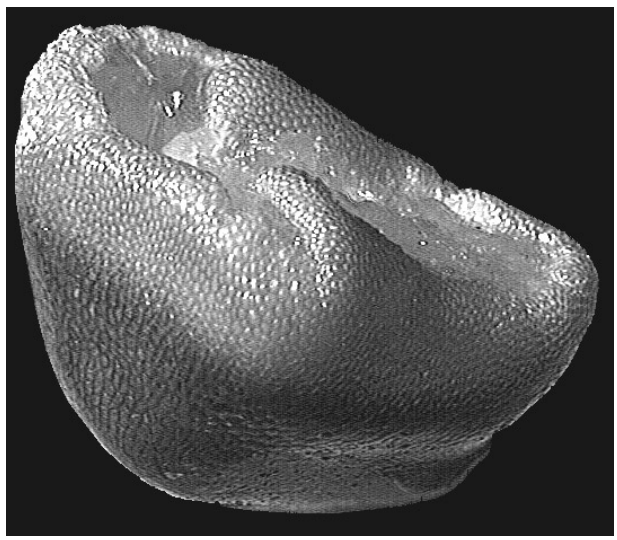

(b)

FIG. 5 Optical cuts detected by the Eq. (1) and focussed image constructed from the optical cuts.

and $P = [c,d]$. Then the set ${}_p\mathcal{L} = {}_cW \times {}_dH$ is called a logical plane, the ordered pair $(w;h)$ its resolution, and its elements logical pixels.

The below theorem follows directly from definitions 6.1. and 6.2.:

6.3. Theorem

Let $\mathcal{F}_2$ be the physical plane of the graphical plane $\mathcal{G}_2$, ${}_p\mathcal{L}_2$ any logical plane of the same graphical plane, ${}_p\varphi: \mathcal{F}_2 \to {}_p\mathcal{L}_2$ a mapping where, for all $i = 0,1,..,m-1$, $j = 0,1,..,n-1$, ${}_p\varphi(F_{i,j}) = {}_pL_{i,j} \Leftrightarrow {}_pL_{i,j} \in F_{i,j}$. Then the mapping ${}_p\varphi$ is a bijection (one-to-one and onto mapping).

6.4. Definition

The mapping ${}_p\varphi: \mathcal{F}_2 \to {}_p\mathcal{L}_2$ in the previous theorem is called a mapping of the physical plane. The mapping from Def. 6.4 is illustrated in Fig. 6.

It is evident that, for each physical plane, an infinite number of logical planes exist since a logical plane ${}_p\mathcal{L}_2$ may be constructed for any $P = [c,d] \in \langle x_0;x_1) \times \langle y_0;y_1)$. Every physical plane can be mapped in an infinite number of ways. In the sequel, I will only use the two most important mappings.

6.5. Definition

The mapping ${}_v\varphi: \mathcal{F}_2 \to {}_v\mathcal{L}_2$, where $V = [x_0;y_0]$, is called a vertex mapping. The mapping ${}_s\varphi: \mathcal{F}_2 \to {}_s\mathcal{L}_2$, where

$$S = \left[\tfrac{1}{2}(x_0 + x_1); \tfrac{1}{2}(y_0 + y_1)\right],$$

is called a centre mapping.

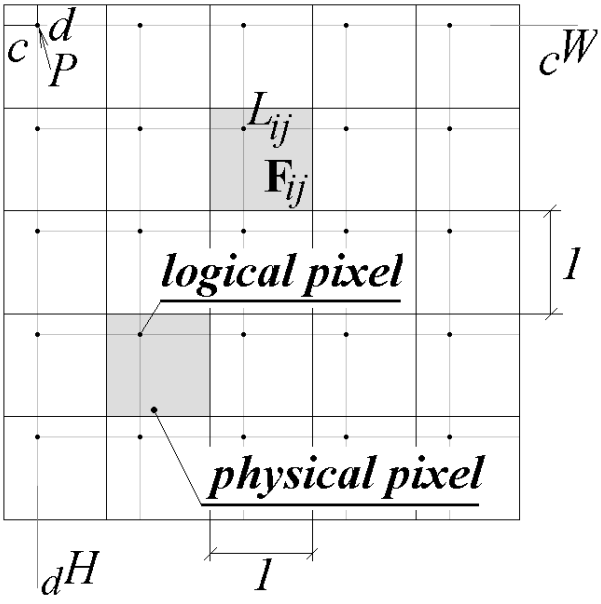

FIG. 6 Mapping of the physical plane.

In this paper we will only concern ourselves with the construction of objects whose surface can be thought of as the graph of a function of two variables $z = f(x;y)$ defined on a rectangle $\langle x_1;x_2\rangle \times \langle y_1;y_2\rangle$. Any computer output device is a physical plane with a finite number of physical pixels. Therefore, it is not possible to construct on it a function continuous in terms of the ordinary definition. Regarding its construction on a computer, any definition of the above-mentioned continuous function is equivalent to assigning values to the logical or physical pixels of the function's domain. This raises the question of how such a function can be constructed.

Two possibilities exist:

1. *The definition set can be thought of as a not mapped physical plane.* If the definition set is a rectangle $\langle x_1;x_2\rangle \times \langle y_1;y_2\rangle \in \mathbf{R}^2$, it is possible to construct equidistant divisions $D_x = \{x_i\}_{i=0}^m$; $m>1$, $D_y = \{y_i\}_{i=0}^n$; $n>1$ of intervals $\langle x_1;x_2\rangle$, $\langle y_1;y_2\rangle$ and thereby a graphic plane and its physical plane as well. To the whole of a physical pixel we assign a constant value, and a 3-D object is composed of blocks (or of theirs surfaces) whose bases are the physical pixels and heights are their values.

It is relatively easy to construct such a surface, but it involves many disadvantages. If the value of a pixel, however, is taken for its height, then the graph of the function $z = f(x,y)$ is modelled as a 3-D surface. This "physical function," however, is not suitable for 3-D reconstructions because with only three normals existing, the figure after shading gives a very unnatural impression (see Fig. 7).

2. The definition set is equipped with a suitable mapping: In this case, the surface is constructed by interpolating the graph of a function in two variables where the function values are known at equidistant points (see Fig. 8). The shading value of a 2-D plane segment is given by the cosine of the angle at which the segment's normal intersects the incident light, which is constant for a 2-D segment. However, if we really paint the whole constructed plane segment with the same colour (the so-called constant shading), the segment edges become visible to the naked eye over all the

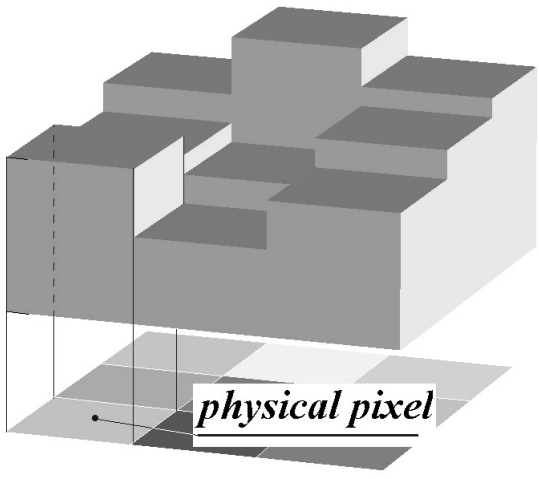

FIG. 7 The definition set of a function as not mapping physical plane.

originally smooth surface, which, improperly, stresses the fact that the constructed segment assumed to be smooth is, in fact, an interpolation (sometimes a very coarse one). This unpleasant effect can be improved by interpolating either the colour or the normal.

8. Spatial Reconstruction by the Method of Constant High Cuts and Filtered Cuts

Let ${}^{(k)}O$; $k = 1,..,n$ be a particular image of the multifocal image O, $\mathbf{F}_{ij}$ its physical pixel, ${}^{(0)}O$ the image, which is ${}^{(0)}O(\mathbf{F}_{ij}) = k$. From the way a multifocal picture is generated, it is evident that, if ${}^{(0)}O(\mathbf{F}_{ij}) = k$, then the physical pixel $\mathbf{F}_{ij}$ contains information about the point P of the preparation for which $P \in {}^{(k)}P$; $k = 1,..,n$. If the zones ${}^{(k)}P$; $k = 1,..,n$ are mutually disjointed, each point in the zone ${}^{(k)}P$ can be assigned an identical height. Thus, we obtain a function of two variables whose graph approximately matches the observed preparation. If we denote by v the total height of the preparation, then the zone sharpness height of a n-focal picture is $\frac{v}{n}$. For the function $f(i,j)$, which approximately describes the observed preparation, we have $f(i,j) = \frac{1}{n}{}^{(0)}O(\mathbf{F}_{ij})$. This method is called the method of constant height cuts (see Fig 9b).

Furthermore, I generalised the notion of linear filters known from image processing. These filters can be used for the construction of the above-mentioned function. A function filtered in this way approximate an observed preparation essentially better. This construction method is called the method of filtered cuts. In Figure 9a, we can see a spatial reconstruction that uses a low-pass filter.

9. Spatial Reconstruction by the Method of Direct Height Determination

In the above, we used the focussing criteria as a quality characteristic. We determined the pixel altitude according to the maximum of the focussing criterion. In this way we can only obtain n levels from n focal images. However, the radius of the Euclidean trace and wave trace of the point depend on the distance of this point from the sharpness plane. The radius of these traces increases with the distance from the sharpness plane but this dependence is nonlinear. The focussing criteria parameters are changed according to this. Analysing the focussing criteria parameters for all the particular images we can determine this distance for each pixel more exactly than in the previous chapter. In this way, it is possible to obtain a 3-D object profile very easily.

Let $\mathcal{G}$: $P_3 \to P_3'$ be a geometric projection where $P \in \omega \Rightarrow \mathcal{G}(P) = P' \in \varphi_2$; $Q \notin \omega \Rightarrow \mathcal{G}(Q) = Q' \notin \varphi_2$. For the Euclidean traces $\mathcal{S}_E^P$; $\mathcal{S}_E^Q$ of the points $P \in \omega$; $Q \notin \omega$, we have the following implication: if $\mathcal{S}_E^P = \{P'\}$, then $d(\mathcal{S}_E^P) = 0$; $d(\mathcal{S}_E^Q) > 0$. Let ${}^{(k)}X{:}F_y \to \mathbf{R}$; $k = 1,..,n$ be a focussing of the image ${}^{(k)}O$ from the multifocal image O, $v({}^{(k)}X)$, $D({}^{(k)}X)$, $T({}^{(k)}X)$ the values of the variation, dispersal and frequency criteria on the same image ${}^{(k)}O$, respectively. We introduce the following denotations:

$$v\left({}^{\max}X\right) = \max\left\{v\left({}^{(k)}X\right);{}^{(k)}O \in O\right\};$$
$$D\left({}^{\max}X\right) = \max\left\{D\left({}^{(k)}X\right);{}^{(k)}O \in O\right\};$$
$$T\left({}^{\max}X\right) = \max\left\{T\left({}^{(k)}X\right);{}^{(k)}O \in O\right\}.$$

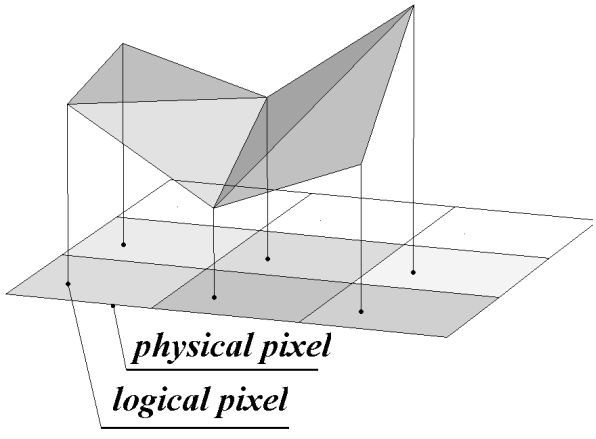

FIG. 8 Mapping of the physical plane.

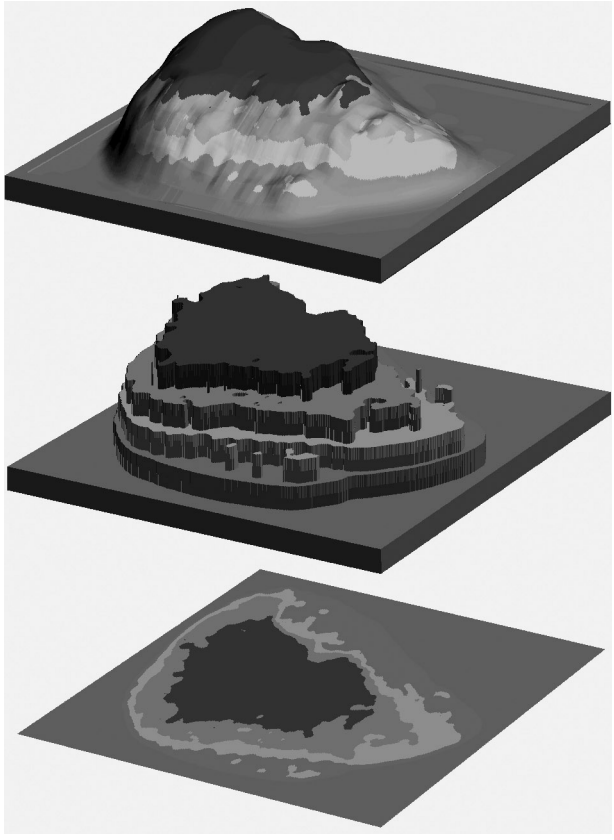

FIG. 9 Method of constant height cuts and fitered cuts.

When using the method of direct height determination, we assume that the values of the focussing criteria depend on the average the Euclidean trace $d({}^{(k)}\mathcal{S}_E^Q)$ of the point Q in the Euclidean scanning ${}^{(k)}\mathcal{M}_E$ or on the length ${}^{(k)}\ell$ represents this average. This means that there exist functions $v({}^{(k)}X) = f_v({}^{(k)}\ell)$, $D({}^{(k)}X) = f_D({}^{(k)}\ell)$, $T({}^{(k)}X) = f_T({}^{(k)}\ell)$ and their inverses $f_v^{-1}, f_D^{-1}, f_T^{-1}$. These inverse functions determine the diameter of the Euclidean trace using the focusing criteria values:

$$
\begin{aligned}
{}^{(k)}\ell = f_v^{-1} = c \cdot \frac{v\left({}^{\max}X\right)}{v\left({}^{(k)}X\right)} \; {}^{(k)}\ell = f_D^{-1} \\
= c \cdot \frac{D\left({}^{\max}X\right)}{D\left({}^{(k)}X\right)} \; {}^{(k)}\ell = f_T^{-1} = c \cdot \frac{T\left({}^{\max}X\right)}{T\left({}^{(k)}X\right)}
\end{aligned}
\tag{4}
$$

Next we have derived the dependence of the diameter d of the Euclidean trace $\mathcal{S}_E^Q$ of the point $Q \notin \omega$ on its distance h from the sharpness plane. From Figure 10 we obtain:

$$
\Delta P' F_2 F_1' \sim \Delta P_x H_1 F_1' \Rightarrow \frac{s}{f} = \frac{s'}{\Delta} \Rightarrow s = \frac{s'f}{\Delta} \tag{5}
$$

$$
\Delta Q_\varphi F_2 H_1 \sim \Delta H_1 P_x Q \Rightarrow \frac{\Delta + f}{s'} = \frac{\delta + f + h}{s} \tag{6}
$$

$$
\Delta P' F_2 H_1 \sim \Delta H_1 P_x P \Rightarrow \frac{\Delta + f}{s' + \ell} = \frac{\delta + f}{s} \tag{7}
$$

After some simplifications of Eq. (5) and after substituting from Eqs. (7) and (5), we obtain:

$$
\frac{\Delta + f}{s'} = \frac{\delta + f}{s} = \frac{h}{s} \overset{(7)}{\Rightarrow} \quad \frac{\Delta + f}{s'} = \frac{\Delta + f}{s' + \ell} + \frac{h}{s} \overset{(5)}{\Rightarrow}
$$

$$
\frac{\Delta + f}{s'} = \frac{\Delta + f}{s' + \ell} + \frac{h\Delta}{s'f}
$$

Calculating h from the last equation, we have

$$
h = \frac{\ell \, f(\Delta + f)}{\Delta(s' + \ell)}
$$

In the event that the main plane distance χ_1 to point Q is smaller than the distance from the sharpness plane, we proceed in an analogous manner to obtain the same result.

Using this expression together with Eq. (4), we can directly determine the distance of a given pixel from the sharpness plane, which yields a 3-D reconstruction of the preparation.

10. Results and Applications

We have written a program based on the above theory. It can process partially focussed images (optical cuts) and makes 2-D reconstructions (focussing) as well as 3-D reconstructions (spatial modelling). The input data can produced by any device with a very small sharpness zone (conventional microscope, CCD camera, etc). This program does not require much in the way of hardware. As a minimum, an IBM-compatible PC (IBM, White Plains, M.d., USA), with a 433 MHz processor and 64 MB RAM is recommended. It runs on lower-level PC models as well, but the run time may be too long. The run time depends on the number of the optical cuts processed, their resolution, the criterion chosen, and the processing parameters. For instance, if we process four optical cuts with a resolution of (500,435), we use a variation criterion with $\varepsilon = 4$ and the method of direct height determination, the run time of different computers is shown in Table I:

The following figures depict 3-D output data from this program. Figure 11 shows a reconstruction of an *Astrophytum Ornatum* cactus seed with four optical cuts (the processing time of this operation can be seen in Table I. A Meopta Meogon 5.6/60 mm lens was used to take the images (Meopta, Prerov, Czech Republic).

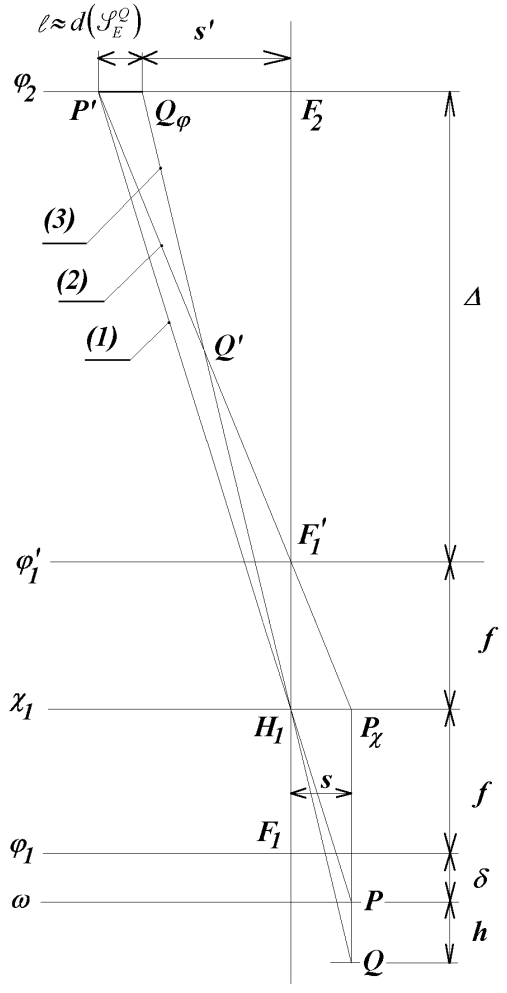

FIG. 10 Principle of spatial reconstruction by method of direct height diagnosis.

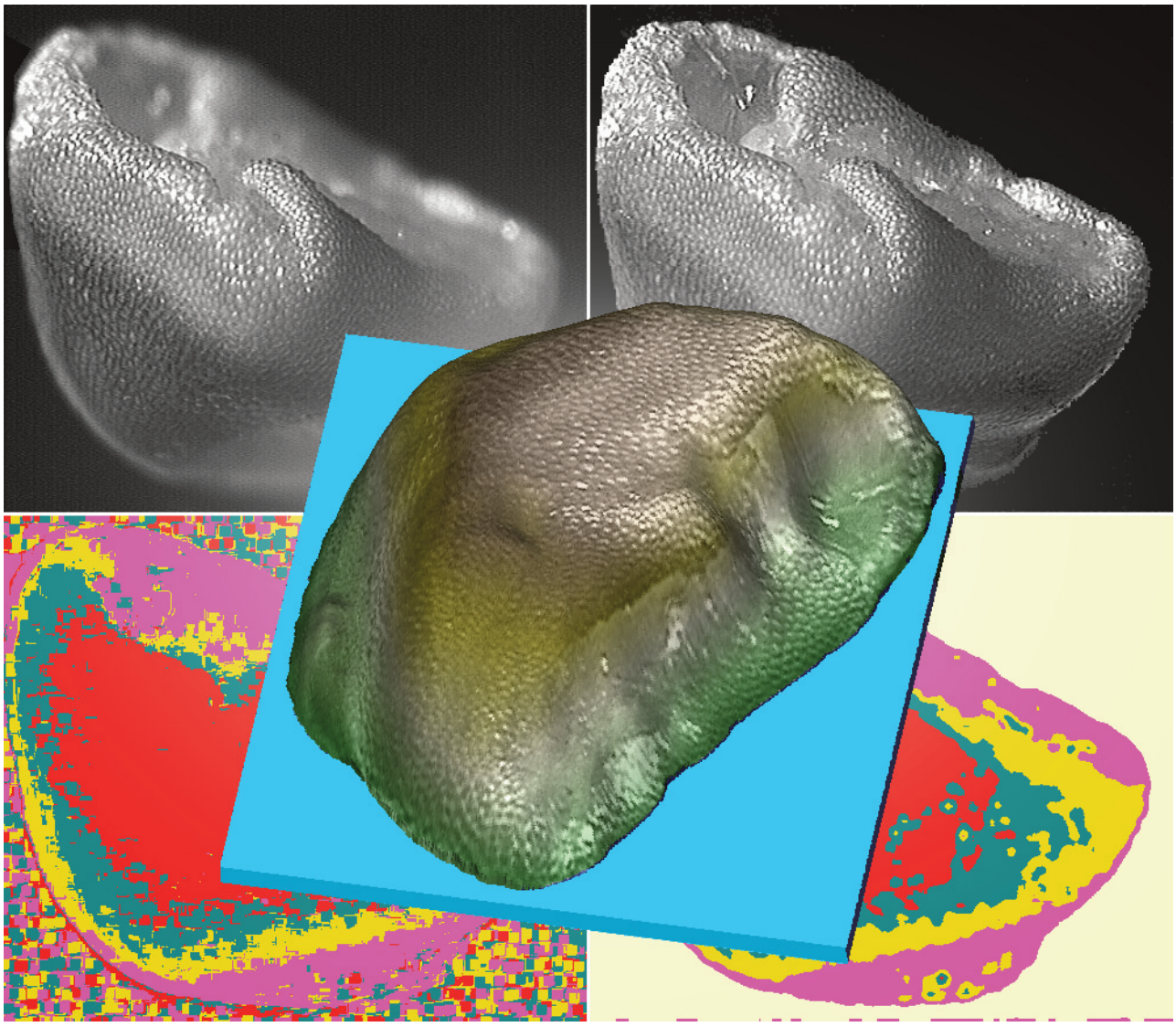

FIG. 11 Three-dimensional reconstruction of *Astrophytum Ornatum* cactus seed by method of direct height determination.

In Figure 12, we can see some of the input data on a lava fragment (data—CCD Camera Olympus DP 10, in complete eight images (Olympus America, Inc., Melville, N.Y., USA) and its 3-D reconstruction. In Figure 13a, a 3-D reconstruction is seen that uses the method of direct height determination at viewing angles of 30° and 40°. Reference microphotograph of this fragment is shown in Figure 13b at the same angles (the original fragment size is about 5 mm).

In Figure 14 we can see the input data of *Drosophila* fly (in complete eight images) (a) and a 2-D reconstruction (b). The frequency criterion was used in this construction. Figure 15 shows the 3-D output produced by our program. Figures 16 and 17 show the input data of a copper sulphate crystal (in complete 10 images) and the results of their 2-D and 3-D processing (the result is obtained by the dispersion criterion).

TABLE I The reconstruction run time at different computers

IBM PC compatible	2-D reconstruction	3-D reconstruction	full time
proc. 100 MHz, 32 MB RAM	12 min	29 min	41 min
proc. 433 MHz 64 MB RAM	1 min 15 sec	3 min 10 sec	4 min 25 sec
proc. 999 MHz 128 MB RAM	19 sec	74 sec	93 sec

Program requires about 150MB disk space per runtime. A demo-version is available at http://www.martisek.webzdarma.cz.

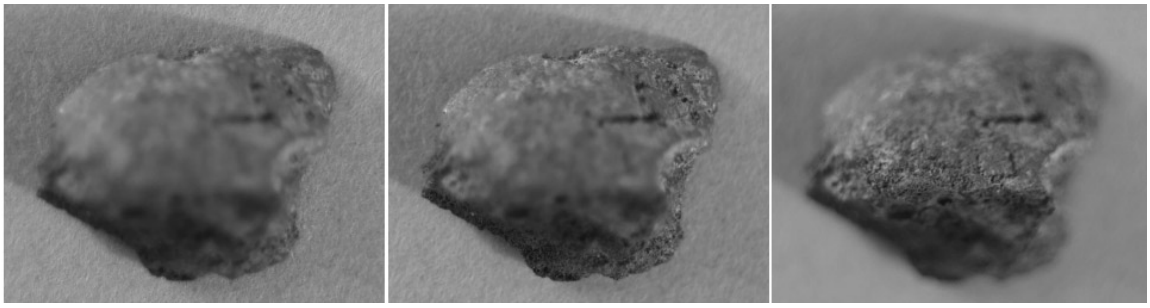

FIG. 12 Input data for three-dimensional reconstruction of the lava fragment

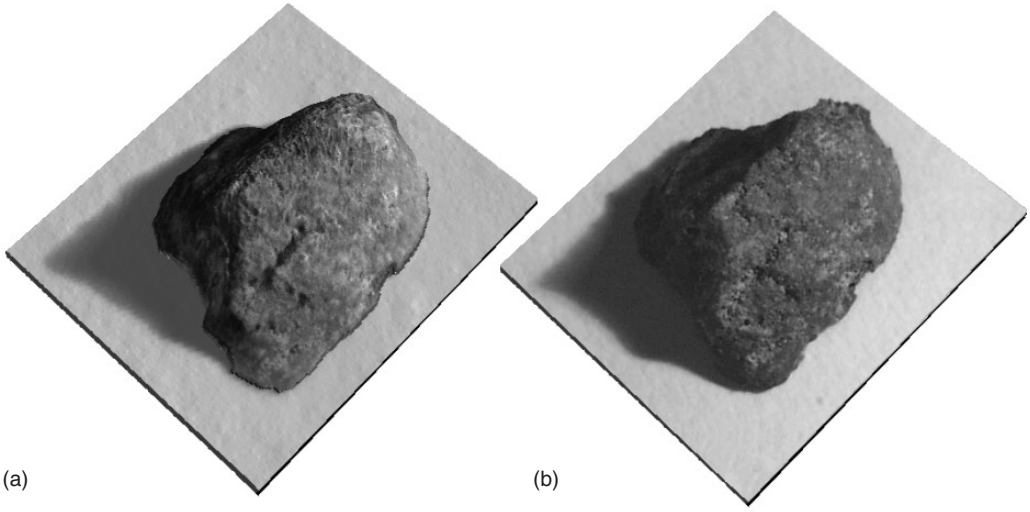

FIG. 13 3-D reconstruction and 3-D photo of the lava fragment

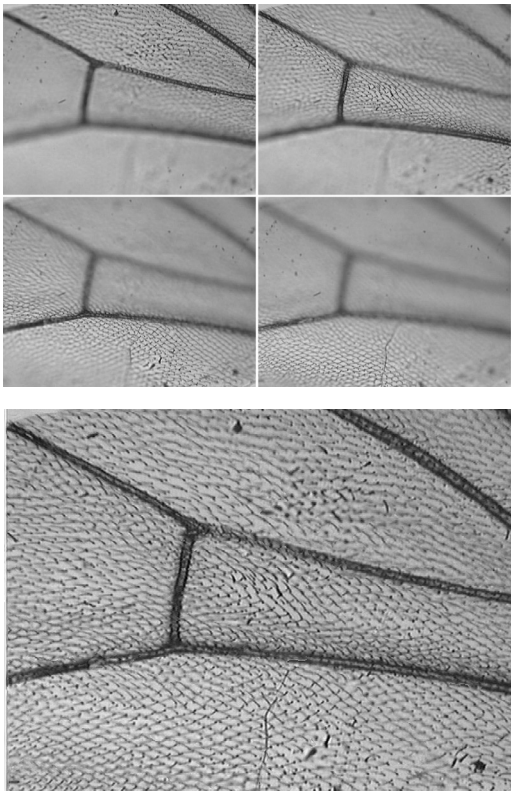

FIG. 14 Input data and sharp image of *Drosophila* fly.

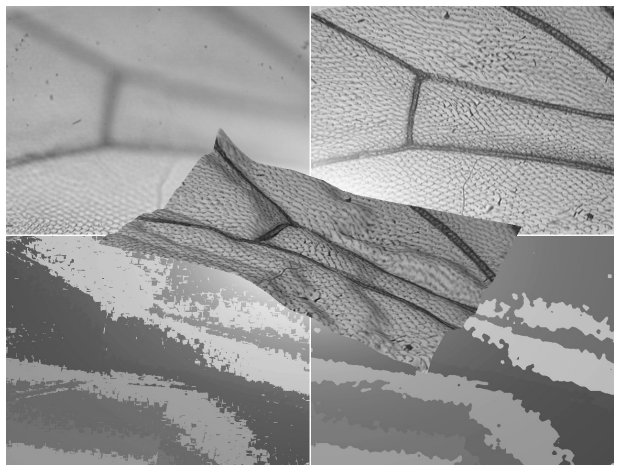

FIG. 15 Three-dimensional output of *Drosophila* fly.

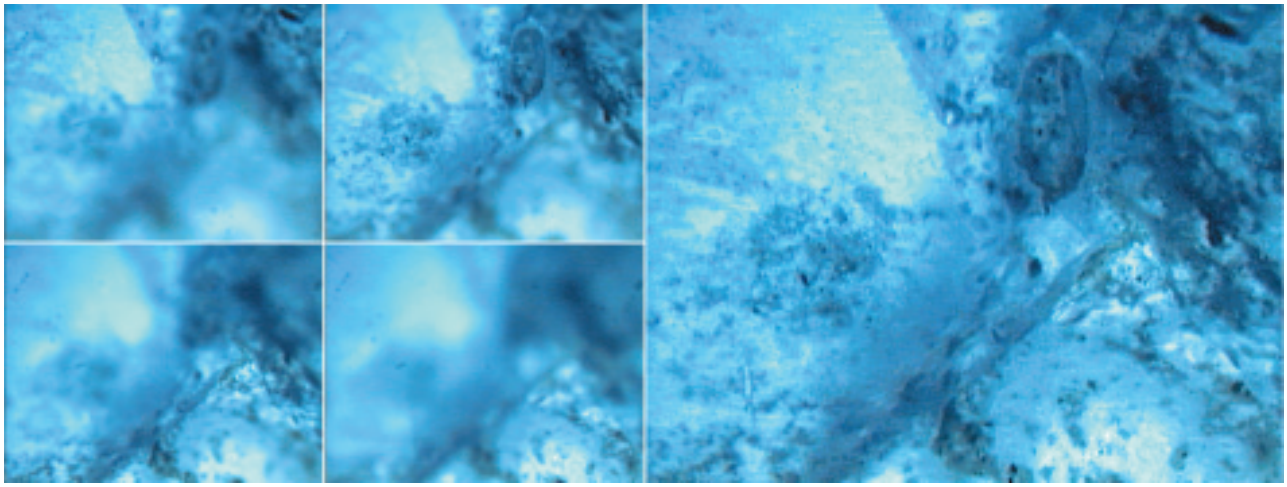

FIG. 16 Input data and sharp image of a copper sulphate crystal.

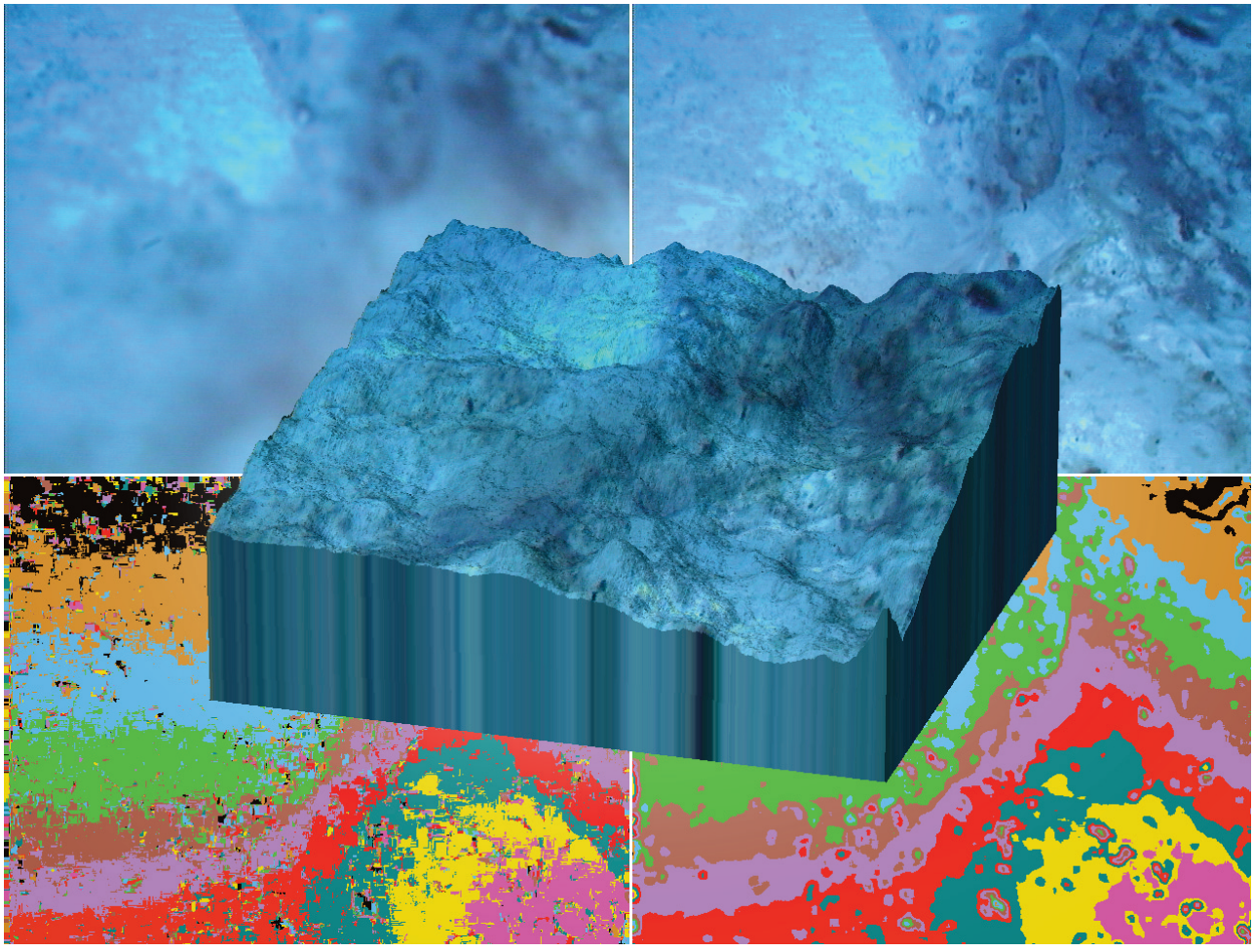

FIG. 17 Three-dimensional output of the copper sulphate crystal.

Acknowledgements

The input data produced by Mr Miloslav Druckmüller and Mr Pavel Štarha were used in this paper. The author thanks them very much for their cooperation.

References

Benson KB: *Television Engineering Handbook,* 2nd Ed. New York (1986)

Druckmüller M, Štarha P: ACC 4.0 Scientific object structure and object analyser, *SOFO Brno*, 1–103 (2000)

Druckmüller M, Heriban P: Scientific Image Analyser DIPS 5.0. *SOFO Brno,* 1–266 (1996)

Foley JD, van Dam A, Feiner SK, Hughes JF: *Computer Graphics: Principles and Practice*, 2nd Ed. Addison-Wesley, Reading, MA (1990)

Galbraith W: Letters to the Editors, Rebuttal on novel method for stereo imaging in light microscopy at high magnifications by Greenberg G. and Boyde A. *Neuroimage* 2, 85–87 (1995)

Geldziler B, Hewitt CW, Doolin EJ, Pro E: Depth of field of mycology specimens using high definition 3-D microscopy employing multiple oblique illumination. (abstr.) *Amer Soc Microbiol,* 270 (1998)

Geldziler B, Ramsamooj R, Catalano E, Doolin EJ, Hewitt CW: Novel high definition 3-D microscopy for evaluating cytopathology and pap smear specimens: 3-D digital image reconstruction and analysis of cell clusters. (abstr.) *Acta Cytologica*, 42(5), 1299 (1998)

Geldziler B, Ramsamooj R, Greenberg G, Doolin EJ, Hewitt CW: Use of 3-D microscopy with multiple oblique illumination in evaluating cytopathology preparations. (abstr.) *Analytical Quantitative Cytol Histol* 193 (1998)

Greenberg G: Direct 3-D imaging using a multiple oblique microscope. *Scanning* 16, 248–249 (1994)

Greenberg G, Boyde A: Convenient and controllable direct-view 3-D imaging in conventional light microscopes: Approaches via illumination and inspection. *Proc RMS* 32/2, 87–101 (1997)

Greenberg G and Boyde A: Direct-view 3-D microscopy using conventional lenses. *Microsco Anal* 22:7–9 (1997)

Hewitt CW: Evaluation of various conventionally and immunostained specimens by novel high definition 3-D microscopy. (abstr.) *Proc Joint Meeting Histochem Soc and Japan Soci Histochem and Cytochem* A6 (1998)

Hewitt CW, Goodman M, Tarnoff M, Doolin EJ: Mathematical evaluation of high definition 3-D microscopy using digital imaging. (abstr.) FASEB Journal, Vol. 11(3), A636 (1997)

Hewitt CW, Geldziler B, Ramsamooj R, Greenberg G, Doolin EJ: *High definition Microscopy Based on Multiple Oblique Illumination for Cytopathology and Pap Smear Analysis: Evaluation of 3-D Digital Image Reconstruction and Analysis.* A communication: 11th International Congress on Diagnostic Quantitative Pathology. Sierra ñ Italy (1997)

Hewitt CW, Salartash K, Dalsey RM, DeLong WG: Cellular changes in the joints of composite tissue allograft recipients analyzed by computerized digital image processing and a 3-D microscope. (abstr.) *FASEB J*, 9(3), A434 (1995)

Netravali AN, Haskel BG: *Digital Pictures Representation and Compression*. Plenum Press, New York, NY (1988)

Roger DF, Adams JA: *Mathematical Elements for Computer Graphics*, New York (1985)

Seyedolali A, Torley RF, Krinsley D, Boggs S Jr: Three-dimensional, high-resolution light microscopy—a new geological tool. *J Geolog Ed* 42, 5, 476–480 (1994)

Watt A: *Fundamentals of Three-Dimensional Computer Graphics*, Addison Wesley, Reading, MA (1989)

Realizovaný grafický návrh

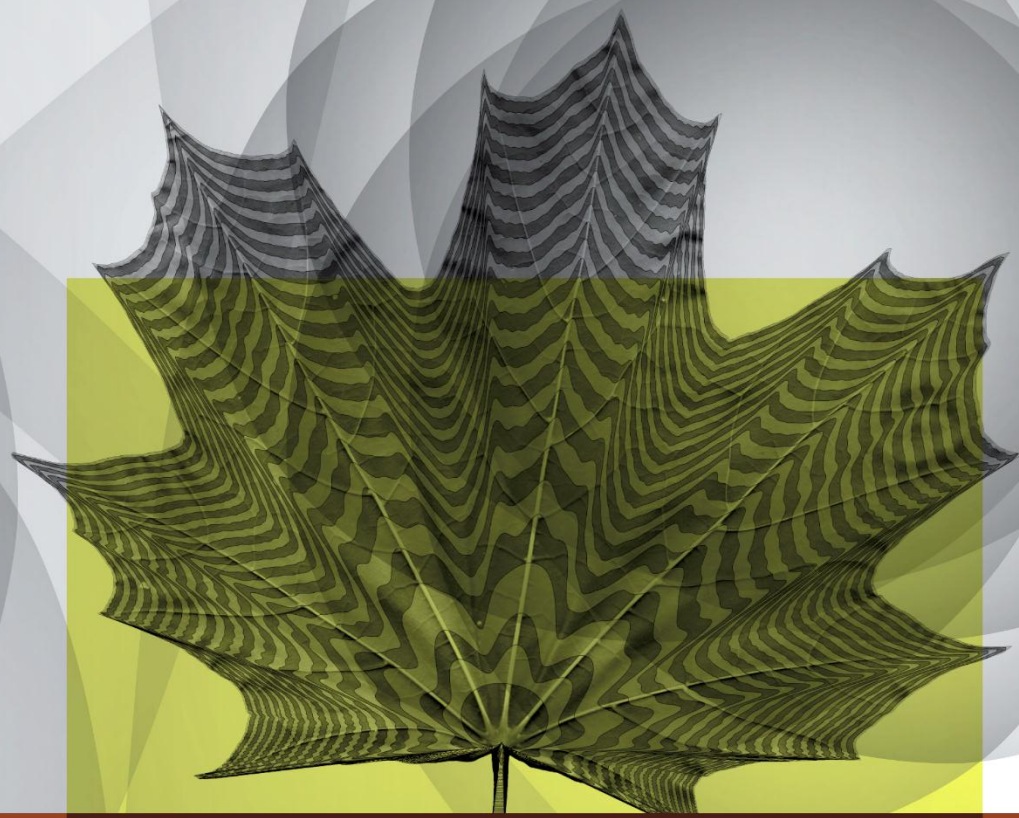

01

Úvod do matematického modelování s využitím Maple

Jiří Hřebíček
Zdeněk Pospíšil
Jaroslav Urbánek

INVESTICE DO ROZVOJE VZDĚLÁVÁNÍ

Úvod do matematického modelování s využitím Maple 2010

ISBN 978-80-7204-691-1

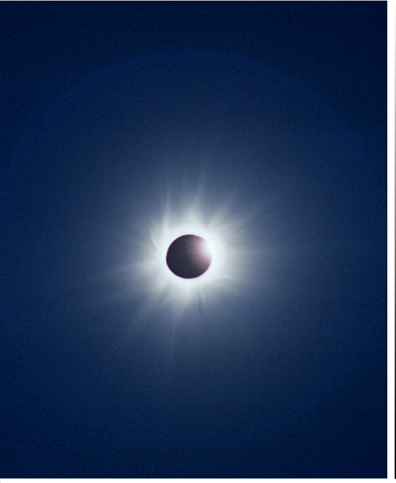
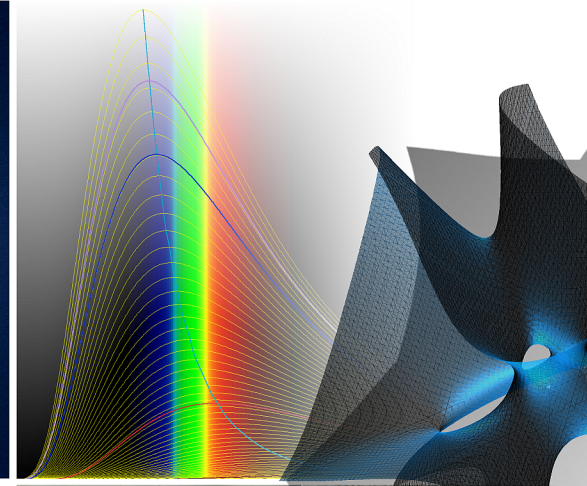
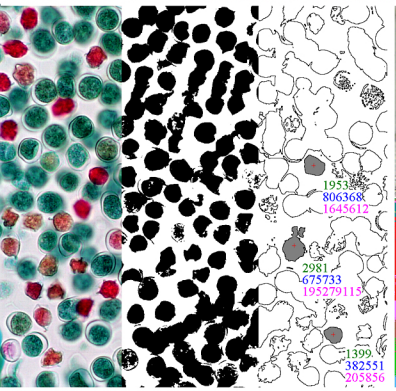
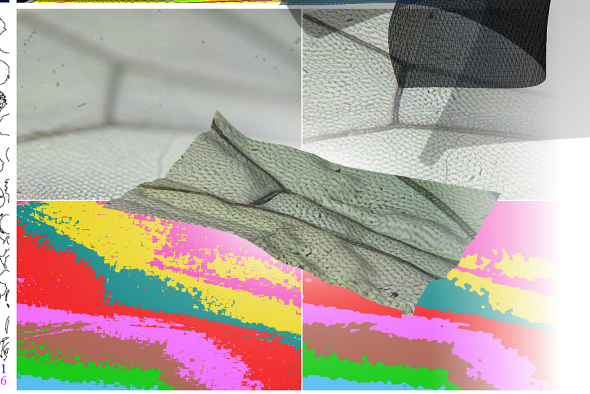
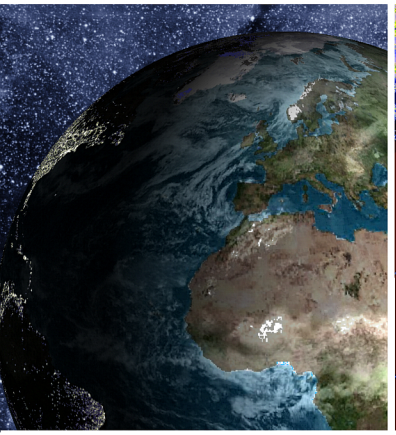
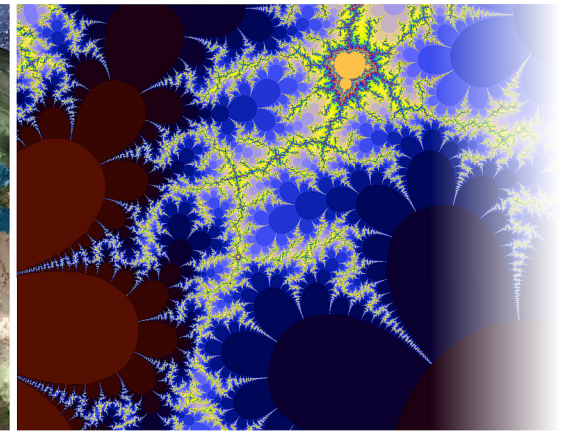
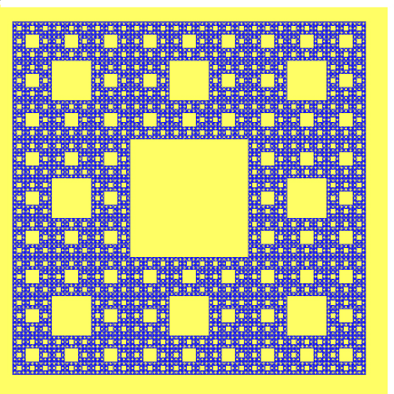
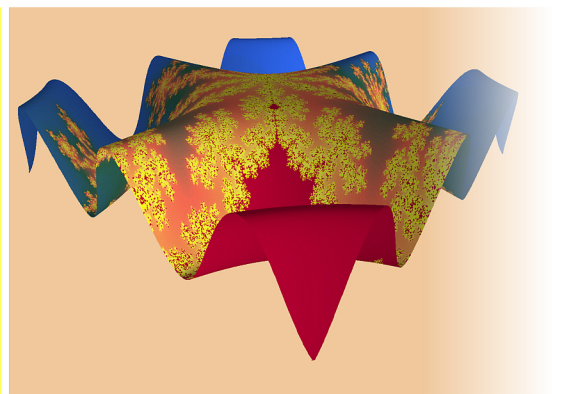

Kam po maturitě?

Váháte mezi studiem matematiky a některého technického oboru ?

Ústav matematiky FSI VUT v Brně Vám nabízí

Matematické inženýrství

progresivní formu studia matematiky

www.mat.fme.vutbr.cz

Stupně studia:

tříleté základní bakalářské (titul Bc.)
dvouleté navazující magisterské (titul Ing.)
dvouleté navazující doktorandské (titul Ph.D.)

Náplň studia:

matematická analýza, algebra, konstruktivní a počítačová geometrie
diferenciální rovnice, funkcionální analýza, pravděpodobnost a matematická statistika
diskrétní matematika, numerické metody, optimalizace
moderní metody programování, počítačová grafika, analýza obrazu, vizualizace dat
základy fyziky, statika, termomechanika, hydromechanika, elektrotechnika a elektronika
základy konstruování, nauka o materiálu, pružnost a pevnost, části a mechanismy strojů
každý semestr bohatá nabídka volitelných a nepovinných předmětů
možnost zahraničních stáží (USA, Norsko, Švédsko, Francie, Německo, Rakousko, Itálie...)
na třetím stupni vědecká práce pod vedením zkušených odborníků

Uplatnění absolventů:

Absolventi jsou erudovanými techniky s hlubokým teoretickým vzděláním. Mají přehled ve všech nosných disciplínách strojního inženýrství a uplatňují se v tvůrčích týmech inženýrských specializací. Matematické modely lze aplikovat v řadě dalších odvětví (fyzika, biologie, lékařství...). Výhodou je dobrá orientace v nejmodernějších výpočetních technologiích. Vzhledem k matematickému vzdělání se lze uplatnit i ve vědeckých týmech, softwarových firmách, ekonomice, bankovnictví...

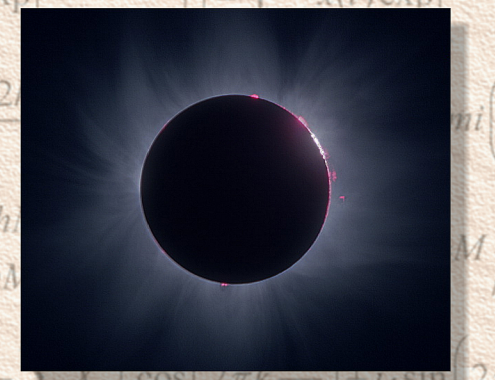

Když Slunce nesvítí

Nezalévejte vodou, ale geometrii

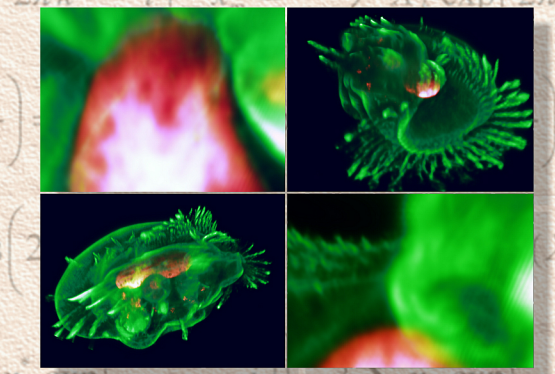

Buňkám vidíme až do „žaludku"

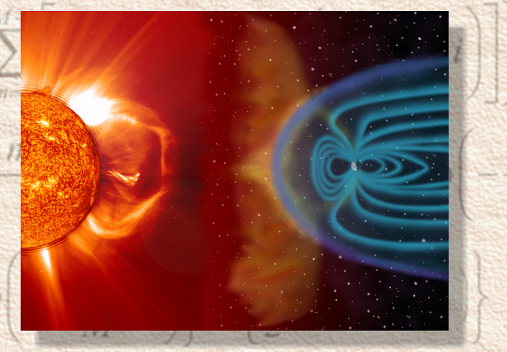

Když se Slunce rozzuří

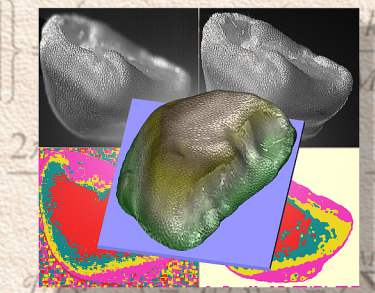

Třetí rozměr v mikroskopu

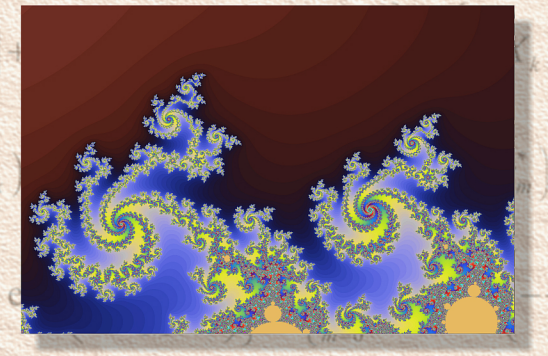

Kvadratická rovnice, to není jen parabola

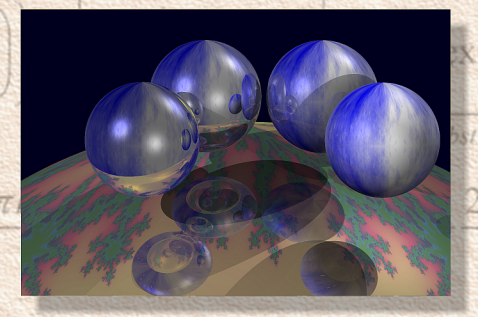

Když se světlo odráží

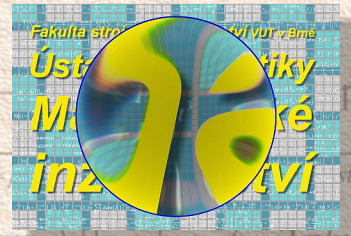

Lom paprsků v počítači

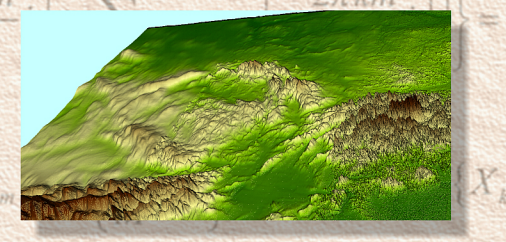

Rekonstrukce zemského povrchu

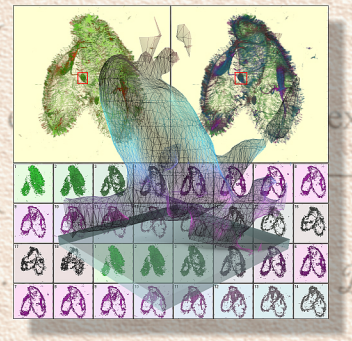

Do hlubin živé hmoty

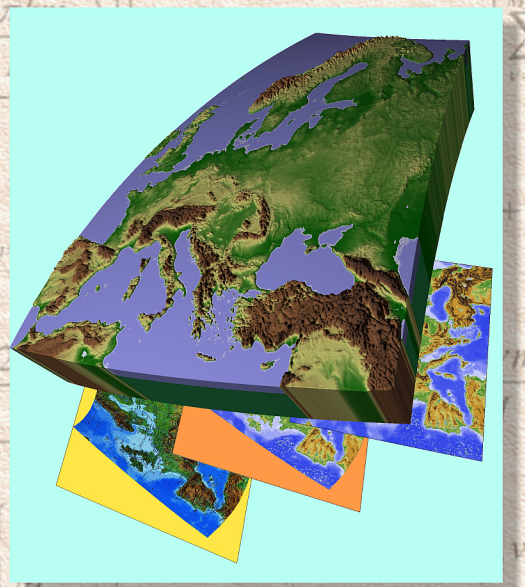

Plastická mapa i z obyčejného atlasu

Realizovaný grafický návrh

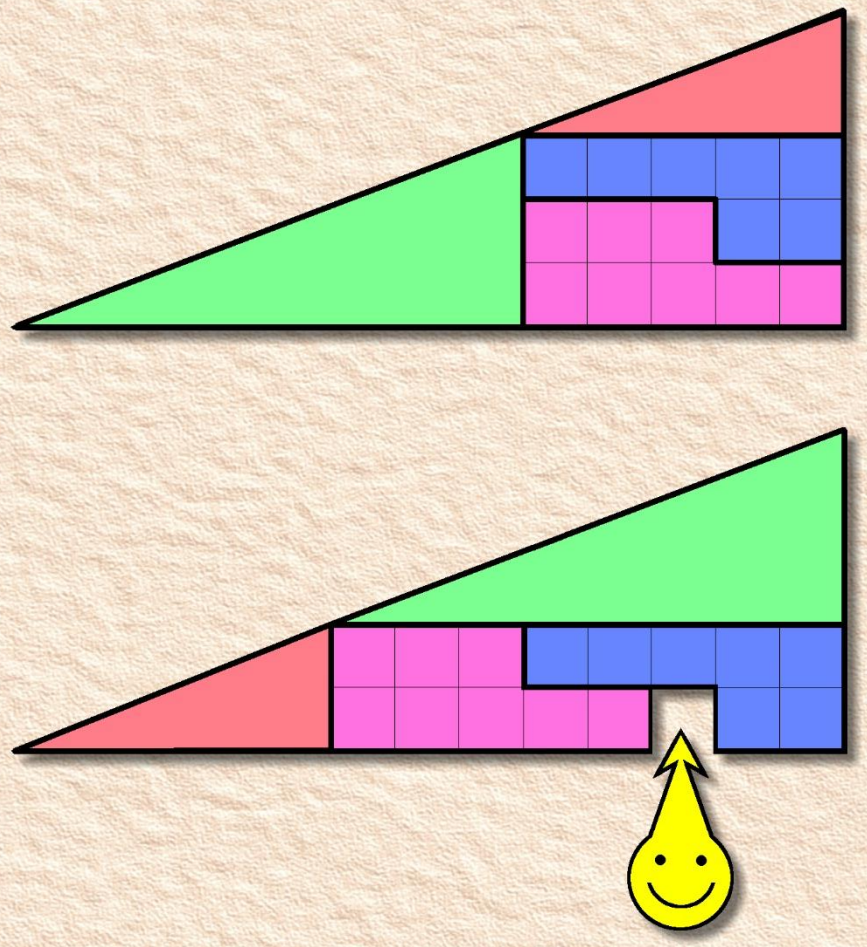

Realizovaný grafický návrh

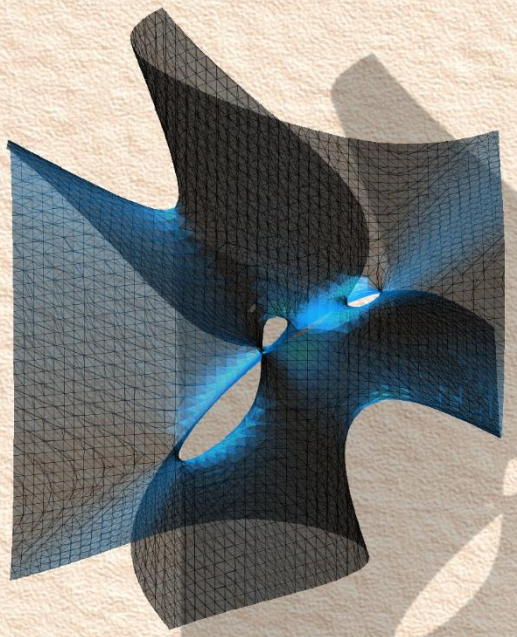

GCG 2007

Geometry & Computer Graphics

Sborník příspěvků

27. mezinárodní konference

o geometrii a počítačové grafice

Nedvědice, 10. – 14. 9. 2007